UNIVERSITÉ DE STRASBOURG

ÉCOLE DOCTORALE SCIENCES CHIMIQUES

ICPEES, UMR 7515 CNRS

THÈSE

présentée par:

Bing LI

Soutenue le: **16 Décembre 2020**

Pour obtenir le grade de: **Docteur de l'université de Strasbourg**

Discipline/ Spécialité: Chimie/Chimie

Design of mesoporous silica-coated carbon nanotubes as components of scaffolds for biomedical applications

Conception de nanotubes de carbones revêtus de silice poreuse en tant que composants de matrices implantables pour des applications biomédicales

THÈSE dirigée par:

M. BEGIN Dominique	Directeur de recherche, Université de Strasbourg, Strasbourg
M. MERTZ Damien	Chargé de recherche, Université de Strasbourg, Strasbourg

RAPPORTEURS:

M. SANDRE Olivier	Directeur de recherche, Université de Bordeaux, Bordeaux
M. CELZARD Alain	Professeur, Université de Lorraine, Nancy

EXAMINATEURS:

M. FRANCIUS Grégory	Directeur de recherche, Université de Lorraine, Nancy
Mme. MENARD-MOYON Cécilia	Chargée de recherche, Université de Strasbourg, Strasbourg

INVITES:

Mme. BEGIN Sylvie	Professeur, Université de Strasbourg, Strasbourg
M. HARLEPP Sebastien	Maître de conférence, Université de Strasbourg, Strasbourg

Acknowledgements

Time flies. It was three years since I first set foot in France. The time spent working and studying at the University of Strasbourg was an interesting and unforgettable experience. It provided me the opportunity to work and interact with the friendly and awesome people from all around the world. It will be a wonderful memory of my life. I would like to express my sincere gratitude to all those who have contributed to this work and provided help to my work and my life during this period.

This work was carried out at the Institut de Chimie et Procédés pour l'Energie, l'Environnement et la Santé (ICPEES, CNRS UMR 7515) and Institut de Physique et Chimie des Matériaux de Strasbourg (IPCMS, CNRS, UMR-7504) in the University of Strasbourg. I would like to thank my supervisor Dr. Dominique BEGIN and my co-supervisor Dr. Damien MERTZ, for their guidance, support, care and understanding during my PhD study and research. They are so professional and friendly, and always ready to help me, guide me when I am confused about my work, and provide me with clear guidance. I feel very happy and honored to be able to complete my PhD work under their guidance.

Many thanks would be given to Sylvie Begin-Colin, who always enthusiastic to provide me with help and advices; to Sebastien Harlepp, Mariana Tasso and Jacky G. Goetz for their work, targeted discussions and suggestions to chapter 2; to Loic Jierry, Miryam Criado-Gonzalez and Christophe Mélart for his work, suggestions and modifications to Chapter 3; to Guy Schlatter and Anne Hebraud, who train me the technique of electrospinning and provide me with useful suggestions to chapter 4. And many thanks to Connor Wells and Ophélie Bringel for their

work on chapter 2; and Dr. Benoit Van der Schueren for his guidance and help at the beginning of my research work. I also sincerely thank my dear friend and colleague Geoffrey Cotin, Alexandre Adam and Paula Duenas-ramirez, who are always willing to help me, introduce me interesting things, as well as French history and culture. I also want to thank Thierry Romero, who shared an office with me and always warmly did SEM for me.

My thanks are also equally given to dear my colleagues and friends for their kindly helps over and over again, as well as for bringing me the memorable memories of my life: Cuong Pham-Huu, Jean-Mario Nhut, Fabrice Vigneron, Thierry Dintzer, Secou Sall, Loic Mager, Cuong Duong-Viet, Lai Truong-Phuoc, Ba Housseinou, Anurag Mohanty, Jagadeesh Yerri, Meng Liang, Wei Wang, Xion Zhang, Ahmed Essyed, Ahmed Aitkhouya, Celine Kiefer, Francis Perton, Kevin Sartori, Pier Berling, Joëlle Bizeau, Barbara Freis.

And I would also like to thank the faculty, administrative staff and technical staff of ICPEES and IPCMS for their friendly help. I would also like to express my great thanks to the Chinese Scholarship Council (CSC) for the grant during my PhD at the University of Strasbourg.

Finally, I will end by thanking my love ones: my family, my in-laws and my friends for their support and affection, and especially my husband, Zhenxin XU for everything he has done for me.

Merci!

Table of Contents

Abbreviations, acronyms and symbols

CBMs	Carbon based materials
CNTs	Carbon nanotubes
SWCNTs	Single-walled carbon nanotubes
MWCNTs	Multi-walled carbon nanotubes
GO	Graphene oxide
rGO	Reduced graphene oxide
CB	Carbon black
GCB	Graphitized carbon black
CDs	Carbon dots
GCDs/GDs	Graphene quantum dots/Graphene dots
MCMs	Mesoporous carbon materials
NDs	Nanodiamonds
MS	Mesoporous silica
SPMS	Small pore mesoporous silica
LPMS	Large pore mesoporous silica
STMS	Stellate mesoporous silica
IBAM	Isobutyramide
APTS	3-aminopropyltriethoxysilane
IBC	Isobutyryl Chloride
Et_3N	Triethylamine
TIB	1, 3, 5-Triisopropylbenzene
TEOS	Tetraethyl orthosilicate
CTAB	Cetyltrimethylammonium bromide

CTATos	Cetyltrimethylammonium p-toluenesulfonate
AHMPD	2-Amino-2-(hydroxymethyl)-1,3-propanediol
HSA	Human serum albumin
HSA^{FITC}	Human serum albumin grafted with fluorescein isothiocyanate
DOX	Doxorubicin hydrochloride
FITC	Fluorescein isothiocyanate
AP	Alkaline phosphatase
AP^{FITC}	Alkaline phosphatase grafted with fluorescein isothiocyanate
Fmoc-FFpY	Fmoc: fluorenylmethyloxycarbonyl, F: phenylalanine; Y: tyrosine; p: phosphate group
HNO_3	Nitric acid
H_2SO_4	Sulfuric acid
EtOH	Ethanol
NaOH	Sodium hydroxide
NH_4NO_3	Ammonium nitrate
$NaHCO_3$	Sodium bicarbonate
$CaCl_2$	Calcium chloride
NH_4OH	Ammonium hydroxide
DMF	Dimethylformamide
DCM	Dichloromethane
DMSO	Dimethylsulfoxide
DMEM	Dulbecco's modified eagle medium
EG	Ethylene glycol
PNP	Paranitrophenylphosphate

pNPP-Na	4-Nitrophenyl phosphate disodium salt hexahydrate
PN	Paranitrophenol
Borax	Sodium tetraborate anhydrous
NBCS	Newborn calf serum
FBS	Fetal bovine serum
NEAA-MEM	MEM non-essential amino acid solution
Algin	Alginic acid sodium salt from brown algae
PEO	Polyethylene glycol
PF127	Pluronic F127
PLA	Polylactic acid

Résumé

1. Introduction

Au cours des dernières années, les nano-matériaux à base de carbone (CBMs) sont devenus des nanomatériaux très attractifs dans le domaine de la science et de la technologie. En raison des dimensions structurelles uniques et des excellentes propriétés mécaniques, électriques, thermiques, optiques et chimiques des CBMs (tels que les nanotubes de carbone (CNTs), le graphène et ses dérivés (oxyde de graphène (GO) et oxyde de graphène réduit (rGO)), noir de carbone (CB), carbon dots (CDs) etc.), ils offrent des opportunités intéressantes pour diverses applications dans les domaines biomédicaux.[1-3] Cependant, la caractère hydrophobe des CBMs nus les rend difficiles à disperser uniformément dans le solvant en raison de l'état agglomérés, ce qui limite grandement leurs applications.[4, 5] Afin d'améliorer les propriétés de solubilité/suspension , de nombreux travaux ont été réalisés pour fonctionnaliser leur surface. Parmi divers « revêtements », les silices mésoporeuses (MSMs) se sont avérées des matrice idéales en raison de leur capacité d'adsorption moléculaire élevée dû à leur grande surface spécifique, de leur compatibilité biologique et de leur excellente dispersion dans les milieux liquides, et notammment aqueux.[6, 7] Par conséquent, la modification de la surface des CBMs par un revêtement de silice mésoporeuse (MS) pour synthétiser des matériaux hybrides CBMs/MS est un moyen efficace de surmonter ces limitations. Les composites CBMs/MS présentent d'excellentes performances globales, non seulement en conservant les caractéristiques uniques des CBMs, mais aussi en ajoutant les propriétés exceptionnelles de la matrice MS.

Les premières recherches sur les composites CBMs/silice ont été réalisées à partir de composites avec une coque de silice non poreuse. Toutefois, la très faible surface externe de la silice non poreuse est considérée comme un inconvénient car elle offre une capacité relativement faible par rapport aux matériaux de silice poreux.[8] Par rapport au revêtement de silice non poreuse, la matrice MS offre de nombreuses autres caractéristiques uniques, telles qu'une structure mésoporeuse stable, une grande surface, une taille de pore réglable et des propriétés de surface bien définies.[9] Les propriétés poreuses distinctives des composites CBMs/MS leur permettent d'absorber diverses molécules de tailles, formes et fonctionnalités différentes, élargissant ainsi le potentiel d'applications de ces nouveaux systèmes multifonctionnels contrôlables.[7, 10, 11] Il est à noter que la taille des pores de la matrice MS joue un rôle clé dans la détermination de la taille de la cargaison qui peut être absorbée par les

mésopores.[12]

De nombreuses stratégies différentes ont été développées pour synthétiser la matrice MS avec différentes tailles de pores à la surface des CBMs. Parmi elles, la synthèse de composites CBMs/MS avec une petite taille de pore de 2 à 5 nm (CBMs/SPMS) est d'une grande importance pour le chargement et le transport de cibles de petite taille, et a été largement étudiée.[7, 10, 13] De nombreux travaux ont été réalisés sur l'utilisation de la silice mésoporeuse à petits pores comme matériau de matrice pour encapsuler les CNTs. Une fois que les CNTs sont chimiquement oxydés, leur surface peut être fonctionnalisée avec des groupes hydroxyles ou différents types de fragments, ce qui est une base importante pour l'auto-assemblage des des MSMs à leur surface.[6, 10] La méthode courante de fabrication des nanocomposites CNT/MS est une méthode modifiée de T. Hyeon pour pour revêtir les NP d'oxyde de fer d'une enveloppe MS.[14] Ce processus de synthèse simple sert de protocole standard pour la préparation de nanostructures d'enveloppe MS à petits pores, et la plupart des matériaux hybrides CNT/SPMS sont synthétisés en conséquence.

Les matériaux hybrides CBMs/MS à grande taille de pores (supérieure à 5 nm) (CBM/LPMS) ont également attiré beaucoup d'attention en raison de leurs caractéristiques poreuses souhaitables pour charger des molécules de haut poids moleculaire. Inversement, la petite taille des pores des composites CBMs/SPMS empêche les grosses molécules de pénétrer dans les pores internes de la matrice MS, ce qui entraîne une utilisation inefficace de la grande surface interne fournie par ces pores.[15, 16] Il est donc très important de construire des hybrides CBMs/MS avec une taille de pores suffisante pour explorer l'application de l'adsorption sélective par la taille des grandes molécules telles que les protéines et les médicaments macromoléculaires. De nombreuses stratégies ont été développées pour synthétiser les matériaux de MS à larges pores avec différentes morphologies et tailles de pores. Cependant, l'encapsulation des CBMs avec des coquilles MS à larges pores est encore difficile, et seuls quelques exemples existent dans la littérature. Récemment, Dillon et al. ont démontré la préparation de MWCNTs conventionnels à revêtement MS avec une grande taille de pores de 6-8 nm en utilisant une voie sol-gel.[17] La fabrication de CNTs revêtus de MS à larges pores a également été développée via une procédure en deux étapes utilisant un agent tensioactif zwitterionique biocompatible (phospholipide), qui est différent de l'agent modèle traditionnel CTAB qui est nocif pour les biomolécules et les cellules.[18] Et les caractéristiques des pores des composites CNT/LPMS peuvent être bien contrôlées en faisant varier le rapport entre les phospholipides et les autres agents de surface traditionnels (tensioactifs cationiques, anioniques et non ioniques).

Par conséquent, ces composites CBMs/MS avec une taille de pore MS réglable, possèdent non seulement les propriétés physiques et chimiques uniques dérivées des matériaux à base de carbone, mais ils introduisent également une interface de silice plus biocompatible pour l'interaction avec les cellules et les tissus, ainsi qu'une structure mésoporeuse ajustable conçue pour des charges moléculaires de différentes tailles. Ces caractéristiques les rendent plus attrayantes pour de nombreuses applications biomédicales, montrant des applications potentielles prometteuses dans l'administration des médicaments et la thérapie du cancer, l'ingénierie tissulaire, la biodétection et l'imagerie (**Fig.1**).

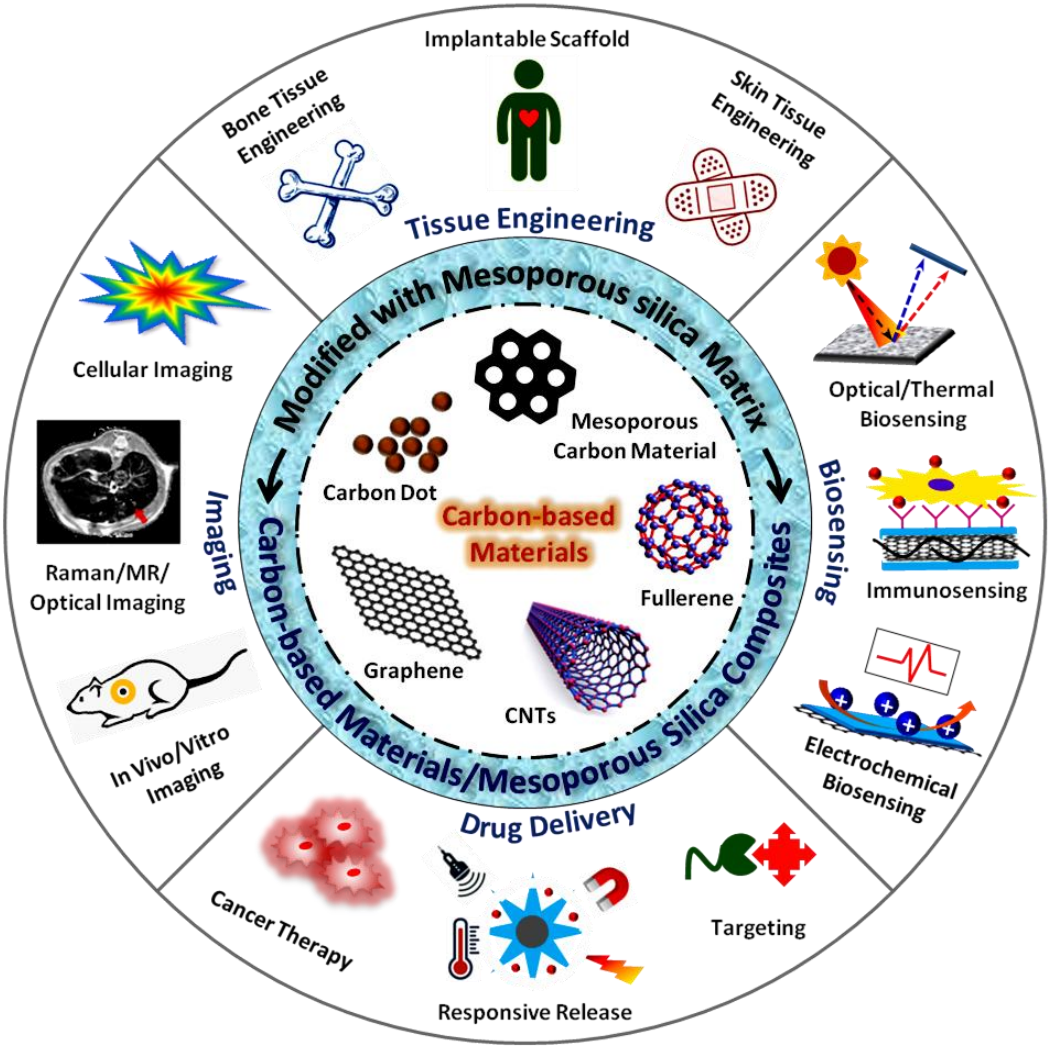

Fig.1 Applications potentielles des CBMs et des matériaux hybrides CBMs/MS dans les domaines biomédicaux, y compris l'administration de médicaments, l'ingénierie tissulaire, l'imagerie et la biodétection.

L'administration de médicaments est l'une des applications les plus étudiées des CBMs dans le domaine biomédical. Les matériaux CBMs/MS sont des "nanotransporteurs"

prometteurs pour l'administration de médicaments, car l'enveloppe de MS fournit des canaux de pores accessibles et réglables pour une charge de molécules thérapeutiques,[19, 20] et la surface de MS peut facilement être fonctionnalisée avec des groupes réagissant aux divers stimuli pour servir de « ponts intelligents » ou « gatekeepers » pour la libération contrôlée et ciblée de médicaments.[21] Le développement de matériaux CBMs/MS en tant que plateformes potentielles d'administration de médicaments pour la combinaison de thérapies anticancéreuses a émergé ces dernières années comme une piste prometteuse. En outre, les CBMs telles que les CNTs, le graphène et les CDs présentent une forte absorption optique dans la région du proche infrarouge (NIR) -une fenêtre de transparence des tissus- ce qui induit la génération d'un chauffage local à partir de ces matériaux CBMs/MS lors de l'irradiation laser NIR pour réaliser l'ablation photothermique des cellules cancéreuses.[22] Par conséquent, ces systèmes efficaces d'administration de médicaments utilisant des matériaux hybrides CBMs/MS permettent non seulement d'obtenir une capacité de charge élevée de médicaments, mais aussi de réaliser une libération contrôlée et ciblée ainsi qu'une thérapie photothermique du cancer.[7, 20, 23]

En outre, les propriétés mécaniques exceptionnelles et la conductivité élevée des CBMs jouent un rôle important dans le renforcement des matrices artificielles organiques/inorganiques, et peuvent également être utilisées pour fournir une stimulation électrique aux matrices artificielles.[24] En raison de ces propriétés très favorables, les CBMs ont été largement étudiés pour des applications d'ingénierie tissulaire, comme alternatives biologiques pour réparer ou remplacer tout ou partie des tissus, que ce soit comme matériaux de matrice ou comme matériaux de renforcement dans des nanocomposites polymères.[25] De même, les hybrides CBMs/MS sont également de candidats potentiels de choix pour le développement d'échafaudages synthétiques dans l'ingénierie tissulaire, en particulier les propriétés structurales et texturales dérivées de la matrice MS ont des applications potentielles dans le développement d'implants osseux et de ciments osseux.[26]

En outre, les CBMs présentent un large spectre d'absorption dans le visible et le proche infrarouge, une photoluminescence dans le proche infrarouge pour certains et une signature fortement marquée en diffusion Raman.[27] En raison de leurs propriétés optiques intrinsèques, beaucoup d'efforts ont été consacrés au développement des CBMs (principalement les SWCNTs, le graphène et ses dérivés et les CDs) comme sondes fluorescentes pour la bioimagerie in vitro et in vivo, allant de l'imagerie monomodale au l'imagerie multimodale, et même à la thérapie chimio-photothermique guidée par l'image.[28-31] Les propriétés optiques des composites CBMs/MS leur permettent de réaliser simultanément l'imagerie et le suivi de

la libération de médicaments, la thérapie chimio-photothermique et le double ciblage spécifique pour parvenir à visualiser la thérapie du cancer.[11, 19, 32] En même temps, en raison de leurs caractéristiques uniques de conductivité électrique, les propriétés électriques des CBMs peuvent être très sensibles aux propriétés biologiques et chimiques du milieu environnant, ce qui rend les CBMs/MS particulièrement intéressants pour les applications de biodétection.[33-35]

Cependant, en dehors des avantages des CBMs/MS , il demeure une toxicité potentielle à long terme des CBMs pour les organismes vivants et les écosystèmes.[36, 37] Avant que les composites CBMs/MS ne soient appliqués au domaine biomédical, le problème de leur cytotoxicité doit être résolu. La biodégradation des CBMs peut être un moyen sûr et efficace d'éliminer et de réduire leurs effets toxiques et de promouvoir leurs applications biomédicales.[38, 39] Par conséquent, des idées et des solutions innovantes sont nécessaires pour développer des bio-nanoplatformes efficaces, sûres et réalisables à partir de matériaux hybrides CBMs/MS.

2. Résultats de la thèse

2.1 Composites de nanotubes de carbone revêtus de silice mésoporeuse sensibles à la lumière proche infrarouge pour la photothermie combinée à l'administration de molecules antitumorales aux cellules cancéreuses

Le développement de nanocomposites multifonctionnels intelligents capables de libérer des molécules thérapeutiques sous divers stimuli externes est devenu un défi majeur ces dernières années dans le domaine biomédical. Ces nanocomposites sont conçus pour être soit injectés sous forme d'objets circulants[40, 41], soit implantés in situ dans une matrice de support polymère[42-44] pour le traitement de différents types de tumeurs. Un autre défi consiste maintenant à concevoir des nanoplateformes multifonctionnelles (NPFs) capables de combiner, en une seule formulation, deux ou plusieurs fonctionnalités, par exemple la thérapie et le diagnostic simultanés (théranostic) pour le suivi de la thérapie en temps réel, et l'action synergique de deux ou plusieurs approches thérapeutiques.

Dans ce chapitre, nous rendons compte de la conception et de l'utilisation de composites à base de carbone chargés de médicaments, incorporés dans un hydrogel biocompatible imitant l'ECM. Une nouvelle classe de nanocomposites fonctionnels à revêtement de silice mésoporeuse à petits pores (CNT@MS) a été conçue. Tout d'abord, les CNTs sont traités dans des conditions acides pour permettre d'obtenir des CNTs raccourcis avec une taille plus adaptée aux applications médicales. Leur enrobage par une coquille MS (avec une petite taille

de pores environ 3 nm) est effectué avec un contrôle précis de l'épaisseur de la coquille de silice. Ensuite, nous avons utilisé ici le greffage de groupes IBAM pour assurer une charge en médicaments élevée et un revêtement protéique final. Les greffons IBAM à la surface de la silice vont permettre de charger la DOX par des interactions non covalentes, suivi d'un revêtement d'HSA pour assurer une bonne intégrité et une surface biocompatible aux nanocomposites. Par conséquent, nous abordons ici la caractérisation complète des nanocomposites CNT@MS, leur charge en DOX et leur enrobage final en albumine du serum humain (HSA) sur CNT@MS@IBAM. Ensuite nous étudions l'efficacité de la libération du médicament lors de l'application de la lumière NIR. Divers profils de libération de médicaments en fonction du temps, de la concentration et de la puissance du laser sont présentés, démontrant la possibilité de libérer un agent therapeutique à distance par la lumière NIR. Enfin, les nanocomposites CNT@MS@IBAM-DOX@HSA chargés de médicaments sont formulés dans un hydrogel composé de divers biopolymères à matrice extracellulaire (Matrigel, hydrogel de type ECM) souvent utilisés dans le domaine des biomatériaux.[45, 46] Le développement de tels nanocomposites d'hydrogel est ainsi très intéressant pour des applications antitumorales et d'ingénierie tissulaire. En effet, l'échafaudage peut présenter certains avantages par rapport aux NPs en circulation, tels que la limitation de l'interaction avec les macrophages, ou la diminution de la perte de médicament (ou de l'administration non ciblée de médicaments) en injectant l'échaffaudage dans le site malade et en évitant ainsi certains effets secondaires.

La capacité de charge du médicament (DLC) et l'efficacité de charge du médicament (DLE) ont été utilisées comme paramètres de charge dans les composites CNT@MS fonctionnalisés. Les évolutions de ces deux paramètres ont été tracées en fonction de la concentration de DOX sur la **Fig.2**. Comme on peut le voir, la DLC augmente avec l'augmentation de la concentration de DOX de 0.25 à 8 mg/mL. À une concentration de 8 mg/mL, la DLC atteint 68%, ce qui équivaut à 0.68 mg de DOX par mg de CNT@MS@IBAM. Il est intéressant de noter que, si l'on considère l'efficacité du processus d'imprégnation des médicaments, la DLE reste constante avec les différentes concentrations, se maintenant autour de 23% quelle que soit la concentration de DOX. Un tel composite semble se comporter comme une matrice de charge qui assure une partition indépendante de la concentration entre les molécules de DOX à l'intérieur et à l'extérieur du composite. Pour l'adsorption ultérieure d'une enveloppe de HSA, trois lavages et une centrifugation ont été nécessaires pour éliminer complètement le DOX libre du surnageant, ce qui a également entraîné une fuite spontanée du DOX chargé, peu lié, diminuant le DLC de 68% à 58%.

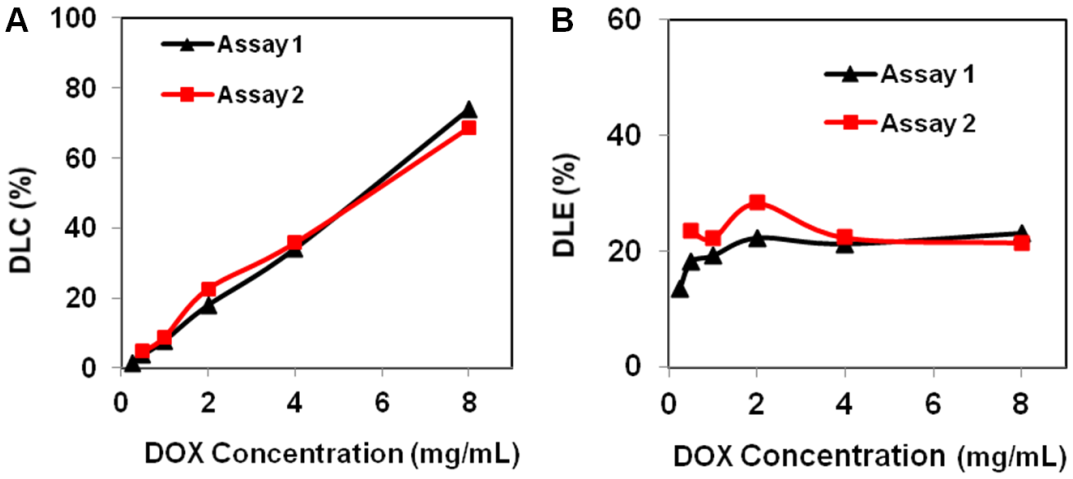

Fig.2 A) Courbes DLC et B) DLE en fonction de la concentration de DOX dans l'eau.

Les CNTs ont une forte absorbance dans la région NIR comprise entre 750 et 1400 nm et peuvent convertir la lumière NIR en chaleur locale. En ajoutant à leur surface un revêtement thermosensible, ils deviennent des nanostructures photosensibles adaptées à la libération à distance de médicaments. Nous avons supposé que la chaleur générée perturberait les interactions intermoléculaires entre le DOX et l'IBAM, facilitant la libération du DOX. Pour évaluer les propriétés photothermiques, des solutions aqueuses (1 mL) de différentes concentrations de CNT@MS@IBAM-DOX@HSA (DLC = 58%) allant de 0.32 à 2.5 mg/mL ont été exposées à un laser NIR de 1064 nm avec des densités de puissance à 1 W/cm^2. Les changements de température ont ensuite été enregistrés en fonction du temps comme le montre la **Fig.3 A**. Comme prévu, un réchauffement photothermique important de la suspension a été observé. La température de la solution sous irradiation NIR de 1 W/cm a augmenté lentement pendant toute la durée de l'essai et s'est avérée être finement ajustée en fonction des concentrations et des durées d'irradiation, de sorte que la température a pu être augmentée de manière contrôlée de 28 à 41 °C. À la densité de puissance de 2.5 W/cm^2, (non indiquée ici), on a constaté que les profils de température des suspensions ne dépendaient pas de la concentration des nanocomposites et augmentaient rapidement de 31 à 68 °C, puis restaient sensiblement constants avec l'augmentation du temps d'exposition. L'effet de la puissance est important lorsqu'il est appliqué aux cellules pour éviter leur nécrose qui est attendue au-dessus de 45 °C.[47, 48] En revanche, en observant l'effet de la lumière NIR dans la solution sans composites, la température de l'eau pure n'a pratiquement pas changé dans les mêmes conditions de puissance. Les excellentes performances photothermiques des CNT@MS, quelle que soit la puissance utilisée, en font donc un agent photothermique

efficace.

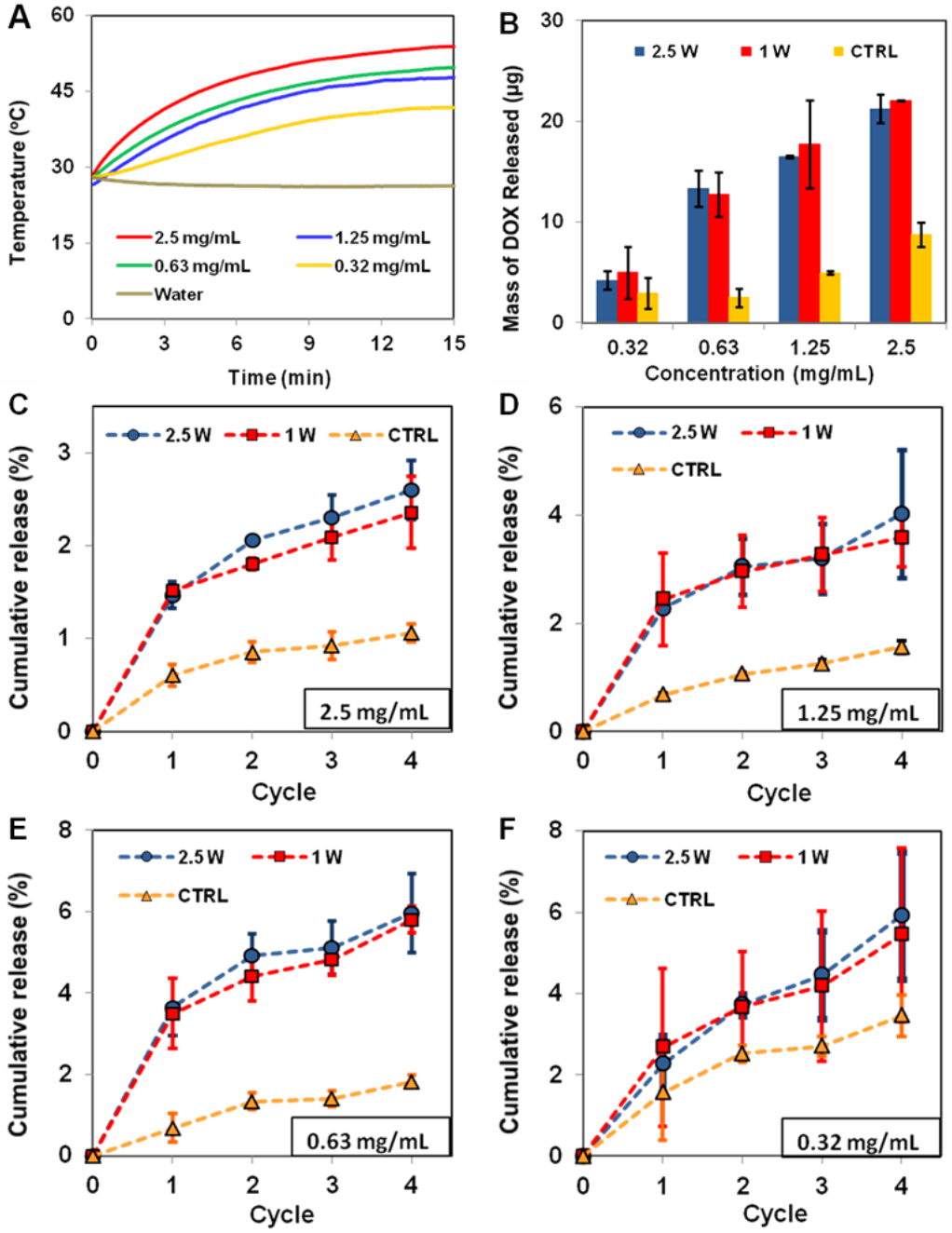

Fig.3 (A) Changements de température de la solution contenant 1 mL de CNT@MS@IBAM-DOX@HSA (DLC = 58%) à différentes concentrations lors de l'irradiation par le laser NIR 1064 nm à une densité de puissance de 1 W/cm^2. (B) Masse de DOX libérée à partir de diverses concentrations lors de l'irradiation laser NIR à des densités de puissance de 2.5 et 1 W/cm^2, et à T ambiante (CTRL). (C-F) Pourcentage cumulé du relarguage de DOX à partir de diverses concentrations lors de quatre cycles consécutifs d'irradiation laser NIR à des densités de puissance de 2.5 et 1 W/cm^2 (15 min ON, 3 jours OFF), et à T ambiante (CTRL).

La libération de médicaments contrôlée par lumière NIR du CNT@MS@IBAM-DOX@HSA (DLC = 58%) a été étudiée en mesurant la quantité de DOX libérée dans des suspensions à différentes concentrations de 0.32 - 2.5 mg/mL sous un laser NIR pendant 15 min à des densités de puissance de 1 et 2.5 W/cm^2. Pour chaque concentration, un échantillon témoin (CTRL) non exposé à la lumière NIR à température ambiante a également été pris en compte. Comme le montre la **Fig.3 B**, l'augmentation de la concentration de l'échantillon a entraîné une augmentation de la libération de DOX sous stimulation lumineuse NIR à deux densités de puissance, 1 et 2.5 W/cm^2, avec des tendances de libération de DOX très similaires pour les deux densités de puissance. Par conséquent, après les 15 premières minutes d'irradiation NIR, environ 21 et 22 µg de DOX ont été libérés à la concentration de 2.5 mg/mL sous des densités de puissance NIR de 2.5 et 1 W/cm^2, respectivement, ce qui correspond à près de trois fois celle de l'échantillon de contrôle (fuite naturelle) de 8 µg. Cette libération naturelle est attribuée à une désorption spontanée de DOX qui se produit avec le temps et qui reste cependant inférieure à celle de la photo-induite.

La libération pulsée a été étudiée en effectuant quatre cycles d'irradiation au laser NIR sur les quatre lots à différentes concentrations (0.32; 0.63; 1.25 et 2.5 mg/mL). Comme l'indique la **Fig.3 C-F**, ce système montre une libération continue, plutôt lente, de DOX en l'absence de lumière NIR, et la libération pulsée montre des salves de DOX libérées lors des irradiations NIR. Pour les nanocomposites à une concentration de 2.5 mg/mL, pendant quatre cycles de traitement NIR consécutifs, l'amélioration de la libération de DOX s'est avérée plus faible que pour la première impulsion, atteignant néanmoins un taux d'environ 5 µg DOX/impulsion. Ceci peut s'expliquer par l'agglomération observée du composite induite par irradiation NIR à la densité de puissance de 2.5 W/cm. Enfin, la quantité cumulative de DOX libérée s'est avérée être d'environ 37 et 34 µg lors de l'application du laser NIR à 2.5 et 1 W/cm^2, respectivement. Pour 1.25, 0.63 et 0.32 mg/mL, la libération cumulative de DOX a également montré une augmentation modérée mais progressive après chaque cycle d'irradiation NIR. Même si la charge de DOX est très élevée par rapport à la littérature, le pourcentage de DOX libéré indique que seulement moins de 10% de la quantité totale de DOX chargé est libéré. Néanmoins, cela permet d'envisager l'utilisation de ces systèmes pour une libération pulsatile durable et à long terme. Dans l'ensemble, ces résultats montrent que la quantité de DOX relarguée est proportionnelle à la concentration composite (à DLC égale).

La cytotoxicité des composites chargés en médicaments sans et avec une irradiation NIR a été estimée à différentes concentrations (**Fig.4**). Tout d'abord, une très faible cytotoxicité de CNT@MS@IBAM@HSA sur les cellules tumorales a été observée lorsqu'aucun rayonnement

NIR n'était appliqué (courbe jaune), indépendamment de la concentration en nanocomposite. Il est intéressant de noter que la cytotoxicité a été observée lorsque les cellules tumorales ont été soumises à des CNT@MS@IBAM-DOX@HSA (courbe bleue), qui pourraient provenir de la fuite de DOX observée précédemment à partir des nanocomposites. Avec l'irradiation par lumière NIR, les cytotoxicités des CNT@MS@IBAM@HSA et des CNT@MS@IBAM-DOX@HSA ont augmenté de manière significative, ce qui suggère que l'augmentation de T est suffisante pour favoriser un effet cytotoxique (courbes vertes et rouges). En effet, si l'on compare les nanocomposites chargés de DOX sous irradiation NIR, la libération de DOX semble augmenter modérément la mort cellulaire (DOX vs No DOX sous lumière NIR). En outre, on peut observer que nous avons obtenu un effet cytotoxique très efficace lorsque le NIR a été appliqués sur le CNT@MS@IBAM-DOX@HSA, démontrant les effets synergiques de la photothermie et de la libération de DOX (**Fig.4 B-C**).

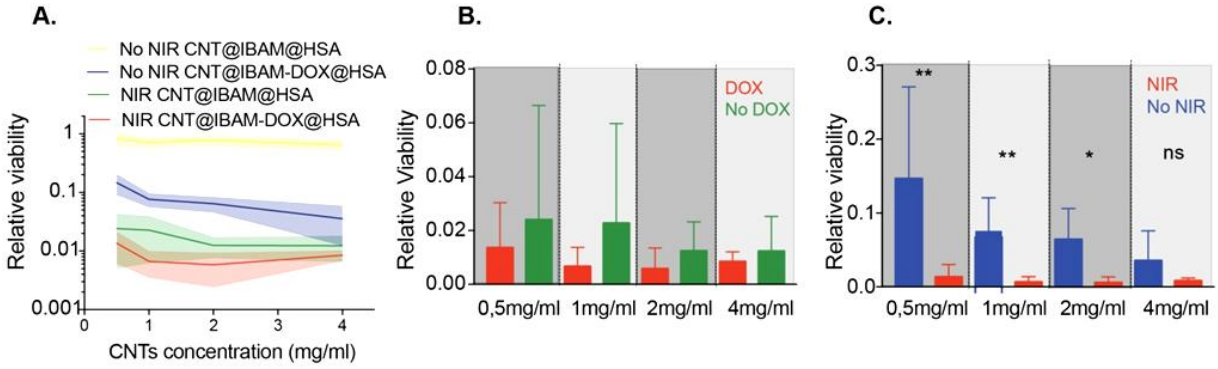

Fig.4 Résultats de l'essai de viabilité. (A) Valeurs d'émission relatives en échelle semi-logarithmique par rapport au témoin (cellules cultivées sans nanocomposites) après 24 h d'incubation avec les nanocomposites suivie de 15 min d'irradiation NIR. Les composites CNT@SPMS@IBAM@HSA (sans DOX) et CNT@SPMS@IBAM-DOX@HSA (DOX) à des concentrations de 0.5, 1, 2 et 4 mg/mL ont été pris en compte. Les valeurs moyennes et le SEM sont représentés sur le graphique. (B) Viabilité cellulaire relative extraite du graphique A, après 15 minutes d'exposition au proche infrarouge pour CNT@SPMS@IBAM@HSA (sans DOX) et CNTSP@MS@IBAM-DOX@HSA (DOX) à des concentrations de 0.5, 1, 2 et 4 mg/mL. (C) Viabilité cellulaire relative avec et sans 15 min d'exposition à la lumière du proche infrarouge sur CNT@SPMS@IBAM-DOX@HSA aux concentrations de 0.5, 1, 2 et 4 mg/mL.

Enfin, afin d'évaluer si ce système d'hydrogel chargé de nanocomposite CNT@MS@IBAM-DOX@HSA présente une cytotoxicité envers les cellules murines du cancer du sein dans des conditions 3D, nous avons évalué la croissance cellulaire en présence

de différents nanocomposites. Les cellules ont été cultivées pendant 5 jours soit dans Matrigel (contrôle sans nanocomposites), soit dans un mélange de Matrigel avec les nanocomposites à 2.5 mg/mL. Alors que le CNT@MS@IBAM@HSA n'a montrée aucune cytotoxicité cellulaire par rapport au contrôle sans nanocomposites, le CNT@MS@IBAM-DOX@HSA a entraîné une mort cellulaire significative dans ces conditions. Une telle propriété pourrait être bénéfique pour les applications antitumorales où la libération de médicaments pourrait être activée par un stimulus externe tel que la lumière NIR.

2.2 Hydrogels supramoléculaires nanocomposites assemblés par des nanotubes de carbone@silice mésoporeuse à larges pores chargés d'enzymes pour la libération de médicaments induite thermiquement

Aujourd'hui, le couplage entre la science macromoléculaire et la synthèse des nanomatériaux permet d'envisager le développement de nouveaux et puissants matériaux composites avancés réagissant aux stimuli[40, 49] pour un large éventail d'applications technologiques telles que le stockage de l'énergie[50], les matériaux autoréparables[51], la catalyse[52] ou la détection[53]. Dans le domaine de la nanomédecine et de l'ingénierie tissulaire en particulier, le développement de ces matériaux composites intelligents issus de la nanotechnologie s'est fortement développé ces dernières années.[54] Les CNTs sont un type de nanomatériaux réactifs intéressants car ils présentent des propriétés mécaniques particulièrement élevées, une conductivité électrique élevée et des propriétés d'activation thermique induites par la lumière NIR.[55] Cependant, pour les applications biomédicales, étant donné leur hydrophobie intrinsèque de surface, il est nécessaire de recouvrir ces matériaux de carbone d'un revêtement hydrophile.[56] Parmi les diverses possibilités de recouvrement décrites dans la littérature, qui englobe les molécules ou les revêtements polymères[57, 58], la silice mésoporeuse (MS) est un revêtement particulièrement intéressant.[6, 10] En effet, en plus de fournir une grande dispersion dans un tampon aqueux, les groupes silanol peuvent être facilement modifiés chimiquement avec une gamme de précurseurs de silane et la surface élevée permet le chargement avec différents types de médicaments.[59] Cependant, la grande majorité de ces concepts concernent les MS à petits pores, tandis que les composites à base de silice à gros pores autour des CNTs (ou autres CBMs) sont à peine signalés.[60] Ce type de composite à larges pores est particulièrement adapté à l'immobilisation de biomolécules à haut poids moléculaire telles qu'enzymes, DNA ou autres biopolymères d'intérêt thérapeutique. Par rapport aux stratégies d'ancrage des polymères ou des molécules, les avantages de la MS reposent sur une meilleure densité de greffage et une meilleure stabilité colloïdale.

Dans ce chapitre, nous proposons une stratégie efficace et facile à mettre en œuvre pour déclencher l'auto-assemblage d'un hydrogel supramoléculaire peptidique à partir de CNT@LPMS (ou NPs de silice à larges pores, STMS) chargés d'enzymes, qui agissent comme initiateurs de l'auto-assemblage peptidique et des points de réticulation de l'hydrogel nanocomposite résultant. L'association de CNT@LPMS avec l'hydrogel peptidique auto-assemblé en tant qu'échafaudage polymère apparaît comme une stratégie innovante pour le développement d'une nouvelle génération de nanocomposites d'hydrogel répondant à des stimuli et présentant des caractéristiques appropriées et innovantes pour des applications en nanomédecine. Nous démontrons d'abord la conception de nouveaux nanocomposites à base de carbone faits de MS à larges pores entourant les CNTs. La conception du LPMS est bien adaptée pour charger des molécules à haut poids moléculaire telles que des enzymes avec des liants de surface appropriés. Ensuite, la surface du LPMS a été fonctionnalisée avec des greffons IBAM comme excellents liants pour immobiliser l'enzyme phosphatase alcaline (AP) avec une capacité de chargement très élevée. Les activités biocatalytiques de ces AP immobilisés sur CNT@LPMS et STMS sont évaluées en suivant la conversion du substrat enzymatique des AP, le paranitrophénylphosphate (PNP) en paranitrophénol (PN). Ensuite, dans le but de créer des nanocomposites d'hydrogel peptidique auto-assemblés originaux dont l'assemblage est déclenché par l'activité catalytique de déphosphorylation de l'AP, l'auto-assemblage du peptide Fmoc-FFpY est évalué en présence de CNT@LPMS (ou de STMS, silices sans carbone)) chargés en AP. Les propriétés mécaniques de ces hydrogels nanocomposites sont étudiées en fonction de leur nature et sans/avec la charge de doxorubicine (DOX). Enfin, la capacité de ces hydrogels à se fragmenter et à libérer de la DOX en réponse à la T a été étudiée.

Les capacité et efficacité d'immobilisation de l'AP sur les CNT@LPMS@IBAM et STMS@IBAM fonctionnalisés ont été tracées en fonction de la concentration en enzymes initiale et ont été comparées aux CNT@LPMS et STMS nus (**Fig.5**). Les résultats montrent que pour les STMS et CNT@LPMS nus, les capacités d'immobilisation de l'AP augmentent avec l'augmentation de la concentration initiale d'enzymes allant de 0.1 à 4 mg/mL et atteignent la capacité de charge maximale à environ 39 µg et 127 µg AP par mg de STMS et CNT@LPMS, respectivement (à une concentration de 1 mg/mL). Bien que la capacité d'immobilisation augmente avec la concentration en AP, l'efficacité de la charge diminue à mesure que la concentration en AP augmente. Il convient de noter que la capacité d'immobilisation et l'efficacité maximales de l'AP sur CNT@LPMS sont beaucoup plus élevées que sur STMS, qui bénéficie probablement de la plus grande surface spécifique de

CNT@LPMS. La capacité d'immobilisation et l'efficacité de chargement de l'AP ont ensuite été étudiées sur les composites fonctionnels STMS@IBAM et CNT@LPMS@IBAM en fonction de la concentration initiale de AP allant de 0.1 mg/mL à 4 mg/mL. Les résultats indiquent que les capacités d'immobilisation de l'AP sur les composites STMS@IBAM et CNT@LPMS@IBAM sont grandement améliorées et que le plateau d'immobilisation maximum a été atteint lorsqu'à la concentration de AP est de 22 mg/mL. Les capacités d'immobilisation maximales de l'AP sur les composites STMS@IBAM et CNT@LPMS@IBAM sont de 4 mg et 4.3 mg de AP adsorbée par mg de composite STMS@IBAM et CNT@LPMS@IBAM (c'est-à-dire 400 % en poids et 430 % en poids), respectivement. L'effet de la concentration initiale de AP sur l'efficacité de chargement sur STMS@IBAM et CNT@LPMS@IBAM indique que l'efficacité de chargement reste d'environ 97% à la concentration étudiée inférieure à 8 mg/mL. Une diminution continue de l'efficacité de chargement a été observée avec l'augmentation continue de la concentration d'imprégnation de AP. Quelles que soient leurs concentrations, les capacités d'immobilisation de AP sur les STMS@IBAM et CNT@LPMS@IBAM fonctionnalisés sont bien plus élevées que dans le cas des STMS et CNT@LPMS nus.

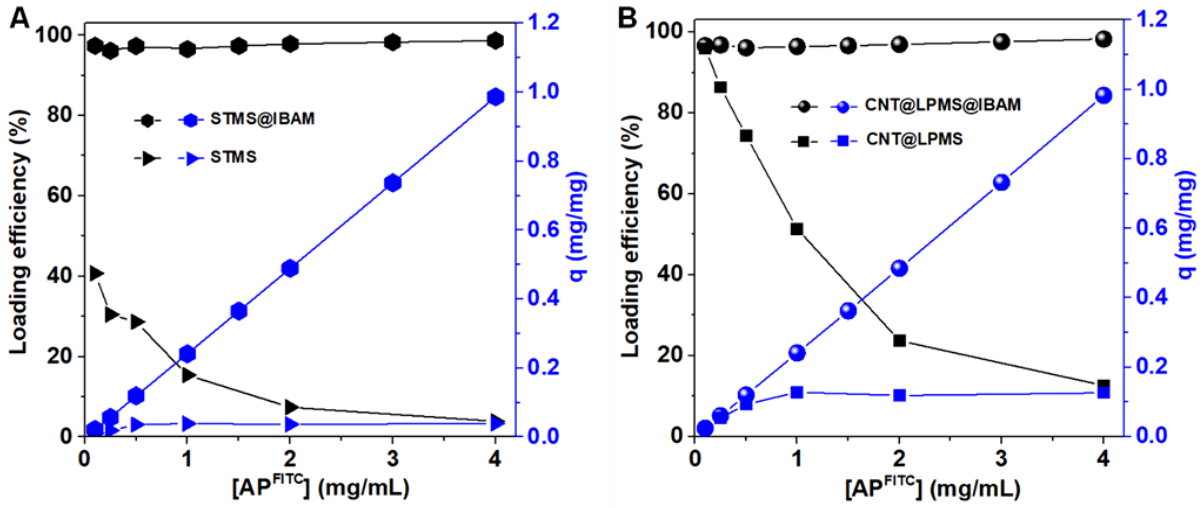

Fig.5 Capacité d'immobilisation de l'enzyme q (mg de PA adsorbée par mg de composite, courbes bleues) et efficacité de charge (en %, courbes noires) sur (A) STMS et STMS@IBAM, (B) CNT@LPMS et CNT@LPMS@IBAM, en fonction de la concentration initiale de l'enzyme.

Ensuite, l'assemblage d'un hydrogel peptidique par l'intermédiaire des nanocomposites chargées en AP pour produire une nouvelle génération d'hydrogel nanocomposite a été réalisé. L'hydrogel supramoléculaire hybride est préparé à partir du tripeptide Fmoc-FFpY, qui est

déphosphorylé en Fmoc-FFY par l'action catalytique de l'AP. Les hydrogels Fmoc-FFY auto-assemblés avec et sans DOX obtenus par STMS@IBAM+AP (100% en poids) et CNT@LPMS@IBAM+AP (100% en poids) ont été obtenus en mélangeant les nanocomposites AP-immobilisés avec le peptide Fmoc-FFpY. Les concentrations des composants Fmoc-FFpY, STMS@IBAM+AP ou CNT@LPMS@IBAM+AP et DOX dans l'hydrogel ont été fixées à 5, 0.1 et 0.5 mg/mL, respectivement. Avant la formation de l'hydrogel, le mélange de composites chargées en AP, de DOX et de peptide Fmoc-FFpY était sous forme d'une solution. Après avoir mis en contact les composites AP-immobilisés avec les peptides Fmoc-FFpY à température ambiante pendant 24 heures, les gels ont été formés et des tests de tubes inversés ont été effectués. Comme on peut le voir sur la **Fig.6 A**, des hydrogels homogènes, opaques et denses ont été obtenus à partir de ces deux composites AP-immobilisés. L'hydrogel contenant le CNT@LPMS est apparu d'une couleur gris foncé en raison de la couleur noire des CNTs. En présence de DOX, les hydrogels résultants sont apparus d'une couleur rouge uniforme et ont adhéré de manière stable et monolithique à la paroi des tubes (**Fig.6 B**), ce qui indique que le DOX était uniformément distribué dans l'hydrogel. Une couleur rouge foncé a été trouvée sur l'hydrogel avec le composite CNT@LPMS.

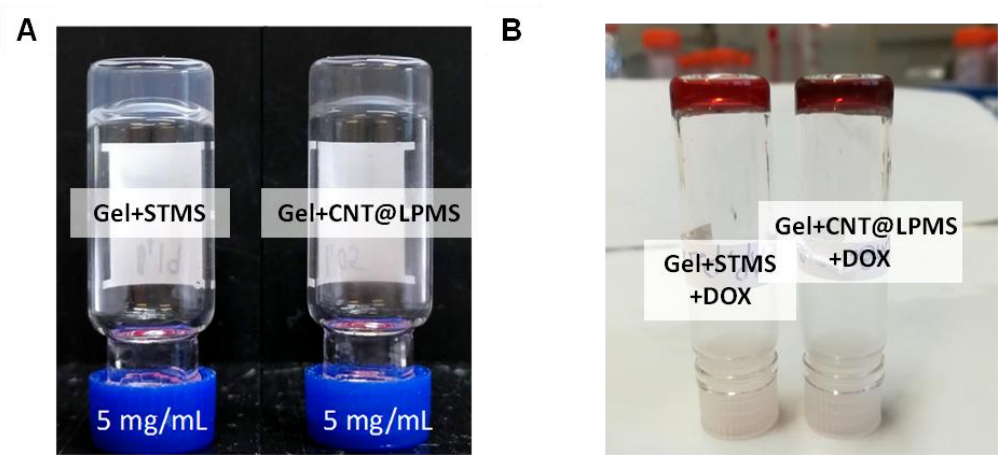

Fig.6 Tests en tube inversé d'hydrogels auto-assemblés à partir de composites chargés en AP immobilisés: (A) sans DOX et (B) avec DOX.

Après la formation de l'hydrogel avec la DOX, 1 ml d'eau distillée a été ajouté le long de la paroi du tube et la libération de DOX a été effectuée à 25 °C et 42 °C pendant 24 h. La **Fig.7 A** montre la libération de la DOX des hydrogels après 24 h de chauffage. Dans le cas des hydrogels traités à 25 °C, seule une petite quantité de DOX a été libérée des hydrogels après 24 h (environ 3 %). Inversement, la quantité de DOX libérée par les hydrogels

Gel+STMS+DOX et Gel+CNT@LPMS+DOX a augmenté lorsque les hydrogels composites ont été chauffés à 42 °C pendant 24 h, la libération atteignant respectivement 15.9% et 13.8%. Les photographies de la **Fig.7 B** montrent les hydrogels avant chauffage et une différence significative de contraste des surnageants après traitement à différentes températures.

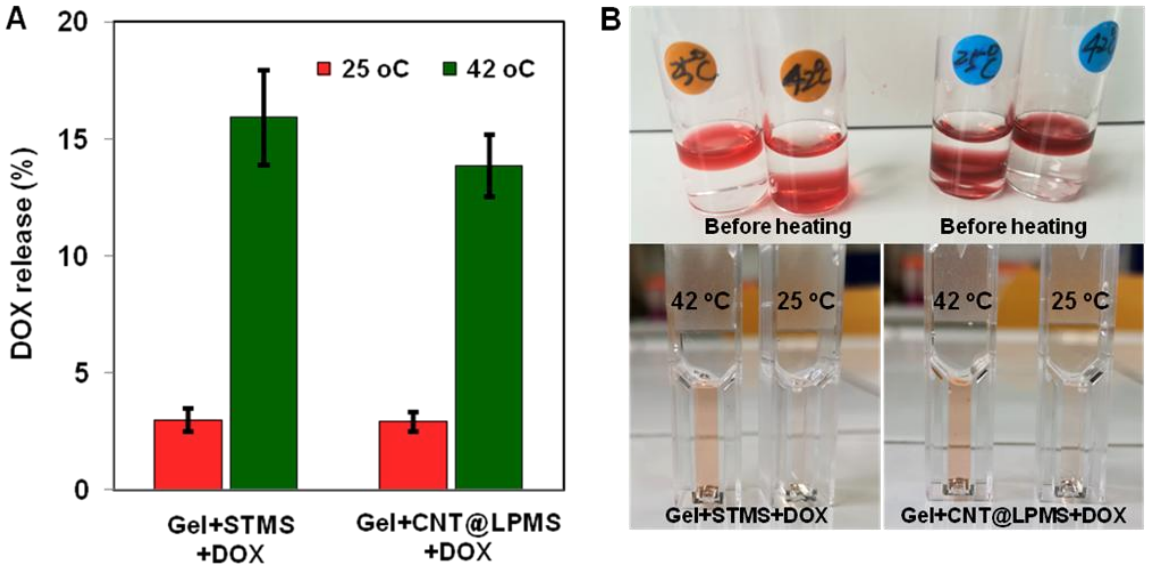

Fig.7 (A) Libération de la DOX à partir de Gel+STMS+DOX et Gel+CNT@LPMS+DOX après chauffage à 25 °C et 42 °C pendant 24 h. (B) Photographies montrant des hydrogels avant chauffage et la DOX libérée dans la solution aqueuse après traitement à 25 °C et 42 °C pendant 24 h.

Les propriétés mécaniques ont été déterminées par rhéologie oscillatoire dynamique fournissant des informations sur le module de conservation (G') et le module de perte (G") en cisaillement des hydrogels étudiés. Des balayages en déformation de 0.1 à 100% à une fréquence fixe de 1 Hz ont été effectués afin de déterminer la région viscoélastique linéaire, définie comme la région où le module de conservation (G') et le module de perte (G") sont parallèles et indépendants de l'amplitude de la déformation. Nous avons constaté que le G' des hydrogels chauffés était considérablement plus faible que celui des échantillons non chauffés. Les modules de conservation G' des hydrogels chauffés Gel+STMS+DOX(T) et Gel+CNT@LPMS+DOX(T) ont été fortement réduits de 66% et 58% respectivement. Ce résultat indique qu'une température plus élevée entraîne une perte appréciable des modules de conservation des gels, qui peut être attribuée au clivage hydrolytique des fibres d'assemblage. Ces résultats indiquent que ces hydrogels supramoléculaires auto-assemblés à partir de composites STMS et CNT@LPMS chargés en AP immobilisés devraient servir de nanoplateformes d'administration de médicaments pour la libération de DOX en réponse à

l'élévation de la température.

2.3 Échafaudages de composites à partir de nanofibres électrofilées incorporant des nanotubes de carbone@silice mésoporeuse: fabrication, propriétés et évaluation biologique

Au cours des dernières années, l'ingénierie tissulaire a été considérée comme un domaine prometteur permettant de grandes avancées prévues pour la régénération des tissus et des organes humains.[61, 62] La conception et la fabrication d'échafaudages bioactifs jouent un rôle clé dans le processus de régeneration tissulaire car ils doivent avoir la capacité de fournir un environnement physique et un support mécanique pour la croissance des cellules, de guider la croissance des cellules, de permettre aux cellules de produire leur propre matrice extracellulaire (ECM) et de promouvoir la formation de nouveaux tissus fonctionnels.[63-65] Les polymères sont utilisés depuis longtemps comme biomatériaux pour la fabrication de dispositifs médicaux et d'échafaudages d'ingénierie tissulaire. Ils peuvent potentiellement imiter de nombreuses fonctions de l'ECM native qui induisent la synthèse de tissus et d'organes.[66, 67] Parallèlement, les CNTs possèdent de nombreuses propriétés physiques et chimiques prometteuses et ont été largement explorés dans le domaine de l'ingénierie tissulaire.[68-70] Ils présentent des propriétés de résistance mécanique, d'élasticité et de résistance à la fatigue élevées, et sont d'excellents candidats pour les matériaux de renforcement dans les échafaudages d'ingénierie des tissus osseux.[71, 72] En outre, les CNTs montrent une forte absorption optique de la lumière NIR et la convertissent en chaleur locale,[73] qui peut être utilisée comme un stimulus pour contrôler à distance et induire la libération d'agents bioactifs (tels que des facteurs de croissance) pour susciter un comportement cellulaire favorable. Le revêtement de la coquille de silice mésoporeuse (MS) sur les CNTs a été décrit dans nos travaux précédents, ce qui pourrait effectivement générer une couche de MS hautement biocompatible et hydrophile pour faciliter la dispersion des CNTs en milieu liquide.[74, 75]

Une technique de synthèse efficace pour la fabrication de nanofibres composites polymères/CNTs est l'électrospinning (ES) ou la technique combinée d'électrospinning/électrospraying. L'ES est une technologie très efficace pour la fabrication d'échafaudages de nanofibres dans le domaine de la régénération des tissus, car elle permet de produire des nanofibres électrofilées continues d'un diamètre allant de quelques dizaines de nanomètres à plusieurs microns en projetant simplement une solution de polymère simple ou mixte sous un champ électrique élevé.[76, 77] La technique combinée

d'électrospinning/électrospraying est également un moyen efficace et flexible de disperser des nano-objets dans la matrice de nanofibres polymères, qui combine le procédé ES tout en projetant un liquide contenant des nano-objets sous forme de gouttelettes dans un champ électrique à haute tension.[78, 79] Par conséquent, les échafaudages électrofilés sont considérés comme une matrice prometteuse pour l'incorporation des CNTs parce qu'elles permettent d'assembler des nanofibres hybrides polymères/CNTs continues, ce qui est supérieur aux autres méthodes de fabrication de fibres discontinues traditionnelles en plusieurs étapes.

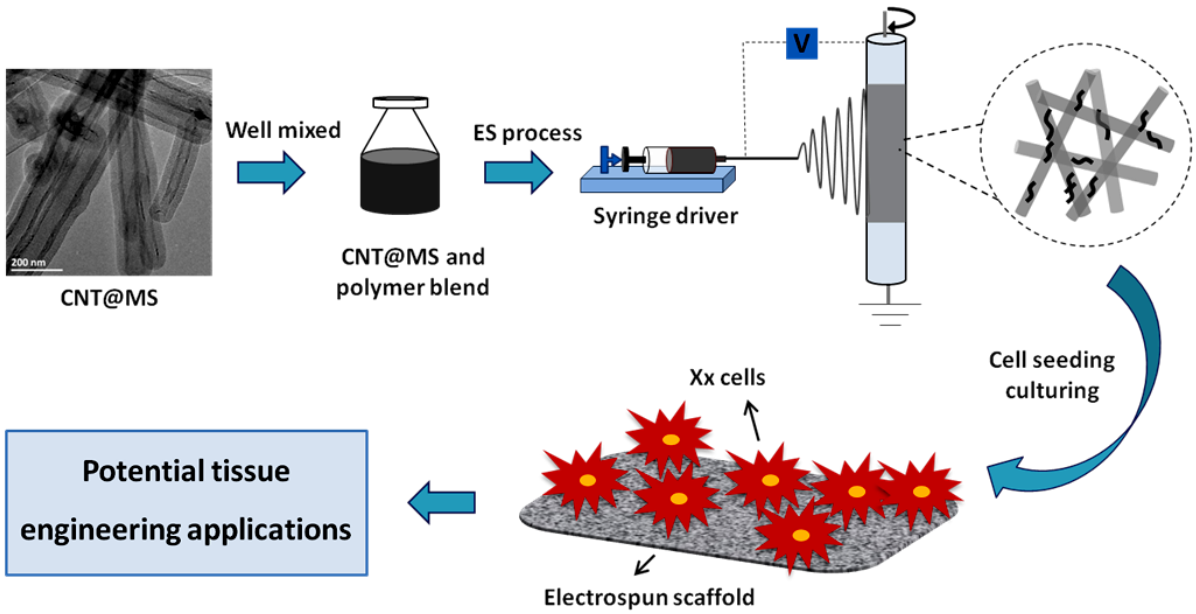

Fig.8 Schéma montrant la préparation et l'évaluation biologique des nanofibres électrofilées incorporées avec les composites CNT@MS

Dans cette étude, des nanofibres hybrides d'alginate (ALG) et d'acide polylactique (PLA) contenant des CNTs recouverts d'une enveloppe homogène de MS (CNT@MS) qui sont alignées le long de l'axe des nanofibres ont été développées en utilisant la technologie ES (**Fig.8**). Les CNTs sont des additifs très intéressants pour améliorer les propriétés mécaniques de la matrice polymère en raison de leur rapport résistance/poids élevé et de leur taille à l'échelle nanométrique. Il a été prouvé que les CNTs transfèrent efficacement les charges et améliorent la résistance et la ténacité de différents échafaudages en polymère.[80, 81] De plus, l'effet photothermique de ces échafaudages composites en nanofibres électrospinnées d'alginate et de PLA incorporé avec les CNT@MS a été étudié. La formation de tels échafaudages de nanofibres peut élargir encore l'application des CNTs dans le domaine biomédical avec une biocompatibilité améliorée, tout en améliorant les propriétés mécaniques de la matrice polymère. Enfin, l'évaluation biologique de ces nanofibres électrofilées

incorporées avec les CNT@MS a été réalisée afin d'explorer leurs applications potentielles dans le domaine de l'ingénierie tissulaire.

La **Fig.9** présente les images SEM des nanofibres électrofilées. Toutes les nanofibres électrofilées, avec ou sans CNT@MS, étaient bien formées sans perles et formaient des tapis uniformes. Il a été constaté que les nanofibres contenant du CNT@MS étaient étirées plus finement que celles sans CNT@MS dans les mêmes conditions. La présence de CNT@MS dans la solution de polymère entraîne une augmentation du changement de surface dans le jet, ce qui affecte le processus d'étirement de la nanofibre, entraînant un diamètre moyen plus petit de la nanofibre. Les images marquent plusieurs distributions typiques du CNT@MS dans les nanofibres hybrides Algin/PEO/PF127/CNT@MS et PLA/CNT@MS avec des cercles rouges. Les fibres CNT@MS de longueur plus courte et de diamètre plus petit (147 ± 10 nm) ont été attachées et dispersées le long de la surface extérieure de l'axe des nanofibres électrofilées d'alginate et de PLA sous forme d'enchevêtrements (composés d'un à plusieurs CNT@MS orientés).

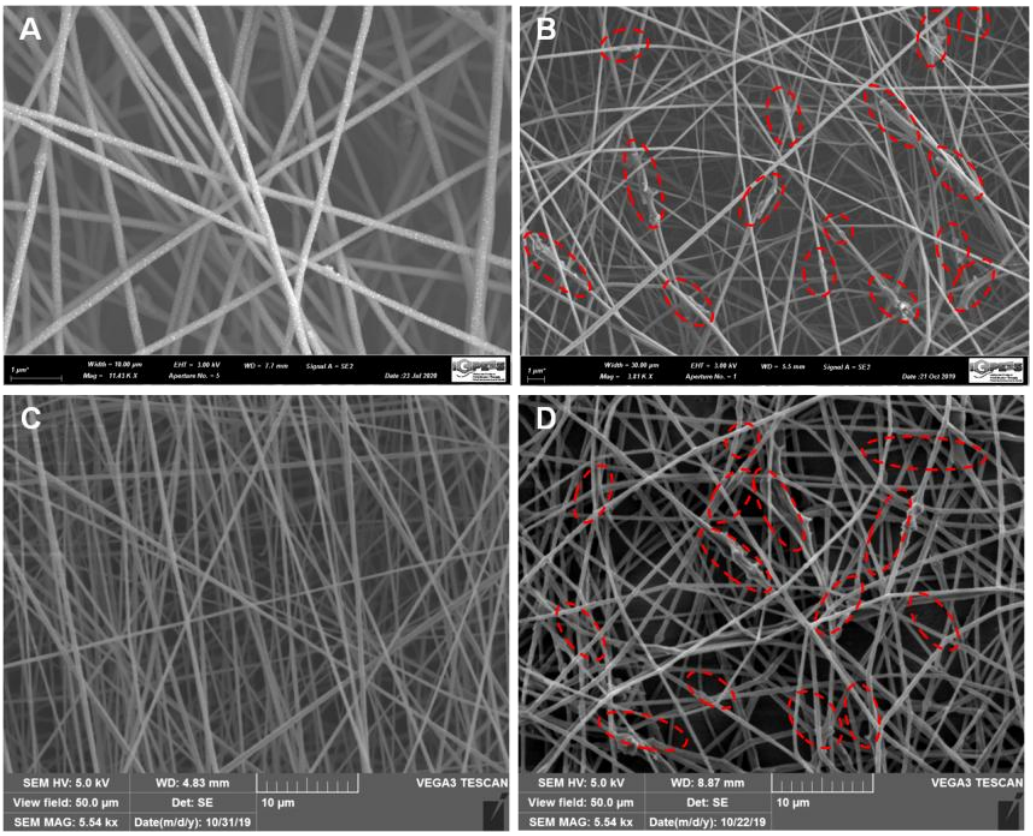

Fig.9 Images SEM de nanofibres électrofilées de (A) Algin/PEO/PF127, (B) Algin/PEO/PF127/CNT@MS, (C) PLA et (D) PLA/CNT@MS.

Pour mieux comprendre l'influence de l'introduction des CNT@MS dans les

échafaudages électrofilés d'alginate et de PLA sur leurs propriétés mécaniques, des mesures de traction ont été effectuées. Comme le montre la **Fig.10**, au cours de la phase de déformation élastique linéaire de l'étirement initial, la contrainte de toutes les membranes électrospinnées testées a augmenté rapidement avec l'augmentation de la déformation jusqu'à environ 4%, puis a augmenté lentement au cours de la phase de renforcement de la résistance à la traction jusqu'à la rupture des échantillons. Par rapport aux nanofibres Algin/PEO/PF127 et PLA, la résistance maximale à la traction des échafaudages électrofilés Algin/PEO/PF127/CNT@MS et PLA/CNT@MS a été considérablement améliorée d'environ 95% (de 0.81 MPa à 1.58 MPa) et de 57% (de 0.87 MPa à 1.37 MPa), respectivement. Cela indique que la dispersion homogène des CNT@MS dans la matrice de nanofibres électrofilées conduit à un renforcement. En effet, on suppose qu'un transfert de charge efficace de la matrice vers les CNT@MS est obtenu grâce à leur forte adhérence interfaciale, ce qui entraîne une amélioration significative des propriétés de traction. Toutefois, avec l'ajout de 5% en poids de CNT@MS dans la matrice de nanofibres d'alginate et de PLA, l'allongement à la rupture a révélé respectivement une réduction de 6% et 29%, indiquant une réduction de la ductilité de la nanofibre, qui a probablement été causée par le raidissement des fibres dû à l'adhésion des CNT@MS.

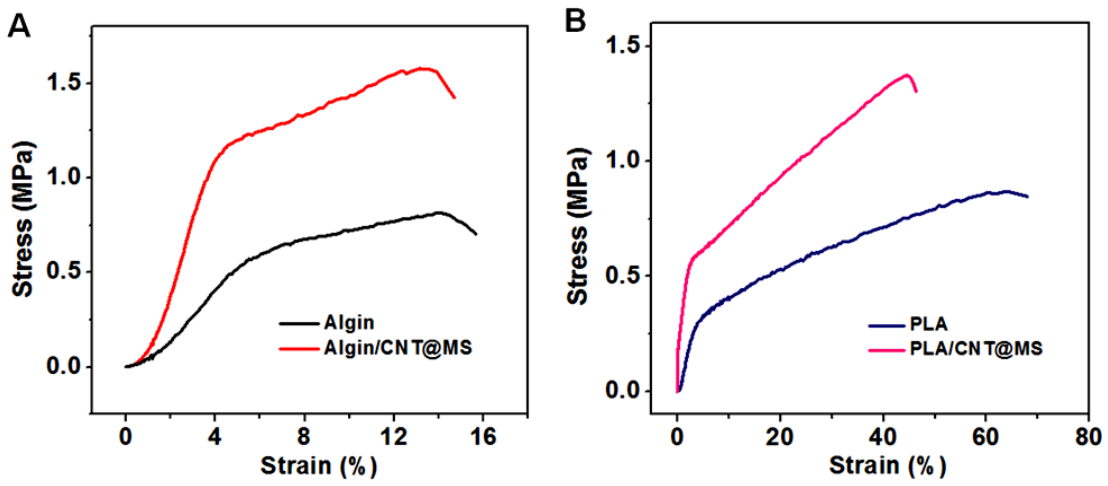

Fig.10 Courbes de contrainte-déformation des (A) échafaudages électrofilés à base d'alginate et (B) échafaudages électrofilés à base d'PLA.

Afin d'évaluer les propriétés photothermiques des échafaudages électrofilés incorporés en CNT@MS, des membrane d'alginate ou PLA de poids similaires ont été immergées dans 1 mL d'eau et exposée à un laser NIR de 1064 nm avec une densité de puissance de 1 W/cm^2 pendant 16 min. Comme le montre la **Fig.11**, les solutions contenant des échafaudages d'alginate ou PLA incorporés en CNT@MS ont présenté un effet de chauffage

photothermique significatif (courbes bleues et rouges). En effet, pour la solution contenant Algin/PEO/PF127/CNT@MS, le profil de température a augmenté lentement de 24 à 50 °C et est resté sensiblement constant avec un temps d'exposition prolongé après 14 min d'irradiation NIR (courbe rouge). De même, pour la solution contenant l'échafaudage PLA/CNT@MS, la température est passée de 24 à 46 °C avec le temps d'irradiation prolongé (courbe bleue). En revanche, en examinant l'effet de l'irradiation de la lumière NIR sur l'eau pure, on a constaté une légère augmentation de T similaire à celle des échafaudages nus, ce qui confirme que l'effet photothermique provient bien essentiellement des CNT@MS dans les échafaudages des nanofibres électrofilées.

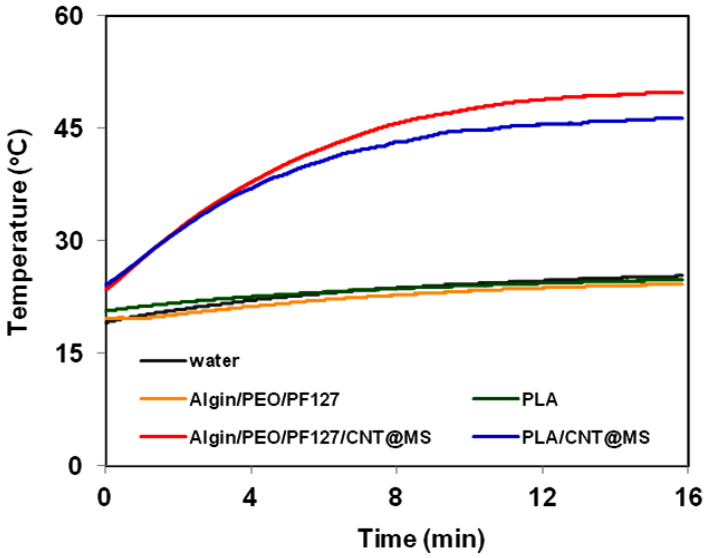

Fig.11 Propriétés photothermiques des échafaudages électrofilés à base d'alginate et de PLA.

3. Conclusion et perspectives

Des nanocomposites CNT@MS avec différentes tailles de pores ont été préparés et utilisés comme nanoplateformes pour le chargement de petites molécules de médicaments anticancéreux (DOX) et d'enzymes à haut poids moléculaire (AP), et comme composants pour la construction d'échafaudages pour des applications biomédicales que l'administration de médicaments ou les applications d'ingénierie tissulaire.

Les conclusions générales de ce travail sont résumées ci-dessous :

(1) Dans le chapitre 2, nous avons conçu de nouveaux nanocomposites photosensibles dans le proche infrarouge, constitués des CNTs recouverts d'une coquille de MS, chargés de doxorubicine (DOX), un médicament antitumoral, et recouverts d'albumine de sérum humain (HSA), une protéine plasmatique, comme interface biocompatible. Nous avons développé ici

une nouvelle façon d'immobiliser la DOX avec une DLC allant jusqu'à 80%, grâce à une stratégie efficace basée sur des liants polyvalents IBAM non covalents greffés sur des coques de CNT@MS qui permettent en outre l'ancrage de l'HSA. Les propriétés photothermiques de ces composites ont été étudiées en fonction de leur concentration et de la puissance du laser. Nous avons constaté que le réglage de la puissance à 1W/cm^2 est bien adapté pour contrôler la température sous la température de nécrose (45 °C). Il a été démontré que ces nanocomposites CNT@MS@IBAM-DOX@HSA chargés en médicaments libèrent de la DOX en réponse à la lumière NIR appliquée. Nous avons démontré que cette libération se produit d'abord par un « saut » ou « burst » qui dépend de la concentration des composites mais qui peut également être contrôlée de manière pulsée par une augmentation constante de la quantité de DOX libérée après chaque application de lumière proche infrarouge. Nous avons démontré qu'une puissance NIR de 1 W/cm^2 est efficace pour contrôler la libération de dose de DOX dans le temps. Nous avons également démontré le potentiel cytotoxique des nanocomposites chargés de DOX et mis en évidence une caractéristique potentiellement intéressante de ces nanocomposites : même si l'effet photothermique des composites de CNT@MS permet une cytotoxicité importante des cellules cancéreuses, la libération engendrée par la DOX assure une cytotoxicité supplémentaire permettant une synergie des deux effets pour tuer les cellules cancéreuses. Enfin, une autre originalité de ce travail est l'intégration de ces nanocomposites dans un hydrogel imitant la matrice extracellulaire qui peut avoir des applications potentielles dans le domaine des matrices antitumorales ou des matrices polymères pour l'ingénierie tissulaire (si la DOX est remplacée par une autre molécule). Nous avons montré ici que l'application de la lumière NIR sur un tel échafaudage d'hydrogel nanocomposite recouvert de cellules murines du cancer du sein murin D2A1 permet de déclencher la libération de DOX dans le milieu cellulaire, ce qui entraîne une toxicité cellulaire au fil du temps. Par conséquent, ces nanosystèmes peuvent présenter un intérêt considérable en tant que composants d'échafaudages implantables pour des applications antitumorales ou d'ingénierie tissulaire. Cette approche rendrait possible le développement de nouveaux (nano) dispositifs médicaux pour la médecine de demain.

(2) Au chapitre 3, une stratégie facile et originale pour déclencher l'auto-assemblage d'un hydrogel peptidique à partir de composites CNT@LPMS enrobés d'enzymes a été conçue pour l'administration de médicaments induite par la chaleur. Tout d'abord, les NTC ont été recouverts d'une couche de silice mésoporeuse homogène à larges pores, ce qui les rend particulièrement adaptés à la charge de biomolécules de haut poids moléculaire. On a constaté qu'une capacité de charge de PA ultra-élevée (jusqu'à 400 % en poids) était obtenue dans les

pores avec les liants IBAM greffés sur la surface de silice. L'excellente capacité de charge en AP des composites CNT@LPMS@IBAM leur a permis d'agir comme initiateurs pour de nombreux points d'auto-assemblage et de réticulation des peptides de l'hydrogel supramoléculaire nanocomposite résultant, permettant la croissance locale de l'architecture des nanofibres auto-assemblées de peptides à partir de la surface de silice. En outre, l'auto-assemblage de l'hydrogel peptidique sur des NP de silice sans carbone (STMS) immobilisés par AP avec des tailles de pores similaires a également été réalisé, démontrant la polyvalence de cette approche d'ingénierie de surface. En outre, une libération significative de DOX a été obtenue à partir de ces hydrogels lorsque les hydrogels chargés de DOX ont été soumis à une stimulation externe à haute température (42 °C). Des études rhéologiques ont montré que le module élastique de ces hydrogels augmentait avec l'introduction de DOX, tandis qu'il diminuait de manière significative après le traitement T (42 °C), ce qui indique que les propriétés mécaniques des hydrogels ont changé après la stimulation T et ont conduit à la libération de DOX. Les résultats ci-dessus indiquent que ces hydrogels supramoléculaires nanocomposites assemblés à partir de matériaux mésoporeux à larges pores enduits d'enzymes peuvent être utilisés comme des nanoplateformes à libération contrôlée thermosensible induite par T. L'association de nanocomposites CNT@LPMS et d'hydrogel peptidique supramoléculaire auto-assemblé comme support est une stratégie innovante qui devrait être utilisée pour développer une nouvelle génération de systèmes d'administration de médicaments sensibles aux stimuli, adaptés aux applications biomédicales.

(3) Au chapitre 4, des échafaudages en nanofibres avec incorporation de CNT@MS dans un substrat d'alginate et de PLA ont été préparés avec succès par le processus d'électrospinning. L'ajout de CNT@MS a conduit à une légère diminution du diamètre moyen des nanofibres à base d'alginate et de PLA qui en résultent. Les images SEM ont montré que les CNT@MS étaient principalement dispersés à la surface de la nanofibre polymère le long de l'axe de la nanofibre. La membrane de nanofibres incorporant les CNT@MS a montré des propriétés mécaniques de traction améliorées, ce qui a augmenté de manière significative la résistance à la traction des membranes : Algin/PEO/PF/CNT@MS et PLA/CNT@MS de 95% et 57%, respectivement. Simultanément, l'incorporation de CNT@MS sur la fibre polymère a également entraîné une légère diminution de l'allongement à la rupture des échafaudages électrospinnés se traduisant par une diminution de la ductilité. En outre, ces échafaudages de nanofibres d'alginate et de PLA incorporant des CNT@MS ont montré une bonne performance photothermique sous irradiation laser NIR, ce qui a entraîné une lente augmentation de la température de 24 à 50 °C. Ces résultats suggèrent que l'électrospinnage

de l'alginate et du PLA avec ajout de CNT@MS est une stratégie efficace pour combiner les bonnes propriétés mécaniques et optiques des CNTs afin de fabriquer un nouveau type d'échafaudage hybride biocompatible et biodégradable. Ces membranes de nanofibres d'alginate et de PLA incorporant des CNT@MS présentent ainsi de bonnes perspectives en tant que matériaux d'échafaudage pour l'ingénierie tissulaire.

Voici un résumé de certaines des perspectives découlant des résultats obtenus dans le cadre de ce travail.

Dans le chapitre 2, nous avons obtenu une très forte capacité de charge de médicaments sur les composites CNT@MS fonctionnalisés, mais la proportion de libération de DOX était très faible en réponse à la lumière NIR appliquée. Par conséquent, il est nécessaire d'explorer de nouvelles stratégies permettant d'atteindre une efficacité élevée de libération de DOX.

Au chapitre 3, le mécanisme de libération de DOX induite thermiquement et son influence sur la structure interne des hydrogels supramoléculaires peptidiques n'est pas encore bien compris et devrait être étudié en profondeur. En outre, la capacité de ces hydrogels supramoléculaires de peptides CNT@LPMS à libérer de la DOX de manière contrôlée à long terme sous irradiation laser NIR peut être étudiée plus en détail.

Au chapitre 4, nous avons confirmé les propriétés mécaniques améliorées et l'excellent effet photothermique des échafaudages de nanofibres électrofilées incorporées avec les CNT@MS, mais le solvant utilisé pour synthétiser la solution de filage est en conflit avec les composants actifs à charger sur les composites CNT@MS. Il est donc nécessaire de trouver des stratégies efficaces et fiables pour réaliser le chargement des composants actifs sur les composites CNT@MS pour les applications ultérieures dans l'ingénierie tissulaire.

En outre, la toxicité potentielle des CNT@MS pour les organismes et les écosystèmes est toujours controversée. Avant d'appliquer les matériaux composites CNT@MS au domaine biomédical, le problème de la cytotoxicité doit être résolu. Par conséquent, des idées et des solutions innovantes sont nécessaires pour développer des bio-nanoplates-formes efficaces, sûres et réalisables basées sur les matériaux hybrides CNT@MS.

Références

1. C. Cha, S. R. Shin, N. Annabi, M. R. Dokmeci and A. Khademhosseini, *ACS Nano*, 2013, **7**, 2891–2897.
2. D. Maiti, X. Tong, X. Mou and K. Yang, *Front. Pharmacol.*, 2018, **9**, 1401.
3. P. Namdari, B. Negahdari and A. Eatemadi, *Biomed. Pharmacother.*, 2017, **87**, 209-222.
4. X. Zhang, S. Wan, J. Pu, L. Wang and X. Liu, *J. Mater. Chem.*, 2011, **21**, 12251.
5. L.-Y. Meng and S.-J. Park, *Carbon lett.*, 2014, **15**, 89-104.
6. C. Wells, O. Vollin-Bringel, V. Fiegel, S. Harlepp, B. Van der Schueren, S. Bégin-Colin, D. Bégin and D. Mertz, *Adv. Funct. Mater.*, 2018, **28**, 1706996.
7. Y. Wang, K. Wang, J. Zhao, X. Liu, J. Bu, X. Yan and R. Huang, *J. Am. Chem. Soc.*, 2013, **135**, 4799-4804.
8. S. Jafari, H. Derakhshankhah, L. Alaei, A. Fattahi, B. S. Varnamkhasti and A. A. Saboury, *Biomed. Pharmacother.*, 2019, **109**, 1100-1111.
9. J. G. Croissant, Y. Fatieiev, A. Almalik and N. M. Khashab, *Adv. Healthcare Mater.*, 2018, **7**, 1700831.
10. J. Liu, C. Wang, X. Wang, X. Wang, L. Cheng, Y. Li and Z. Liu, *Adv. Funct. Mater.*, 2015, **25**, 384-392.
11. C.-W. Lai, Y.-H. Hsiao, Y.-K. Peng and P.-T. Chou, *J. Mater. Chem.*, 2012, **22**, 14403.
12. R. Narayan, U. Y. Nayak, A. M. Raichur and S. Garg, *Pharmaceutics*, 2018, **10**, 118.
13. S. Huang, L. Song, Z. Xiao, Y. Hu, M. Peng, J. Li, X. Zheng, B. Wu and C. Yuan, *Anal. Methods,*, 2016, **8**, 2561-2567.
14. H. Lim, J. Lee, S. Jin, J. Kim, J. Yoon and T. Hyeon, *Chem. Commun.*, 2006, 463-465.
15. H. J. Liu and P. Xu, *Nanomaterials*, 2019, **9**, 1-23.
16. D. Saikia, J. R. Deka, C. E. Wu, Y. C. Yang and H. M. Kao, *Mater. Sci. Eng. C*, 2019, **94**, 344-356.
17. F. C. Dillon, J. Moghal, A. Koós, J. G. Lozano, L. Miranda, H. Porwal, M. J. Reece and N. Grobert, *Microporous Mesoporous Mater.*, 2015, **217**, 159-166.
18. M. Zhang, J. Zheng, P. Xia, Y. Zheng, J. Xu, L. Chen, X. He and Q. Fang, *New J. Chem.*, 2014, **38**, 3212-3219.
19. R. K. Singh, K. D. Patel, J. J. Kim, T. H. Kim, J. H. Kim, U. S. Shin, E. J. Lee, J. C. Knowles and H. W. Kim, *ACS Appl. Mater. Interfaces*, 2014, **6**, 2201-2208.
20. L. Shao, R. Zhang, J. Lu, C. Zhao, X. Deng and Y. Wu, *ACS Appl. Mater. Interfaces*, 2017, **9**, 1226-1236.

21. M. Karimi, H. Mirshekari, M. Aliakbari, P. Sahandi-Zangabad and M. R. Hamblin, *Nanotechnol. Rev.*, 2016, **5**, 195–207.
22. Z. Liu, J. T. Robinson, S. M. Tabakman, K. Yang and H. Dai, *Mater. Today*, 2011, **14**, 316-323.
23. Q. Zhao, S. Wang, Y. Yang, X. Li, D. Di, C. Zhang, T. Jiang and S. Wang, *Mater. Sci. Eng. C*, 2017, **78**, 475-484.
24. R. Eivazzadeh-Keihan, A. Maleki, M. de la Guardia, M. S. Bani, K. K. Chenab, P. Pashazadeh-Panahi, B. Baradaran, A. Mokhtarzadeh and M. R. Hamblin, *J. Adv. Res.*, 2019, **18**, 185-201.
25. S. H. Ku, M. Lee and C. B. Park, *Adv. Healthc. Mater.*, 2013, **2**, 244-260.
26. N. Shadjou and M. Hasanzadeh, *Mater. Technol. Adv. Bio Mater.*, 2016, **31**, 806-811.
27. K. D. Patel, R. K. Singh and H.-W. Kim, *Mater. Horiz.*, 2019, **6**, 434-469.
28. J. J. Khandare, A. Jalota-Badhwar, S. D. Satavalekar, S. G. Bhansali, N. D. Aher, F. Kharas and S. S. Banerjee, *Nanoscale*, 2012, **4**, 837-844.
29. D. W. Li, Y. S. Zhou, X. Huang, L. Jiang, J. F. Silvain and Y. F. Lu, *Nanoscale*, 2015, **7**, 3651-3659.
30. N. Rubio, L. M. Hirvonen, E. Z. Chong, J. T. Wang, M. Bourgognon, H. Kafa, H. A. Hassan, W. T. Al-Jamal, D. McCarthy, C. Hogstrand, F. Festy and K. T. Al-Jamal, *Chem. Commun.*, 2015, **51**, 9366-9369.
31. L. Hou, X. Yang, J. Ren, Y. Wang, H. Zhang, Q. Feng, Y. Shi, X. Shan, Y. Yuan and Z. Zhang, *Int. J. Nanomedicine*, 2016, **11**, 607-624.
32. Y. Wang, R. Huang, G. Liang, Z. Zhang, P. Zhang, S. Yu and J. Kong, *Small*, 2014, **10**, 109-116.
33. B. Wu, C. Hu, X. Hu, H. Cao, C. Huang, H. Shen and N. Jia, *Biosens. Bioelectron.*, 2013, **50**, 300-304.
34. S. K. Maji, S. Sreejith, A. K. Mandal, X. Ma and Y. Zhao, *ACS Appl. Mater. Interfaces*, 2014, **6**, 13648-13656.
35. M. Amjadi and R. Jalili, *Biosens. Bioelectron.*, 2017, **96**, 121-126.
36. R. Madannejad, N. Shoaie, F. Jahanpeyma, M. H. Darvishi, M. Azimzadeh and H. Javadi, *Chem. Biol. Interact.*, 2019, **307**, 206-222.
37. M. Ema, K. S. Hougaard, A. Kishimoto and K. Honda, *Nanotoxicology*, 2016, **10**, 391-412.
38. Z. Peng, X. Liu, W. Zhang, Z. Zeng, Z. Liu, C. Zhang, Y. Liu, B. Shao, Q. Liang, W. Tang and X. Yuan, *Environ. Int.*, 2020, **134**, 105298.

39. M. Chen, X. Qin and G. Zeng, *Trends Biotechnol.*, 2017, **35**, 836-846.
40. M. A. Stuart, W. T. Huck, J. Genzer, M. Muller, C. Ober, M. Stamm, G. B. Sukhorukov, I. Szleifer, V. V. Tsukruk, M. Urban, F. Winnik, S. Zauscher, I. Luzinov and S. Minko, *Nat. Mater.*, 2010, **9**, 101-113.
41. S. Mura, J. Nicolas and P. Couvreur, *Nat. Mater.*, 2013, **12**, 991-1003.
42. N. S. Satarkar, D. Biswal and J. Z. Hilt, *Soft Matter*, 2010, **6**, 2364–2371.
43. Y. Zhang, J. Yu, H. N. Bomba, Y. Zhu and Z. Gu, *Chem. Rev.*, 2016, **116**, 12536-12563.
44. S. Talebian, J. Foroughi, S. J. Wade, K. L. Vine, A. Dolatshahi-Pirouz, M. Mehrali, J. Conde and G. G. Wallace, *Adv. Mater.*, 2018, **30**, e1706665.
45. S. H. Lu, Q. Lin, Y. N. Liu, Q. Gao, T. Hao, Y. Wang, J. Zhou, H. Wang, Z. Du, J. Wu and C. Y. Wang, *J. Tissue Eng. Regen. Med.*, 2012, **6**, 786-792.
46. M. W. Laschke, M. Rucker, G. Jensen, C. Carvalho, R. Mulhaupt, N. C. Gellrich and M. D. Menger, *J. Biomed. Mater. Res. A*, 2008, **85**, 397-407.
47. S. Li, S. Chien and P.-I. Brinemark, *J. Orthop. Res.* , 1999, **17**, 891–899.
48. S. S. Mambula and S. K. Calderwood, *Int. J. Hyperthermia*, 2006, **22**, 575-585.
49. D. Roy, J. N. Cambre and B. S. Sumerlin, *Prog. Polym. Sci.*, 2010, **35**, 278-301.
50. F. Alvi, M. K. Ram, P. A. Basnayaka, E. Stefanakos, Y. Goswami and A. Kumar, *Electrochimica Acta*, 2011, **56**, 9406-9412.
51. V. K. Thakur and M. R. Kessler, *Polymer*, 2015, **69**, 369-383.
52. A. Doring, W. Birnbaum and D. Kuckling, *Chem. Soc. Rev.*, 2013, **42**, 7391-7420.
53. Alamusi, N. Hu, H. Fukunaga, S. Atobe, Y. Liu and J. Li, *Sensors*, 2011, **11**, 10691-10723.
54. S. Merino, C. Martin, K. Kostarelos, M. Prato and E. Vazquez, *ACS Nano*, 2015, **9**, 4686–4697.
55. H. DAI, *Acc. Chem. Res.*, 2002, **35**, 1035-1044.
56. K. Kostarelos, A. Bianco and M. Prato, *Nat. Nanotechnol.*, 2009, **4**, 627-633.
57. Z. Liu, X. Sun, N. Nakayama-Ratchford and H. Dai, *ACS Nano*, 2007, **1**, 50–56.
58. C. Samori, H. Ali-Boucetta, R. Sainz, C. Guo, F. M. Toma, C. Fabbro, T. da Ros, M. Prato, K. Kostarelos and A. Bianco, *Chem. Commun.*, 2010, **46**, 1494-1496.
59. Z. Li, J. C. Barnes, A. Bosoy, J. F. Stoddart and J. I. Zink, *Chem. Soc. Rev.*, 2012, **41**, 2590-2605.
60. N. Z. Knezevic and J. O. Durand, *Nanoscale*, 2015, **7**, 2199-2209.
61. K. Y. Lee and D. J. Mooney, *Chem. Rev.*, 2001, **101**, 1869–1880.
62. T. L. Jenkins and D. Little, *NPJ Regen. Med.*, 2019, **4**, 15.

63. F. J. O'Brien, *Materials Today*, 2011, **14**, 88-95.
64. S. Pina, V. P. Ribeiro, C. F. Marques, F. R. Maia, T. H. Silva, R. L. Reis and J. M. Oliveira, *Materials*, 2019, **12**, 1824.
65. M. P. Nikolova and M. S. Chavali, *Bioact. Mater.*, 2019, **4**, 271-292.
66. S. A. Sell, P. S. Wolfe, K. Garg, J. M. McCool, I. A. Rodriguez and G. L. Bowlin, *Polymers*, 2010, **2**, 522-553.
67. F. M. Chen and X. Liu, *Prog. Polym. Sci.*, 2016, **53**, 86-168.
68. B. S. Harrison and A. Atala, *Biomaterials*, 2007, **28**, 344-353.
69. A. R. Boccaccini, F. Chicatun, J. Cho, O. Bretcanu, J. A. Roether, S. Novak and Q. Z. Chen, *Advanced Functional Materials*, 2007, **17**, 2815-2822.
70. E. L. Hopley, S. Salmasi, D. M. Kalaskar and A. M. Seifalian, *Biotechnol Adv.*, 2014, **32**, 1000-1014.
71. D. Mata, M. Amaral, A. J. Fernandes, B. Colaco, A. Gama, M. C. Paiva, P. S. Gomes, R. F. Silva and M. H. Fernandes, *Nanoscale*, 2015, **7**, 9238-9251.
72. X. Liu, M. N. George, L. Li, D. Gamble, A. L. Miller Ii, B. Gaihre, B. E. Waletzki and L. Lu, *ACS Biomaterials Science & Engineering*, 2020, **6**, 4653-4665.
73. J. Liu, C. Wang, X. Wang, X. Wang, L. Cheng, Y. Li and Z. Liu, *Advanced Functional Materials*, 2015, **25**, 384-392.
74. C. Wells, O. Vollin-Bringel, V. Fiegel, S. Harlepp, B. Van der Schueren, S. Bégin-Colin, D. Bégin and D. Mertz, *Advanced Functional Materials*, 2018, **28**, 1706996.
75. B. Li, S. Harlepp, V. Gensbittel, C. J. R. Wells, O. Bringel, J. G. Goetz, S. Begin-Colin, M. Tasso, D. Begin and D. Mertz, *Materials Today Chemistry*, 2020, **17**, 100308.
76. H. Liu, X. Ding, G. Zhou, P. Li, X. Wei and Y. Fan, *Journal of Nanomaterials*, 2013, **2013**, 1-11.
77. D. Ahirwal, A. Hébraud, R. Kádár, M. Wilhelm and G. Schlatter, *Soft Matter*, 2013, **9**, 3164.
78. Y. Xu, Y. Zhu, F. Han, C. Luo and C. Wang, *Advanced Energy Materials*, 2015, **5**, 1400753.
79. M. E. Darzi, S. I. Golestaneh, M. Kamali and G. Karimi, *Renewable Energy*, 2019, **135**, 719-728.
80. S. Shao, S. Zhou, L. Li, J. Li, C. Luo, J. Wang, X. Li and J. Weng, *Biomaterials*, 2011, **32**, 2821-2833.
81. X. Zhao, J. Luo, C. Fang and J. Xiong, *RSC Adv.*, 2015, **5**, 99179-99187.

Abstract

Carbon based materials (CBMs), such as CNTs, graphene and its derivatives (GO, rGO), and CDs, possess outstanding mechanical, optical, electrical and thermal properties, making them an excellent nanoplatform for extensive research and application in biomedical fields. In this thesis, carbon nanotubes (CNTs) as one of the most widely studied materials in carbon-based materials, were used to synthesize homogeneous mesoporous silica (MS) shell coated CNTs composites with tunable pore size. Such CNT@MS composites with small and large pore size were respectively used as nanoplatforms for loading of small molecule anticancer drug (DOX) and macromolecular enzyme alkaline phosphatase (AP), and as components for the construction of hydrogel scaffolds for controllable drug delivery and cancer therapy. Such CNT@MS composites were also used as a reinforcing material to be embedded in the electrospinning nanofiber scaffolds to explore the possibility of being nano-platforms for tissue engineering applications.

This thesis is organisezd in 5 chapters as briefly resumed as follows:

In chapter 1, we comprehensively reviewed the design and synthesis of CBMs/MS composites with tunable pore size of MS matrix, as well as their latest developments in biomedical applications, particularly in drug delivery, tissue engineering, imaging and biosensing.

In chapter 2, small pore mesoporous silica (MS)-coated carbon nanotubes (CNTs) nanoplatforms were designed to provide phototherapy combined with drug release mediated by NIR laser excitation. The responsive CNT@MS are chemically modified with original isobutyramide (IBAM) grafts acting as non-covalent binders, which ensure a very high drug loading capacity of the antitumor drug doxorubicin (DOX) as well as the final adsorption of a human serum albumin (HSA) shell as biocompatible interface and drug gate-keeping. The drug is demonstrated to unbind from the nanocomposite only upon photothermal excitation and to release in the solution. Such smart platforms are further shown to deliver drug upon several pulsatile NIR excitations with controlled temperature profiles. Regarding antitumor action, we demonstrate here that the NIR light induced photothermic effect from the nanocomposites is the main effect accounting for cancer cell toxicity and that DOX delivery mediated by the NIR light brings an additional toxicity allowing a synergistic effect to efficiently kill tumor cells. Finally, the DOX-loaded CNT@MS nanocomposites are embedded within a hydrogel mimicking extracellular matrix, the resulting smart responsive

scaffolds efficiently release DOX upon NIR light to the cells localized above the composite hydrogel. These results demonstrate that such nanocomposites are highly promising as new components of implantable antitumor scaffolds that are able to respond to external stimuli in time and location for a better disease management.

In chapter 3, we propose a powerful and facile strategy to trigger the self-assembly of a peptide hydrogel from enzyme-coated CNT@LPMS composites, which act as initiators of the peptide self-assembly and cross-linking points of the resulting nanocomposite hydrogel. The self-assembly by enzyme-coated (carbon free) stellate spherical large pore silica NPs (STMS) is also achieved in parallel to demonstrate the versatility of the surface engineering approach. Firstly, the design of new carbon-based nanocomposites made of large pore MS surrounding CNTs is achieved, which is well adapted for loading high MW molecules such as enzymes with suitable surface binders. Secondly, the immobilization of enzyme alkaline phosphatase (AP) with very high loading capacity (sup 100%) within the porous shell thanks to the use of IBAM grafts is demonstrated. The biocatalytic activities of such AP-coated CNT@LPMS and AP-coated STMS are then assessed by following the conversion of AP enzymatic substrate paranitrophenylphosphate (PNP) into paranitrophenol (PN). Thirdly, with the aim to create new and powerful self-assembled peptide hydrogel nanocomposites whose assembly is triggered by the dephosphorylation catalytic activity of AP, the self-assembly of Fmoc−FFpY peptide (Fmoc: fluorenylmethyloxycarbonyl; F: phenylalanine; Y: tyrosine; p: phosphate group) is assessed in the presence of AP-coated STMS or AP-coated CNT@LPMS. The mechanical properties of such nanocomposite hydrogels are investigated without/with the two types of NPs through rheological studies and depending on its nature and without/with the loading of DOX, an antitumor drug. Finally, the ability to release DOX upon T elevation is investigated.

In chapter 4, biocompatible polymers alginate and polylactic acid (PLA) hybrid nanofiber scaffolds are fabricated through electrospinning technique, in which mesoporous silica shell coated-CNTs (CNT@MS) were incorporated. Detailed optimizations were made to produce continuous and uniform nanofibers without beads or drops. The topographical features and the distribution of CNT@MS composites in nanofiber are observed by SEM. The tensile mechanical properties of the manufactured fibrous membranes are then investigated to confirm that CNT@MS composites play a role in improving the mechanical properties of the electrospun scaffolds. The synthesized hybrid CNT@MS-incorporated alginate and PLA platforms are further shown with photothermal performance under NIR laser irradiation. Finally, in vitro biological evaluation of the CNT@MS-incorporated alginate and PLA

nanofiber scaffolds was investigated to study the potential use of these electrospun nanofibrous systems as substrates for cell/tissue culture. It is expected that these CNT@MS-incorporated alginate and PLA electrospun nanofiber mats can be used as potential scaffolds for tissue engineering.

In chapter 5, we drew general conclusions based on the results obtained, and presented some perpectives that can be further explored.

Chapter 1 General Introduction

1.1 Carbon based materials

Carbon is one of the most important and most abundant elements in nature. Due to the diverse electron orbital properties of carbon (*sp*, sp^2, sp^3), it can form various forms of allotropes with unique structures and different physical properties, thus forming a huge family of carbon-based materials.[1, 2] In 1985, three scientists Richard E. Smalley, Robert F. Curl, and Harold W. Kroto discovered buckminsterfullerene (the “buckyball”) and other fullerenes for the first time, and they were awarded the Nobel Prize in Chemistry in 1996. The discovery of these "carbon cages" refreshed the scientific community's initial understanding of carbon and opened up a whole new field of chemical research.[3] In 1991, Japanese scientist Sumio Iijima fortuitously observed carbon nanotubes (CNTs) by TEM for the first time in the insoluble materials of arc-burned graphite rods.[4] After years of vigorous development, carbon based materials (CBMs) have been widely discovered and investigated. At present, CBMs such as CNTs, graphene, carbon black and carbon dots are currently widely applied in various fields such as optics, electricity, catalysis, aerospace, magnetic media, new materials, biomedicine, etc.[5-8]

1.1.1 Carbon nanotubes

Carbon nanotubes are cylindrical carbon tubes composed of hexagonal arrangements of sp^2 hybrid carbon atoms, with diameter from nanometer to tenth of nanometer and a length of a several microns. Carbon nanotubes are an allotrope form of carbon, which can be regarded as seamless tube formed by multi-layer or single-layer graphene sheets curled from an angle around a central axis. According to the number of graphene layers, carbon nanotubes are classed into two types: single-walled carbon nanotubes (SWCNTs) and multi-walled carbon nanotubes (MWCNTs). In the case of SWCNTs, the hexagonal crimping of planar carbon atoms can start from different angles, resulting in three categories of carbon nanotubes with different chiral indices (*n*, *m*): zig-zag (*n*, 0), armchair (*n*, *n*) and chiral (*n*, *m*).[9] Typical examples of these types of nanotubes are shown in **Fig.1-1**.

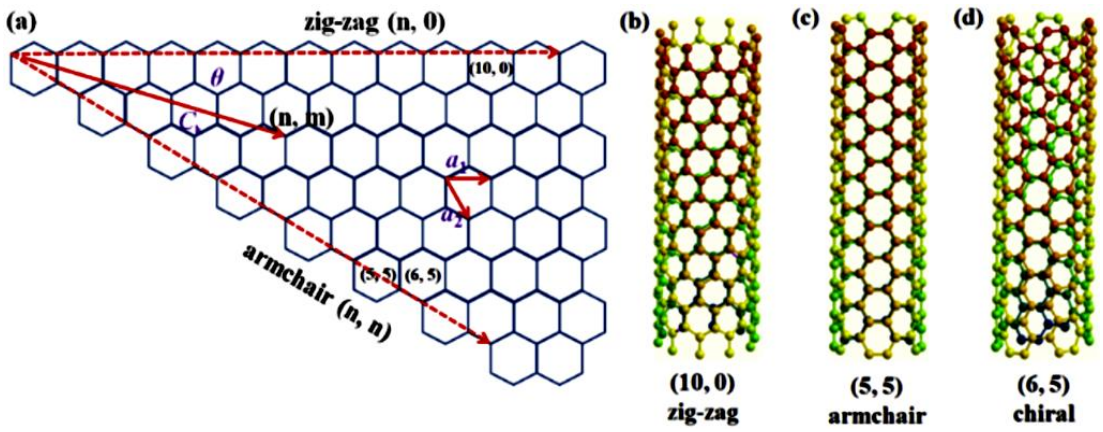

Fig.1-1 (a) Unrolled single layer graphene sheet showing the geometry of the SWCNT. Examples of the three types of nanotube sidewall: (b) zig-zag, (c) armchair and (d) chiral.[10]

CNTs have very interesting and distinctive mechanical, electrical and optical properties (**Fig.1-2**), all of which have been extensively studied.

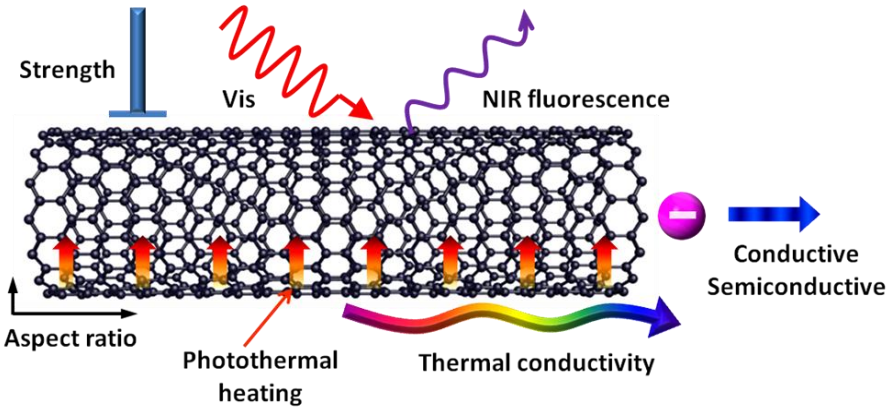

Fig.1-2 Distinctive mechanical, electrical and optical properties of CNTs

(1) Mechanical properties. CNTs are considered to be the strongest and stiffest material in nature in terms of the tensile strength and elastic modulus.[11] The Young's modulus value of SWCNT is estimated as high as 1 TPa, which is equivalent to that of diamond, about 5 times that of steel.[12] When under a great axial compressive force, the CNTs will bend and twist, and will return to its original structure without damaging.[13] The mechanical tensile strength of CNTs is up to 50-200 GPa, which is at least an order of magnitude higher than that of graphite fibers. CNTs are therefore called "super fibers".

(2) Electrical properties. The carbon atoms in CNTs are arranged in a hexagonal lattice,

and each carbon atom is covalently bonded to three neighbor carbon atoms through the sp^2 molecular orbital. Therefore, one electron in each carbon unit remains free and delocalized over all carbon atoms, which gives CNTs with remarkable electrical properties.[14] The radial confinement and specific boundary conditions of electrons in CNTs lead to inhomogeneous spatial distributions for conduction electrons, resulting in a typical quantum confinement effect.[15] Furthermore, CNTs can show characteristics between semiconductor and conductor according to the angle of carbon atom arrangement along the tube.[16]

(3) Thermal properties. The one-dimensional CNTs have a very high aspect ratio greater than 1000, so they exhibit very good thermal conductivity along the tube axis, but have extremely low thermal conductivity in the lateral direction of the tube axis.[17] Theoretical molecular dynamic simulation predicted that the thermal conductivity of an isolated CNT at room temperature is as high as 6 600 W/m/K.[18] The thermal conductivity of CNTs is related to many other factors, such as the arrangement of carbon atoms, the length of the tube, the number and morphology of the structural defects, and the purity of CNTs.[19, 20]

(4) Optical properties. SWCNTs exhibit efficient near-infrared photoluminescence in broad excitation (250-1500 nm) and emission (800-1700 nm) ranges. The converted excitation wavelength is within a specific near-infrared optical range, corresponding to the "optical transmission window" of biological tissues.[21] In addition, CNTs possess special light absorption characteristics, which have strong optical absorbance in the near infrared light region, and can effectively convert the near infrared radiation (NIR) into local heat.[22] The unique optical properties of CNTs have great advantages in the applications of biological imaging and photothermal therapy.

Regarding the synthesis of CNTs, there are currently three main ways:

(1) *Arc discharge method*. The arc discharge is generated by running a high DC current between two electrodes in the vacuum chamber, which is filled with a certain pressure of inert gas, and contains cathode graphite rod and anode graphite rod doped with metal catalyst (such as Co, Ni, Fe, or some other metal).[23] During the arc discharge, the anode graphite rod is continuously consumed by evaporation, CNTs and other by-products are deposited on the

cathode.

(2) *Laser ablation method*. The specific process of the laser ablation method consists of a block graphite target mixed with a metal catalyst which is placed in the middle of a long quartz tube, and the tube is heated in a furnace at 1200 ^{o}C. When a high-power laser beam is introduced, the graphite target evaporates and generates gaseous carbon under the laser irradiation. The evaporated carbon and the metal catalyst particles are carried away by the argon flow and condensed on the cooling wall and growth into SWCNTs.

(3) *Chemical vapor deposition method*. Chemical vapor deposition (CVD) method is one of the most popular methods for preparing CNTs. This method allows producing a large quantity of controlled and ordered CNTs under milder conditions.[24] The final morphology and characteristics of CNTs produced by CVD have a great relationship with the synthesis parameters such as operating pressure, reactor temperature, carbon source, deposition time, catalyst support, active metal component, and so on.[25-27]

1.1.2 Graphene

Graphene is a two-dimensional nanosheet composed of sp^2 hybrid carbon atoms arranged in honeycomb lattice. It is the basic component of all other allotrope form of graphite materials, which can be wrapped into 0 D fullerenes, rolled into 1D CNTs or stacked into 3 D graphite (**Fig.1-3 A**).

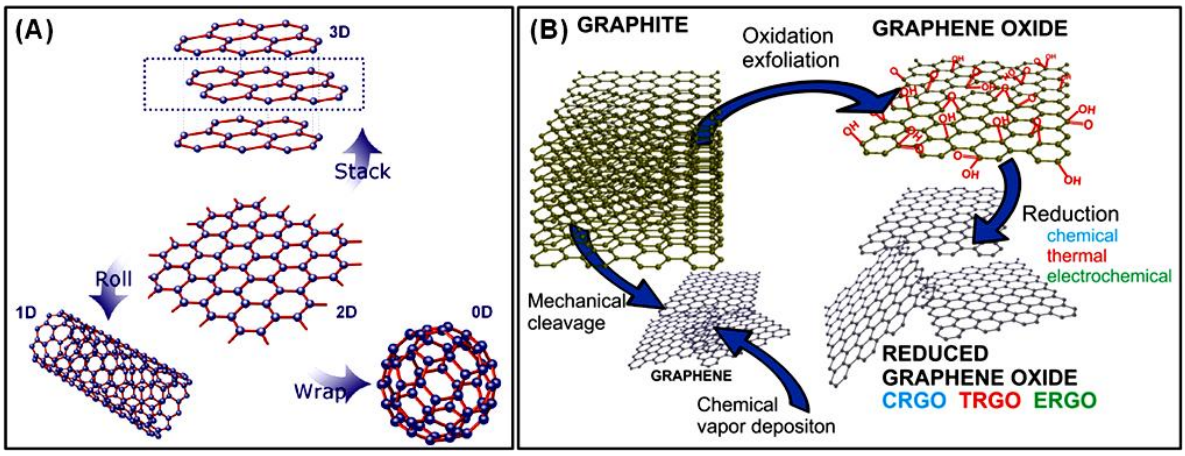

Fig.1-3 (A) Graphene: the basic building block for other carbon allotropes, graphite (3D), fullerene (0D), and CNT (1D).[28] (B) A schematic illustration of possible ways for preparation

of graphene and rGO.[29]

Since the first isolation of graphene via mechanical exfoliation of graphite by Geim, Novoselov and co-workers in 2004,[30] the study of graphene and its derivatives has always been a research hotspot in various fields of science and engineering.[31, 32] Graphene materials have been widely used because of their unique physical and chemical properties such as the high specific surface area (theoretically 2630 m^2/g),[33] great electrical conductivity of 1738 S/m,[34] strong mechanical strength (about 1100 GPa),[35] and excellent thermal conductivity of about 5000W/m/K.[36] In addition, graphene based materials possess excellent electrochemical and optical properties, as well as the ability to absorb a variety of aromatic biomolecules through π-π stacking interaction.[37] Moreover, thanks to its intrinsic near-infrared (NIR) absorbance, graphene oxide (GO) can be used as a photothermal agent.[38] Graphene can be easily modified with targeting ligands due to the large number of oxygen-containing groups thereon.[39]

So far, great progress has been made in the preparation of graphene and its derivatives. Different synthetic routes can be generally divided into bottom-up and top-down approaches. The bottom-up strategy refers to the direct synthesis of graphene from carbon sources by the means of CVD process. While the top-down approach is based on the treatment of pre-existing graphite materials, including the exfoliation of graphite through mechanical and liquid-phase such as ball milling and ultrasonication. Ten years ago, the modified Hummers method was the most used with a strong acidic treatment, but the resulting product was GO of poor quality, which should be reduced into reduced graphene oxide (rGO) for different applications (**Fig.1-3 B**).[40] Nowadays, the direct exfoliation of graphite into graphene by ultrasonic treatment in the presence of surfactants is a convenient method for generating high-yield and pure graphene.[41]

1.1.3 Carbon black

Carbon black (CB) is essentially composed of elemental carbon (higher than 97 wt%) in the form of extremely agglomerated fine particles with amorphous molecular structure.[42] CB has been widely used in many fields of modern life from black coloring pigment to electric

conductive agents due to its low cost, extensive physical and chemical properties. CB possesses a typical particle size range of 10 nm to 500 nm, and excellent electrical and thermal conductivities.[43-45] CB can be produced by incomplete combustion of petroleum products (typically acetylene), or thermal decomposition of gaseous or liquid hydrocarbons under controlled conditions.[46] The characteristics of a particular type of CB depend on the manufacturing process. More than 80% of the CB in the world is made by the furnace process. Another form of CB is graphitized carbon black (GCB), which is a non-porous form of amorphous carbon. The GCB powder is composed of highly agglomerated nanoparticles with a spherical morphology and a core-shell structure, which has been observed from high-resolution TEM images (**Fig.1-4**).

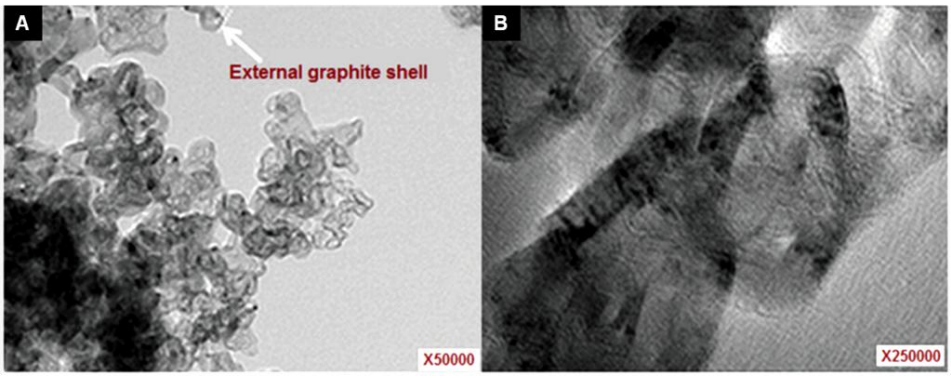

Fig.1-4 TEM images of GCB material.[47]

1.1.4 Carbon dots

Carbon dots (CDs) are a kind of carbon nanoparticles with particle size lower than 10 nm, which is mainly composed of sp^2 hybrid conjugated carbon.[48] CDs have received widespread attention since Xu et al. first accidentally discovered them in 2004 and have become a new star in the field of carbon nanomaterials.[49] CDs exhibit unique and tunable properties, including the excellent chemical stability, good water solubility, excellent biocompatibility, and special near-infrared fluorescence characteristic, as well as the significant electrochemiluminescence (ECL) emission performance.[50] Currently, CDs can be produced by a variety of synthesis methods, such as hydrothermal or solvothermal synthesis,[51] electrochemical method,[52] microwave-assisted synthesis[53] and electro-beam lithography[54].

Generally, the formation mechanism of CDs includes the “top-down” and “bottom-up” routes. The “top-down” formation is based on the cleaving or breaking down of large carbon structures such as carbohydrates and carbon fibers.[55] The "bottom-up" approach involves the pyrolysis or carbonization of small organic molecules.[56] In addition, graphene quantum dots or graphene dots (GQDs or QDs) are also a kind of CDs. The main difference is that the precursors for synthesis of GQDs are graphene based materials.

1.1.5 Fullerenes

Fullerene is a kind of symmetrical cage with 5- or 6-membered rings (12 pentagons and 20 hexagons), which is composed of sp^2 hybridized carbon.[57] Fullerenes are a unique family of carbon-based cage molecules that have attracted much attention due to their excellent performance and potential applications. The most abundant form of fullerene is Buckminster fullerene (C60) with 60 carbon atoms arranged in a spherical structure. The unique molecular structure of fullerene determines its extraordinary physical properties, including the high tensile strength, good electrical conductivity, outstanding ductility, excellent thermal conductivity and high chemical stability.[58] The general strategy for the synthesis of fullerenes is based on the synthesis of specially-designed polycyclic aromatic hydrocarbons (PAH) precursor molecules that contain the carbon skeleton required to form the target fullerene cage.[59] There are different methods for producing fullerene, the most known being the arc discharge method (like with CNTs), the incomplete combustion of benzene in oxygen and the microwave method.

1.1.6 Other CBMs

Other kind of CBMs such as mesoporous carbon materials (MCMs), nanodiamonds (NDs), etc. have also attracted much attention in recent years. MCMs with pore size in the range 2−50 nm exhibit well-defined porous structures, high pore volume, and high biocompatibility.[60] MCMs possess both the carbonaceous composition and the mesoporous structure. Compared with other carbon-based materials, MCM has superior properties, including high specific surface area, large pore volume, tunable pore size and shape.[61] Therefore, MCM becomes an ideal candidate for a series of applications such as

supercapacitors, catalysis, separation, controlled drug delivery and synergistic therapy.[62-64] NDs referring to an octahedral architecture with a size of 5-50 nm, are promising candidates for molecular theranostic applications due to their excellent biocompatibility, versatility for easy functionalization, their high adsorption capacity and their thermal properties.[65] NDs can be produced with photoluminescence in the range of 575-750 nm without fluorescence quenching and can provide magnetic properties because of their facet-specific electrostatics.[66] Therefore, the development of NDs for future applications in various fields has extensive prospects.

1.2 Carbon based materials/silica composites

CBMs are widely used in various fields of nanoscience and nanotechnology due to their unique physical and chemical properties. However, the hydrophobic characteristic of naked CBMs makes them difficult to homogeneously disperse in aqueous solvents due to their agglomeration state, which greatly limits their applications.[67, 68] In order to improve the solubility properties of CBMs, much works have been done to functionalize the CBMs surfaces with other coating materials. Among such coatings, silica material has proved to be an ideal matrix due to its high molecule adsorption capacity, biological compatibility and excellent dispersibility in liquid media.[69] Therefore, the surface modification of CBMs with silica to synthesize CBMs/silica hybrid materials is an effective way to overcome their deficiencies. The CBMs/silica composites exhibit excellent overall performance, not only maintaining the unique characteristics of CBMs, but also adding the remarkable properties of the silica material.

1.2.1 Mesoporous silica materials

According to the classification of IUPAC, the mesoporous silica materials (MSMs) are silica-based materials with ordered pore structure and a pore size between 2 and 50 nm. MSMs exhibit excellent physicochemical characteristics such as uniform and precisely tunable pore size, extremely large specific surface area, hydrophilicity, chemical functionality and thermal stability.[70, 71] In addition, both in vitro and in vivo studies have shown that MSMs also exhibit good biocompatibility and biodegradability.[72] Due to the outstanding advantages,

MSMs have a wide range of applications in adsorption and separation, catalysis, biomedical, and many other fields. Particularly, the unique ability to control properties, and outcome of MSMs make them promising for specific biomedical applications, especially for the drug delivery systems, including the delivery of small molecule drugs (molecular size <2 nm) or macromolecular drugs such as proteins and peptides.[73-75]

The vast majority of MSMs are synthesized by the sol-gel method, which was adapted from the Stöber method.[76] The typical sol-gel process involves the hydrolysis and condensation of alkoxysilanes ($Si(OR)_4$), such as tetraethylorthosilicate (TEOS). The hydrolysis stage develops colloidal micelles in aqueous solution by using a structure directing agent, which can be catalyzed by acid and base.[77] Then the silica precursor starts to condense to form a gel, and the strength and stiffness of which increase with the increase in the degree of cross-linking of siloxane. Researchers have made various improvements of the sol-gel process to prepare MSMs with controlled pore size and also with different shapes as shown in **Fig.1-5**, including the investigation of a range of surfactants or amphiphilic block copolymers as the structure directing templates.[78, 79] When the concentration of surfactant is higher than the critical micelle concentration (CMC), the surfactant molecules self-assemble with silica precursor into hierarchically ordered composite.[80] This cooperative assembly process between micelles and silica precursors plays a key role in achieving control of the geometry of desired MSMs.[81] The properties of the MSMs produced by the sol-gel method can be controlled by monitoring the reaction parameters, such as the pH and temperature of the process, the characteristics of surfactant, the concentration of silica source.[76, 82, 83]

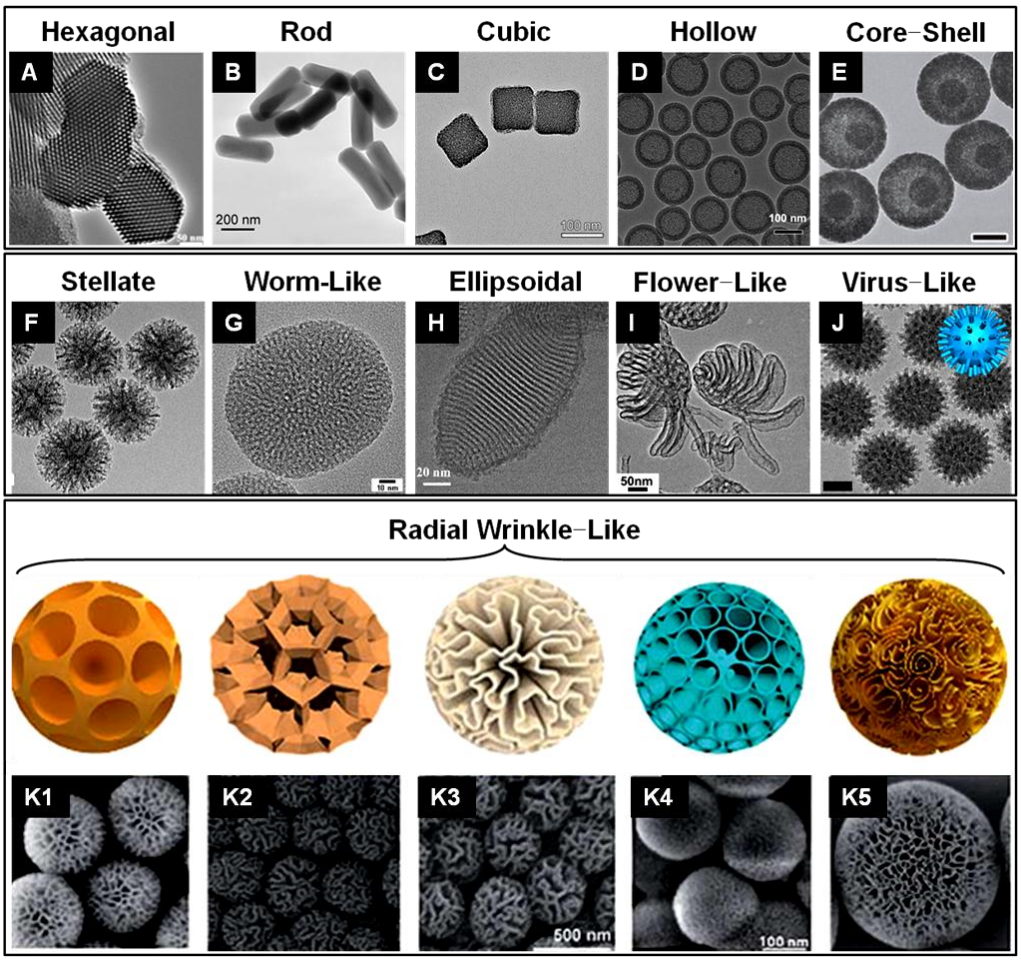

Fig.1-5 TEM and SEM images of MSMs with different morphologies and pre structures.[84-95]

With the fast development of MSMs for various applications, many requirements on the morphology and structure of MSMs have been proposed. Numerous studies have demonstrated that the performance of mesoporous silica (MS) based materials system is strongly related to their composition, morphology and structure.[96-98] Therefore, various strategies have been developed to achieve controlled fabrication of ordered MSMs with tunable pore size, diverse morphologies and mesostructures. The synthesis of MSMs in the desired mesostructures and morphologies can be obtained by selecting the appropriate structure directing agent and carefully controlling the self assembly and the reaction conditions (e.g. temperature, pH, concentration of surfactant, or addition of co-surfactant and oil phase).[76] As shown in **Fig.1-5**, up to now a large variety of MSMs with versatile morphologies such as nanospheres, nanorods, cubic core-shell and radial-like structures have

been designed and synthesized. The control of the size, morphology and multi-layer structure of MSMs is not only of a more esthetic appearance, but it can also be applied to selectively load multiple cargos of various sizes, which greatly helps to expand their applications.[99]

Among MSMs with abundant morphologies and nanostructures, an interesting design of hierarchical MSMs depicting several layers of MS has attracted tremendous attention. Lee et al. synthesized a series of hierarchical MSMs with controlled radial wrinkle structures by adjusting the water-surfactant-oil mixing ratio.[100] They observed that when the volume ratio of cyclohexane to aqueous solution was changed in the range of 0 to 1, the structure of the resulting silica NPs varied from very tight mesoporous to expanded mesoporous to mixed (or broken) mesoporous, and finally to the wrinkled structure with pore size in 15-50 nm range (see **Fig.1-6 A-J**). The triple porosity in MSMs has also been described by a continuous growth strategy. A kind of 3D-dendritic MS nanosphere with three hierarchies, tunable size and controllable center-radial mesoporous (**Fig.1-6 K-P**) was demonstrated by the team of D.Y Zhao.[89] The average pore diameter of each generation of the dendritic silica nanosphere could be controlled from 2.8 nm to 13 nm, which was monitored by adjusting the type of hydrophobic solvents and the concentration of silica source in the upper oil phase. Moreover, the thickness of each generation could be adjusted from 5 to 180 nm by controlling the reaction time and the amount of silica source.

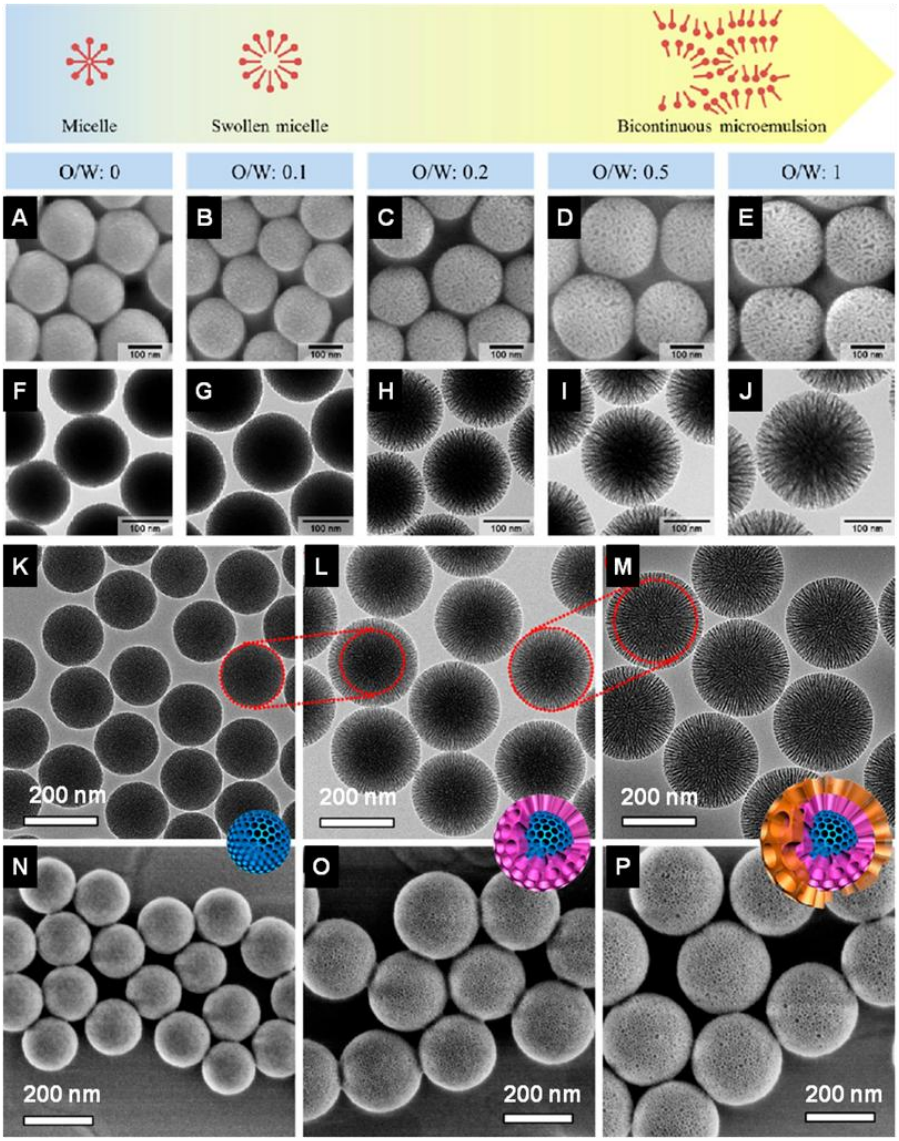

Fig.1-6 Schematic (upper panel), (A-J) SEM and TEM images showing the morphology changes of MSMs as a function of the ration of cyclohexane to aqueous solution.[100] (K-P) TEM and SEM images of the 3D-dendritic MS nanospheres with one (K, N), two (L, O), and three generations (M, P).[89]

The pore size adjustability is of great importance for practical applications of MSMs where different sizes of molecules might be involved. CTAB is the most commonly used template agent, and as a single directing agent in the sol-gel method typically produces MSMs with a pore diameter of up to 3 nm and poor particle size uniformity.[101] Hence, research on MSMs with large pores and wide pore openings is of substantial interest. Currently, many reports have been published to improve the CTAB-template system to obtain MSMs with an

expanded pore size, for example by swelling the template micelles with additives[102-104] or using a co-template method with mixed surfactants[105-107]. The dual template approach synergistically controls the micelles self-aggregated and directs the growth of MSM. A series of dendritic mesoporous silica nanoparticles (MSNs) with a controlled structure through the dual-templating strategy were prepared, in which CTAB was used as a template associated with a variety of amphipathic therapeutic agent molecules with hydrophobic chains.[108] The pore size (from several nanometers to tens of nanometers) and pore morphology of the obtained MSNs could be finely controlled by selecting auxiliary templates with different structural characteristics (**Fig.1-7**).

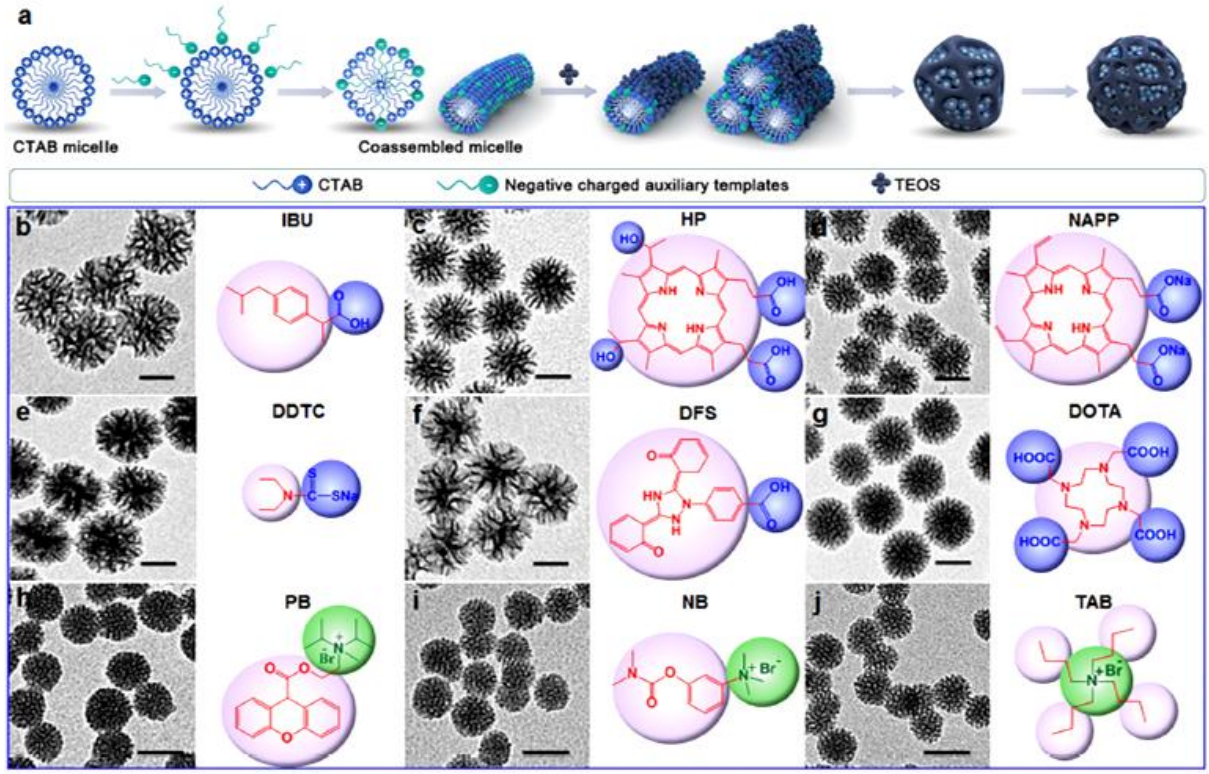

Fig.1-7 (a) Co-assembly process of CTAB and auxiliary templates with negative charge and formation mechanism of MSNs using dual templating strategy. (b-j) TEM images of MSNs using different auxiliary templates.[108]

Generally, the larger the micelle the larger the pore size, so the pore size of MSMs can be adjusted by adjusting the size of the surfactant-constructed micelle. The introduction of swelling agents causes the expansion of the hydrophobic core or the spacing of hydrophilic

heads of the surfactant-constructed micelles,[101] thus the pore diameter of MSMs can be enlarged in a large range from the well defined enlarged micelle-template structures. There are a range of compounds that can be used as swelling agents, such as benzene[109] and the alkyl-substituted derivatives of benzene[110], straight-chain alkanes[111] and long-chain amines[112]. With the use of pore-expanding agent, the pore size of MSMs can be finely controlled in a wide range while maintaining a monodispersity. **Fig.1-8** shows typical TEM images of radial pore structure MSMs with different pore sizes various from 45 to 5 nm. It is worth noting that excessive addition of swelling agent may result in the damage of structure. By consulting a large number of published papers, it is usually classified as small pore MSMs with a pore size of 2-5 nm and large pore MSMs with a pore size of >5 nm.[71, 113-115] These tunable pore structures of MSMs are ideal scaffolds for biological, medical, adsorption and catalytic applications, as the controllable pore structures are accessible by various molecules of different sizes.

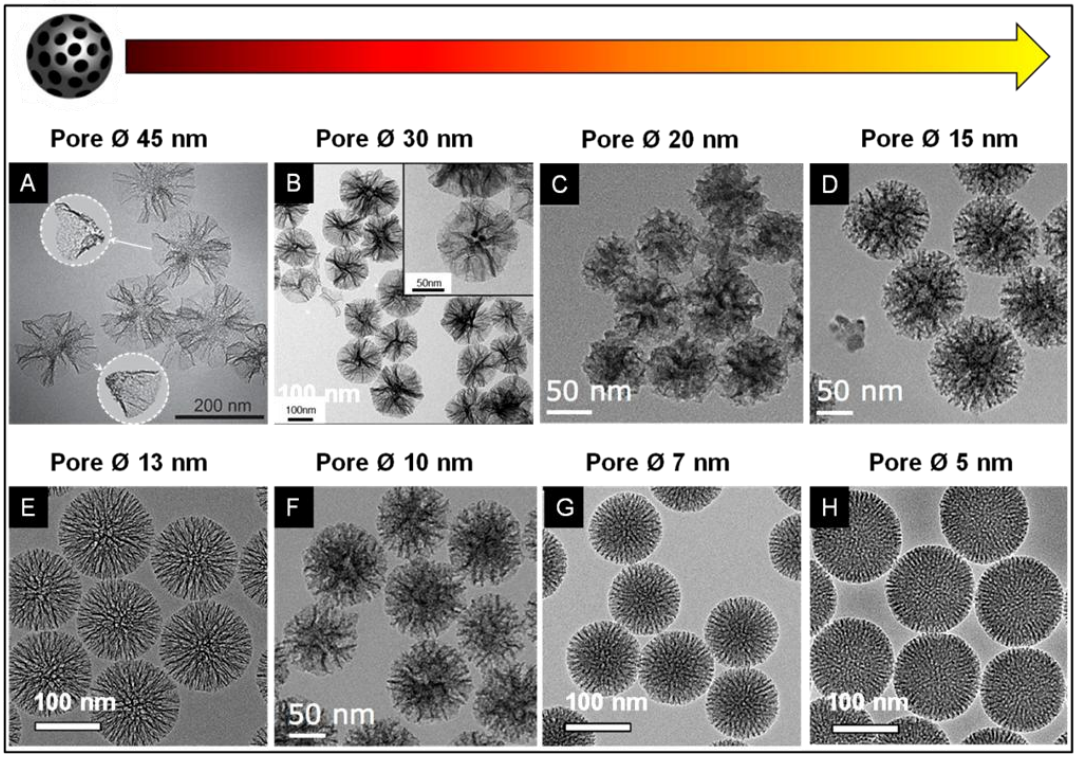

Fig.1-8 TEM images of MSNs with tunable pore diameter from 45 to 5 nm.[89, 94, 116-118]

1.2.2 Carbon based materials/non-porous silica composites

The earliest research on CBMs/silica composites was based on the formation of composites with a non-porous silica shell. The very low external surface area of the non-porous silica is considered disadvantageous because it provides a relatively low capacity compared to the porous silica materials. However, some advantages of the non-porous silica are extremely attractive, such as maximum surface accessibility, controlled topography of ligands, and a smooth surface resulting in better biocompatibility relative to the porous silica.[119] Therefore, in recent years, the scientific community has made some attempts in the synthesis and application of CBMs/non-porous silica composites, and used them as potential platforms for various applications in science and engineering.

The unique physical properties of CNTs attract many researchers to explore new or improved applications with composite materials. However, the functionalization of CNTs to promote their dispersion in different solvents is still a central theme. Coating with non-porous silica on CNTs is considered to be an effective approach to solve the poor solubility and process ability while maintaining their excellent physical properties. The specific synthesis scheme of coating CNT with non-porous silica is shown in **Fig.1-9 A**, which results in the formation of a uniform silica layer on the CNTs surface as shown by TEM in **Fig.1-9 B**. For example, N. Pinna's group synthesized a uniform SiO_2 coated CNTs composites through low-temperature ozone-assisted atomic layer deposition (ALD) of SiO_2 (TEM in **Fig.1-9 C**) and led to the formation of SiO_2 nanotubes as CNTs were removed during the ongoing deposition.[120] Fu and co-workers selectively coated SWCNTs sidewalls with a thin layer of SiO_2 and further functionalized with a large variety of functional groups by utilizing the chemistry of SiO_2 surface.[121] Furthermore, a well-defined silica coated CNT coaxial nanocable was developed as a reinforcing support for the construction of high-performance electrochemical devices, and showed great potential as a Raman scattering substrate for biological tags and biological molecular detection.[122]

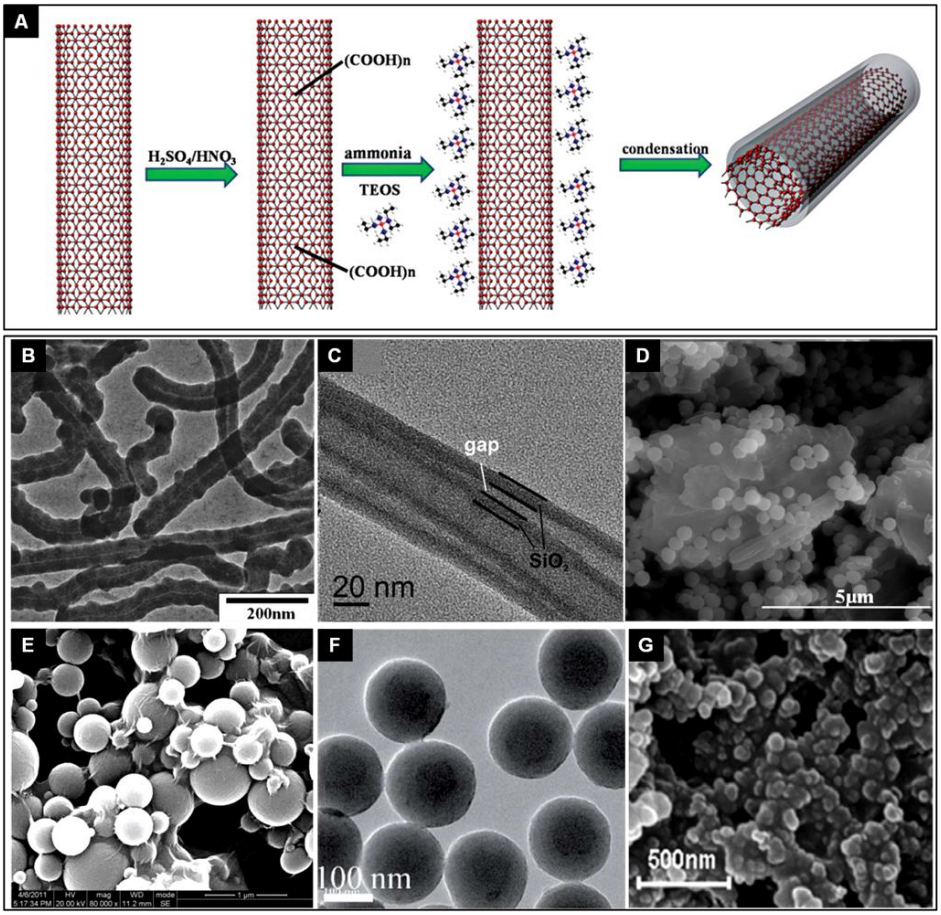

Fig.1-9 (A) The synthetic preparation of CNT@SiO_2.[123] TEM images of (B) individual CNTs covered by a uniform and thick layer of silica[124] and (C) CNTs after deposition of 100 cycles of SiO_2[120]. SEM images of (D) silica coated GO hybrid composite[125] and (E) GO coated silica composite[126]. (F) TEM image of silica/CDs composite.[127] (G) SEM image of CB-SiO_2 composite[128].

Graphene and GO, have a large number of oxygen functional groups on the substrate plane, resulting in a hydrophobic and inert structure, which makes them easy to agglomerate in the water. Therefore, much work has been conducted to form graphene-based materials/silica composites. The introduction of non-porous silica materials to form nanohybrids with GO can achieve higher degree of dispersion and exfoliation. There are two common forms of GO-silica composites, including the introduction of a uniform silica layer or even small spherical silica nanoparticles deposited at the surface of GO (**Fig.1-9 D**), and the coating of GO layer on the surface of silica particles (**Fig.1-9 E**). Over the past decade, there have been many attempts on the design of silica nanoparticles-coated GO nanohybrids,

in which the silica nanoparticles acting as spacers between the GO sheets can prevent them from aggregating and achieve a higher degree of exfoliation.[129-131] The multilayered ultrathin structure of graphene film also allows its use as a coating layer for silica particle. For example, Liu prepared a new form of graphene-coated silica particle hybrid, which showed a rough surface densely covered with carbon-like material.[132]

In the view of carbon dots (CDs) having small particle size, good water solubility and easy chemical functionalization, the surface of CDs can be easily covered with a homogeneous silica layer. Tian et al. synthesized silica/carbon dot (SCDs) composite nanoparticles with unique photoluminescence properties.[127] As shown in **Fig.1-9 F**, the SCDs exhibit a uniform spherical morphology and the size can be easily tuned from 100 to 230 nm. Moreover, the coating technique could be explored to constitute a sensing strategy for practical application. Liu et al. developed a tunable fluorescent silica-coated CDs nanoparticles of <10 nm in size, which had a high water solubility and enhanced selectivity for biological analysis.[133] Another attractive carbon-based material, carbon black (CB), has received much attention due to its rather high electrical conductivity. The main drawback of CB is the strong agglomeration state caused by its hydrophobicity, which will seriously affect its conduction response. Very recently, CB has also been embedded in solid-state silica as a reinforced conductive material. E. Enr íquez et al., reported a conductive submicronic coating of CB/silica composites (as shown in **Fig.1-9 G**) prepared by a sol-gel process.[128] The inorganic dielectric silica matrix formed a homogeneous and efficient coating on the surface of CB nanoparticles, which avoided their thermal degradation during thermal treatment.

1.2.3 Carbon based materials/small pore mesoporous silica composites

In comparison to the coating of CBMs with non-porous silica, MS matrix offers many other unique characteristics, such as stable mesoporous structure, large surface area, tunable pore size, and well-defined surface properties.[126, 127] The distinctive porous properties of carbon based materials/mesoporous silica (CBMs/MS) composites allow for the accommodation of various molecules with different sizes, shapes and functionalities, broadening the potential of applications of these new controllable multifunctional

systems.[134-136] In addition, the pore size of the MS matrix in the CBMs/MS hybrids plays a key role in determining the size of cargo that can be absorbed within the mesopores.[137] Among them, the construction of CBMs/MS composites with small pore size of 2-5 nm (CBMs/SPMS) is of great significance for the loading and transportation of small size targets, and has been widely studied.

Much work has been carried out on using small pore mesopores silica as a matrix material to encapsulate CNTs. The surface of CNTs can be functionalized with hydroxyl groups or different types of moieties after a specific acidic treatment, which is an important basis for the self-assembly of MSMs on the surface. The common method for fabricating CNTs/MS nanocomposites is a modified method from T. Hyeon for coating iron oxide NPs with MS shell.[138] Generally, the pre-processed CNTs are mixed with the silica precursor (e.g. TEOS) and the template agent (e.g. CTAB), and the template/silicate clusters are adsorbed on the CNTs surface and drive the nucleation and growth of MS shell. This simple synthetic process serves as a standard protocol for the preparation of small pore MS shell nanostructures, and most of the CNTs/SPMS hybrid materials are synthesized accordingly.[139]

For examples, Zhang's group reported the fabrication of MS-coated CNTs and their application in size selective protein separation.[69] The pore size of this mesoporous CNTs@SiO_2 composite was finely tuned within 2-3 nm by adjusting the ratio of CTAB/CNTs. And recently, Liu et al. proposed a complex nanoplatform based on polyethylene glycol (PEG) modified small pore-MS coated SWCNTs and utilized it as a multi-functional platform for cancer imaging combined therapy.[140] The obtained SWNT@MS and the synthesis process of SWNT@MS-PEG are shown in **Fig.1-10 A-B**. In our previous work,[141, 142] we synthesized a kind of hybrid composites based on the CNTs coated with a small pore-MS shell with a pore size of about 2-3 nm (in **Fig.1-10 C**). The thickness of the MS shell could be tailored by changing the parameters of sol-gel process (e.g. amount of precursor, sol-gel time).

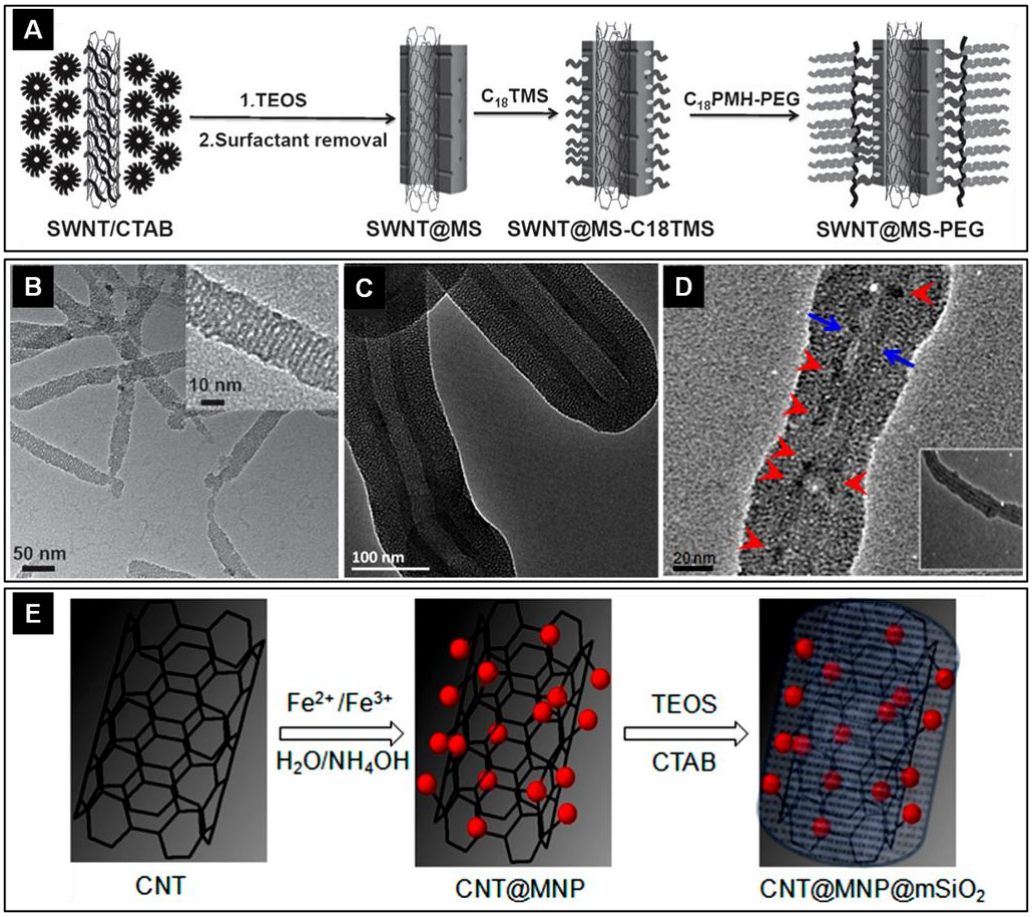

Fig.1-10 (A) A schematic illustration of the synthesis of SWNT@MS-PEG and (B) TEM image of SWNT@MS.[140] (C) TEM image of CNT@MS showing the mesoporosity of the composite.[142] (D) TEM image and (E) schematic illustration showing the synthesis of CNT@MNP@mSiO$_2$.[143]

In recent years, the development of multifunctional forms of CNTs/SPMS hybrid nanomaterials based on the magnetic nanoparticles (MNPs)-decorated CNTs sheathed with small pore-MS layer, has been extensively studied.[143, 144] The MNPs-decorated CNTs (CNT@MNPs) has shown excellent magnetic properties, while preserving the merits of CNTs, potentially expanding its possible use in various applications. **Fig.1-10 E** depicts the synthesis scheme of CNT@MNPs@mSiO$_2$ hybrid nanomaterial. First, MNPs were first decorated onto the multi-walled CNTs and then layered with MS (mSiO$_2$), as shown in **Fig.1-10 D**. Such new type of multifunctional hybrid nanomaterial retained the excellent magnetic resonance imaging properties of magnetite nanoparticles within the structure, as well as created a high mesoporosity and a more biocompatible interface due to the surface-layered mSiO$_2$, which

might be potentially useful for the simultaneous use for drug delivery and imaging.

The idea of embedding the two-dimensional graphene sheets into a MS matrix is obviously also attractive because of the introduction of tunable and open porosity, making the nanocomposites promising for a wide range of applications. Graphene or rGO sheets are often viewed as interactive functional platforms for bonding or growing other nano-objects due to their planar nature. The most common way for the construction of graphene-based/MS hybrid composites is therefore by using graphene or rGO as the substrate for the growth of MS layer with controlled properties on both surfaces, thus allowing the formation of sandwich mesoporous structures.[145, 146] To date, a lot of investigations have been done on the construction of free-standing sandwich structures made of graphene-based/SPMS hybrid materials, demonstrating promising properties of such platform materials for various applications.[147-150] The specific TEM images in **Fig.1-11 A-B** show the graphene/MS hybrids covered with a rough MS surface. In addition to the synthesis of MS layer with cylindrical pores, Y. Wang et al. presented a new special architecture of multifunctional small pore-MS coated graphene nanosheet sandwich nanocomposites, in which the MS layers have a hexagonal array of pores and an ordered structure (**Fig.1-11 C**).[151]

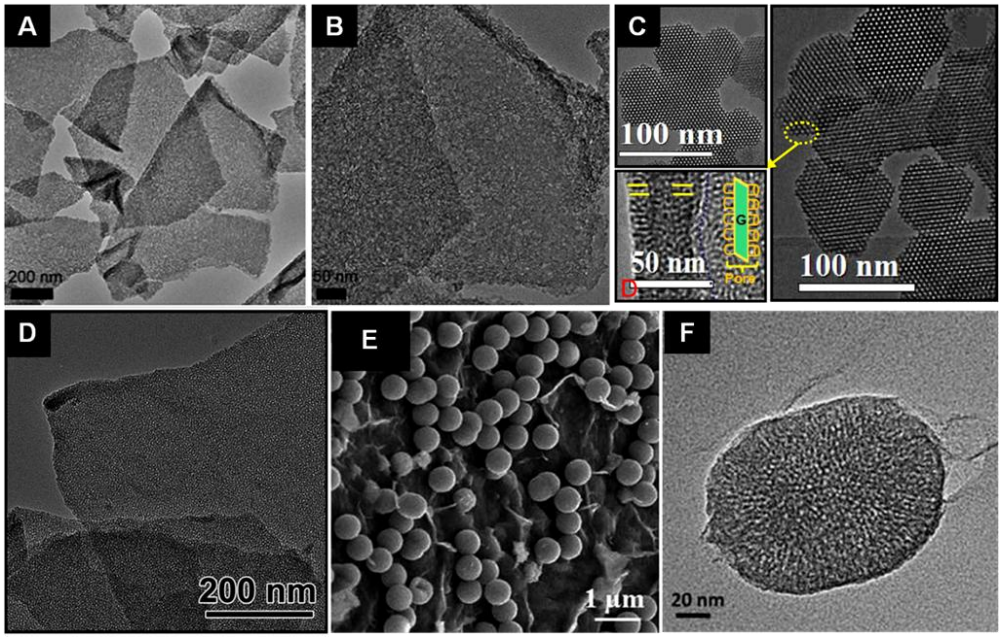

Fig.1-11 (A-B) TEM images of graphene/MS hybrids.[152] (C) HRTEM and TEM images of MS-coated graphene nanosheet.[151] (D) TEM image of Pt-rGO@mSiO_2.[153] (E) SEM image of

SiO_2 particles decorated GO.[154] (F) HR-TEM image of GO-enwrapped MSNPs.[155]

On the other hand, the unique sandwich structure of graphene/MS composites can be exploited to encapsulate small nanoparticles between the graphene nanosheets and the MS layer. In addition, the pore characteristics of the mesostructure in the outer layer of the sandwich can also be used to immobilize other responsive nanostructures such as metallic nanoparticles or functional molecules, allowing the design of multifunctional graphene/MS systems.[156] Very recently, a facile and scalable wet-chemical process has been reported for encapsulating graphene nanosheet loaded with ultrafine metal nanoparticles by thin mesoporous SiO_2 layers with a small pore of 2.8 nm (in **Fig.1-11 D**).[153] The coverage of the graphene nanosheets by mesoporous SiO_2 layers not only stabilized the ultrafine metal nanoparticles, but also prevented their aggregation, resulting in an enhanced catalytic performance of this hybrid system. A new type of 2D GO/MS hybrid system of well-dispersed gold nanoparticles over the sandwich-like periodic mesoporous silica (PMS) coated rGO was proposed.[146] The MS layer with a pore size of ~3.1 nm covering on the surface of rGO acted as a stabilizing agent, which also prevented the serious aggregation of individual GO by weakening the π-π stacking interaction between GO nanosheets.

An interesting design for combining small pore-MS materials with graphene-based materials was proposed by S. Abraham et al, indeed, instead of covering layered MS on graphene, the authors used sub-micron sized (~ 500 nm) homogeneous MSNs with an average pore diameter of about 5 nm to decorate the GO surfaces.[154] SEM image in **Fig.1-11 E** reveals the morphology and microstructure of this MS particle embedded GO hybrid system. A similar structure of polyethylenimine-modified magnetic MS on GO sheets (MMSP-GO) was also reported by Wang et.al.[157] Another challenging fabrication of graphene-based/SPMS hybrids (**Fig.1-11 F**) was recently reported by wrapping ultrathin GO sheets via electrostatic interactions around the surface of the MS fluorescent nanoparticles for bioimaging applications.[155] The coating of ultrathin GO layer on the dye-loaded NPs prevented dye leakage and nucleophilic attack on the dye, and ensured the optimal properties of the fluorescent hybrid.

Many strategies have also been applied to the fabrication of small pore-MS hybrids with carbon-based materials having spherical shape such as CDs and CB. The construction of CDs/MS hybrid materials provides a universal platform for the design of functional materials, which takes advantage of the abundant mesopores of small pore-MS matrix and the unique fluorescent properties introduced by CDs. Basically, The CDs/MS hybrids so far described involve the incorporation of CDs within the MS walls, or covering the CDs at the surface of MS or embedding in the pores.[158-160] For example, Lei et al. successfully incorporated CDs into the pore walls of MS to produce monodisperse nanometer-sized periodic mesoporous organosilicas nanoparticles (CD-PMO NPs, shown in **Fig.1-12 A-C**) with excellent photoluminescence performance.[161] These hybrid materials simultaneously assembled with unobstructed ordered pore channels and excellent photoluminescence performance.

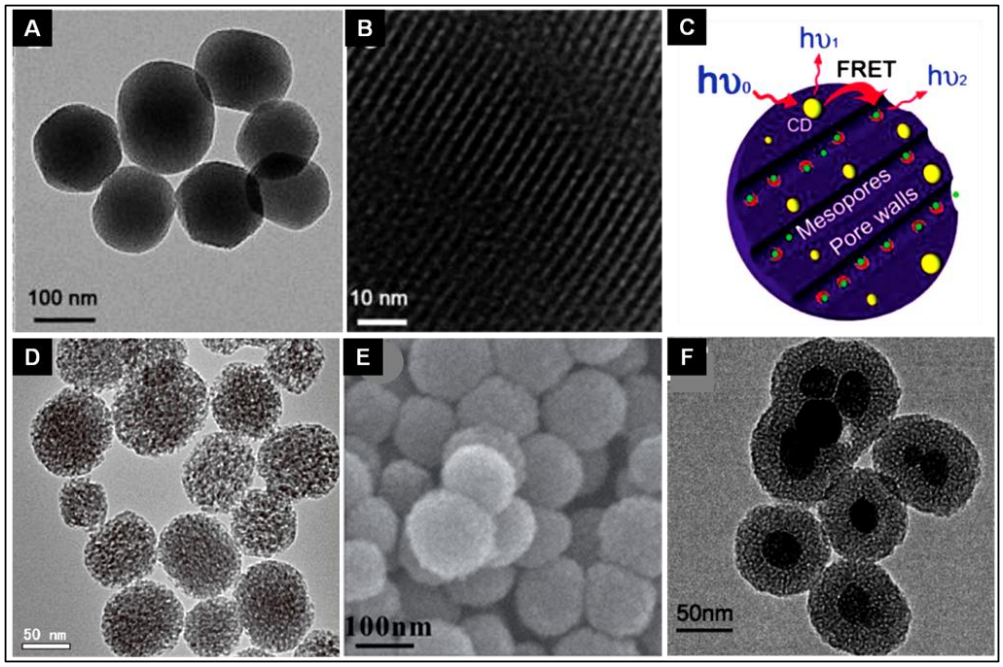

Fig.1-12 (A-C) TEM, HRTEM images and structural illustration of CD-PMO NPs.[161] (D) TEM image of MSNs@CDs.[162] (E) SEM images of MSNs@GQDs.[163] (F) TEM image of MMSN/GQDs nanoparticles.[164]

Another form of hybrid is based on the immobilization through electrostatic interactions of fluorescent CDs and GQDs at the surface of small pore size MSNs (MSNs@CDs and MSNs@GQDs), as shown in **Fig.1-12 D-E**.[162, 163] A similar protocol has also been

successfully applied when using a magnetic MS matrix. Yao et al. introduced a multifunctional platform constructed with GQDs-capped magnetic core MSNs (MMSN/GQDs, in **Fig.1-12 F**) that effectively produced heat under an alternating magnetic field (AMF) and/or in response to NIR irradiation.[164] Regarding CB nanoparticles, there are few reports on the synthesis of CB/SPMS hybrids. Very recently, a carbon black supported-Pd catalyst encapsulated by a robust and homogeneous small-pore mesoporous SiO_2 layer has been proposed. This composite material showed a good stability and sintering resistance at high temperature.[165]

1.2.4 Carbon based materials/large pore mesoporous silica composites

CBMs/MS hybrid materials with a large pore size (greater than 5 nm) have attracted a lot of attention due to their desirable porous characteristics for large-size cargo loading. In general, the small pore size of CBM/SPMS composites prevents the large objects from entering the internal pores of MS matrix, which results in the inefficient use of the protective environment of the pores inside the MS and the large internal surface area provided by these pores.[166-169] Thus, it is of great significance to construct CBMs/MS hybrids with a sufficient pore size to explore the application of the size-selective adsorption of large molecules such as proteins and macromolecular drugs.

Many strategies have been developed to synthesize large pore MS materials with various morphologies and pore sizes. However, the encapsulation of CNTs with large-pore MS shells is still challenging, and only a few examples exist in literature dealing with encapsulation of CNTs with large-pore MS layer. Generally, the surface chemistry properties of CNTs were adjusted by using special surfactants or by "doping" CNTs with different kinds of heteroatoms to achieve an improved interface with the silica matrix, preventing CNTs from agglomerating during the densification process and promote the formation of MS shells.[170, 171] Recently, Dillon et al demonstrated the preparation of MS coated conventional MWCNTs with a large pore size of 6-8 nm by using a sol-gel route (as shown in **Fig.1-13 A**).[172] The fabrication of large pore MS coated CNTs (**Fig.1-13 B**) has been also developed *via* a two-step procedure using a biocompatible zwitterionic surfactant (phospholipid), which was

different from the traditional template agent CTAB that is harmful to bio-molecules and cells.[173] The pore characteristics of CNTs/MS composites could be well controlled by varying the ratio of phospholipids and other traditional surfactants (cationic, anionic and nonionic surfactants). **Fig.1-13 C** shows a SEM image of MS shell over the SWCNT core. Another form of CNTs/LPMS nanostructures based on the 2D hexagonal mesoporous ordered silica SBA-15 and CNTs was reported by M. Vila, in which CNTs were well dispersed and distributed throughout the composite assuring the 3D conducting network.[174]

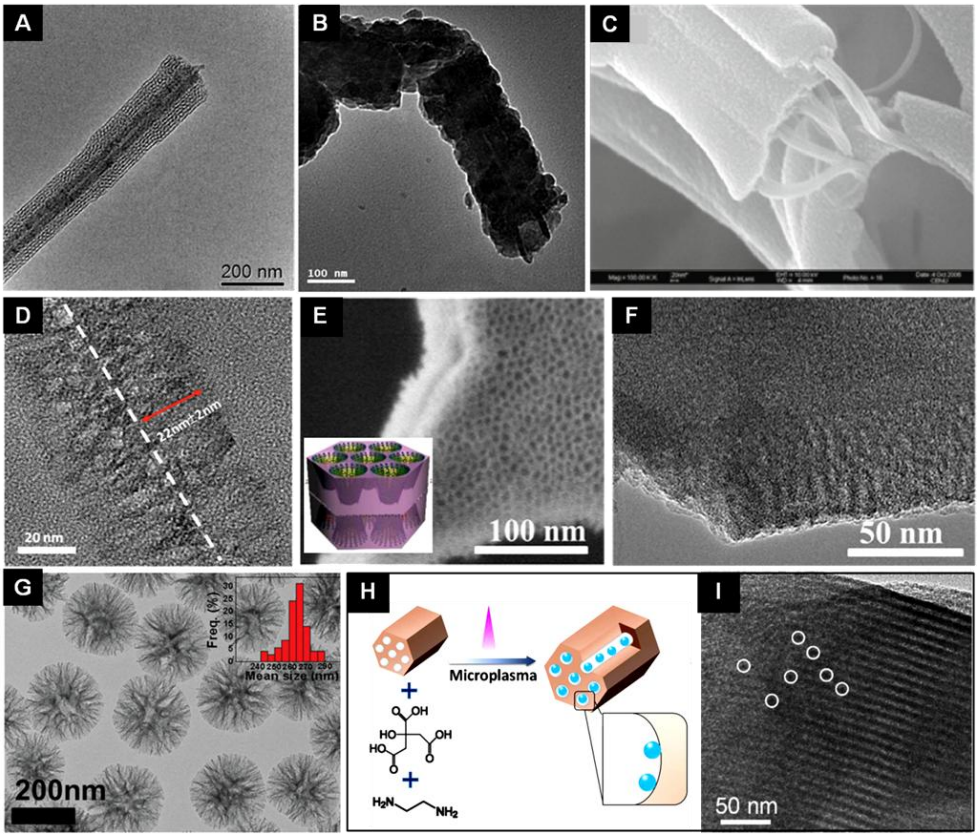

Fig.1-13 TEM images of (A) MS coated N-doped SWCNTs[172] and (B) CNTs@SiO_2 [173]. (C) SEM image of CNT/MS core–shell composite.[175] (D) TEM image of rGO/MS nanosheeets[176]. (E-F) Cross-section FESEM and TEM images of the sandwich-like structured rGO@mSiO_2.[177] (G) TEM image of dSCSs.[178] (H-I) Schematic diagram and TEM image of CDs/SBA-15 nanocomposites.[179]

To date, many attempts have been reported to prepare graphene-based/LPMS hybrid materials.[180-182] For example, Chen et al. have constructed a nanosystem by MS self-assembly

on the reduced graphene oxide (rGO) nanosheets for encapsulating and arranging gold nanoparticles inside the nanochannels of the MS layer.[176] The pore size of prepared rGO/MS nanosheeets (in **Fig.1-13 D**) was controlled from 2.3 nm to 13.3 nm by adding different volumes of styrene as the pore expanded agent. Furthermore, Zhao et al. have developed reduced graphene oxide@mesoporous silica (rGO@mSiO_2) sandwich-like sheets with vertically oriented "funneling" mesochannels and tunable large pore size up to 8.9 nm by an oil-water biphase stratification approach.[177] The resulting rGO@mSiO_2 nanosheets (in **Fig.1-13 E-F**) possessed a uniform mesoporous structure with thin thickness (~50 nm) and large aspect ratio, as well as a rapid photothermal heating effect, showing promising prospects in light-induced drug delivery applications. Another multi-layer graphene/MS system composed of about 8 nm-sized vertical channels in a hexagonal symmetry has been recently used for the electrochemical deposition of an ordered array of CdSe quantum dots on graphene sheets.[183]

Spherical CBMs, mainly CDs, have been widely studied with large pore-MSMs to construct hybrid materials. Very recently, Zhao et al. synthesized good monodispersity dendritic silica@CDs@silica spheres (dSCSs) by using ordered dandelion-like MSNs with central-radial pore channels and a pore size of about 10 nm as carriers for immobilization of CDs.[178] The TEM image and fluorescence intensity of the dSCSs in **Fig.1-13 G** show that the introduction of CDs did not destroy the original structure of MSNs while maintain good fluorescence characteristics. At last, SBA-15 type MS with a larger pore size has been widely studied in the synthesis of CDs/LPMS hybrid materials.[184, 185] A type of luminescent MS-CDs composite material was synthesized by Wang et al., in which CDs precursors (citric acid and ethylenediamine) were filled in the large pore MS molecular sieve (SBA-15), and the CDs were prepared in situ by microplasma-assisted method.[179] The schematic diagram and TEM image of the obtained CDs/SBA-15 nanocomposites are shown in **Fig.1-13 H-I**. The prepared CDs/SBA-15 composites preserved the high specific surface area of the MS substrate, as well as the fluorescent properties of the CDs.

1.3 CBMs and CBMs/MS composites for biomedical applications

Owing to their special structural dimensions and outstanding mechanical, electrical, thermal, optical and chemical properties, CBMs (including CNTs, graphene and its derivatives, carbon-based quantum dots) have attracted a significant interest for biomedical applications. Besides, CBMs/MS composites not only possess the physical and chemical properties derived from carbon-based materials, but also introduce a more biocompatible silica interface for the interaction with cells and tissues, as well as a mesoporous structure designed to improve drug loading and delivery capacity. All these characteristics make them attractive for many biomedical applications, such as for drug delivery and cancer therapy, tissue engineering, biosensing and imaging.

1.3.1 Drug delivery and cancer therapy

Drug delivery is one of the most extensively explored applications of CBMs in biomedical field. At present, the development of CBMs/MS materials as potential drug delivery platforms for combination of cancer therapies has also been explored to some extent. CBMs/MS materials are promising nanocarriers for the delivery of drugs because the MS shell provides accessible and tunable pore channels for high loading of drug molecules, and the MS surface can easily be functionalized with stimuli-responsive groups to serve as smart gatekeepers for controlled and targeted drug release.[186] Furthermore, CBMs such as CNTs, graphene and CDs, exhibit strong optical absorption in the NIR region, which is a tissue transparency window, and the CBMs and CBMs/MS materials generate local heating upon NIR laser irradiation to achieve photothermal ablation of cancer cells.[187] Therefore, the effective drug delivery systems in addition to achieving a high drug loading capacity, and can also enable controlled and targeted release as well as photothermal cancer therapy, which can be achieved by using CBMs/MS hybrid materials.

CBMs as independent nanocarriers have been extensively investigated for drug delivery application. Pristine CBMs are intrinsically hydrophobic and cannot be evenly dispersed in most solvents and biological media. Therefore, it is often necessary to functionalize CBMs to improve their biocompatibility and solubility for subsequent application to the loading of drug

molecules. Many different strategies have been developed to achieve the attachment of therapeutic molecules to the functionalized CBMs via either covalent conjugation or con-covalent adsorption. The covalently chemical bonding of drug molecules is usually connected by the functional groups or polymer chains on the surface of CBMs. [188-191] The specific example of CNT in **Fig.1-14 A** shows that various approaches are applied for drug delivery and anti-cancer therapy. Oxidation of CBMs by acid treatment is one of the most common methods for covalently linking, which produces carboxylic acid groups and the covalent bonds can be formed via 1, 3-dipolar cycloaddition, esterification and amidation.[192-194] It has been reported, for example, that anti-fungal drugs were linked by the 1, 3-dipolar cycloaddition with functionalized CNTs via amide bonds for drug delivery.[195] Besides, graphene and GO, CDs and GQDs with satisfactory electronic properties have also been used as multifunctional drug nanocarriers to load drugs for cancer treatment.[196-200] Anticancer drugs such as methotrexate (MTX) and DOX covalently bonded onto the functionalized GO via amide bonding for targeted drug delivery have been studied.[201, 202] Yang and co-workers loaded DOX onto the functionalized CDs through an acid-labile hydrazone bond (**Fig.1-14 B**), which was cleavable in the weakly acidic intracellular compartments, resulting in an enhanced antitumor activity.[203]

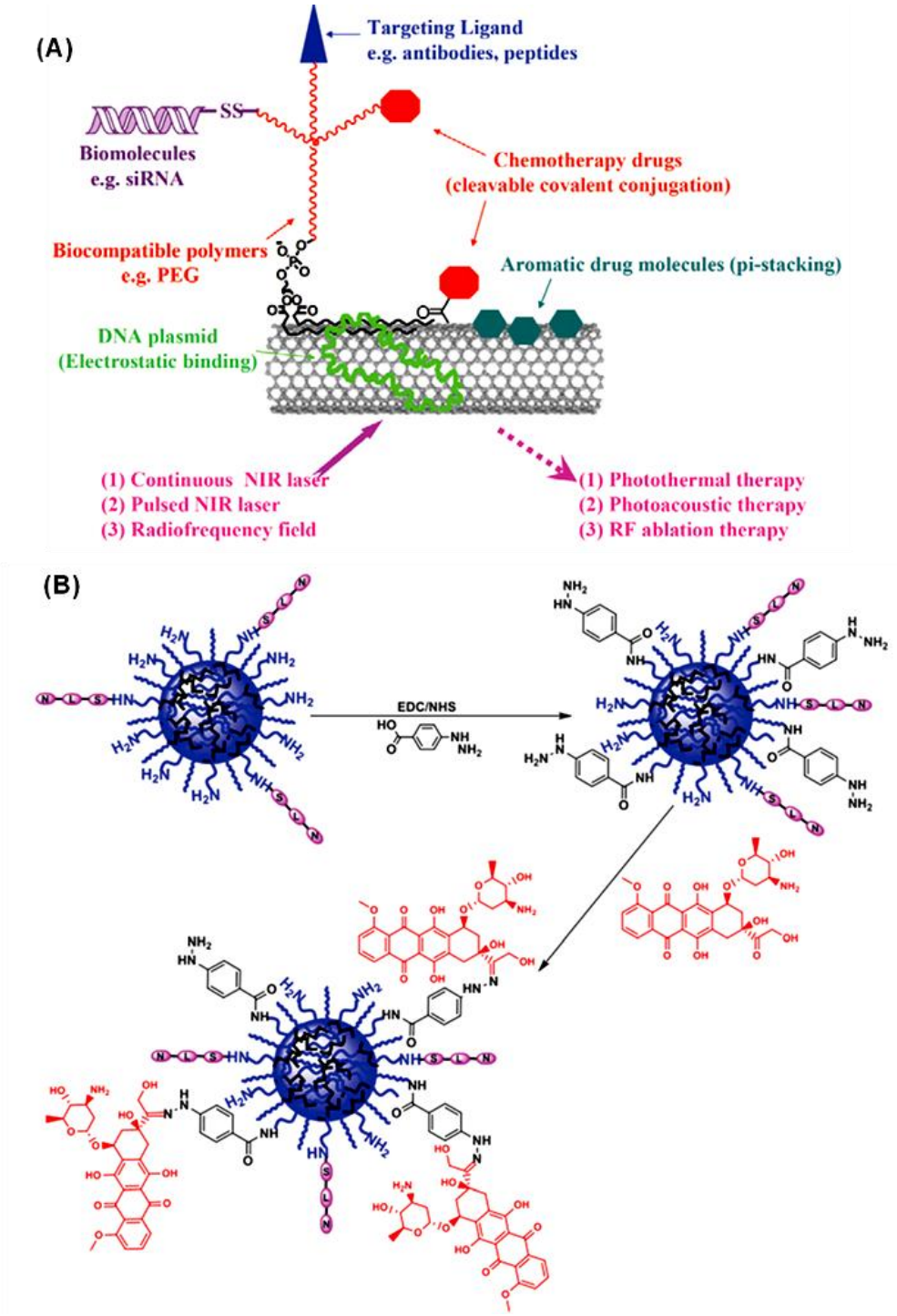

Fig.1-14 (A) Schematic diagram showing various approaches of CNT-based drug delivery and anti-cancer therapy.[204] (B) Illustration of the procedure for synthesizing DOX-CDs.[203]

The surface of CNTs or graphene has delocalized π electrons, which can effectively load aromatic anticancer drugs through π-π stacking. For instance, CNTs functionalized with polymers are able to form supramolecular complexes with the aromatic molecules and

anticancer agent via π-π stacking and enhance its cytotoxic activity.[205, 206] Anticancer drug doxorubicin (DOX) was successfully non-covalently attached onto the surface of PEGylated SWCNTs to construct a new drug loading formulation (**Fig.1-15 A**), which exhibited a remarkably high drug-loading capacity of up to DLC=400% (i.e., 4 times the mass of the CNT carrier) and a remarkable reduced toxicity compared to free DOX.[207] Such constructs can also be applied to GO, which has been extensively studied for the anticancer drug loading via simple non-covalent adsorption, including π-π stacking and hydrophobic interactions.[208, 209] It has reported by Dai's group that simple physisorption via π-π stacking could be applied for loading anticancer drugs SN-38 (**Fig.1-15 B**) and DOX onto the functionalized GO.[210, 211] Zhang et al. controlled the loading of two anticancer drugs (DOX and camptothecin (CPT)) onto the folic acid-conjugated nanoscale GO (FA-NGO) via π–π stacking and hydrophobic interactions (**Fig.1-15 C**), achieving the controlled loading and targeted delivery of mixed anticancer drugs.[212] It has also been found that CDs can load drug molecules through π-π stacking and electrostatic interactions to form supramolecular hybrids, showing enhanced drug loading and releasing behavior.[213-216] Lately, Tang et al. demonstrated a direct and sensitive Förster resonance energy transfer (FRET)-based CDs drug delivery system (FRET-CDot-DDS) through a direct surface coupling strategy (**Fig.1-15 D**).[217] Therefore, the stable fluorescence emission of CDs and the effective FRET signal (which was extremely sensitive to the separation distance between the donor and the acceptor) allowed for cell imaging and real-time monitoring of drug release.

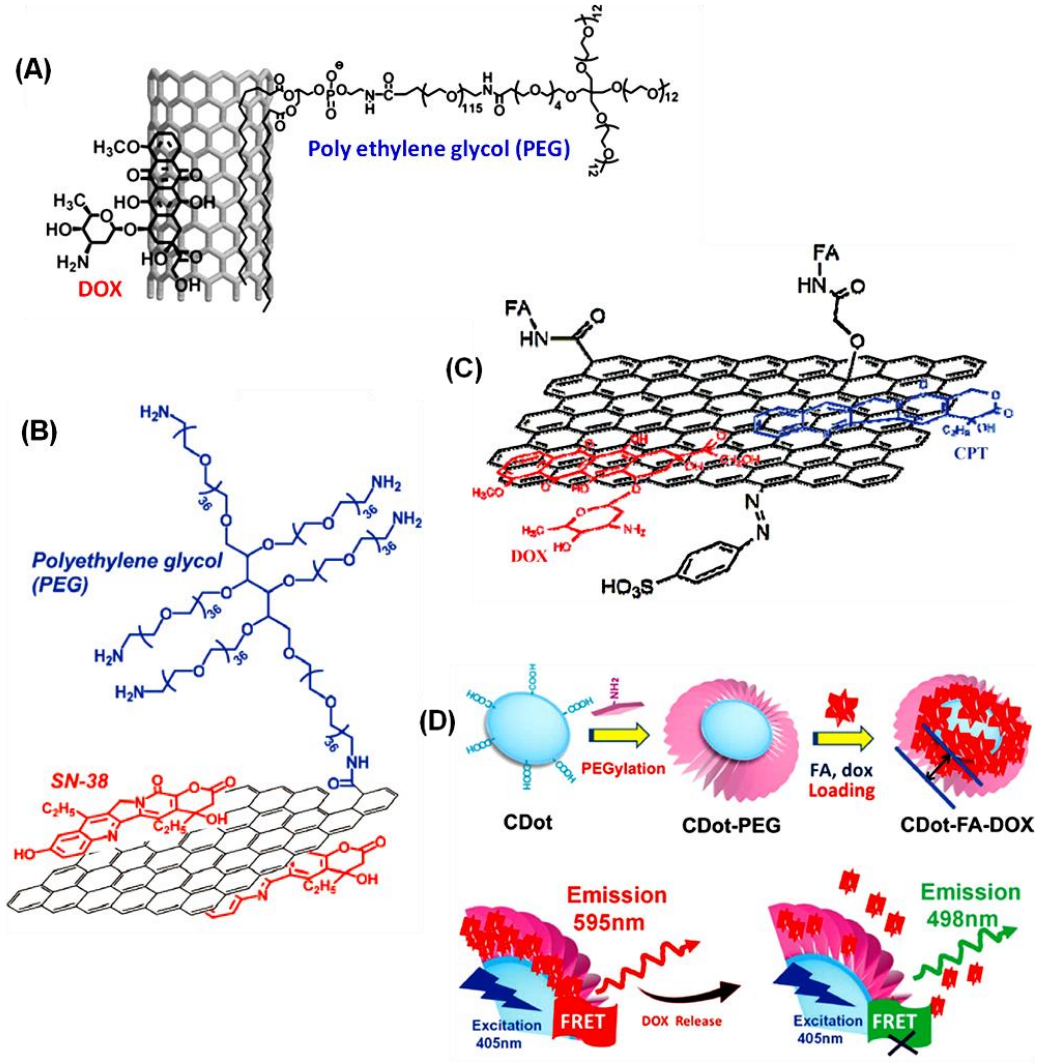

Fig.1-15 (A) PEGylated SWCNTs loaded with DOX.[207] (B) Schematic draw of SN-38 loaded NGO-PEG.[210] (C) Schematic image representing the loading of DOX and CPT onto FA–NGO.[212] (D) A schematic representation of the surface coupling chemistry of FRET-CDot-DDS for drug delivery.[217]

Regarding the CBMs/MS materials, as detailed above, the MS matrix allows CBMs/MS materials to have more advantages in drug delivery and cancer therapy, such as achieving high drug-loading efficiency, easily functionalized surfaces and good biocompatibility. In recent years, there have been many reports on the development of MS coated carbon-based materials as delivery platforms for combined cancer treatment.[143, 171, 218]

For example, MS coated SWCNTs and MWCNTs drug nanocarriers with copolymers modification were fabricated by Liu et al., and utilized as multifunctional platforms for

anticancer drug loading.[140, 219] This multifunctional systems could be covalently bonded with anticancer drug with improved drug loading capacity, and significantly enhancing the release dynamics of drugs under multi-stimuli responsiveness, realizing a synergistic cancer cell killing effect through the combination of photothermal and chemotherapy. In previous works of our group, we reported the fabrication of MS coated-CNTs and graphene nanocomposite platforms for drug delivery applications (**Fig.1-16 A**). Such CBMs/MS hybrid nanoplatforms were optimized by the functionalization of polysiloxane layer or isobutyramide (IBAM) grafts to form strongly bounded non-covalent bonds, achieving an ultrahigh drug payload as well as remotely stimulus release under the activation of pH, temperature and NIR-light.[142, 220, 221]

Graphene and its derivatives -based/MS hybrid materials showing excellent photo-to-thermal-energy transfer efficiency under NIR irradiation have been widely studied for drug delivery combining photothermal therapy and chemotherapy.[222, 223] To date, many efforts to seek the synergistic antitumor efficacy of chemo-photothermal therapy of graphene-based/MS hybrids rely upon the standard approach of grafting the MS layer with tumor-targeting moieties, such as specific ligands, peptides, and hyaluronic acid (HA).[151, 224] A versatile nanoplatform of MS coated polydopamine functionalized rGO modified with HA (pRGO@MS-HA) was reported and utilized for synergistic targeted chemo-photothermal therapy against cancer, showing remarkable tumor cell killing efficiency and specificity to target tumor cells (**Fig.1-16 B**).[223] Another multifunctional remote controlled release system based on graphene and its derivatives -capped functionalized drug loaded MSNs was designed (**Fig.1-16 C**), where GO (or rGO) was not only used for NIR photothermal therapy, but also used for gating control of the drug release. Such uncapping mechanism makes it possible to release the loaded drug molecules more effectively upon irradiation with NIR light.[225-227]

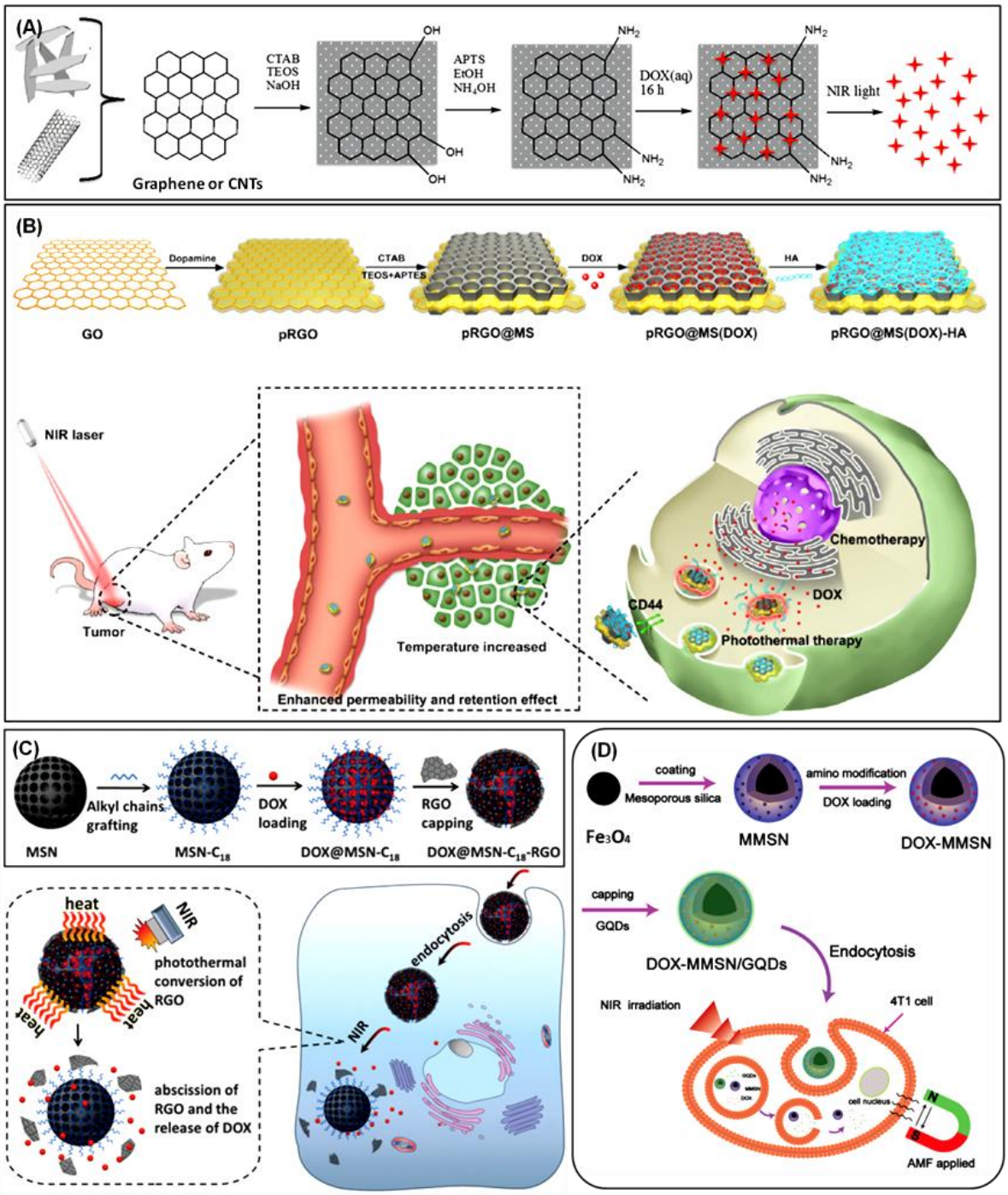

Fig.1-16 (A) Scheme showing the synthesis of CNT@MS or FLG@MS grafted with APTS, the loading with doxorubicin and the drug release actuated by T, pH, or NIR light.[142] (B) Schematic illustration of the synthesis route of pRGO@MS(DOX)-HA nanocomposite and the combined chemo-photothermal targeted therapy of tumors.[228] (C) Schematic representation of the non-covalent assembly of rGO and alkyl-grafted MS as an effective drug carrier for NIR light-responsive controlled drug release.[226] (D) Schematic illustration of the

preparation process of the DOX-MMSN/GQDs nanoparticles and synergistic therapy combined with controlled drug release, magnetic hyperthermia, and photothermal therapy.[164]

At the same time, the fluorescence imaging properties of CDs allow following the optical signal of the drug molecules themselves, making them ideal modes for the real-time monitoring of drug delivery systems. The biocompatible CDs are usually used as caps to anchor the openings of MSNs via covalent or non-covalent interactions, in which CDs act as gatekeepers to simultaneously achieve the roles of both capping agents and imaging agents, thereby constructing a multifunctional drug release system.[229-231] The resulted CDs/MS drug delivery systems can release the loaded drugs at the specific location in the response to diverse stimuli, including pH-, temperature-, photo irradiation-, redox potential- and enzyme-responsiveness.[232-235] An example as shown in **Fig.1-16 C**, a multifunctional platform composed of graphene quantum dots (GQDs) as caps and local photothermal generators as well as magnetic MSNs as drug carriers and magnetic thermal-seeds was designed to achieve controlled drug release and with synergistic effect of chemo-magnetic hyperthermia and chemo-photothermal therapy.[164]

1.3.2 Tissue engineering

Beyond drug delivery, CBMs are considered to be ideal physical analogues of extracellular matrix (ECM) components because of their similar dimensions. Furthermore, the outstanding mechanical properties and high conductivity of CBMs play an important role in reinforcing organic/inorganic artificial scaffolds, and can also be used to provide electrical stimulation to artificial scaffolds.[236] Due to these favorable properties, CBMs have been extensively studied for tissue engineering applications, as biological alternatives for repairing or replacing whole or a portion of tissue, whether as a matrix material or as additional reinforced materials in polymer nanocomposites.[237] Similarly, CBMs/MS hybrids are also great potential candidates for the development of synthetic scaffolds in tissue engineering, especially the structural and textural properties derived from the MS matrix have potential applications in the development of bone implants and bone cements.

Carbon-family nanomaterials, such as CNTs, graphene and its derivative, or CDs are

important tissue engineering materials. They are expected to be used as ideal substrates, scaffolds and components of implant devices, suitable for cell adhesion, proliferation and differentiation, and so on.[238-241] For example, many studies have shown that both SWCNTs and MWCNTs, graphene and its derivatives, CDs (or GQDs) hold high potential for mammalian cells adhesion, spreading, proliferation, and gene transfection, showing high biocompatibility, especially as surface coating materials for implants, without inducing notable deleterious effects while enhancing some cellular functions.[242-245] CBMs have a great potential in neural tissue engineering because the electrical properties of CBMs have an effect on the behavior of the electro-active neural cells. According to the previous papers, CNTs, graphene or its derivatives, and doped CDs have been applied in many fields of nerve tissue engineering to probe and enhance cell behavior, to label and track subcellular components, and to investigate the growth and organization of neural networks.[246-249] For instance, Cellot et al. demonstrated that CNTs could sustain and promote neuronal electrical activity in networks of cultured cells by forming tight contacts with the cell membranes.[250] It was also found that human neural stem cells (hNSCs) showed good long-term viability and differentiated toward neurons when cultured on graphene.[251]

Another very important application of CBMs in tissue engineering is the construction of CBMs-based multifunctional scaffolds as physical substrates for cell attachment, proliferation, and differentiation for neural, cardiac, and skeletal-muscle tissue engineering. These scaffolds include CBMs-hydrogels, CBMs-polymer or inorganic composites, and CBMs-polymer-inorganic hybrid materials, etc. For example, Shin's group has made many efforts to develop the incorporation of CNTs, graphene and rGO into photo-cross-linkable gelatin methacrylate (GelMA) hydrogels (**Fig.1-17 A**) for cardiac-tissue engineering.[252-254] The CBMs-GelMA hydrogel scaffolds exhibited excellent mechanical and electrical properties, and improved the adhesion, organization, and cell-cell coupling of cardiac cells. Such scaffolds were expected to be used in the production of multifunctional cardiac scaffolds for therapeutic purposes and in vitro research. In a recent study, a layer-by-layer (LBL) assembly approach was developed to engineer 3D multilayer constructs by depositing cells

onto poly (L-lysine) (PLL) coated GO-GelMA hydrogel (**Fig.1-17 B**). The GO-based scaffolds served as cell adhesive sheets that significantly promote the formation of multilayer cell constructs with interlayer connectivity.

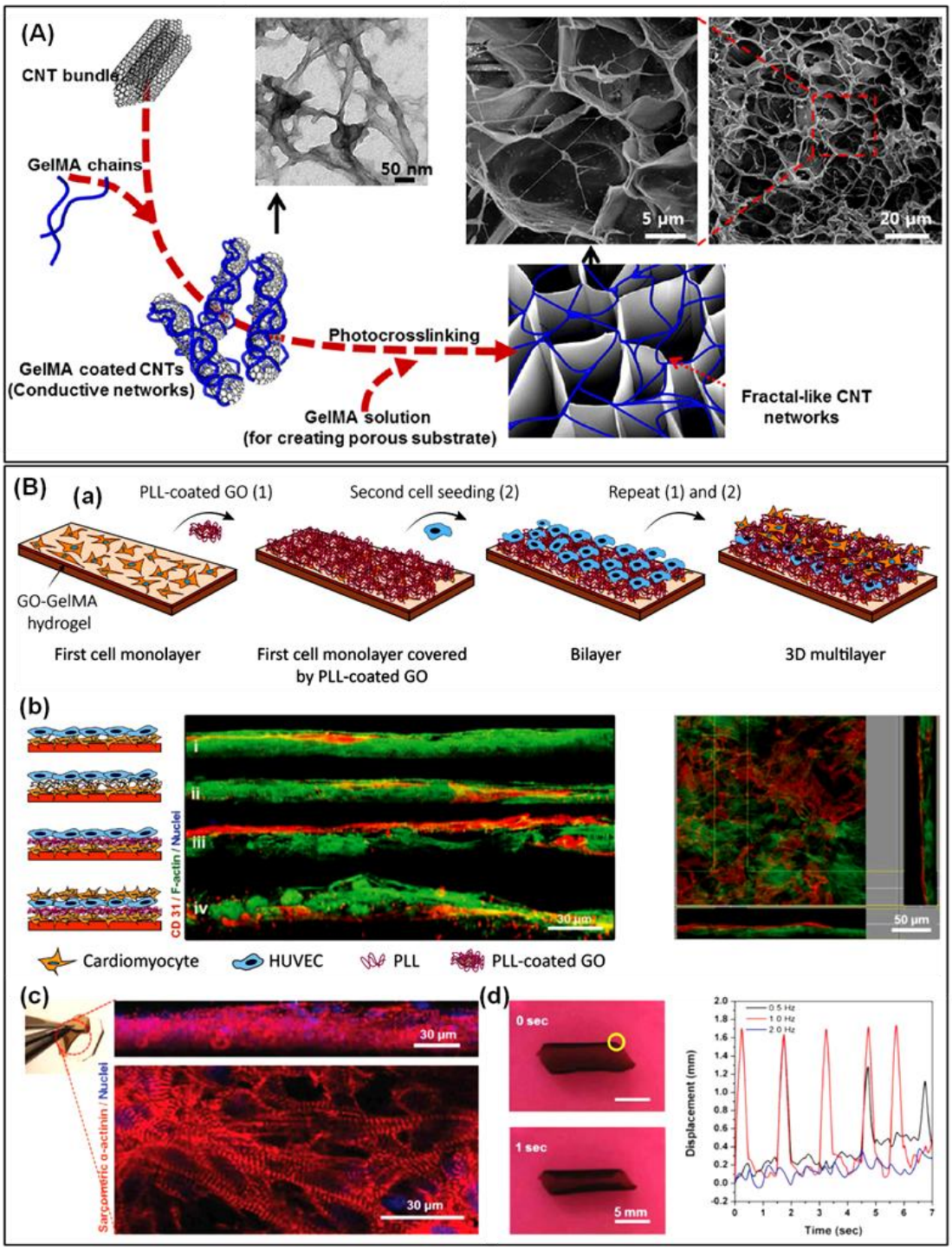

Fig.1-17 (A) Preparation procedure, TEM and SEM images of CNTs-GelMA hydrogels.[252] (B) Multilayered GO-GelMA hybrid hydrogels for cardiac tissue engineering. (a) Schematic diagram of the multilayer tissue constructs fabricated via layer-by-layer seeding and

deposition on GO-GelMA hydrogel. (b) Confocal images demonstrating the formation of a multilayered cell-sheet consisting of cardiac and endothelial cells. (c) Cells in the multilayered cellular construct remained functional and viable after cell-layer exfoliation. (d) Displacement of the actuator over time under electrical stimulation.[254, 255]

The polymeric scaffolds fabricated from polymers and CBMs were extensively studied for tissue engineering because of the biocompatibility of CBMs-polymer composites that provide suitable microenvironment to cells and tissues with appropriate chemical composition and physical structure. The improved mechanical properties of the CBMs-polymer composites also help to support and promote bone tissue regeneration. According to recent reports, the incorporation of MWCNTs or graphene in biodegradable polymer polycaprolactone (PCL) to form reinforced MWNTs/PCL composite scaffolds have great potential for bone tissue engineering.[256, 257] Recently, the synthesis of CBMs-containing polymeric nanofiber scaffolds through electrospinning technique has been developed. Due to the strong interfacial interaction between the CBMs and the polymer chain, it is possible to incorporate CBMs such as CNTs, graphene and its derivatives, or CDs into electrospun polymer scaffolds, which can significantly improve the mechanical and thermal stability properties of the polymeric scaffolds.[258-261] The random oriented and aligned electrically conductive biodegradable poly-DL-lactide (PLA) nanofibers embedded with MWCNTs are shown in **Fig.1-18 A**.[262] These conductive nanofiber scaffolds showed enhanced mechanical properties and served as unique systems for studying the synergistic effect of topographical cues and electrical stimulation on the growth of osteoblasts, and exploring their potential applications in bone tissue engineering. It is also found that chitosan-PVA nanofibers containing graphene (**Fig.1-18 B-D**) had antibacterial properties which can be benefit for wound healing.[263]

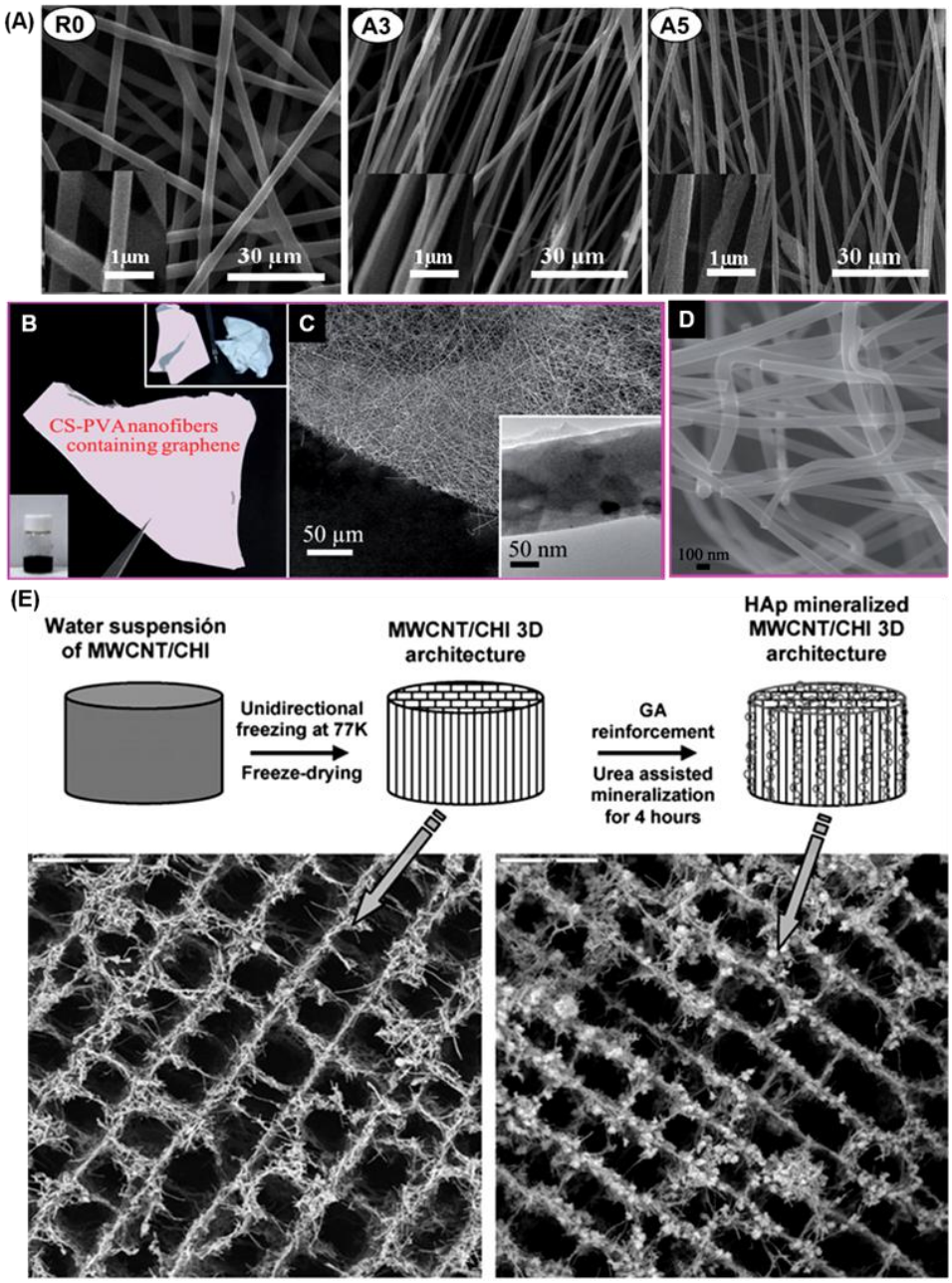

Fig.1-18 (A) SEM images of MWCNTs-PLA electrospun nanofiber scaffolds with weight ratios of MWCNTs: 0 - 5 %.[262] (B-D) Photograph and SEM images of chiosan-PVA nanofibers containing graphene.[263] (E) Schematic representation of the preparation process of MWCNTs/chitosan scaffolds and SEM images of corresponding products.[264]

In addition, reinforced CBMs integrated with inorganic matrices such as hydroxyapatite (HAp) and calcium phosphate, show distinct mechanical properties and is considered to be a useful method for synthesizing potential candidate scaffolds for bone tissue engineering.[265, 266] For example, the HAp mineralized MWCNTs/chitosan (**Fig.1-18 E**) scaffolds obtained

through a separation-induced self-assembly process were found to have good suitability in vitro for proliferation and viability of osteoblastic cell.[264]

The application of CBMs alone or MS alone in tissue engineering has been extensively discussed. At the same time, the application of CBMs/MS composites combining the properties of both CBMs and silica based ordered mesoporous materials in tissue engineering is relatively newly and such approaches have gained much research interest. Hence, only a few attempts have been done on the use of CBMs/MS hybrid materials as scaffolds for tissue engineering. Among the few, an example of the application of CNMs/MS composites for tissue engineering was reported by Vila's team. They presented the effect of osteoblasts cells on the biological response of the conductive CNT/MS composites and found increasing proliferation of osteoblasts cells when exposed to external electrical stimulation.[267] With the application of electrical stimulation on the CNT/MS scaffolds, mitochondrial activity increased up to seven times, indicating their potential application in bone regeneration. Finally, although some CBMs/MS nanoplatforms had been fabricated, there is still a lack of full investigation on their applications in tissue engineering.

1.3.3 Imaging

Most imaging probes currently used in bio-imaging work in the visible range, however, tissue absorption, scattering, and autofluorescence are strong in this range.[268] Therefore, the development of optical probes functioning in the NIR "biological transparent window" (650-1350 nm) to minimize optical interference from tissues has great potential for non-invasive biomedical imaging. CBMs exhibit a wide absorption spectrum in the visible and near infrared range, photoluminescence in the NIR region and strong resonance Raman scattering. Owing to their intrinsic optical properties, much effort has been devoted to the development of CBMs mainly SWCNTs, graphene and its derivatives, CDs as fluorescent probes for in vitro and in vivo bioimaging, ranging from single-modal imaging to multimodal, and even image-guided chemo-photothermal therapy.[269-272]

The excellent photo-stability and NIR-II emission (1000-1700 nm) characteristics of SWCNTs make them ideal probes for tracking molecular events and contrast agents for in

vivo imaging in both diagnostics and therapeutics.[273-275] Non-invasive tracking was achieved by Fakhri et al. by imaging highly stable near-infrared luminescence of SWCNTs targeted to kinesin-1 motor proteins in COS-7 cells (**Fig.1-19 A**).[276] The combined high tumor accumulation ability and ideal fluorescence excitation/emission properties of SWCNTs were also demonstrated for tumor detection and imaging.[277, 278] Recently, Yudasaka et al. reported SWCNTs coated with an amphiphilic and biocompatible polymer PMB (2-methacryloyloxyethyl phosphorylcholine-*co*-*n*-butyl methacrylate) for imaging of brown fat (**Fig.1-19 B**).[279] PMB-CNTs system selectively accumulated in brown fats, providing clearer NIR photoluminescent (PL) images of these tissues than conventional organic dyes, as the high level of transmit light passed through the body with less light scattering.

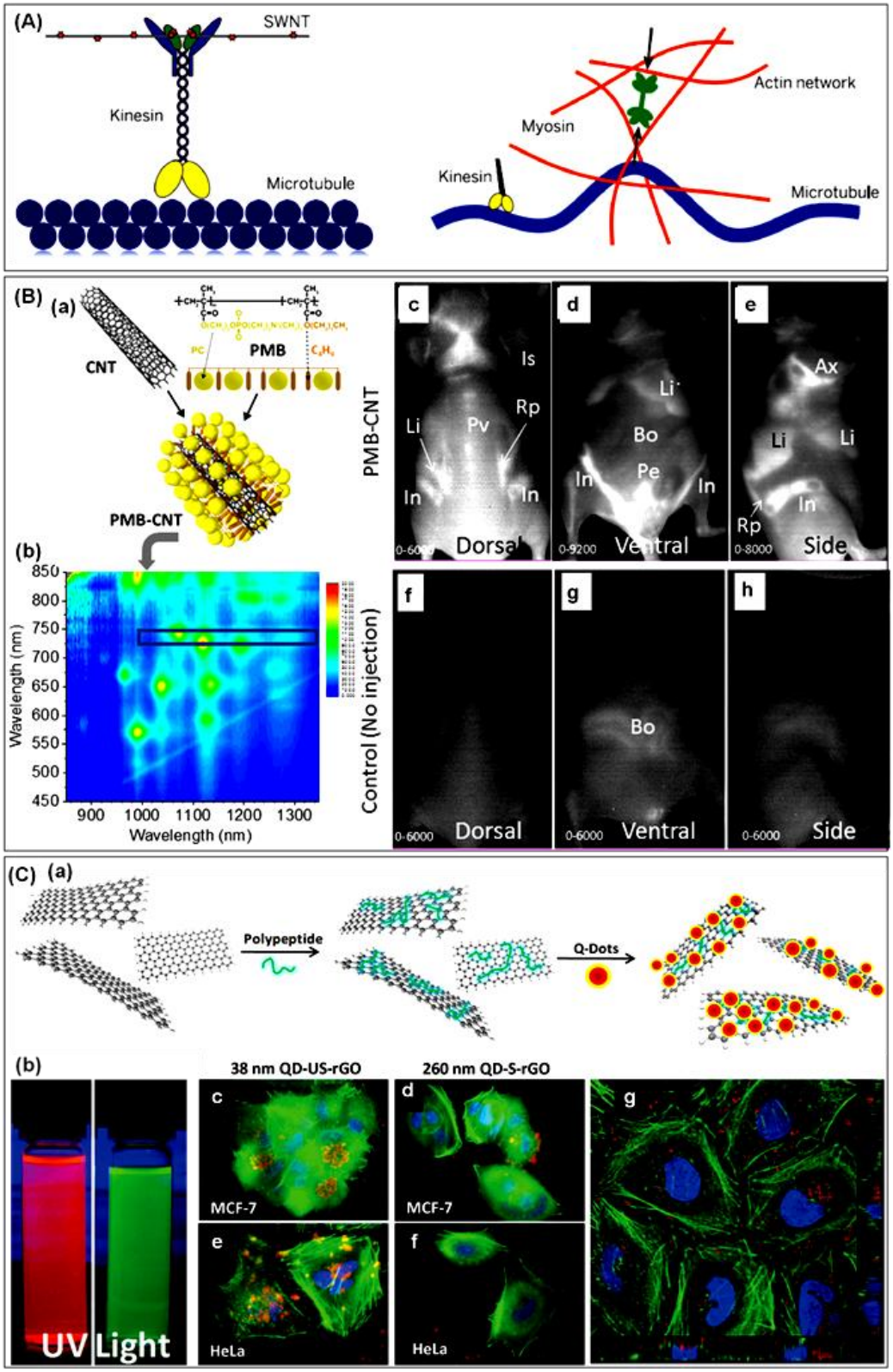

Fig.1-19 (A) SWNT-labeled kinesin motor moving along a MT embedded in an actin-myosin network.[276] (B) NIR-PL CNTs for imaging of brown fat: (a) Schematics of CNT, PMB, and PMB-coated CNT, (b) PL spectra of PMB-CNT dispersed in water, (c-h) Typical NIR-PL images of a mouse 5 h after injection of PMB-CNT or without injection.[279] (C) QD-tagged

rGO composites for bright fluorescence bio-imaging: (a) Schematic representation of the synthesis of QD-rGO, (b) Suspensions of two QD-rGO samples under UV light, (c-f) Cellular uptake of FA-QD-rGO composites, (g) Confocal images of multiple cross-sections, exhibiting various locations of the QD-rGO within the cells.[280]

Graphene and its derivatives have been reported to be modified with various functional nanoparticles such as gold nanoparticles,[281] magnetic nanoparticles[282, 283] and CDs,[284] to combine multiple functionalities for imaging. For example, it was reported that the strongly fluorescent, nontoxic QDs-tagged rGO (QD-rGO) nanocomposite (in **Fig.1-19 C)** showed the capability to combine in situ imaging, tumor treatment and monitoring.[280] Remarkably, QD-rGO absorbed NIR light to achieve photo-thermal therapy and cells killing, and the heat generated simultaneously caused the temperature to rise while the QDs brightness to decrease significantly, which provided an approach for in-situ heat/temperature sensing as well as an indicator for detecting the progress of photo-thermal therapy. In addition, due to their high photostability and biocompatibility, CDs are also well suited for cellular imaging, as well as monitoring the distribution of drugs and their effects.[285-287] For instance, phosphorus and nitrogen dual-doped hollow carbon dots (PNHCDs) multifunctional nanocarriers combining imaging, nucleus targeting, and in vivo therapeutic efficacy were reported recently.[288]

CBMs can also be covalently linked to visible light fluorophores for cellular imaging. For example, El-Sayed et al. demonstrated for the first time that SWCNTs chemically conjugated with recombinant thermo-stable *Luciola cruciata* luciferase (LcL) was used for in vivo imaging.[289] The chemiluminescence of LcL allowed imaging of CNTs and their cargo in at an organ resolution in nonsuperficial locations without excitation sources. In vivo imaging of LcL-CNTs system using IVIS spectrum showed the uptake of LcL-CNTs by different organs in mice.

CBMs/MS composites possess the outstanding optical properties derived from CBMs and can also be widely used in biological imaging. More specifically, the porosity of the MS matrix serves as good drugs or nanoparticles loading platforms, so that CBMs/MS hybrids can simultaneously perform fluorescent biological imaging and other functions, such as drug

delivery and selectively targeting chemo-photothermal therapy.[140, 176, 234, 290]

For example, a multifunctional hybrid nanomaterial of magnetic CNTs sheathed with MS was developed for the simultaneous applications in drug delivery and imaging (**Fig.1-20 A**).[143] The hybrid nanoplatform showed excellent magnetic properties, including MRI in vitro and in vivo, and can potentially be used as a drug delivery and imaging system. Wang et al. reported a multifunctional theranostic platform developed from magnetic graphene-coated MS modified with targeting peptide, which combined pH and photothermal responsive drug release, chemo-photothermal therapy with specific dual-targeting and MRI monitoring for visualize glioma therapy.[224] Sreejith et al. developed a hybrid material of GO-sheet-coated MSNs (**Fig.1-20 B**), which was applied for the protection of squaraine dyes (a class of organic dyes showing intense fluorescence, which can be used as the second generation of photosensitizers for photodynamic therapy), and showed a good prospect as a fluorescent hybrid for application in fluorescence imaging in vitro.[155] CDs/MS composites are promising multifunctional platforms for in vivo bioimaging and controlled drug release because CDs can be anchored to the entrance of MS to control the on-demand drug release.[231, 233, 235] Chen et al. reported MSNs capped with GQDs for intracellular drug delivery and imaging, where GQDs were regarded as capping agents and imaging agents to construct a multifunctional drug release system through acetal bonds.[234] Multifunctional CDs/MS nanohybrids with the capabilities of multicolor PL and two-photon imaging, photothermal effect and anti-cancer drug delivery also have been proposed.[291]

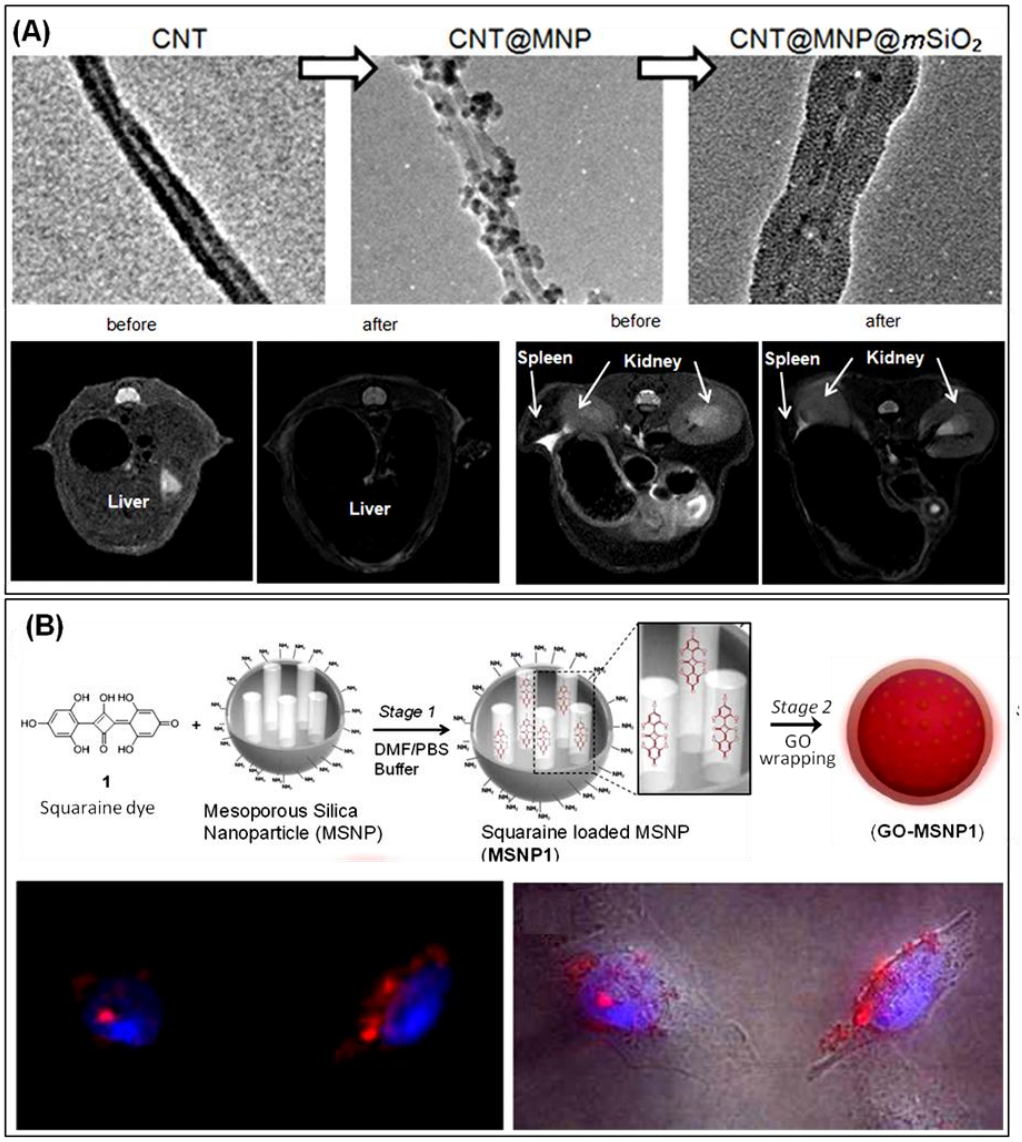

Fig.1-20 (A) In vivo T2-weighted MRI images of liver and kidney and spleen before and after intravenous administration of CNT@MNP@mSiO$_2$ nanocarriers.[143] (B) Synthesis of GO-MSNP1 hybrid and epifluorescence microscopy images of HeLa cancer cells labeled with GO-MSNP1. The blue fluorescence was from the DAPI nuclear counterstain, and the red fluorescence was from GO-MSNP1.[155]

1.3.4 Biosensing

CBMs are sensitive to the electrical changes due to their electrochemical activity and electrical conductivity, which makes them particularly attractive for biosensing applications.[292] In particular, CBMs can be used as nanoplatforms for the immobilization of multiple molecules on their surface to achieve multiplexed sensing, which makes them

suitable systems for transduction of signals associated with the recognition of various analytes.[293]

An ever-growing number of biosensing systems based on CBMs-conjugates have been developed for the detection of various proteins,[294-297] DNA,[298-300] disease biomarkers,[301-303] phenolic compounds,[304, 305] enzymes,[306, 307] etc. Some specific examples are demonstrated below. Huang et al. have developed an amplified SWCNT-mediated chemiluminescence (CL) turn-on biosensing platform for ultrasensitive DNA detection through the amplification of the read-out signal.[308] Dai et al. have constructed an electrochemical biosensing platform based on MWCNTs/$Mn_2P_2O_7$ (**Fig.1-21 A**), which displayed good performances for superoxide anions detection and provided a reliable platform to adhere living cells.[309] Such platforms have a promising prospect for living cells monitoring and diagnosis of reactive oxygen species-related diseases. A versatile graphene-based biosensing platform capable of achieving ultrasensitive detection of both small-molecule and macromolecular targets was also developed by Liu's group.[310] Furthermore, CDs-based inorganic-organic probes constructed by Kong et al. were reported to perform two-photon biosensing at physiological pH in living cells and in tissues with depths of 65–185 μm without interference from other biologically relevant species.[311]

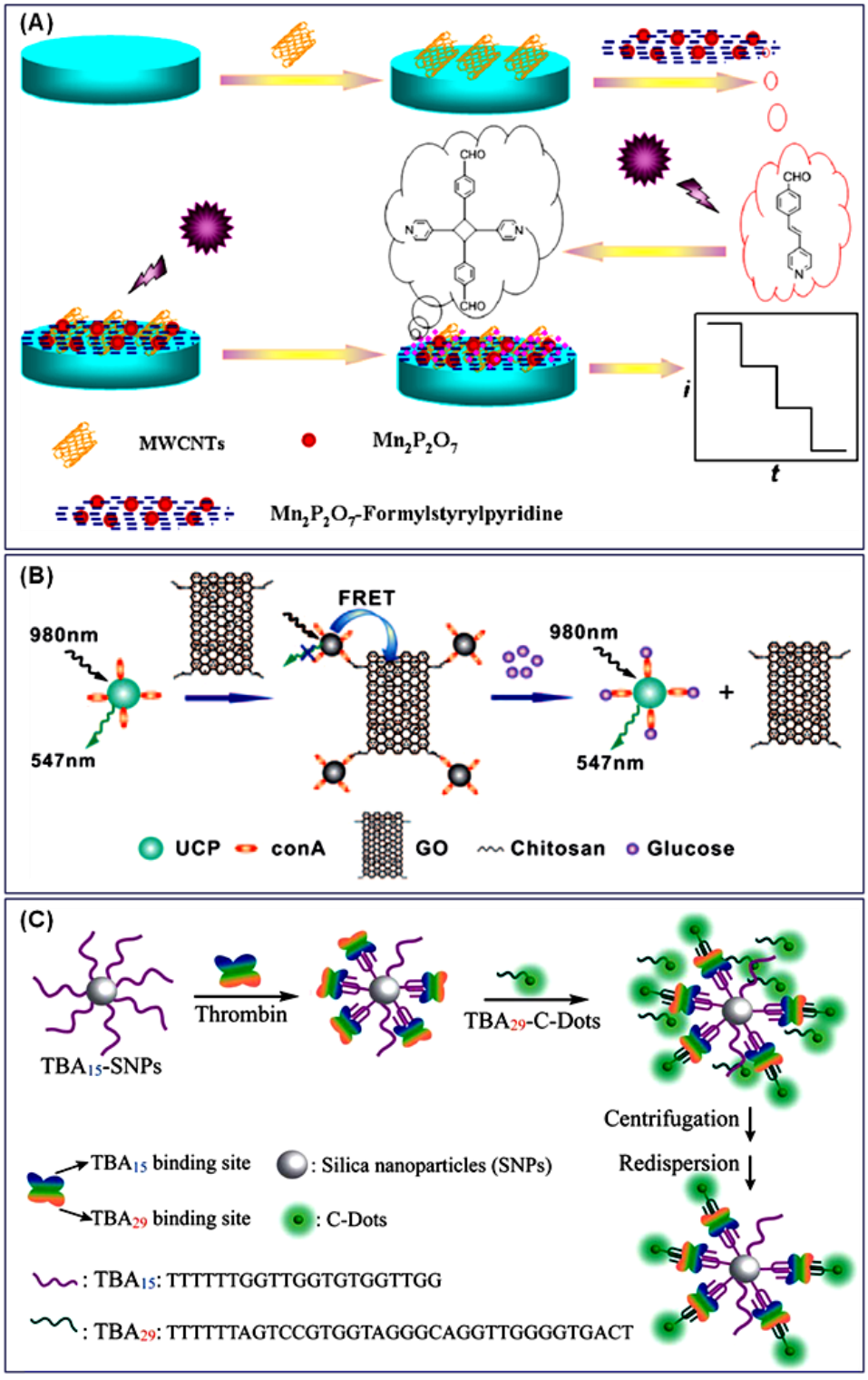

Fig.1-21 (A) Schematic diagram of the construction of MWCNTs/$Mn_2P_2O_7$ -Formylstyrylpyridine electrochemical biosensing platform for immobilization of biomimetic superoxide dismutase (SOD) under ultraviolet irradiation (UV) irradiation and then for real-time monitoring the superoxide anion released from living cells.[309] (B) Schematic illustration of the UCP-GO biosensing platform and the mechanism of glucose

determination.[312] Conca- navalinA (conA) and chitosan (CS) are covalently attached to upconverting phosphors (UCP) and GO. The tight binding of ConA with CS bring UCP and GO into appropriate proximity and induce fluorescence resonance energy transfer (FRET), and the FRET sensor has favorable analytical performance for glucose determination. (C) Schematic illustration of the aptamer-functionalized CDs for fluorescent detection of protein. TBA_{15}-bound silica nanoparticles (SNPs) were bonded to the fibrinogen recognition exosite of thrombin, and TBA_{29}-labeled CDs recognized the heparin-binding exosite.[313]

In addition, the inherent optical properties of CBMs in the NIR region (where there is minimal interference from biological media) is an exceptional characteristic for optical biosensing.[314] The performance of CBM-based optical biosensors operating in these NIR regions may be superior to traditional optical biosensors operating at visible wavelengths, especially for in vivo sensing, because blood, cells, and tissues are strongly absorbing and auto-fluorescent at visible wavelengths.[315-317] For example, M. Iverson et al. proposed tissue-localizable NIR-fluorescent SWCNTs for in vivo biosensing, which could be injected intravenously into mice and selective detection of local nitric oxide concentration with a detection limit of 1 mM.[318] Based on fluorescence resonance energy transfer (FRET) from upconverting phosphors to GO, Zhang et al. constructed a novel UCP-GO biosensing platform for glucose determination (**Fig.1-21 B**), which showed favorable analytical performance in a complex biological sample matrix when excited with NIR light.[312] In addition, taking advantages of their low cytotoxicity and photoluminescent property, CDs have been employed as novel, ideal fluorescent probes for smart biosensing. An example of aptamer-functionalized CDs for fluorescent detection of protein was presented in **Fig.1-21 C**. This strategy showed high sensitivity and selectivity toward thrombin with detection limit of 1nM, which was significant improved as compared to other reported fluorescence-based thrombin detection assays.[313]

Biosensing platforms based on the CBMs/MS hybrid nanomaterials were also reported. Thanks to the uniform accessible mesopores and easy chemical functionalization of MS, CBMs/MS composites modified with various functionalities have been widely studied for

biosensing.[319-321] Regarding CNTs/MS composites, for example, a novel biosensing platform based on Nafion-coated MWCNTs and hemoglobin (Hb) functionalized MCM41 hybrid material was reported for the detection and selective quantification of nitrite (NO_2^-) and trichloroacetic acid (TCA).[322] In another work, a sandwich-type immunosensor for sensitive detection of retinol-binding protein (RBP) based on MWCNTs and $Ru(bpy)_3^{2+}$ doped MSNs was developed by Wu et al.[323] The designed electrochemiluminescence (ECL) immunosensor exhibited high sensitivity and effienciency for the detection of RBP, and showed a linear response to the clinically-relevant RBP at the concentration of 78 - 5000 ng/mL (**Fig.1-22 A**).

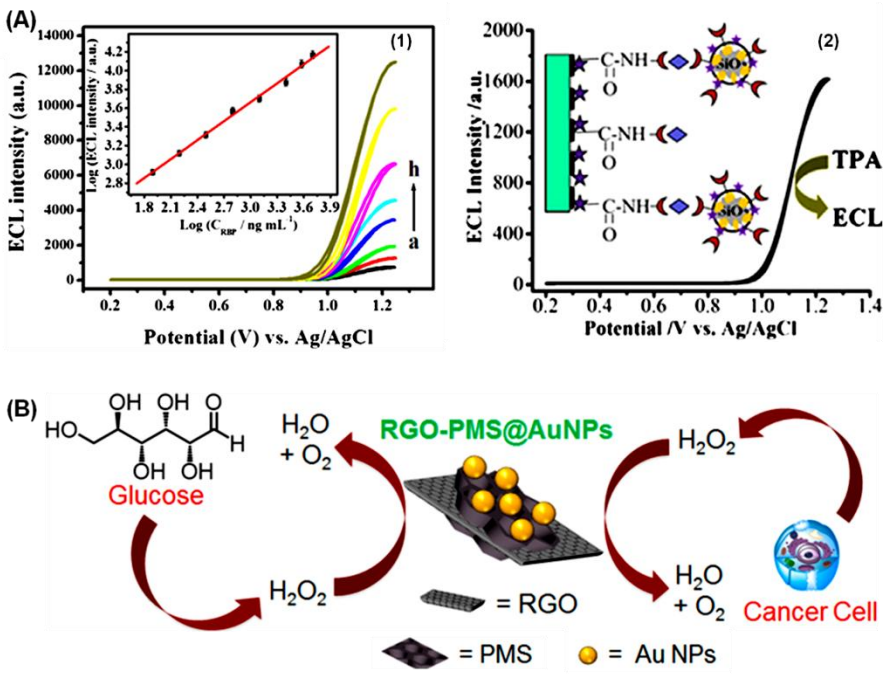

Fig.1-22 (A) MWCNTs/MS based immunosensor for detection of retinol-binding protein: (1) ECL signals of immunosensor incubated with different concentrations of RBP. Inset: calibration curve for RBP determination, (2) ECL response of electrodes modified with the designed immunosensor.[323] (B) Schematic representation of RGO-PMS@AuNPs for the electrochemical sensing of H_2O_2 liberated from cancer cells and glucose in human urine.[146]

In view of the special characteristics of graphene-based/MS composites, different functionalities have been introduced thereby giving rise to unique properties to these nanohybrid materials for biosensing applications. Very recently, MSNs embedded GO hybrid system was prepared by Srivastava et al. and used as an efficient platform for the

electrochemical biosensing of urea.[154] The optimized GO-SiO_2 (GOS) composite electrode showed a high sensitivity and a good detection limit of urea, and is expected to be promising biosensing platform in clinical diagnosis. On the other hand, a new kind of 2D electrochemical biosensor by the immobilization of ultrasmall gold NPs (AuNPs, ~3 nm) onto sandwich-like periodic MS (PMS) coated rGO was fabricated (**Fig.1-22 B**).[146] Such hybrid-based electrode sensor could sensitively detect trace amounts of H_2O_2 liberated from bioactive species and certain cancerous cells, showing a promising versatile platform for biosensing, bioanalysis, and biomedical applications. In addition, some work on biosensing applications of CDs/MS hybrid materials has also been carried out. For instance, a bimodal sensing platform comprising of a nanostructured Fabry-Pérot porous silicon (PSi) thin film encapsulated CDs was designed, and the orthogonal, bimodal sensing of biomolecules was achieved by modulating the optical reflectance associated with the PSi matrix and the fluorescence of the CDs.[324]

1.4 Potential toxicity issues of CBMs for biomedical applications

As discussed above, CBMs and CBMs/MS composites as potential nanoplatforms have been extensively studied in various biomedical fields including drug delivery for cancer therapy, tissue engineering, biomedical imaging and biosensing. The widespread and rapid development of CBMs and their composites have also led to numerous investigations on their impact on health and environment. For instance, it has been demonstrated that silica nanoparticles can be hydrolytically degraded intracellularly and the derived products (mainly orthosilicic acid) are eliminated through the kidney without apparent toxic effects.[325-327] However, the inert physical and chemical nature of CBMs makes them difficult to degrade under natural conditions, and they can accumulate in the biological environment or agglomerate with other substances, which may cause toxicity to organisms. Therefore, the most concerned and discussed issue related to the applicability of CBMs and CBMs/MS composites for biomedical applications is their biosafety.

1.4.1 Toxicity impact of CBMs

There is a broad consensus that CBMs have potential risks to organisms and ecosystems

due to their cell and tissue toxicity. Considerable works have been done, in vitro and in vivo, to investigate the potential toxicity of CBMs, although conflicting results exist. Up to now, the potential long-term toxicity concerning CBMs is still not completely addressed. It is generally considered that the behavior and cytotoxicity of CBMs are not only related to the differences in physicochemical properties of CBMs themselves, but also associated with other potential parameters such as the impurities introduced during the synthesis of CBMs, surface functional groups introduced in post-processing, and the influence of dosage, etc.[328, 329]

CNTs have been shown to induce inflammation, fibrosis, epithelioid granuloma formation in the lungs, cellular cytotoxicity, and cardiopulmonary and vascular irregularities.[40, 61, 330] In addition, numerous studies revealed that graphene and its derivatives could create dose-dependent toxicity in cells with decreased cell viability and apoptosis, and in animals resulting, for example, in lung, liver, spleen or kidney injuries, lung granuloma formation.[41, 49, 331, 332] On the other hand, CBMs including SWCNTs, MWCNTs, graphene and mixed carbon nanoparticles show to potentially aggravate platelet aggregation and disrupt the circulatory system responsible for blood clotting and hemostasis, which may cause fatal consequences such as stroke, myocardial infarction and deep vein thrombosis.[333-335] Among different materials of the carbon family, it seems that the smaller size of CDs is superior to CNTs, graphene and its derivatives in terms of toxicity. It is theoretically showed that the potential cytotoxicity of CDs depended on their size and concentration. For example, it was evaluated that the high concentration of GQDs could induce changes in the structure properties and diffusion properties of the lipid bilayer, and it might affect the cell signal transduction.[336] Although many works have been performed to study the physicochemical properties and toxicity of CBMs, the exact toxicity mechanism of CBMs remain obscure. Nevertheless, according to current knowledge, the biological toxic effects of CBMs are sample specific and need to be assessed on a case-by-case basis.

The toxicity of CBMs in biological systems are greatly affected by many parameters including their physical properties such as length, type and degree of agglomeration, concentration, impurities, surface property and functional groups, etc. Studies have shown

that the size of CBMs had a great influence on the toxicity of CBMs, and the differences in toxicity vary greatly depending on the materials themselves. For instance, it was demonstrated that the length of CNTs clearly influenced their uptake and the shorter (< 1 μm) MWCNTs were easier internalized through an energy-independent pathway,[66] while longer CNTs would cause bio-persistence or CNTs retention leading to severe inflammation and fibrosis.[337, 338] The factors of length contributing to the toxicity and the plausible mechanisms by which CNTs exert their toxicological effects are shown in **Fig.1-23 A**. The lateral dimension factor of graphene has also been reported to significantly affect its toxicity by affecting the mode of action of cellular uptake, renal clearance, blood-brain barrier transport, and many other biological interactions.[339, 340] Generally, graphene with small dimensions, sharp edges and rough surfaces easily internalize into the cell.

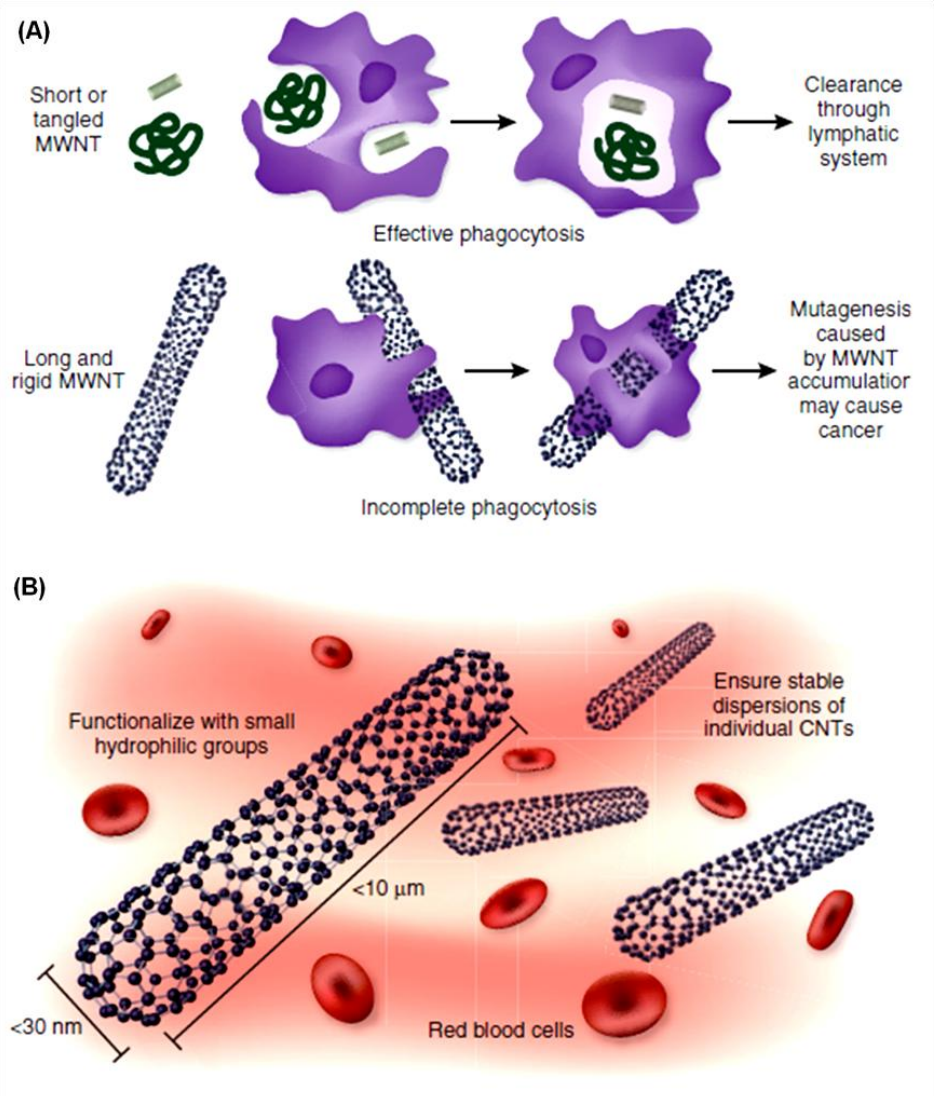

Fig.1-23 Factors affecting the safety of CNTs in vivo. (A) The effect of CNT structure on phagocytosis by macrophages and clearing from tissues. (B) Other considerations relevant to the safety of CNTs.[341]

Besides their dimensions, some other factors should be taken into consideration when it comes to the safety of CBMs, such as preventing their aggregation and sedimentation to prevent their accumulation in organ tissues. The high agglomeration state of CNTs in vivo will cause the accumulation of CNTs in lungs and livers, subsequently initiating an inflammatory response.[342-344] The residual impurities such as chemical additives or metallic impurities introduced during the synthesis of CBMs are important considerations because they may be responsible for the observed toxicity, rather than the carbon nanomaterials themselves.[345-347] It has been noted that the large variation in the types and concentrations of the residual metal impurities leads to uncertain toxicity of CNTs from the generated toxic free radicals.[348] Similarly, traditionally prepared GO usually contains high levels of Mn^{2+} and Fe^{2+}, which are highly mutagenic to cells, and the non-specific release of these ions results in unusually high levels of cytotoxicity and DNA fracturing.[41]

The surface chemistry of CBMs determines their hydrophilicity or hydrophobicity, stability, and dispersibility in physiological conditions. The functionalization of CBMs helps to achieve greater compatibility with the physiological systems and can regulate their cytotoxicity. A large number of studies have confirmed that functionalizing CBMs with polymers such as PEG,[349] poly (ε-caprolactone),[350] polyvinyl alcohol (PVA),[351] or functional groups such as carboxyl [352] can greatly reduce their toxicity and improve their in vitro or in vivo biocompatibility. For example, it was found that PEG-coated GO could effectively relieve GO-induced acute tissue injuries, and prevent the accumulation of GO in organ tissues as well as promote the clearance of GO.[353] The carboxylated GQDs were desirable to increase aqueous solubility, and no severe symptoms of inflammation were observed in the liver, kidney, spleen, heart, or lung at 22 days after their administration.[354] However, the role of functionalizing group may lead to the induction of toxicity. SWCNTs functionalized with carboxylic acid were shown to induce higher toxicity compared to the non-functionalized

SWCNTs,[355] indicating the importance of selecting the appropriate functional groups for the intended application. Furthermore, the conjugation of biological molecules such as proteins, aptamers and antibodies with CBMs may help cell specific targeting, cellular processing and elimination, resulting in reduced toxicity.[284, 329, 356] A markedly less cytotoxicity of SWCNTs, GO and rGO nanosheets was observed by mediating them with blood protein coating.[357, 358]

1.4.2 Biodegradation of CBMs

CBMs are considered to be very resilient and persistent materials due to their rigid and strong structure, which are characterized by a high resistance to different chemical treatments. Thus, they are expected to have a very high bio-persistence for organs and tissues, the non-biodegradable CBMs being able to accumulate in tissues, causing harmful side effects. Biodegradability is a safe and effective way to remove CBMs from the environment, to reduce their toxic effects and other unknown risks, and to facilitate their biomedical applications. The biodegradation ways of CBMs mainly include enzymatic and microbial degradations.

Enzymatic degradation is the most widely studied method for the biodegradation of CBMs. The commonly used enzymes include myeloperoxidase (MPO),[359] horseradish peroxidase (HRP),[360] lactoperoxidase (LPO),[361] manganese peroxidase (MnP),[362] lignin peroxidase (LiP),[363] etc, which usually require H_2O_2 to participate in the degradation of CBMs. The degrading enzymes have positively charged amino acid residues, and these residues are combined with negatively charged functional groups on the surface of CBMs through electrostatic interaction.[364] E. Kagan's group has proved that the natural enzyme HRP and MPO enzyme in human neutrophils could catalyse the degradation of SWCNTs in vitro.[365] The catalytic biodegradation of CDs in vitro by the oxidative activity of pancreatic lipase and at low concentrations of hydrogen peroxide was also demonstrated by Srivastava et al.[366] Unfunctionalized CBMs may not be easily degraded, and the degradation usually begins with defects. Therefore, surface modification or functionalization of CBMs can usually promote their biodegradation because it will cause more defects and change the energetic properties and enzymatic conformations, thereby facilitating the occurrence of degradation.[367,

368

Compared with enzymatic degradation, microbial degradation seems to be a promising method for practical applications, because enzymatic degradation is affected by many factors such as temperature and pH. Multiple types of microbes including bacteria and fungi have the ability to degrade CNTs, graphene and their derivatives. The complete degradation of these carbon materials by microorganisms is proposed as an effective method for detoxification. Liu et al. successfully isolated a naphthalene-degrading bacterium from contaminated soil in a graphite mine that could degrade oxidize graphite, GO and rGO.[369] Recently, the degradation of pristine MWCNTs and oxidized MWCNTs by the white rot fungus Phanerochaete chrysosporium was evaluated by Ma et al.[370]

1.5 References

1. V. Georgakilas, J. A. Perman, J. Tucek and R. Zboril, *Chem. Rev.*, 2015, **115**, 4744-4822.
2. M. Hu, F. Tian, Z. Zhao, Q. Huang, B. Xu, L.-M. Wang, H.-T. Wang, Y. Tian and J. He, *J. Phys. Chem. C*, 2012, **116**, 24233-24238.
3. S. Goodarzi, T. D. Ros, J. o. Conde, F. Sefat and M. Mozafari, *Materials Today*, 2017, **20**, 460-480.
4. S. lijima, *Nature*, 1991, **354**, 56-58.
5. V. ı. D. N. Bezzon, T. ı. L. A. Montanheiro, B. R. C. d. Menezes, R. G. Ribas, V. A. N. Righetti, K. F. Rodrigues and G. P. Thim, *Adv. Mater. Sci. Eng.*, 2019, **2019**, 1-21.
6. I. Khan, K. Saeed and I. Khan, *Arab. J. Chem.*, 2019, **12**, 908-931.
7. S. Nasir, M. Z. Hussein, Z. Zainal and N. A. Yusof, *Materials*, 2018, **11**, 295-319.
8. X. Wang, Y. Feng, P. Dong and J. Huang, *Front. Chem.*, 2019, **7**, 671-680.
9. L.-C. Qin, *Phys. Chem. Chem. Phys.*, 2007, **9**, 31-48.
10. F. Zhang, P.-X. Hou, C. Liu and H.-M. Cheng, *Carbon*, 2016, **102**, 181-197.
11. M.-F. Yu, O. Lourie, M. J. Dyer, K. Moloni, T. F. Kelly and R. S. Ruoff, *Science*, 2000, **287**, 637-641.
12. R. S. Ruoff, J. Tersoff, D. C. Lorents, S. Subramoney and B. Chan, *Nature*, 1993, **364**, 514-516.
13. A. Eatemadi, H. Daraee, H. Karimkhanloo, M. Kouhi, N. Zarghami, A. Akbarzadeh, M. Abasi, Y. Hanifehpour and S. W. Joo, *Nanoscale Res. Lett.*, 2014, **9**, 393-406.
14. C. N. R. Rao, A. Govindaraj, G. Gundiah and S. R. C. Vivekchand, *Chem. Eng. Sci.*, 2004, **59**, 4665-4671.
15. L. D. Filip and V. Filip, *Solid State Electron. Lett.*, 2019, **1**, 1-9.
16. Z. El-Moussawi, A. Nourdine, H. Medlej, T. Hamieh, P. Chenevier and L. Flandin, *Carbon*, 2019, **153**, 337-346.
17. B. Kumanek and D. Janas, *J. Mater. Sci.*, 2019, **54**, 7397-7427.
18. S. Berber, Y.-K. Kwon and D. Tománek, *Phys. Rev. Lett.*, 2000, **84**, 4613-4616.
19. Z. Han and A. Fina, *Prog. Polym. Sci.*, 2011, **36**, 914-944.
20. A. Aqel, K. M. M. A. El-Nour, R. A. A. Ammar and A. Al-Warthan, *Arab. J. Chem.*, 2012, **5**, 1-23.
21. N. Akizuki, S. Aota, S. Mouri, K. Matsuda and Y. Miyauchi, *Nat. Commun.*, 2015, **6**, 8920-8925.
22. J. T. Robinson, K. Welsher, S. M. Tabakman, S. P. Sherlock, H. Wang, R. Luong and H. Dai, *Nano Res.*, 2010, **3**, 779-793.
23. G. Rahman, Z. Najaf, A. Mehmood, S. Bilal, A. Shah, S. Mian and G. Ali, *C-J. Carbon Res.*, 2019, **5**, 1-31.
24. W. Z. Li, S. S. Xie, L. X. Qian, B. H. Chang, B. S. Zou, W. Y. Zhou, R. A. Zhao and G. Wang, *Science*, 1996, **274**, 1701-1703.
25. K. Varshney and A. Professor, *Int. J. Eng. Res. Gen. Sci.*, 2014, **2**, 660-678.
26. K. Mukul and A. Yoshinori, *J. Nanosci. Nanotechnol.*, 2010, **10**, 3739-3758.
27. S. Venkatesan, B. Visvalingam, G. Mannathusamy, V. Viswanathan and A. G. Rao, *Int. Nano Lett.*, 2018, **8**, 297-308.
28. X. Wan, Y. Huang and Y. Chen, *Acc. Chem. Res.*, 2012, **45**, 598-607.

29. J. Filip and J. Tkac, *Electrochimica Acta*, 2014, **136**, 340-354.
30. K. S. Novoselov, A. K. Geim, S. V. Morozov, D. Jiang, Y. Zhang, S. V. Dubonos, I. V. Grigorieva and A. A. Firsov, *Science*, 2004, **306**, 666-669.
31. H. Shen, L. Zhang, M. Liu and Z. Zhang, *Theranostics*, 2012, **2**, 283-294.
32. V. Georgakilas, J. N. Tiwari, K. C. Kemp, J. A. Perman, A. B. Bourlinos, K. S. Kim and R. Zboril, *Chem. Rev.*, 2016, **116**, 5464-5519.
33. Y. Zhu, S. Murali, W. Cai, X. Li, J. W. Suk, J. R. Potts and R. S. Ruoff, *Adv. Mater.*, 2010, **22**, 3906-3924.
34. N. O. Weiss, H. Zhou, L. Liao, Y. Liu, S. Jiang, Y. Huang and X. Duan, *Adv. Mater.*, 2012, **24**, 5782-5825.
35. X. An, T. Butler, MorrisWashington, S. K. Nayak and S. Kar, *ACS Nano*, 2011, **5**, 1003–1011.
36. A. A. Balandin, S. Ghosh, W. Bao, I. Calizo, D. Teweldebrhan, F. Miao and C. N. Lau, *Nano Lett.*, 2008, **8**, 902-907.
37. Z. Liu, J. T. Robinson, X. Sun and H. Dai, *J. Am. Chem. Soc.*, 2008, **130**, 10876–10877.
38. M. Li, X. Yang, J. Ren, K. Qu and X. Qu, *Adv. Mater.*, 2012, **24**, 1722-1728.
39. V. Georgakilas, M. Otyepka, A. B. Bourlinos, V. Chandra, N. Kim, K. C. Kemp, P. Hobza, R. Zboril and K. S. Kim, *Chem. Rev.*, 2012, **112**, 6156-6214.
40. W. Zheng, W. McKinney, M. L. Kashon, D. Pan, V. Castranova and H. Kan, *Nanoscale Res. Lett.*, 2018, **13**, 189-197.
41. L. Ou, B. Song, H. Liang, J. Liu, X. Feng, B. Deng, T. Sun and L. Shao, *Part. Fibre Toxicol.*, 2016, **13**, 57-80.
42. N. Cardona, F. Campuzano, M. Betancur, L. Jaramillo and J. D. Mart ńez, *Mater. Sci. Eng.*, 2018, **437**, 1-16.
43. M. Hindermann-Bischoff and F. Ehrburger-Dolle, *Carbon*, 2001, **39**, 375–382.
44. J. H. ATKINS, *Carbon*, 1965, **3**, 299-303.
45. P. E. Khizhnyak, A. V. Chechetkin and A. P. Glybin, *J. Eng. phys.*, 1979, **37**, 1073–1075.
46. F. Fabry, G. Flamant and L. Fulcheri, *Chem. Eng. Sci.*, 2001, **56**, 2123-2132.
47. Q.-L. Yan, M. Gozin, F.-Q. Zhao, A. Cohen and S.-P. Pang, *Nanoscale*, 2016, **8**, 4799-4851.
48. S. Anwar, H. Ding, M. Xu, X. Hu, Z. Li, J. Wang, L. Liu, L. Jiang, D. Wang, C. Dong, M. Yan, Q. Wang and H. Bi, *ACS Appl. Bio. Mater.*, 2019, **2**, 2317-2338.
49. M. Ema, M. Gamo and K. Honda, *Regul. Toxicol. Pharmacol.*, 2017, **85**, 7-24.
50. H. Li, X. He, Y. Liu, H. Huang, S. Lian, S.-T. Lee and Z. Kang, *Carbon*, 2011, **49**, 605-609.
51. M. X. Gao, C. F. Liu, Z. L. Wu, Q. L. Zeng, X. X. Yang, W. B. Wu, Y. F. Li and C. Z. Huang, *Chem. Commun.*, 2013, **49**, 8015-8017.
52. J. Deng, Q. Lu, N. Mi, H. Li, M. Liu, M. Xu, L. Tan, Q. Xie, Y. Zhang and S. Yao, *Chem. Eur. J.* , 2014, **20**, 4993-4999.
53. L.-L. Li, J. Ji, R. Fei, C.-Z. Wang, Q. Lu, J.-R. Zhang, L.-P. Jiang and J.-J. Zhu, *Adv. Funct. Mater.*, 2012, **22**, 2971-2979.

54. L. A. Ponomarenko, F. Schedin, M. I. Katsnelson, R. Yang, E. W. Hill, K. S. Novoselov and A. K. Geim1, *Science*, 2008, **320**, 356-358.
55. J. Peng, W. Gao, B. K. Gupta, Z. Liu, R. Romero-Aburto, L. Ge, L. Song, L. B. Alemany, X. Zhan, G. Gao, S. A. Vithayathil, B. A. Kaipparettu, A. A. Marti, T. Hayashi, J. J. Zhu and P. M. Ajayan, *Nano Lett.*, 2012, **12**, 844-849.
56. M. L. Liu, B. B. Chen, C. M. Li and C. Z. Huang, *Green Chem.*, 2019, **21**, 449-471.
57. H. W. Kroto, J. R. Heath, S. C. O'Brien, R. F. Curl and R. E. Smalley, *Nature*, 1985, **318**, 162-163.
58. R. Macovez, *Front. Mater.*, 2018, **4**, 1-7.
59. L. T. Scott, M. M. Boorum, B. J. McMahon, S. Hagen, J. Mack, J. Blank, H. Wegner and A. d. Meijere, *Science*, 2002, **295**, 1500-1503.
60. Z. A. Qiao, B. Guo, A. J. Binder, J. Chen, G. M. Veith and S. Dai, *Nano Lett.*, 2013, **13**, 207-212.
61. J. Dong and Q. Ma, *Nanotoxicology*, 2019, **13**, 1244-1274.
62. N. V. Salim, S. Mateti, P. Cizek, N. Hameed, J. Parameswaranpillai and B. Fox, *ACS Appl. Nano Mater.*, 2019, **2**, 1727-1736.
63. H. Wang, K. Wang, Q. Mu, Z. R. Stephen, Y. Yu, S. Zhou and M. Zhang, *Nanoscale*, 2017, **9**, 1434-1442.
64. C. Li, Y. Meng, ShanshanWang, M. Qian, JianxinWang, W. Lu and R. Huang, *ACS Nano*, 2015, **9**, 12096–12103.
65. R. Kaur and I. Badea, *Int. J. Nanomedicine*, 2013, **8**, 203-220.
66. V. Raffa, G. Ciofani, S. Nitodas, T. Karachalios, D. D'Alessandro, M. Masini and A. Cuschieri, *Carbon*, 2008, **46**, 1600-1610.
67. J. Feng and Z. Guo, *Nanoscale Horiz.*, 2019, **4**, 339-364.
68. M. Sianipar, S. H. Kim, K. Khoiruddin, F. Iskandar and I. G. Wenten, *RSC Adv.*, 2017, **7**, 51175-51198.
69. M. Zhang, Y. Wu, X. Feng, X. He, L. Chen and Y. Zhang, *J. Mater. Chem.*,, 2010, **20**, 5835.
70. D. TARN, C. E. ASHLEY, M. XUE, E. C. CARNES, J. I. ZINK and C. J. BRINKER, *Acc. Chem. Res.*, 2013, **46**, 792-801.
71. J. Tu, A. L. Boyle, H. Friedrich, P. H. Bomans, J. Bussmann, N. A. Sommerdijk, W. Jiskoot and A. Kros, *ACS Appl. Mater. Interfaces*, 2016, **8**, 32211-32219.
72. A. M. Pandele, C. Andronescu, A. Ghebaur, S. A. Garea and H. Iovu, *Materials*, 2018, **12**, 1-14.
73. D. Xiao, J. J. Hu, J. Y. Zhu, S. B. Wang, R. X. Zhuo and X. Z. Zhang, *Nanoscale*, 2016, **8**, 16702-16709.
74. L. Pan, Q. He, J. Liu, Y. Chen, M. Ma, L. Zhang and J. Shi, *J. Am. Chem. Soc.*, 2012, **134**, 5722-5725.
75. M. Manzano and M. Vallet‐Reg í, *Adv. Funct. Mater.*, 2019, **30**, 1902634.
76. S. H. Wu, C. Y. Mou and H. P. Lin, *Chem. Soc. Rev.*, 2013, **42**, 3862-3875.
77. W. Stöber, A. Fink and E. Bohn, *J. Colloid Interface Sci.*, 1968, **26**, 62-69.
78. P. Kipkemboi, A. Fogden, V. Alfredsson and K. Flodström, *Langmuir*, 2001, **17**, 5398-5402.
79. Y. Deng, J. Wei, Z. Sun and D. Zhao, *Chem. Soc. Rev.*, 2013, **42**, 4054-4070.

80. T.-J. Ha, H.-G. Im, S.-J. Yoon, H. W. Jang and H.-H. Park, *J. Nanomater.*, 2011, **2011**, 1-5.
81. Q. Huo, D. I. Margolese, U. Ciesla, P. Feng, T. E. Gier, P. Sieger, R. Leon, P. M. Petroff, F. Schüth and G. D. Stucky, *Nature*, 1994, **368**, 317-321.
82. L. P. Singh, S. K. Bhattacharyya, G. Mishra and S. Ahalawat, *Appl. Nanosci.*, 2011, **1**, 117-122.
83. S.-w. Ui, I.-s. Choi and S.-c. Choi, *ISRN Mater. Sci.*, 2014, **2014**, 1-6.
84. L. Liu, X. Fu, H. Zhang, W. Ma, L. Zhang, Y. Zhang, M. Liu, K. Liang, S. Hou and A. Chen, *J. Mater. Res.*, 2018, **33**, 1442-1448.
85. X. Huang, X. Teng, D. Chen, F. Tang and J. He, *Biomaterials*, 2010, **31**, 438-448.
86. F. Li, Z. Wang and A. Stein, *Angew. Chem. Int. Ed. Engl.*, 2007, **46**, 1885-1888.
87. F. Chen, H. Hong, S. Shi, S. Goel, H. F. Valdovinos, R. Hernandez, C. P. Theuer, T. E. Barnhart and W. Cai, *Scientifix Reports*, 2014, **4**, 5080-5058.
88. Q. Zhang, J. Ge, J. Goebl, Y. Hu, Z. Lu and Y. Yin, *Nano Res.*, 2010, **2**, 583-591.
89. D. Shen, J. Yang, X. Li, L. Zhou, R. Zhang, W. Li, L. Chen, R. Wang, F. Zhang and D. Zhao, *Nano Lett.*, 2014, **14**, 923-932.
90. J. S. Kang, J. Lim, W. Y. Rho, J. Kim, D. S. Moon, J. Jeong, D. Jung, J. W. Choi, J. K. Lee and Y. E. Sung, *Scientific reports*, 2016, **6**, 30829-30832.
91. Y. Yang, J. Wan, Y. Niu, Z. Gu, J. Zhang, M. Yu and C. Yu, *Chem. Mater.*, 2016, **28**, 9008-9016.
92. Y. Wang, X. Du, Z. Liu, S. Shi and H. Lv, *J. Mater. Chem. A*, 2019, **7**, 5111-5152.
93. W. Wang, P. Wang, X. Tang, A. A. Elzatahry, S. Wang, D. Al-Dahyan, M. Zhao, C. Yao, C. T. Hung, X. Zhu, T. Zhao, X. Li, F. Zhang and D. Zhao, *ACS Cent. Sci.*, 2017, **3**, 839-846.
94. K. Zhang, L. L. Xu, J. G. Jiang, N. Calin, K. F. Lam, S. J. Zhang, H. H. Wu, G. D. Wu, B. Albela, L. Bonneviot and P. Wu, *J. Am. Chem. Soc.*, 2013, **135**, 2427-2430.
95. N. Hao, Y. Nie, A. Tadimety, A. B. Closson and J. X. J. Zhang, *Mater. Res. Lett.*, 2017, **5**, 584-590.
96. R. Narayan, U. Y. Nayak, A. M. Raichur and S. Garg, *Pharmaceutics*, 2018, **10**, 118.
97. C. Argyo, V. Weiss, C. Bräuchle and T. Bein, *Chem. Mater.*, 2013, **26**, 435-451.
98. D. Douroumis, I. Onyesom, M. Maniruzzaman and J. Mitchell, *Crit. Rev. Biotechnol.*, 2013, **33**, 229-245.
99. J. G. Croissant, Y. Fatieiev and N. M. Khashab, *Adv. Mater.*, 2017, **29**.
100. D. S. Moon and J. K. Lee, *Langmuir*, 2012, **28**, 12341-12347.
101. N. Z. Knezevic and J. O. Durand, *Nanoscale*, 2015, **7**, 2199-2209.
102. D. Niu, Z. Liu, Y. Li, X. Luo, J. Zhang, J. Gong and J. Shi, *Adv. Mater.*, 2014, **26**, 4947-4953.
103. X. Du and J. He, *Langmuir*, 2010, **26**, 10057-10062.
104. M. Mizutani, Y. Yamada, T. Nakamura and K. Yano, *Chem. Mater.*, 2008, **20**, 4777-4782.
105. D. Chen, Z. Li, Y. Wan, X. Tu, Y. Shi, Z. Chen, W. Shen, C. Yu, B. Tu and D. Zhao, *J. Mater. Chem.*,, 2006, **16**, 1511-1519.
106. M. Wu, Q. Meng, Y. Chen, Y. Du, L. Zhang, Y. Li, L. Zhang and J. Shi, *Adv. Mater.*, 2015, **27**, 215-222.

107. S. M. Egger, K. R. Hurley, A. Datt, G. Swindlehurst and C. L. Haynes, *Chem. Mater.*, 2015, **27**, 3193-3196.
108. Z. Guo, L. Wu, Y. Wang, Y. Zhu, G. Wan, R. Li, Y. Zhang, D. Qian, Y. Wang, X. Zhou, Z. Liu and X. Yang, *ACS Appl. Mater. Interfaces*, 2020, **12**, 18823-18832.
109. S. K. Jana, R. Nishida, K. Shindo, T. Kugita and S. Namba, *Microporous Mesoporous Mater.*, 2004, **68**, 133-142.
110. Y. Li and M. Kruk, *RSC Adv.*, 2015, **5**, 69870-69877.
111. H. Zhang and X. Li, *J. Chem.*, 2016, **2016**, 1-16.
112. A. Sayari, Y. Yang, M. Kruk and M. Jaroniec, *J. Phys. Chem. B*, 1999, **103**, 3651-3658.
113. H.-Y. Chiu, D. Gößl, L. Haddick, H. Engelke and T. Bein, *Chem. Mater.*, 2018, **30**, 644-654.
114. H. S. Shin, Y. K. Hwang and S. Huh, *ACS Appl. Mater. Interfaces*, 2014, **6**, 1740-1746.
115. N. Hao, Y. Nie, Z. Xu, A. B. Closson, T. Usherwood and J. Z. JX, *Chem. Eng. J.*, 2019, **366**, 433-438.
116. C. Xu, M. Yu, O. Noonan, J. Zhang, H. Song, H. Zhang, C. Lei, Y. Niu, X. Huang, Y. Yang and C. Yu, *Small*, 2015, **11**, 5949-5955.
117. M. Huang, L. Liu, S. Wang, H. Zhu, D. Wu, Z. Yu and S. Zhou, *Langmuir*, 2017, **33**, 519-526.
118. D. Kwon, B. G. Cha, Y. Cho, J. Min, E. B. Park, S. J. Kang and J. Kim, *Nano Lett.*, 2017, **17**, 2747-2756.
119. Z. Xu, X. Ma, Y.-E. Gao, M. Hou, P. Xue, C. M. Li and Y. Kang, *Mater. Chem. Front.*, 2017, **1**, 1257-1272.
120. M. Karg, K. S. Lokare, C. Limberg, G. Clavel and N. Pinna, *Chem. Mater.*, 2017, **29**, 4920-4931.
121. Q. Fu, C. Lu and J. Liu, *Nano Lett.*, 2002, **2**, 329-332.
122. S. Guo, J. Li, W. Ren, D. Wen, S. Dong and E. Wang, *Chem. Mater.*, 2009, **21**, 2247-2257.
123. A. Li, W. Li, Y. Ling, W. Gan, M. A. Brady and C. Wang, *RSC Adv.*, 2016, **6**, 23318-23326.
124. T. Kempa, D. Carnahan, M. Olek, M. Correa, M. Giersig, M. Cross, G. Benham, M. Sennett, Z. Ren and K.Kempa, *J. Appl. Phys.*, 2005, **98**, 034310-034314.
125. W. L. Zhang and H. J. Choi, *Langmuir*, 2012, **28**, 7055-7062.
126. J. C. Wang, P. Chen, L. Chen, K. Wang, H. Deng, F. Chen, Q. Zhang and Q. Fu, *Express Polym. Lett.*, 2012, **6**, 299-307.
127. Y. Tian, Z. Ran and W. Yang, *RSC Adv.*, 2017, **7**, 43839-43844.
128. E. Enríquez, J. F. Fernández and M. A. de la Rubia, *Carbon*, 2012, **50**, 4409-4417.
129. L. Kou and C. Gao, *Nanoscale*, 2011, **3**, 519-528.
130. Y. Ma, H. Di, Z. Yu, L. Liang, L. Lv, Y. Pan, Y. Zhang and D. Yin, *Appl. Surf. Sci.*, 2016, **360**, 936-945.
131. B. Ramezanzadeh, Z. Haeri and M. Ramezanzadeh, *Chem. Eng. J.*, 2016, **303**, 511-528.
132. X. Liu, H. Zhang, Y. Ma, X. Wu, L. Meng, Y. Guo, G. Yu and Y. Liu, *J. Mater. Chem. A*, 2013, **1**, 1875-1884.
133. Y. Lin, C. Wang, L. Li, H. Wang, K. Liu, K. Wang and B. Li, *ACS Appl. Mater. Interfaces*, 2015, **7**, 27262-27270.

134. G. Mera, P. Kroll, I. Ponomarev, J. Chen, K. Morita, M. Liesegang, E. Ionescu and A. Navrotsky, *Dalton T.*, 2019, **48**, 11018-11033.
135. R. Liu, H. Zhang, F. Zhang, X. Wang, X. Liu and Y. Zhang, *Mater. Sci. Eng. C*, 2019, **96**, 138-145.
136. S. Fan, Y. Wang, Z. Li, Z. Zeng, D. Yao, S. Huang and X. Ma, *Appl. Catal. A: Gen.*, 2019, **583**, 117123-117132.
137. T. Zhang, B. Huang, A. A. Elzatahry, A. Alghamdi, Q. Yue and Y. Deng, *ACS Appl. Mater. Interfaces*, 2020, **12**, 17901-17908.
138. H. Lim, J. Lee, S. Jin, J. Kim, J. Yoon and T. Hyeon, *Chem. Commun.*, 2006, 463-465.
139. X. Deng, P. Qin, M. Luo, E. Shao, H. Zhao, X. Yang, Y. Wang, H. Shen, Z. Jiao and M. Wu, *Langmuir*, 2013, **29**, 6815-6822.
140. J. Liu, C. Wang, X. Wang, X. Wang, L. Cheng, Y. Li and Z. Liu, *Adv. Funct. Mater.*, 2015, **25**, 384-392.
141. Vincent Fiegel, SebastienHarlepp, SylvieBegin-Colin, D. Begin and DamienMertz, *Chem. Eur.J. 2*, 2018, **24**, 4662–4670.
142. C. Wells, O. Vollin-Bringel, V. Fiegel, S. Harlepp, B. Van der Schueren, S. Bégin-Colin, D. Bégin and D. Mertz, *Adv. Funct. Mater.*, 2018, **28**, 1706996.
143. R. K. Singh, K. D. Patel, J. J. Kim, T. H. Kim, J. H. Kim, U. S. Shin, E. J. Lee, J. C. Knowles and H. W. Kim, *ACS Appl. Mater. Interfaces*, 2014, **6**, 2201-2208.
144. Y. Tong, M. Zhang, P. Xia, L. Wang, J. Zheng, W. Li and J. Xu, *J. Magn. Magn. Mater.*, 2016, **406**, 35-41.
145. Z.-M. Wang, W. Wang, N. Coombs, N. Soheilnia and G. A. Ozin, *ACS Nano*, 2010, **4**, 7437–7450.
146. S. K. Maji, S. Sreejith, A. K. Mandal, X. Ma and Y. Zhao, *ACS Appl. Mater. Interfaces*, 2014, **6**, 13648-13656.
147. J. Feng, X. She, X. He, J. Zhu, Y. Li and C. Deng, *Food Chem.*, 2018, **239**, 612-621.
148. L. Guardia, F. Suárez-García, J. I. Paredes, P. Solís-Fernández, R. Rozada, M. J. Fernández-Merino, A. Martínez-Alonso and J. M. D. Tascón, *Microporous Mesoporous Mater.*, 2012, **160**, 18-24.
149. W. Czepa, D. Pakulski, S. Witomska, V. Patroniak, A. Ciesielski and P. Samorì, *Carbon*, 2020, **158**, 193-201.
150. B. Barik, A. Kumar, P. S. Nayak, L. S. K. Achary, L. Rout and P. Dash, *Mater. Chem. Phys.*, 2020, **239**, 122028.
151. Y. Wang, K. Wang, J. Zhao, X. Liu, J. Bu, X. Yan and R. Huang, *J. Am. Chem. Soc.*, 2013, **135**, 4799-4804.
152. Y. Du, S. Guo, S. Dong and E. Wang, *Biomaterials*, 2011, **32**, 8584-8592.
153. L. Shang, T. Bian, B. Zhang, D. Zhang, L. Z. Wu, C. H. Tung, Y. Yin and T. Zhang, *Angew. Chem. Int. Ed. Engl.*, 2014, **53**, 250-254.
154. S. Abraham, V. Ciobota, S. Srivastava, S. K. Srivastava, R. K. Singh, J. Dellith, B. D. Malhotra, M. Schmitt, J. Popp and A. Srivastava, *Anal. Methods*, 2014, **6**, 6711-6720.
155. S. Sreejith, X. Ma and Y. Zhao, *J. Am. Chem. Soc.*, 2012, **134**, 17346-17349.

156. P. Innocenzi, L. Malfatti and D. Carboni, *Nanoscale*, 2015, **7**, 12759-12772.
157. Y. Wang, S. Liang, B. Chen, F. Guo, S. Yu and Y. Tang, *PLoS One*, 2013, **8**, 65634-65641.
158. W. Dong, Y. Cheng, L. Luo, X. Li, L. Wang, C. Li and L. Wang, *RSC Adv.*, 2014, **4**, 45939-45945.
159. S. Zhou, D. Huo, C. Hou, M. Yang, H. Fa, C. Xia and M. Chen, *Anal. Methods*, 2015, **7**, 9649-9654.
160. Z. Guo, Z. Zhu, X. Zhang and Y. Chen, *Solid State Sci.*, 2018, **76**, 100-104.
161. J. Lei, L. Yang, D. Lu, X. Yan, C. Cheng, Y. Liu, L. Wang and J. Zhang, *Adv. Optical Mater.*, 2015, **3**, 57-63.
162. L. Zhou, Z. Li, Z. Liu, J. Ren and X. Qu, *Langmuir*, 2013, **29**, 6396-6403.
163. S. Huang, L. Song, Z. Xiao, Y. Hu, M. Peng, J. Li, X. Zheng, B. Wu and C. Yuan, *Anal. Methods*, 2016, **8**, 2561-2567.
164. X. Yao, X. Niu, K. Ma, P. Huang, J. Grothe, S. Kaskel and Y. Zhu, *Small*, 2017, **13**, 1602225-1602235.
165. T. Haynes, O. Ersen, V. Dubois, D. Desmecht, K. Nakagawa and S. Hermans, *Appl.Catal. B: Environ.*, 2019, **241**, 196-204.
166. D. M. Schlipf, S. E. Rankin and B. L. Knutson, *Microporous Mesoporous Mater.*, 2017, **244**, 199-207.
167. H. J. Liu and P. Xu, *Nanomaterials*, 2019, **9**, 1-23.
168. D. Mahony, A. S. Cavallaro, F. Stahr, T. J. Mahony, S. Z. Qiao and N. Mitter, *Small*, 2013, **9**, 3138-3146.
169. D. Saikia, J. R. Deka, C. E. Wu, Y. C. Yang and H. M. Kao, *Mater. Sci. Eng. C*, 2019, **94**, 344-356.
170. T. C. Canevari, P. A. Raymundo-Pereira, R. Landers, E. V. Benvenutti and S. A. Machado, *Talanta*, 2013, **116**, 726-735.
171. A. Kumar, G. D. Park, S. K. S. Patel, S. Kondaveeti, S. Otari, M. Z. Anwar, V. C. Kalia, Y. Singh, S. C. Kim, B.-K. Cho, J.-H. Sohn, D. R. Kim, Y. C. Kang and J.-K. Lee, *Chem. Eng. J.*, 2019, **359**, 1252-1264.
172. F. C. Dillon, J. Moghal, A. Koós, J. G. Lozano, L. Miranda, H. Porwal, M. J. Reece and N. Grobert, *Microporous Mesoporous Mater.*, 2015, **217**, 159-166.
173. M. Zhang, J. Zheng, P. Xia, Y. Zheng, J. Xu, L. Chen, X. He and Q. Fang, *New J. Chem.*, 2014, **38**, 3212-3219.
174. M. Vila, J. L. Hueso, M. Manzano, I. Izquierdo-Barba, A. de Andrés, J. Sánchez-Marcos, C. Prieto and M. Vallet-Regí, *J. Mater. Chem.*,, 2009, **19**, 7745-7752.
175. J. Seo, S. Sankarasubramanian and B. Lee, *B. Mater. Sci.*, 2018, **41**.
176. Y. W. Chen, T. Y. Liu, P. J. Chen, P. H. Chang and S. Y. Chen, *Small*, 2016, **12**, 1458-1468.
177. Y. Liu, W. Li, D. Shen, C. Wang, X. Li, M. Pal, R. Zhang, L. Chen, C. Yao, Y. Wei, Y. Li, Y. Zhao, H. Zhu, W. Wang, A. M. El−Toni, F. Zhang and D. Zhao, *Chem. Mater.*, 2015, **27**, 5577-5586.
178. L. Zhao, X. Ren, J. Zhang, W. Zhang, X. Chen and X. Meng, *New J. Chem.*, 2020, **44**, 1988-1992.
179. Z. Wang, C. Xu, Y. Lu, F. Wu, G. Ye, G. Wei, T. Sun and J. Chen, *ACS Appl. Mater. Interfaces*, 2017, **9**, 7392-7398.

180. K. Li, Y. Huang, L. Yan, Y. Dai, K. Xue, H. Guo, Z. Huang and J. Xiong, *Catal. Commun.*, 2012, **18**, 16-20.
181. J. Lin, Z. Wei, H. Zhang and M. Shao, *Biosensors & bioelectronics*, 2013, **41**, 342-347.
182. L. M. Henning, U. Simon, A. Gurlo, G. J. Smales and M. F. Bekheet, *RSC Adv.*, 2019, **9**, 36271-36284.
183. Y. T. Kim, J. H. Han, B. H. Hong and Y. U. Kwon, *Adv. Mater.*, 2010, **22**, 515-518.
184. Y. Peng, F. Liu, L. Wang, Y. Liu, J. Lei and J. Zhang, *RSC Adv.*, 2017, **7**, 52626-52631.
185. H. Xu, S. Zhou, J. Liu and Y. Wei, *RSC Adv.*, 2018, **8**, 5500-5508.
186. M. Karimi, H. Mirshekari, M. Aliakbari, P. Sahandi-Zangabad and M. R. Hamblin, *Nanotechnol. Rev.*, 2016, **5**, 195–207.
187. D. Maiti, X. Tong, X. Mou and K. Yang, *Front. Pharmacol.*, 2018, **9**, 1401.
188. M. PRATO, K. KOSTARELOS and A. BIANCO, *Acc. Chem. Res.*, 2008, **41**, 60-68.
189. M. H. Zainal-Abidin, M. Hayyan, G. C. Ngoh and W. F. Wong, *ACS omega*, 2020, **5**, 1656-1668.
190. Z. He, R. Jiang, W. Long, H. Huang, M. Liu, J. Chen, F. Deng, N. Zhou, X. Zhang and Y. Wei, *Mater. Sci. Eng. C* 2020, **109**, 110442.
191. K. Nava Andrade, P. Knauth, Z. López, G. A. Hirata, S. J. Guevara Martinez and G. G. Carbajal Arízaga, *Appl. Clay Sci.*, 2020, **192**, 105661.
192. E. Vázquez and M. Prato, *Pure Appl. Chem.*, 2010, **82**, 853-861.
193. M. Quintana, K. Spyrou, M. Grzelczak, W. R. Browne, P. Rudolf and M. Prato, *ACS Nano*, 2010, **4**, 3527–3533.
194. S. Peretz and O. Regev, *Curr. Opin. Coll. Interface Sci.*, 2012, **17**, 360-368.
195. G. Pastorin, W. Wu, S. Wieckowski, J. P. Briand, K. Kostarelos, M. Prato and A. Bianco, *Chem. Commun.*, 2006, 1182-1184.
196. G. Wei, R. Dong, D. Wang, L. Feng, S. Dong, A. Song and J. Hao, *New J. Chem.*, 2014, **38**, 140-145.
197. P. Das, S. Ganguly, T. Agarwal, P. Maity, S. Ghosh, S. Choudhary, S. Gangopadhyay, T. K. Maiti, S. Dhara, S. Banerjee and N. C. Das, *Mater. Chem. Phys.*, 2019, **237**, 121860.
198. S. D. Hettiarachchi, R. M. Graham, K. J. Mintz, Y. Zhou, S. Vanni, Z. Peng and R. M. Leblanc, *Nanoscale*, 2019, **11**, 6192-6205.
199. T. Yang, J. L. Huang, Y. T. Wang, A. Q. Zheng, Y. Shu and J. H. Wang, *ChemNanoMat*, 2019, **5**, 479-487.
200. G. Shim, M. G. Kim, J. Y. Park and Y. K. Oh, *Adv. Drug Deliver. Rev.*, 2016, **105**, 205-227.
201. H. Wu, H. Shi, Y. Wang, X. Jia, C. Tang, J. Zhang and S. Yang, *Carbon*, 2014, **69**, 379-389.
202. M. Wojtoniszak, K. Urbas, M. Perużyńska, M. Kurzawski, M. Drożdzik and E. Mijowska, *Chem. Phys. Lett.*, 2013, **568-569**, 151-156.
203. L. Yang, Z. Wang, J. Wang, W. Jiang, X. Jiang, Z. Bai, Y. He, J. Jiang, D. Wang and L. Yang, *Nanoscale*, 2016, **8**, 6801-6809.
204. Z. Liu, J. T. Robinson, S. M. Tabakman, K. Yang and H. Dai, *Mater. Today*, 2011, **14**, 316-323.

205. H. Ali-Boucetta, K. T. Al-Jamal, D. McCarthy, M. Prato, A. Bianco and K. Kostarelos, *Chem. Commun.*, 2008, 459-461.
206. Zhuang Liu, X. Sun, N. Nakayama-Ratchford and H. Dai, *ACS Nano*, 2007, **1**, 50-56.
207. Z. Liu, A. C. Fan, K. Rakhra, S. Sherlock, A. Goodwin, X. Chen, Q. Yang, D. W. Felsher and H. Dai, *Angew. Chem. Int. Ed. Engl.*, 2009, **48**, 7668-7672.
208. N. M. Dinan, F. Atyabi, M. R. Rouini, M. Amini, A. A. Golabchifar and R. Dinarvand, *Mater. Sci. Eng. C*, 2014, **39**, 47-55.
209. Y. Oz, A. Barras, R. Sanyal, R. Boukherroub, S. Szunerits and A. Sanyal, *ACS Appl. Mater. Interfaces*, 2017, **9**, 34194-34203.
210. Z. Liu, J. T. Robinson, X. Sun and H. Dai, *J. Am. Chem. Soc.*, 2008, **130**, 10876–10877.
211. X. Sun, Z. Liu, K. Welsher, J. T. Robinson, A. Goodwin, S. Zaric and H. Dai, *Nano Res.*, 2008, **1**, 203-212.
212. L. Zhang, J. Xia, Q. Zhao, L. Liu and Z. Zhang, *Small*, 2010, **6**, 537-544.
213. T. Sun, M. Zheng, Z. Xie and X. Jing, *Mater. Chem. Front.*, 2017, **1**, 354-360.
214. J. Du, N. Xu, J. Fan, W. Sun and X. Peng, *Small*, 2019, **15**, 1805087-1805102.
215. D. W. Zheng, B. Li, C. X. Li, J. X. Fan, Q. Lei, C. Li, Z. Xu and X. Z. Zhang, *ACS Nano*, 2016, **10**, 8715-8722.
216. T. Feng, X. Ai, G. An, P. Yang and Y. Zhao, *ACS Nano*, 2016, **10**, 4410-4420.
217. J. Tang, B. Kong, H. Wu, M. Xu, Y. Wang, Y. Wang, D. Zhao and G. Zheng, *Adv. Mater.*, 2013, **25**, 6569-6574.
218. A. Pourjavadi, Z. M. Tehrani and S. Jokar, *J. Ind. Eng. Chem.*, 2015, **28**, 45-53.
219. R.-Q. Zhang, Z.-Q. Liu, Y.-L. Luo, F. Xu and Y.-S. Chen, *J. Ind. Eng. Chem.*, 2019, **80**, 431-443.
220. V. Fiegel, SebastienHarlepp, SylvieBegin-Colin, D. Begin and DamienMertz, *Chem. Eur. J.* , 2018, **24**, 4662–4670.
221. L. Lacerda, J. Russier, G. Pastorin, M. A. Herrero, E. Venturelli, H. Dumortier, K. T. Al-Jamal, M. Prato, K. Kostarelos and A. Bianco, *Biomaterials*, 2012, **33**, 3334-3343.
222. Y.-W. Chen, P.-J. Chen, S.-H. Hu, I. W. Chen and S.-Y. Chen, *Adv. Funct. Mater.*, 2014, **24**, 451-459.
223. X. Liu, X. Wu, Y. Xing, Y. Zhang, X. Zhang, Q. Pu, M. Wu and J. X. Zhao, *ACS Appl. Bio. Mater.*, 2020, **3**, 2577-2587.
224. Y. Wang, R. Huang, G. Liang, Z. Zhang, P. Zhang, S. Yu and J. Kong, *Small*, 2014, **10**, 109-116.
225. D. He, X. He, K. Wang, Z. Zou, X. Yang and X. Li, *Langmuir*, 2014, **30**, 7182-7189.
226. D. He, X. Li, X. He, K. Wang, J. Tang, X. Yang, X. He, X. Yang and Z. Zou, *J. Mater. Chem. B*, 2015, **3**, 5588-5594.
227. T. T. Wang, J. Lan, Y. Zhang, Z. L. Wu, C. M. Li, J. Wang and C. Z. Huang, *J. Mater. Chem. B*, 2015, **3**, 6377-6384.
228. L. Shao, R. Zhang, J. Lu, C. Zhao, X. Deng and Y. Wu, *ACS Appl. Mater. Interfaces*, 2017, **9**, 1226-1236.
229. X. Yao, Z. Tian, J. Liu, Y. Zhu and N. Hanagata, *Langmuir*, 2017, **33**, 591-599.

230. F. F. Zheng, P. H. Zhang, Y. Xi, J. J. Chen, L. L. Li and J. J. Zhu, *Anal. Chem.*, 2015, **87**, 11739-11745.
231. C.-W. Lai, Y.-H. Hsiao, Y.-K. Peng and P.-T. Chou, *J. Mater. Chem.*, 2012, **22**, 14403.
232. Y. Gao, S. Zhong, L. Xu, S. He, Y. Dou, S. Zhao, P. Chen and X. Cui, *Microporous Mesoporous Mater.*, 2019, **278**, 130-137.
233. Q. Zhao, S. Wang, Y. Yang, X. Li, D. Di, C. Zhang, T. Jiang and S. Wang, *Mater. Sci. Eng. C*, 2017, **78**, 475-484.
234. T. Chen, H. Yu, N. Yang, M. Wang, C. Ding and J. Fu, *J. Mater. Chem B.*, 2014, **2**, 4979-4982.
235. J. Jiao, C. Liu, X. Li, J. Liu, D. Di, Y. Zhang, Q. Zhao and S. Wang, *J. Colloid Interface Sci.*, 2016, **483**, 343-352.
236. R. Eivazzadeh-Keihan, A. Maleki, M. de la Guardia, M. S. Bani, K. K. Chenab, P. Pashazadeh-Panahi, B. Baradaran, A. Mokhtarzadeh and M. R. Hamblin, *J. Adv. Res.*, 2019, **18**, 185-201.
237. S. H. Ku, M. Lee and C. B. Park, *Adv. Healthc. Mater.*, 2013, **2**, 244-260.
238. W. C. Lee, C. H. Y. X. Lim, H. Shi, L. A. L. Tang, YuWang, C. T. Lim and K. P. Loh, *ACS Nano*, 2011, **5**, 7334–7341.
239. C. Gaillard, G. Cellot, S. Li, F. M. Toma, H. Dumortier, G. Spalluto, B. Cacciari, M. Prato, L. Ballerini and A. Bianco, *Adv. Mater.*, 2009, **21**, 2903-2908.
240. X. Xie, K. Hu, D. Fang, L. Shang, S. D. Tran and M. Cerruti, *Nanoscale*, 2015, **7**, 7992-8002.
241. L. Jin, K. Ren, Q. Xu, T. Hong, S. Wu, Y. Zhang and Z. Wang, *Polym. Compos.*, 2018, **39**, 73-80.
242. S.-R. Ryoo, Y.-K. Kim, M.-H. Kim and D.-H. Min, *ACS Nano*, 2010, **4**, 6587–6598.
243. D. Cui, F. Tian, C. S. Ozkan, M. Wang and H. Gao, *Toxicol. Lett.*, 2005, **155**, 73-85.
244.F. J. Rodriguez-Lozano, D. Garcia-Bernal, S. Aznar-Cervantes, M. A. Ros-Roca, M. C. Alguero, N. M. Atucha, A. A. Lozano-Garcia, J. M. Moraleda and J. L. Cenis, *J. Mater. Sci. Mater. Med.*, 2014, **25**, 2731-2741.
245. E. Yavuz, S. Dinc and M. Kara, *Appl. Phys. A*, 2020, **126**.
246. D. Y. Lewitus, J. Landers, J. Branch, K. L. Smith, G. Callegari, J. Kohn and A. V. Neimark, *Adv. Funct. Mater.*, 2011, **21**, 2624-2632.
247. N. Mansouri, S. F. Al-Sarawi, J. Mazumdar and D. Losic, *RSC Adv.*, 2019, **9**, 36838-36848.
248. M. Tang, Q. Song, N. Li, Z. Jiang, R. Huang and G. Cheng, *Biomaterials*, 2013, **34**, 6402-6411.
249. V. B. Kumar, R. Kumar, A. Gedanken and O. Shefi, *Ultrason. Sonochem.*, 2019, **52**, 205-213.
250. G. Cellot, E. Cilia, S. Cipollone, V. Rancic, A. Sucapane, S. Giordani, L. Gambazzi, H. Markram, M. Grandolfo, D. Scaini, F. Gelain, L. Casalis, M. Prato, M. Giugliano and L. Ballerini, *Nat. Nanotechnol.*, 2009, **4**, 126-133.
251.S. Y. Park, J. Park, S. H. Sim, M. G. Sung, K. S. Kim, B. H. Hong and S. Hong, *Adv. Mater.*, 2011, **23**, H263-H267.
252. S. R. Shin, S. M. Jung, M. Zalabany, K. Kim, P. Zorlutuna, S. b. Kim, Mehdi Nikkhah, M. Khabiry, M. Azize, J. Kong, Kai-takWan, T. Palacios, M. R. Dokmeci, H. Bae, X. S. Tang and A. Khademhosseini, *ACS Nano*, 2013, **7**, 2369–2380.

253. S. R. Shin, C. Zihlmann, M. Akbari, P. Assawes, L. Cheung, K. Zhang, V. Manoharan, Y. S. Zhang, M. Yuksekkaya, K. T. Wan, M. Nikkhah, M. R. Dokmeci, X. S. Tang and A. Khademhosseini, *Small*, 2016, **12**, 3677-3689.
254. S. R. Shin, B. Aghaei-Ghareh-Bolagh, X. Gao, M. Nikkhah, S. M. Jung, A. Dolatshahi-Pirouz, S. B. Kim, S. M. Kim, M. R. Dokmeci, X. S. Tang and A. Khademhosseini, *Adv. Funct. Mater.*, 2014, **24**, 6136-6144.
255. M. Mehrali, A. Thakur, C. P. Pennisi, S. Talebian, A. Arpanaei, M. Nikkhah and A. Dolatshahi-Pirouz, *Adv. Mater.*, 2017, **29**, 1603612-1603637.
256. L. Pan, X. Pei, R. He, Q. Wan and J. Wang, *Coll. Surf. B-Biointer.*, 2012, **93**, 226-234.
257. W. Wang, G. Caetano, W. S. Ambler, J. J. Blaker, M. A. Frade, P. Mandal, C. Diver and P. Bartolo, *Materials*, 2016, **9**, 992-1002.
258. P. Zadehnajar, S. Karbasi, B. Akbari and L. Ghasemi, *Mater. Technol.*, 2019, **35**, 39-49.
259. N. M. Aboamera, A. Mohamed, A. Salama, T. A. Osman and A. Khattab, *Mechan. Adv. Mater. Struct.*, 2017, **26**, 765-769.
260. H. Ke, Z. Pang, Y. Xu, X. Chen, J. Fu, Y. Cai, F. Huang and Q. Wei, *J. Therm. Anal. Calorim.*, 2014, **117**, 109-122.
261. Y. Zhai, X. Bai, H. Cui, J. Zhu, W. Liu, T. Zhang, B. Dong, G. Pan, L. Xu, S. Zhang and H. Song, *Nanotechnology*, 2018, **29**, 025706-025712.
262. S. Shao, S. Zhou, L. Li, J. Li, C. Luo, J. Wang, X. Li and J. Weng, *Biomaterials*, 2011, **32**, 2821-2833.
263. B. Lu, T. Li, H. Zhao, X. Li, C. Gao, S. Zhang and E. Xie, *Nanoscale*, 2012, **4**, 2978-2982.
264. M. a. J. Hortigu ̈ela, M. a. C. Gutie ́rrez, I. Aranaz, M. a. Jobba ́gy, A. Abarrategi, C. Moreno-Vicente, A. Civantos, V. Ramos, J. L. Lo ́pez-Lacomba, M. a. L. Ferrer and F. d. Monte, *J. Mater. Chem.*, 2008, **18**, 5933–5940.
265. M. Lee, S. H. Ku, J. Ryu and C. B. Park, *J. Mater. Chem.*,, 2010, **20**, 8848.
266. Q. Cai, J. Mao, X. Li and X. Yang, *Mater. Lett.*, 2014, **128**, 238-241.
267. M. Vila, M. Cicuendez, J. Sanchez-Marcos, V. Fal-Miyar, M. Manzano, C. Prieto and M. Vallet-Regi, *J. Biomed. Mater. Res. A*, 2013, **101**, 213-221.
268. J. Pan, F. Li and J. H. Choi, *J. Mater. Chem. B*, 2017, **5**, 6511-6522.
269. J. J. Khandare, A. Jalota-Badhwar, S. D. Satavalekar, S. G. Bhansali, N. D. Aher, F. Kharas and S. S. Banerjee, *Nanoscale*, 2012, **4**, 837-844.
270. D. W. Li, Y. S. Zhou, X. Huang, L. Jiang, J. F. Silvain and Y. F. Lu, *Nanoscale*, 2015, **7**, 3651-3659.
271. N. Rubio, L. M. Hirvonen, E. Z. Chong, J. T. Wang, M. Bourgognon, H. Kafa, H. A. Hassan, W. T. Al-Jamal, D. McCarthy, C. Hogstrand, F. Festy and K. T. Al-Jamal, *Chem. Commun.*, 2015, **51**, 9366-9369.
272. L. Hou, X. Yang, J. Ren, Y. Wang, H. Zhang, Q. Feng, Y. Shi, X. Shan, Y. Yuan and Z. Zhang, *Int. J. Nanomedicine*, 2016, **11**, 607-624.
273. C. Paviolo, F. N. Soria, J. S. Ferreira, A. Lee, L. Groc, E. Bezard and L. Cognet, *Methods*, 2020, **174**, 91-99.

274. F. A. Mann, Z. Lv, J. Grosshans, F. Opazo and S. Kruss, *Angew. Chem. Int. Ed. Engl.*, 2019, **58**, 11469-11473.
275. T. Takeuchi, Y. Iizumi, M. Yudasaka, S. Kizaka-Kondoh and T. Okazaki, *Bioconjug. Chem.*, 2019, **30**, 1323-1330.
276. N. Fakhri, A. D. Wessel, C. Willms, M. Pasquali, D. R. Klopfenstein, F. C. MacKintosh and C. F. Schmidt, *Science*, 2014, **344**, 1031-1036.
277. J. T. Robinson, G. Hong, Y. Liang, B. Zhang, O. K. Yaghi and H. Dai, *J. Am. Chem. Soc.*, 2012, **134**, 10664-10669.
278. A. L. Antaris, J. T. Robinson, O. K. Yaghi, G. Hong, S. Diao, R. Luong and H. Dai, *ACS Nano*, 2013, **7**, 3644–3652.
279. M. Yudasaka, Y. Yomogida, M. Zhang, T. Tanaka, M. Nakahara, N. Kobayashi, Y. Okamatsu-Ogura, K. Machida, K. Ishihara, K. Saeki and H. Kataura, *Scientific reports*, 2017, **7**, 44760-44771.
280. S. H. Hu, Y. W. Chen, W. T. Hung, I. W. Chen and S. Y. Chen, *Adv. Mater.*, 2012, **24**, 1748-1754.
281. C.-y. Zhang, R. Hao, B. Zhao, Y.-w. Hao and Y.-q. Liu, *Appl. Surf. Sci.*, 2017, **409**, 306-313.
282. G. Wang, G. Chen, Z. Wei, X. Dong and M. Qi, *Mater. Chem. Phys.*, 2013, **141**, 997-1004.
283. D. O. Idisi, J. A. Oke, S. Sarma, S. J. Moloi, S. C. Ray, W. F. Pong and A. M. Strydom, *J. Appl. Phys.*, 2019, **126**, 035301.
284. S. Jain, S. M. Dongave, T. Date, V. Kushwah, R. R. Mahajan, N. Pujara, T. Kumeria and A. Popat, *ACS Biomater. Sci. Eng.*, 2019, **5**, 3361-3372.
285. S.-T. Yang, L. Cao, P. G. Luo, F. Lu, X. Wang, H. Wang, M. J. Meziani, Y. Liu, G. Qi and Y.-P. Sun, *J. Am. Chem. Soc.*, 2009, **131**, 11308–11309.
286. S. Sahu, B. Behera, T. K. Maiti and S. Mohapatra, *Chem. Commun.*, 2012, **48**, 8835-8837.
287. S.-T. Yang, X. Wang, H. Wang, F. Lu, P. G. Luo, L. Cao, M. J. Meziani, J.-H. Liu, Y. Liu, M. Chen, Y. Huang and Y.-P. Sun, *J. Phys. Chem. C*, 2009, **113**, 18110–18114.
288. X. Gong, Q. Zhang, Y. Gao, S. Shuang, M. M. Choi and C. Dong, *ACS Appl. Mater. Interfaces*, 2016, **8**, 11288-11297.
289. R. El-Sayed, M. Eita, A. Barrefelt, F. Ye, H. Jain, M. Fares, A. Lundin, M. Crona, K. Abu-Salah, M. Muhammed and M. Hassan, *Nano Lett.*, 2013, **13**, 1393-1398.
290. K. T. Nguyen, S. Sreejith, J. Joseph, T. He, P. Borah, E. Y. Guan, S. W. Lye, H. Sun and Y. Zhao, *Part. Part. Syst. Charact.*, 2014, **31**, 1060-1066.
291. S. Sun, S. Zhao, K. Jiang, Y. Wang, Q. Shu, S. Jin, Z. Li and H. Lin, *ChemNanoMat*, 2020, **6**, 953-962.
292. X. Zhang, J. Yin, C. Peng, W. Hu, Z. Zhu, W. Li, C. Fan and Q. Huang, *Carbon*, 2011, **49**, 986-995.
293. C. M. Tilmaciu and M. C. Morris, *Front. Chem.*, 2015, **3**, 59-79.
294. J. Janssen, M. Lambeta, P. White and A. Byagowi, *Biosensors*, 2019, **9**, 144-154.
295. L. Xu, Y. Wen, S. Pandit, V. Mokkapati, I. Mijakovic, Y. Li, M. Ding, S. Ren, W. Li and G. Liu, *BMC Chem.*, 2019, **13**, 112-123.
296. J. Wang, G. Liu and M. R. Jan, *J. Am. Chem. Soc.*, 2004, **126**, 3010-3011.

297. P. Kara, A. de la Escosura-Muniz, M. Maltez-da Costa, M. Guix, M. Ozsoz and A. Merkoci, *Biosensors & bioelectronics*, 2010, **26**, 1715-1718.
298. Y. Sun, Z. Peng, H. Li, Z. Wang, Y. Mu, G. Zhang, S. Chen, S. Liu, G. Wang, C. Liu, L. Sun, B. Man and C. Yang, *Biosensors & bioelectronics*, 2019, **137**, 255-262.
299. W. Qiu, H. Xu, S. Takalkar, A. S. Gurung, B. Liu, Y. Zheng, Z. Guo, M. Baloda, K. Baryeh and G. Liu, *Biosensors & bioelectronics*, 2015, **64**, 367-372.
300. H. Cai, X. Cao, Y. Jiang, P. He and Y. Fang, *Anal. Bioanal. Chem.*, 2003, **375**, 287-293.
301. S. Taniselass, M. K. M. Arshad and S. C. B. Gopinath, *Biosensors & bioelectronics*, 2019, **130**, 276-292.
302. B. Jin, P. Wang, H. Mao, B. Hu, H. Zhang, Z. Cheng, Z. Wu, X. Bian, C. Jia, F. Jing, Q. Jin and J. Zhao, *Biosensors & bioelectronics*, 2014, **55**, 464-469.
303. S. Myung, A. Solanki, C. Kim, J. Park, K. S. Kim and K. B. Lee, *Adv. Mater.*, 2011, **23**, 2221-2225.
304. Y. Wee, S. Park, Y. H. Kwon, Y. Ju, K. M. Yeon and J. Kim, *Biosensors & bioelectronics*, 2019, **132**, 279-285.
305. Y. Qu, M. Ma, Z. Wang, G. Zhan, B. Li, X. Wang, H. Fang, H. Zhang and C. Li, *Biosensors & bioelectronics*, 2013, **44**, 85-88.
306. C. He, L. Peng, L. Lv, Y. Cao, J. Tu, W. Huang and K. Zhang, *RSC Adv.*, 2019, **9**, 15084-15091.
307. J. Yang, S. Deng, J. Lei, H. Ju and S. Gunasekaran, *Biosensors & bioelectronics*, 2011, **29**, 159-166.
308. Y. Huang, S. Zhao, Y. M. Liu, J. Chen, Z. F. Chen, M. Shi and H. Liang, *Chem. Commun.*, 2012, **48**, 9400-9402.
309. L. Yuan, S. Liu, W. Tu, Z. Zhang, J. Bao and Z. Dai, *Anal. Chem.*, 2014, **86**, 4783-4790.
310. M. Liu, J. Song, S. Shuang, C. Dong, J. D. Brennan and Y. Li, *ACS Nano*, 2014, **8**, 5564–5573.
311. B. Kong, A. Zhu, C. Ding, X. Zhao, B. Li and Y. Tian, *Adv. Mater.*, 2012, **24**, 5844-5848.
312. C. Zhang, Y. Yuan, S. Zhang, Y. Wang and Z. Liu, *Angew. Chem. Int. Ed. Engl.*, 2011, **50**, 6851-6854.
313. B. Xu, C. Zhao, W. Wei, J. Ren, D. Miyoshi, N. Sugimoto and X. Qu, *The Analyst*, 2012, **137**, 5483-5486.
314. J. Wen, Y. Xu, H. Li, A. Lu and S. Sun, *Chem. Commun.*, 2015, **51**, 11346-11358.
315. A. Jain, A. Homayoun, C. W. Bannister and K. Yum, *Biotechnol. J.*, 2015, **10**, 447-459.
316. Z. Chen, X. Zhang, R. Yang, Z. Zhu, Y. Chen and W. Tan, *Nanoscale*, 2011, **3**, 1949-1956.
317. E. Morales-Narvaez and A. Merkoci, *Adv. Mater.*, 2019, **31**, 1805043-1805044.
318. N. M. Iverson, P. W. Barone, M. Shandell, L. J. Trudel, S. Sen, F. Sen, V. Ivanov, E. Atolia, E. Farias, T. P. McNicholas, N. Reuel, N. M. Parry, G. N. Wogan and M. S. Strano, *Nat. Nanotechnol.*, 2013, **8**, 873-880.
319. L. Zhang, W. C. Geng, S. Z. Qiao, H. J. Zheng, G. Q. Lu and Z. F. Yan, *ACS Appl. Mater. Interfaces*, 2010, **2**, 2767-2772.
320. A. Boujakhrout, E. Sánchez, P. Díez, A. Sánchez, P. Martínez-Ruiz, C. Parrado, J. M. Pingarrón and R. Villalonga, *ChemElectroChem*, 2015, **2**, 1735-1741.

321. J. Zong, X. Yang, A. Trinchi, S. Hardin, I. Cole, Y. Zhu, C. Li, T. Muster and G. Wei, *Biosens. Bioelectron.*, 2014, **51**, 330-335.
322. M. Eguilaz, R. Villalonga and G. Rivas, *Biosens Bioelectron.*, 2018, **111**, 144-151.
323. B. Wu, C. Hu, X. Hu, H. Cao, C. Huang, H. Shen and N. Jia, *Biosens Bioelectron.*, 2013, **50**, 300-304.
324. N. Massad-Ivanir, S. K. Bhunia, N. Raz, E. Segal and R. Jelinek, *NPG Asia Mater.*, 2018, **10**, e463-e463.
325. J. H. Park, L. Gu, G. von Maltzahn, E. Ruoslahti, S. N. Bhatia and M. J. Sailor, *Nat. Mater.*, 2009, **8**, 331-336.
326. H. Yamada, C. Urata, Y. Aoyama, S. Osada, Y. Yamauchi and K. Kuroda, *Chem. Mater.*, 2012, **24**, 1462-1471.
327. L. Bergman, P. Kankaanpaa, S. Tiitta, A. Duchanoy, L. Li, J. Heino and M. Linden, *Mol. Pharm.*, 2013, **10**, 1795-1803.
328. X. Yuan, X. Zhang, L. Sun, Y. Wei and X. Wei, *Part. Fibre Toxicol.*, 2019, **16**, 18-44.
329. S. Taghavi, A. H. Nia, K. Abnous and M. Ramezani, *Int. J. Pharm.*, 2017, **516**, 301-312.
330. S. Luanpitpong, L. Wang and Y. Rojanasakul, *Nanomedicine*, 2014, **9**, 895-912.
331. D. Bitounis, H. Ali-Boucetta, B. H. Hong, D. H. Min and K. Kostarelos, *Adv. Mater.*, 2013, **25**, 2258-2268.
332. S. Kanakia, J. D. Toussaint, S. Mullick Chowdhury, T. Tembulkar, S. Lee, Y. P. Jiang, R. Z. Lin, K. R. Shroyer, W. Moore and B. Sitharaman, *Biomaterials*, 2014, **35**, 7022-7031.
333. G. F. Guidetti, A. Consonni, L. Cipolla, P. Mustarelli, C. Balduini and M. Torti, *Nanomedicine*, 2012, **8**, 1329-1336.
334. J. Fent, P. Bihari, M. Vippola, E. Sarlin and S. Lakatos, *Toxicol. In Vitro*, 2015, **29**, 1132-1139.
335. A. Sasidharan, L. S. Panchakarla, A. R. Sadanandan, A. Ashokan, P. Chandran, C. M. Girish, D. Menon, S. V. Nair, C. N. Rao and M. Koyakutty, *Small*, 2012, **8**, 1251-1263.
336. L. Liang, Z. Kong, Z. Kang, H. Wang, L. Zhang and J.-W. Shen, *ACS Biomater. Sci. Eng.*, 2016, **2**, 1983-1991.
337. S. K. Smart, A. I. Cassady, G. Q. Lu and D. J. Martin, *Carbon*, 2006, **44**, 1034-1047.
338. X. Cui, B. Wan, Y. Yang, X. Ren and L. H. Guo, *Sci. Rep.*, 2017, **7**, 1518-1530.
339. X. Guo and N. Mei, *J. Food Drug Anal.*, 2014, **22**, 105-115.
340. O. Akhavan, E. Ghaderi and A. Akhavan, *Biomaterials*, 2012, **33**, 8017-8025.
341. K. Kostarelos, *Nat. Nanotechnol.*, 2008, **26**, 774-776.
342. G. Qu, Y. Bai, Y. Zhang, Q. Jia, W. Zhang and B. Yan, *Carbon*, 2009, **47**, 2060-2069.
343. M. Zhang, Y. Xu, M. Yang, M. Yudasaka and T. Okazaki, *Nanoscale Adv.*, 2020, **2**, 1551-1559.
344. E. Principi, R. Girardello, A. Bruno, I. Manni, E. Gini, A. Pagani, A. Grimaldi, F. Ivaldi, T. Congiu, D. De Stefano, G. Piaggio, M. de Eguileor, D. M. Noonan and A. Albini, *Int. J. Nanomedicine*, 2016, **11**, 4299-4316.
345. T. Nezakati, B. G. Cousins and A. M. Seifalian, *Archives of toxicology*, 2014, **88**, 1987-2012.
346. J. M. Gernand and E. A. Casman, *Risk Anal.*, 2014, **34**, 583-597.

347. P. T. Yin, S. Shah, M. Chhowalla and K. B. Lee, *Chem. Rev.*, 2015, **115**, 2483-2531.

348. E. Aldieri, I. Fenoglio, F. Cesano, E. Gazzano, G. Gulino, D. Scarano, A. Attanasio, G. Mazzucco, D. Ghigo and B. Fubini, *J. Toxicol. Environ. Health A*, 2013, **76**, 1056-1071.

349. F. A. Girardi, G. E. Bruch, C. S. Peixoto, L. Dal Bosco, S. K. Sahoo, C. O. Goncalves, A. P. Santos, C. A. Furtado, C. Fantini and D. M. Barros, *J. Appl. Toxicol.*, 2017, **37**, 214-221.

350. N. Diban, S. Sánchez-González, M. Lázaro-Díez, J. Ramos-Vivas and A. Urtiaga, *J. Membrane Sci.*, 2017, **540**, 219-228.

351. C.-Y. Huang, J.-S. Lin, W.-H. Pan, C.-M. Shih, Y.-L. Liu and S. J. Lue, *J. Power Sour.*, 2016, **303**, 267-277.

352. Y. Liu, W. Han, Z. Xu, W. Fan, W. Peng and S. Luo, *Environ. Pollut.*, 2018, **237**, 218-227.

353. B. Li, X. Y. Zhang, J. Z. Yang, Y. J. Zhang, W. X. Li, C. H. Fan and Q. Huang, *Int. J. Nanomedicine*, 2014, **9**, 4697-4707.

354. M. Nurunnabi, Z. Khatun, K. M. Huh, S. Y. Park, D. Y. Lee, K. J. Cho and a. Y.-k. Lee, *ACS Nano*, 2013, **7**, 6858–6867.

355. D. Gutierrez-Praena, S. Pichardo, E. Sanchez, A. Grilo, A. M. Camean and A. Jos, *Toxicol. In Vitro*, 2011, **25**, 1883-1888.

356. M. Mohammadi, Z. Salmasi, M. Hashemi, F. Mosaffa, K. Abnous and M. Ramezani, *Int. J. Pharm.*, 2015, **485**, 50-60.

357. C. Gea, J. Dua, Y. Zhao, L. Zhaoa, Z. Chaid, L. Wanga, Y. Liua and C. Chen, *PNAS*, 2011, **108**, 16968–16973.

358. Y. Chong, C. Ge, Zaixing Yang, J. A. Garate, Z. Gu, J. K.Weber, J. Liu and R. Zhou, *ACS Nano*, 2015, **9**, 5713–5724.

359. K.-X. Xie, S.-S. Jia, J.-H. Zhang, H. Wang and Q. Wang, *New J. Chem.*, 2019, **43**, 14220-14223.

360. J. Russier, C. Menard-Moyon, E. Venturelli, E. Gravel, G. Marcolongo, M. Meneghetti, E. Doris and A. Bianco, *Nanoscale*, 2011, **3**, 893-896.

361. K. Bhattacharya, R. El-Sayed, F. T. Andón, S. P. Mukherjee, J. Gregory, H. Li, Y. Zhao, W. Seo, A. Fornara, B. Brandner, M. S. Toprak, K. Leifer, A. Star and B. Fadeel, *Carbon*, 2015, **91**, 506-517.

362. M. Chen, G. Zeng, C. Lai, C. Zhang, P. Xu, M. Yan and W. Xiong, *Chemosphere*, 2017, **184**, 127-136.

363. G. Chandrasekaran, S.-K. Choi, Y.-C. Lee, G.-J. Kim and H.-J. Shin, *J. Ind. Eng. Chem.*, 2014, **20**, 3367-3374.

364. Z. Peng, X. Liu, W. Zhang, Z. Zeng, Z. Liu, C. Zhang, Y. Liu, B. Shao, Q. Liang, W. Tang and X. Yuan, *Environ. Int.*, 2020, **134**, 105298.

365. V. E. Kagan, N. V. Konduru, W. Feng, B. L. Allen, J. Conroy, Y. Volkov, Vlasova, II, N. A. Belikova, N. Yanamala, A. Kapralov, Y. Y. Tyurina, J. Shi, E. R. Kisin, A. R. Murray, J. Franks, D. Stolz, P. Gou, J. Klein-Seetharaman, B. Fadeel, A. Star and A. A. Shvedova, *Nat. Nanotechnol.*, 2010, **5**, 354-359.

366. I. Srivastava, D. Sar, P. Mukherjee, A. S. Schwartz-Duval, Z. Huang, C. Jaramillo, A. Civantos, I. Tripathi, J. P. Allain, R. Bhargava and D. Pan, *Nanoscale*, 2019, **11**, 8226-8236.
367. M. Chen, G. Zeng, P. Xu, Y. Zhang, D. Jiang and S. Zhou, *Environ. Sci.: Nano*, 2017, **4**, 720-727.
368. C. Bussy, C. Hadad, M. Prato, A. Bianco and K. Kostarelos, *Nanoscale*, 2016, **8**, 590-601.
369. L. Liu, C. Zhu, M. Fan, C. Chen, Y. Huang, Q. Hao, J. Yang, H. Wang and D. Sun, *Nanoscale*, 2015, **7**, 13619-13628.
370. Q. Ma, A. Yilihamu, Z. Ming, S. Yang, M. Shi, B. Ouyang, Q. Zhang, X. Guan and S. T. Yang, *Nanomaterials*, 2019, **9**, 1340-1352.

Chapter 2 Near infra-red light responsive carbon nanotubes@mesoporous silica for photothermia and drug delivery to cancer cells

Bing Li[1,2] , Sébastien Harlepp[3-5], Valentin Gensbittel[3-5], Connor J. R. Wells[1], Ophélie Bringel[2], Jacky G. Goetz[3-5], Sylvie Begin-Colin[1], Mariana Tasso[6], Dominique Begin[2], Damien Mertz[1,*]

[1] *Institut de Physique et Chimie des Matériaux de Strasbourg (IPCMS), UMR-7504 CNRS-Université de Strasbourg, 23 rue du Læss, BP 34 67034, Strasbourg Cedex 2, France*

[2] *Institut de Chimie et Procédés pour l'Energie, l'Environnement et la Santé (ICPEES), UMR-7515 CNRS-Université de Strasbourg, 25 rue Becquerel, 67087 Strasbourg, Cedex 2, France*

[3] T*umor Biomechanics, INSERM UMR_S1109, Strasbourg, France*

[4] *Université de Strasbourg, Strasbourg, France*

[5] *Fédération de Médecine Translationnelle de Strasbourg (FMTS), Strasbourg, France*

[6] *Instituto de Investigaciones Fisicoquímicas Teóricas y Aplicadas (INIFTA), Departamento de Química, Facultad de Ciencias Exactas, Universidad Nacional de La Plata - CONICET, Diagonal 113 y 64, 1900 La Plata, Argentina*

***Corresponding authors:*
damien.mertz@ipcms.unistra.fr (Damien Mertz)

This chapter is a reproduction of our published paper on ***Materials Today Chemistry,*** 17 (**2020**) 100308.
https://doi.org/10.1016/j.mtchem.2020.100308

Abstract

Among smart activable nanomaterials used for nanomedecine applications, carbon-based nanocomposites are well known to ensure phototherapy while their use for controlled drug delivery is still rarely investigated. In this work, original hybrid mesoporous silica (MS)–coated carbon nanotubes (CNTs) nanoplatforms have been designed to provide phototherapy combined with drug release mediated by NIR laser excitation. The responsive CNT@MS are chemically modified with original isobutyramide (IBAM) grafts acting as non-covalent binders, which ensure a very high drug loading capacity (≥to 80 wt%) of the antitumor drug doxorubicin (DOX) as well as the final adsorption of a human serum albumin (HSA) shell as biocompatible interface and drug gate-keeping. The drug is demonstrated to unbind from the nanocomposite only upon photothermal excitation and to release in the solution. Such smart platforms are further shown to deliver drug upon several pulsatile NIR excitations with controlled temperature profiles. Regarding antitumor action, we demonstrate here that the NIR light induced photothermic effect from the nanocomposites is the main effect accounting for cancer cell toxicity and that DOX delivery mediated by the NIR light brings an additional toxicity allowing a synergistic effect to efficiently kill tumor cells. Finally, when our nanocomposites are embedded within a hydrogel mimicking extracellular matrix, the resulting smart responsive scaffolds efficiently release DOX upon NIR light to the cells localized above the composite hydrogel. These results demonstrate that such nanocomposites are highly promising as new components of implantable antitumor scaffolds that are able to respond to external stimuli in time and location for a better disease management.

Keywords:

Phototherapy, NIR-light induced drug delivery, Carbon nanotubes, Mesoporous silica coatings, Nanocomposite hydrogels, Cancer cells

2.1 Introduction

The development of smart multi-functional nanocomposites capable of releasing therapeutic molecules under various external stimuli has become a major challenge in recent years in the biomedical field. These nanocomposites are designed to be either injected as circulating objects [1–6] or implanted *in situ* in a polymer support matrix [7–12] for the treatment of different types of tumors. Another challenge now is the design of multifunctional nanoplatforms (NPFs) able to combine, in one formulation, two or more functionalities, e.g. simultaneous therapy and diagnostic (theranostic) for real-time therapy monitoring, and synergic action of two or more therapeutic approaches.

In the field of tissue engineering, the incorporation of activable inorganic materials (e.g. iron oxide, gold or carbon materials) into polymer scaffolds (e.g. hydrogels or electrospun fibers) is a way to formulate new composite materials that would be used as smart implants or integrated devices in the body.[13–15] The advantages of adding remote responsive NPs into such polymer matrix are: i) improved mechanical properties; ii) the response to external stimuli (near infrared light, mechanical force, electric or magnetic field, etc.); iii) the eventual clinical imaging property (MRI, X rays, etc); and iv) the encapsulation of the activable material into a biocompatible scaffold, thus preventing material-related toxicity issues. In this work, we report on the design and use of drug-loaded carbon-based composites incorporated in a biocompatible hydrogel mimicking the extracellular matrix (ECM).

Among the different materials needed to produce such activable nanocomposites, carbon-based materials are promising materials.[16–18] Besides their exceptional mechanical and electrical conductive properties, they are able to release heat under near-infrared radiation by vibrational relaxation of graphite structures in the near infrared (NIR) range (750-1400 nm). Given the relative transparency of biological tissues in the NIR optical window, this property is of huge interest for combining both phototherapy and remotely activable drug delivery under such external stimuli.[19–23] Indeed, the use of infrared light to trigger the release of an active ingredient locally could be of great interest in the treatment of tumors because of its easier implementation than other sources of radiation (X-ray scanner, gamma radiation, magnetic waves, etc.). However, the design of carbon-based composites for biomedical applications endowed with phototherapy and remote drug delivery faces important challenges as follows. Main issues with CNTs are their asbestos form factor (very long length-to-diameter ratio) and the inherent hydrophobicity of carbon leading to self-aggregation in biological medium.[24–26] To solve these problems, newly processed

CNTs with a better form factor were developed. Several fractionation and split treatments decrease the form factor of these carbon nanotubes, such as mechanical grinding (length of about less than 500 nm), or CNT compression induced by ultrasonic effects [27] or by harsh acidic treatment of CNTs [28].

Besides, CNTs can be rendered hydrophilic by the cutting treatment which introduces hydroxyl groups or by a post-functionalization.[19,20,29] A capping layer playing the role of drug reservoirs may also be obtained by the surface modification with various polymers[30–33] or chemical groups[20] or by the deposition of a uniform layer of porous silica [34–36]. Among current coating layers for drug loading, mesoporous silica (MS) shells are particularly attractive materials as they are robust, biocompatible, hydrophilic, easily chemically modified and have a high drug delivery capability thanks to their important pore volume and after a suitable surface functionalization.[37]

Recently, we and coworkers developed various functionalized MS NPs having well-controlled pore sizes (from 2 to 15 nm) [38,39] and translated these approaches to coat CNTs but also iron oxide NPs with various MS shell nanostructures [40–43]. Especially small pore MS around CNTs allowed loading of such nanocomposites with doxorubicin, (DOX, an antitumor anthracycline molecule with antimitotic action by DNA intercalation) with increased rates (up to several times the mass of the carrier) when compared to past work [42]. However, different issues were raised in this previous work: i) the loading of DOX was initially performed at an aminosiloxane surface which is not optimal for biomedical applications given its high surface charge and marked fouling, ii) the drug release was activated with a quite high laser power (6 W/cm^2) which may lead to overheating in a biological medium; iii) these nano-composites were also shown to release a moderate proportion of immobilized DOX under near IR radiation (1064 nm) and iv) no functional study on cells was done with these systems.

Herein, to address these issues, we designed a new class of functional CNT@MS nanocomposites **(Fig.2-1)**. First, the CNTs are processed in acidic conditions to afford sliced CNTs with a more suitable size distribution adapted for medical applications. Their coating by a MS shell having small pore size (*ca.* 3 nm) is performed with a precise control over silica shell thickness. Then, we used here the grafting of IBAM groups to ensure high drug loading and a final protein capping. Indeed, IBAM groups grafted at silica surfaces were reported previously to be versatile non-covalent surface binders of a range of proteins through a single step adsorption. [44–46]. Here, IBAM grafts at silica surface are assessed for the first time to load DOX through non-covalent interactions followed by HSA coating to ensure a good

integrity of the nanocomposites. We assumed here that IBAM grafts play the role of a thermoresponsive interface that unbind the loaded drugs from the surface upon the photo-induced local heating generated from the underneath CNTs. Hence, we address here the full characterization of CNT@MS nanocomposites and of DOX loading and subsequent HSA wrapping on CNT@MS@IBAM and we investigated the efficiency of drug release upon NIR light application. Various drug profiles as a function of time, concentration, and laser power are provided demonstrating the possibility for NIR light remote release.

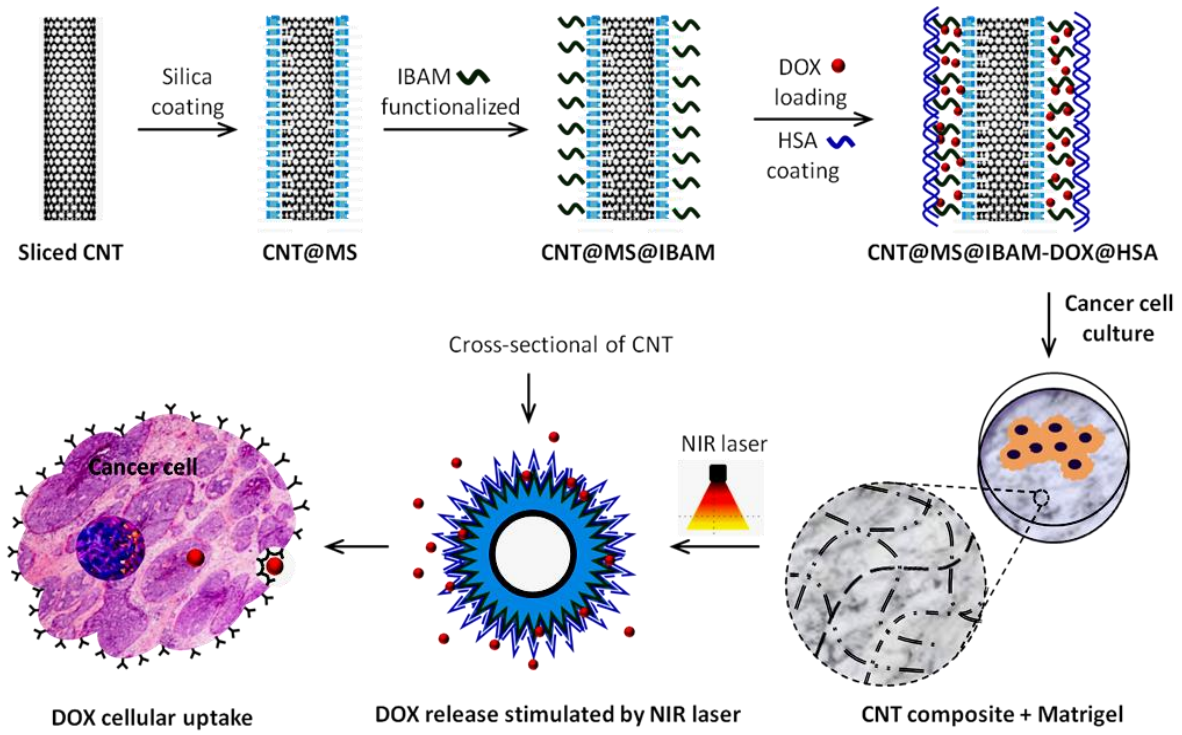

Fig.2-1 Scheme describing the formation of the CNT@MS@IBAM-DOX@HSA nanoconstructs and their formulation into a hydrogel assessed with breast cancer cells.

In the last step of this design, with the aim to create a drug releasing scaffold upon NIR light exposure, the drug loaded nanocomposites CNT@MS@IBAM-DOX@HSA are formulated within a hydrogel made of various extracellular matrix biopolymers (Matrigel, ECM-like hydrogel) often used in biomaterials field.[47–49] The development of such hydrogel nanocomposites is very attractive for antitumor and tissue engineering applications. Indeed, the scaffold can display some advantages over circulating NPs, such as limiting macrophage uptake, or decreasing the drug loss (or the non-targeted drug delivery) by injecting the scaffold in the diseased site and thus avoiding side effects.

2.2 Materials and methods

2.2.1 Chemicals

Carbon nanotubes PR-24-XT-PS (CNTs) were supplied by Pyrograf-III. Cetyltrimethylammonium bromide (CTAB) was obtained from Roth (France). Nitric acid (HNO_3), sulfuric acid (H_2SO_4), ethanol (EtOH), tetraethyl orthosilicate (TEOS), sodium hydroxide (NaOH), ammonium nitrate (NH_4NO_3, >99%), 3-aminopropyltriethoxysilane (APTS), isobutyryl chloride (IBC), triethylamine (Et_3N), dimethylformamide (DMF), dimethylsulfoxide (DMSO), sodium bicarbonate ($NaHCO_3$), human serum albumin (HSA, >97%) and fluorescein isothiocyanate (FITC) were obtained from Sigma-Aldrich (France). Doxorubicin hydrochloride (DOX, purity 99%) was purchased from OChem Incorporation (France). Ammonium hydroxide solution (25% in H_2O) was obtained from Fluka. The MTS reagents CellTiter 96® AQ_{ueous} were obtained from Promega. The D2A1 cells were seeded and grown up at 37 ℃ at 5% CO2, using DMEM high glucose medium supplemented with with 5% NBCS, 5% FBS, 1% NEAA-MEM, 1% Penstrep (Sigma Aldrich). For 2D or 3D growth the cells were seeded into either an opaque-walled 96 well plate (Fisher scientific) or a 15 well plate suited for 3D cell culture (Ibidi). The Membrane Matrix used to build the 3D scaffold was obtained from Thermo Fisher Scientific.

2.2.2 Procedures

(1) Synthesis of cleaved CNTs

The acid treatment was performed by adding 0.75 g of CNTs into a mixture of H_2SO_4/HNO_3 (3:1, 108 mL) and then bath sonicated (Bandelin SONOREX RK 255 S) for 24 h under at 0 ℃. After this time, 100 mL of NaOH aqueous solution (10 M) was added dropwise into the acidic black suspension for neutralization, and finally the mixture was adjusted to neutral by the dropwise addition of NaOH (1 M). The CNTs were then centrifuged (13000 g, 13 min, Eppendorf Centrifuge 5804 R) and washed with distilled water (twice with 25 mL each). After washing, the CNTs were reduced at 900 ℃ for 2 h with a heating ramp of 10 ℃/min under argon. The resulting material was used as the initial material for the following functionalization procedures.

(2) Synthesis of mesoporous silica coated CNTs

In a typical procedure, 372 mg of CTAB was added into a mixture of H_2O (90 mL) and EtOH (60 mL) with stirring at 60 ℃ for 2 h. 72 mg of CNTs were dispersed in the CTAB solution by ultrasonication (2 x 20 min, power = 750 W, amplitude = 40%, temperature = 30 °C, runs: 50” ON, 50” OFF, Vibracell 75043 from Bioblock Scientific), yielding a black

suspension. The sol gel process was initiated after addition of TEOS (180 µL) and NaOH (180 µL, 1M) into the above mixture. The mixture was stirred for 16 h at room temperature. Finally, the composite was centrifuged and washed with EtOH (2 x 25 mL, 12000 g, 12 min) and re-dispersed in EtOH. The process resulted in the formation of a uniform layer of silica on every individual CNT.

(3) CTAB extraction from CNT@MS composite

The removal of mesostructural templating agent CTAB from the silica pores was done by mixing the CNT@MS composite with 25 mL NH_4NO_3 (20 mg/mL in EtOH) under 60 ℃ with stirring for 1 h. The surface charge of CNT@MS was measured by Zeta potential after each washing, in order to make sure that the majority of CTAB was removed. This process was repeated approximately 5 times.

(4) CNT@MS surface modification with aminopropyltriethoxysilane APTS

50 mg of CNT@MS were dispersed in 27 mL of EtOH. Then, 1.2 mL of NH_4OH (25 % in water) and 5 mL of APTS were added respectively and the mixture was agitated on a mechanical wheel (40 rpm) at room temperature for 2 h. After that, the amino-modified composite was centrifuged and washed with EtOH (2 x 20 mL, 13000 g, 14 min). The composite after APTS modification was denoted as CNT@MS@APTS.

(5) CNT@MS surface functionalization with IBAM moieties

In a typical procedure, the resulting CNT@MS@APTS composite was washed and centrifuged with 20 mL DMF (13000 g, 13 min). Once the supernatant had been removed, a mixture of 1.2 mL Et_3N and 1.5 mL DMF was added. The mixture was vortexed for 10 s before the addition of 1.65 mL of IBC pre-mixed with 1.5 mL of DMF. The reaction was left on the mechanical wheel for 1 h 30 min. After this time, a small volume of water (*ca.* 1-2 mL) was added to dissolve the precipitate formed by the reaction. This was followed with centrifugation and washing at 13000 g for 14 min (1 x 20 mL wash in DMF, 1 x 20 mL wash in H_2O). The composite at this point was denoted as CNT@MS@IBAM.

(6) Impregnation of doxorubicin

Typically, 2.5 mg of CNT@MS@IBAM after surface functionalization were dispersed in 1 mL of DOX aqueous solution at a given concentration and agitated on a mechanical wheel (40 rpm) for 16 h. After impregnation, the mixture was centrifuged (13000 g, 10 min) and 400 µL of the supernatant were mixed with 3.6 mL of H_2O to obtain a solution diluted 10 times. The composite was denoted as CNT@MS@IBAM-DOX. The DOX loading capacities were calculated by measuring the UV/Vis spectra (Lambda 950 UV/VIS Spectrometer by Perkin Elmer) of the diluted supernatant. A series of additional washes with water (3 x 1 mL) were

implemented to remove loosely-bound impregnated DOX prior HSA modification (as follows).

(7) FITC labeling of HSA

531 µL of fluorescein isothiocyanate (10 mg/mL in DMSO) were mixed with 30 mL of HSA (10 mg/mL) in sodium bicarbonate buffer ($NaHCO_3$ 0.1 M, pH 8.5). The mixture was stirred overnight and then dialyzed (membrane pore size: 10 kDa) in MilliQ water to remove free FITC. Finally, the concentration of HSA^{FITC} was adjusted to 10 mg/mL in water for further use.

(8) HSA coating

6.4 mg of CNT@MS@IBAM-DOX composite after surface functionalization and DOX impregnation were dispersed in 3 mL HSA at a concentration of 0.21 mg/mL, then the mixture was stirred on a mechanical wheel for 1 h. Afterwards, the solution was centrifuged and washed with H_2O (2 x 2 mL, 13000 g, 13 min). The composite was denoted as CNT@MS@IBAM-DOX@HSA. The supernatant was measured with UV/vis spectroscopy to detect the mass loss of DOX during this step.

(9) DOX release stimulated by NIR laser

To study the release of DOX under NIR irradiation, 1 mL of a given concentration of CNT@MS@IBAM-DOX@HSA solution (DLC ca 58%) was placed in a 1 mL plastic cuvette and then irradiated with the 1064 nm laser with power densities at either 1 or 2.5 W/cm^2. For every trial, the sample was exposed to NIR light for 15 min, followed by a break lasting 3 days at 4 ℃. The mixture was centrifuged after this period and the released DOX in the supernatant was removed and measured by UV/vis spectrometry to determine the amount of DOX released. Then 1 mL of fresh water was added and the composite was dispersed by 10 s of sonication and stored in a 4 ^oC refrigerator. Regarding pulsatile assay, the same procedure was applied: the samples were passed for the next NIR exposure and rest period and so on for four times. The cumulative DOX release is the sum of each trial of DOX release.

2.2.3 Cell culture and NIR exposure setup for in vitro experiments.

(1) D2A1 cells (CVCL_0I90)

Mouse mammary carcinoma (BALB/c female). Major infomation on the D2A1 cell line can be found following this link: https://web.expasy.org/cellosaurus/CVCL_0I90. Culture conditions: 37 ^oC/5% CO_2. DMEM HG with 5% NBCS, 5% FBS, 1% NEAA-MEM and 1% Penstrep.

(2) Bidimensional cell proliferation and viability assays

D2A1 cells were seeded (8000 cells per well in 50 µL of DMEM) in each well of the

opaque 96 well plate and incubated at 37 ^{o}C in 5% CO_2 for 45min to an hour to allow the cells to adhere [50,51]. Then, DMEM medium (150 µL) supplemented with the final concentration of CNT@MS@IBAM@HSA or CNT@MS@IBAM-DOX@HSA suspensions were introduced and incubated at 37 ^{o}C, 5% of CO_2 for 24h. NIR irradiation (at 1W/cm^2 for 15 min) was applied and the cells were further incubated at 37 ^{o}C in 5% CO_2 for 24 h. NIR irradiation was performed with a homemade setup. The illumination was performed from the top cover towards the well. Cell Titer Glo (Promega) reagent was then added to each well (20 µL) followed by one-hour incubation at room temperature, allowing cell lysis to be completed and luciferin to be oxidized by the cellular ATP. The 96 well plate was introduced into a plate cell reader (SpectraMaxID5 from MolecularDevices) and luminescence was collected. The intensity of control wells (cells without CNTs called Luminescence Control) were used to normalize the luminescence values (all values are between 0 and 1, value of the control wells). We checked the luminescence values from wells filled with medium and the values were at the noise level, therefore we decided to not correct with these values. Nevertheless, CNTs have a black aspect and therefore have the ability to absorb part of the emitted light from the viability experiments such as for Optical density filters. We, thus, characterized the part of absorbed light. We cultured different wells with 8000 cells per well for 48h in normal cell growth conditions. Before running the Cell Titer Glo experiment, we first added the 4 studied concentrations of CNT@MS@IBAM@HSA in different wells. Assuming that the contact time between CNT and cell is very short, it will only affect the emitted light. We observed that only $\approx$ 23% of the luminescence was collected. Therefore, we used the average values of what we introduced as Absorption for the different concentrations of CNTs to correct all the signals measured in presence of CNTs. Using the mathematical formulation we can write:

$$Relative\ Viability = \frac{Measured\ luminescence}{Luminescence\ Control} \times \frac{1}{Absorption}$$

(3) Short time 3D cell culture and DOX cellular uptake after NIR irradiation

To study the cellular uptake of DOX upon NIR irradiation, a 50 µL total volume of Matrigel with a given concentration of CNT@MS@IBAM-DOX@HSA or CNT@MS@IBAM@HSA composite was mixed and coated before subsequent cell seeding. D2A1 cells were incubated for 24 h and subjected to laser irradiation of 1W/cm^2 for 15 min. NIR-illuminated cells were cultivated for an additional 24 h before assessing DOX release. NIR irradiation was performed for 15 min at power density of 1W/cm^2. DOX release/delivery was characterized using a Leica SP5 confocal microscopy. To follow intracellular DOX

fluorescence, we excited the sample at 488 nm (argon laser) and collected the fluorescence on a broad range in emission from 520 to 650 nm on stacks of images with steps in *z* of about 400 nm. Each image from the stack was then analyzed with *Image J* and the average intensity from the cell with respect to its area in each plane was computed. Thus we could address the intensity distribution or the average signal from a single cell or cluster of cells.

(4) Longer time 3D cell culture in presence of CNT@MS

To study the toxicity linked to the presence of CNTs embedded in a 3D scaffold close to the tumor cells, a 50 μL total volume of Matrigel with a given concentration of CNT@MS@IBAM-DOX@HSA or CNT@MS@IBAM@HSA composite was mixed and coated before subsequent cell seeding. Murine breast carcinoma cells labelled with Nuclear Localization Signal fused with Green Fluorescent Protein (D2A1, n=8000) were added on top of the gel and again incubated for 5 days allowing the growth of tumor spheroids[52]. The cells were grown in 3 different conditions. In the first condition, cells were seeded on just Matrigel without any CNT@MS. In the second condition, 2.5 mg/mL of CNT@MS@IBAM@HSA^{FITC} was complemented in the Matrigel composition, whereas in the last condition 2.5 mg/mL of CNT@MS@IBAM-DOX@HSA was added. Upon 5 days of culture, tumor spheroids were imaged under the confocal microscope.

(5) Statistical analysis

Statistical analysis of the obtained results was performed using the GraphPad Prism program version 5.04. The Shapiro-Wilk normality test was used to confirm the normality of the data. For data not following a Gaussian distribution, the Mann-Whitney test was used.

2.2.4 Characterization Methods

(1) Transmission electron microscopy

Morphologies of the different nanocomposites were characterized by transmission electron microscopy (TEM) with a JEOL 2100 ultra-high-resolution microscope operating at 200 kV. The sample was first dispersed in EtOH and then we deposited 2 drops of the nanocomposite solution on a carbon-coated copper grid. The thickness of the silica shell was determined using Image J software on the TEM pictures. Results are indicated as mean layer thickness (nm) ± standard deviation (nm).

(2) Zeta potential

Zeta potential measurements at different synthesis stages were measured by using a Zetasizer nano ZS by Malvern Instruments. The measurements were performed by diluting 10 μL of a nanoparticles' suspension in 1 mL water using a DTS1070 folded capillary cell. The

pH of the measured solution was adjusted with HCl (100 mM) and NaOH (100 mM) aqueous solution.

(3) Nitrogen adsorption / desorption analysis

Specific surface area of the silica coated CNTs were characterized by N_2 adsorption/desorption analysis and was calculated by the Brunauer-Emmett-Teller (BET) method. The pore size and pore volume were calculated by the Barrett-Joyner-Halenda (BJH) method. All the measurements were done on a Tristar 3000 Gas Adsorption Analyzer by Micromeritics Instruments. Before the tests, the samples were outgassed under vacuum at 150 ^{o}C for about 4h.

(4) Thermal gravimetric analysis (TGA)

TGA was performed with a Q5000 Automatic Sample Processor by TA Instruments. The sample was dried in an oven at 150 ℃ for 24 h to remove the solvent and water before the TGA analysis. The runs were started from room temperature to 800 ℃ at a heating rate of 10 ℃/min under air with a flow rate of 25 mL/min.

(5) UV/Vis spectroscopy

UV-vis spectroscopy was used to determine the amount of drug loaded and released. The UV-vis spectra were recorded with a Lambda 950 UV/vis Spectrometer by Perkin Elmer. The solutions and the quartz cell were always protected from light using aluminum foil until the measurements were done.

(6) Confocal microscopy

Microscopy of tumor cells was performed on a Leica SP5 confocal microscope. Samples were imaged with a 40X oil immersion objective. DOX was excited with a single 488 nm wavelength, and the emission was collected between 520 and 650nm. All the image intensities were further analyzed and processed with the Image J software.

2.3 Results and discussion

2.3.1 Synthesis of mesoporous silica coated carbon nanotubes

In a first step, the commercial CNTs were sliced from the microscale to the nanoscale using a solution of sulphuric and nitric acids. This acidic treatment increased the number of oxidative functional groups on the surface of the CNTs, resulting in break points which led to mechanical cleavage. NaOH was then used to neutralize the CNTs, followed by washings to subtract the salts produced. Then the CNTs oxygenated groups on the outer surface were reduced under a flow of argon in an oven at 900 ℃ for 2 hours. The average length of the nanotubes was found in a range of 100 - 1000 nm, using transmission electron microscopy

(TEM) whereas the initial CNTs had lengths of several tens of microns (in the range of 50-200 microns) (F**ig.2-2 A** and **B** before and after reduction).

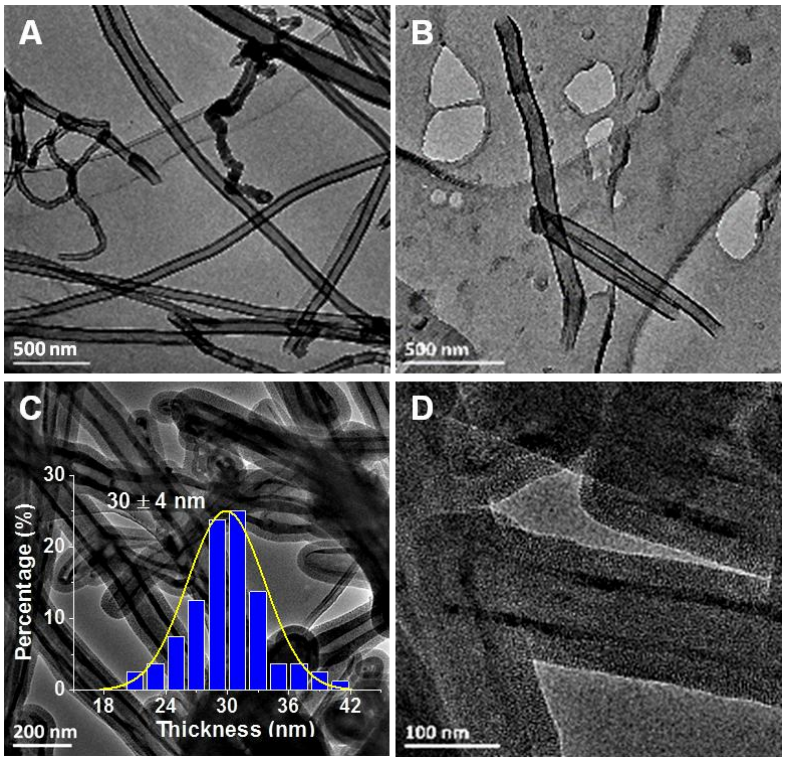

Fig.2-2 Representative TEM images of (A) uncleaved CNTs, (B) Acid-treated sliced CNTs, (C) CNT@MS in a large area associated with the silica layer thickness distribution and (D) CNT@MS in a zoomed image showing the mesoporous structures.

Then a MS shell was coated around the CNTs using a modified procedure from Bian et al.[36]. A solution of cetyltrimethylammonium bromide (CTAB), water and ethanol was heated to 60 ℃ for 2 h. CTAB is a well-known surfactant that forms positively charged micelles in solution. When CNTs are dispersed in this mixture and given the hydrophobicity of heat-treated CNTs, the micelles arrange around the carbon nanotubes. The sol gel process begins upon addition of tetraethyl orthosilicate (TEOS) and NaOH. NaOH catalyzes the hydrolysis of TEOS, which condenses into silicate polyanions, leading to further condensation reactions, forming a network of Si-O-Si bonds. Once this MS structure is obtained, surfactant extractions are necessary to remove the CTAB from the pores of the silica. This was achieved with NH_4NO_3; Zeta potential (ZP) measurements allowed to monitor the surface charge change from positive to negative. Five extractions were required to reach a stable negative zeta potential value indicating the completion of the process. The composites from this point onwards will be referred to as CNT@MS. TEM images showed homogenous coverage of the

CNT@MS (**Fig.2-2 C**) on almost all the CNTs and a zoomed image (**Fig.2-2 D**) indicated the well-organized mesoporous structure of the MS shell around the CNTs. TEM images were used to establish the thickness of the MS shell, which was of 30 ± 4 nm.

The porosity was investigated by nitrogen adsorption-desorption isotherms. **S.2-1** shows the nitrogen adsorption-desorption isotherm curves which exhibit a type IV isotherm, characteristic of mesoporous materials and which was used to calculate the surface area, pore size and pore volume. The Brunauer-Emmett-Teller (BET) surface area was thus calculated as 594 ± 14 m^2/g and the pore size was found to be of *ca.* 3.4 nm with a pore volume of 0.53 cm^3/g. These data are consistent with the results obtained by Bian *et al.*[36], and in our previous studies [41,42]. Thermogravimetric analysis (TGA) was used to determine the C/SiO_2 composition of CNT@MS (**Fig.2-3A**). The analysis of the curve indicated that CNTs started to decompose into CO_2 from 400 to 600 ℃. This allowed us estimating a C/SiO_2 mass ratio of 63/37 for the CNT@MS composite system.

2.3.2 Surface functionalization with APTS and IBAM moieties

Next, after CTAB extraction from the pores, the surface of the MS was modified with APTS according to a standard process of multilayered siloxane condensation adapted from Wang *et al.* [53] and thereafter reacted with isobutyrylchloride (IBC) molecules to form grafted isobutyramide (IBAM) moieties **(Fig.2-3 A)** [54]. For that, the CNT@MS were first dispersed in ethanol, and then a catalytic amount of NH_4OH was added followed by 3-aminopropyltriethoxysilane (APTS). The presence of NH_4OH allowed the APTS to condense on the silica surface over a 2 h period. The amine-functionalized silica surface was then further modified with isobutyrylchloride (IBC) resulting in IBAM functional groups on the outer surface of the silica shell. In previous works, IBAM moieties were, in particular, proved to non-covalently bind human serum albumin (HSA) and other proteins at the surface of MS carriers, leading to a tight biomacromolecular shell [41,43–45]. The APTS and IBAM grafting steps were characterized by TGA (**Fig.2-3 B)**. TGA on the bare CNT@MS was used as a baseline and the TGA of CNT@MS@APTS and CNT@MS@IBAM allowed estimating by subtraction the amount of grafted aminosilane and then of the IBAM moieties. As can be seen, decomposition of APTS is achieved in the T range 300-450 ℃ and the weight loss was estimated at 10.4% of CNT@MS. Similarly, the IBAM grafts decomposition was overlapped with the APTS one and, by subtraction, the mass of IBAM decomposition was estimated at 7.0% of CNT@MS. TGA results of these hybrids enabled us to evaluate the grafting density: the number of APTS and IBAM molecules grafted on the silica surface was calculated to be of ca. 3.0 and 2.0 molecules per nm^2, respectively.

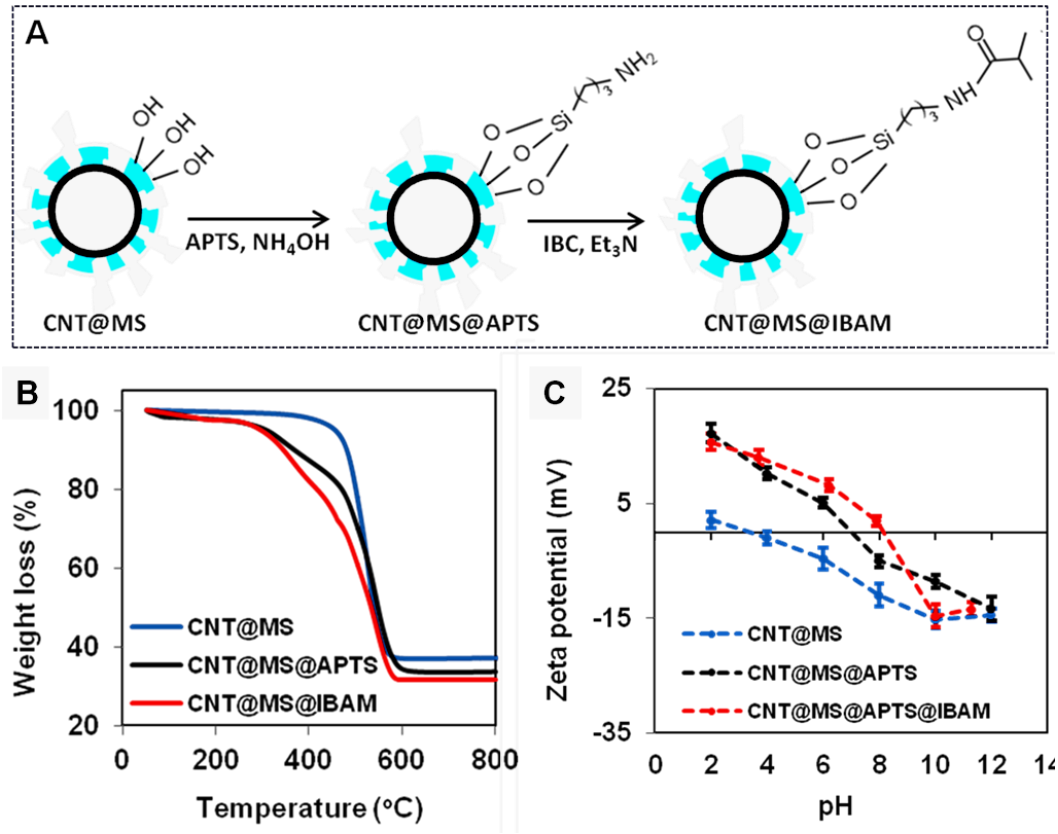

Fig.2-3 (A) The process of reactions for CNT@MS@APTS and CNT@MS@IBAM composite. (B) TGA curves of CNT@MS, CNT@MS@APTS and CNT@MS@IBAM. (C) Zeta potential measurements of CNT@MS, CNT@MS@APTS and CNT@MS@IBAM as a function of pH value.

The surface functionalization steps of the MS layer were also investigated by zeta potential (ZP) measurements in water (**Fig.2-3 C**). The ZP curves as a function of pH value for bare CNT@MS and CNT@MS modified with APTS and IBAM moieties were thus traced. The ZP being the electrical potential at the slipping plane of the double ionic layer of the coated surface, gives in a first approximation indication of the surface charge changes. An iso-electric point (IEP) of ca. 2-3 was found on bare CNT@MS, consistent with the IEP value of bare silica surface chemistry as reported in the literature. After APTS modification, the ZP curve shifted towards higher pHs inducing a shift of the IEPs from ca. 3 for bare CNT@MS to a ca. 7 for the APTS-modified CNT@MS. This is consistent with the APTS presence on the silica surface providing a positive ammonium charge. After IBAM modification, CNT@MS@IBAM, the ZP curve was again shifted to higher pH and displayed an IEP of around 8, which indicate that a fraction of APTS moieties still remain after the reaction. Hence, overall, the TGA and ZP results sevidenced that the surface of CNT@MS was effectively chemically modified with APTS and IBAM.

2.3.3 Drug loading and HSA coating

As we aimed at loading the CNT@MS@IBAM with an antitumoral agent (DOX) and then wrapping them with a serum albumin capping to ensure a biocompatible surface, our strategy was to adsorb DOX directly onto IBAM followed by the HSA coating. Firstly, this required investigating the loading in water of the hydrophilic DOX within the porous structure modified with IBAM groups. DOX displays strong absorption characteristics at 480 nm that allows its suitable detection and to quantify its adsorption. A UV/vis calibration curve of DOX in water measuring the absorbance at 480 nm at different DOX concentrations was plotted (**S.2-2**). For different [DOX] concentrations in water, an impregnation (during 16 hours) of the drug within CNT@MS@IBAM was carried out to load the composite. The suspensions were then centrifuged, and the resulting supernatants were dosed by UV/Vis spectroscopy to determine the mass of DOX that stayed outside of the composite. From that, the mass of DOX that entered the composite could be calculated. The drug loading capacity (DLC) and the drug loading efficacy (DLE) were used as loading parameters to establish the amount of drug within the composites. Their expressions are given below.

$$\mathrm{DLC\%} = \frac{\text{weight of DOX loaded}}{\text{weight of CNT@MS}} \times 100\%$$

$$\mathrm{DLE\%} = \frac{\text{weight of DOX loaded}}{\text{weight of DOX initial}} \times 100\%$$

Evolutions of these both parameters were plotted along with [DOX] (see DLC and DLE curves respectively in **Fig.2-4**). As can be seen in **Fig.2-4 A**, the DOX DLC increased with the increasing concentration of DOX from 0.25 to 8 mg/ml. At a concentration of 8 mg/mL $DOX_{(aq)}$ solution, the DLC reached 68%, equivalent to 0.68 mg DOX per mg of CNT@MS. Interestingly, looking at the efficiency of the drug impregnation process, the DLE remained constant with the various concentrations, maintaining around DLE=23% regardless of the DOX concentration (**Fig.2-4 B**). Such composite seems to behave as a loading matrix which ensures a concentration independent partition between DOX molecules in and outside of the composite. For the subsequent adsorption of a human serum albumin (HSA) shell, three times washes and centrifugation was required to completely remove the free DOX from the supernatant, which also resulted in the spontaneous leaking of the loosely-bound loaded DOX decreasing the DLC from 68% (after impregnation determined by UV vis) to ~58% (after washing steps determined by UV vis).

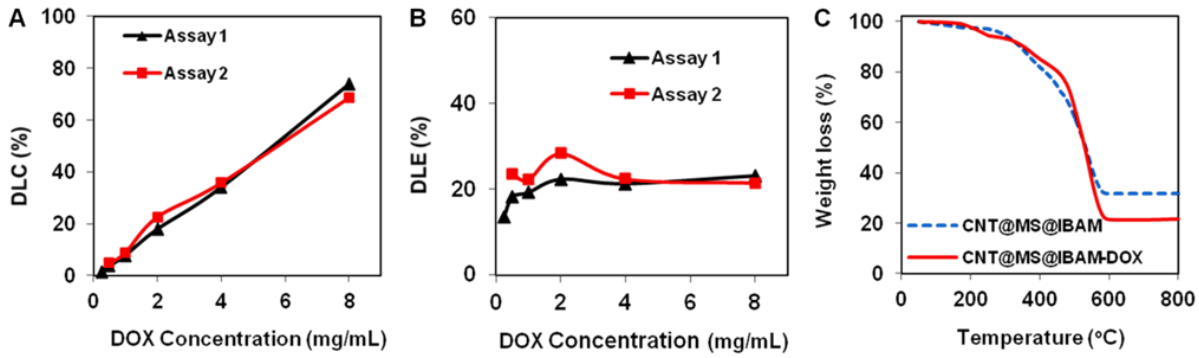

Fig.2-4 (A) DLC and (B) DLE curves as a function of DOX concentration in water. (C) TGA curves of CNT@MS@IBAM and CNT@MS@IBAM-DOX (DLC= 56% after washing steps)

The DOX loading amount was also evaluated by TGA analysis performed directly on the nanocomposite after the three washing steps. TGA measurements of CNT@MS@IBAM-DOX were performed in the temperature range of 50-800 ℃ and the result is presented in **Fig.2-4 C**. With CNT@MS@IBAM as the baseline, the amount of DOX loaded could be calculated; the TGA curve revealed a weight loss correlated to the DOX decomposition of ca. 56% of CNT@MS (see **S.2-3** for the TGA of DOX decomposition itself and **Table S2-1** for explanations about the calculations by TGA). This value is consistent with the DOX content calculated from UV/vis, considering that ca.10% loosely bound DOX was lost during washing steps. These DLC values are particularly high in the field of MS nanosystems as a usual range of 10-40% is reported, depending on the drug loading conditions [55–58]. We expect that in the case of IBAM grafts, a mechanism of drug-sponge effect similar to the one encountered with APTS in our previous work [42] may be the reason for such high drug loading.

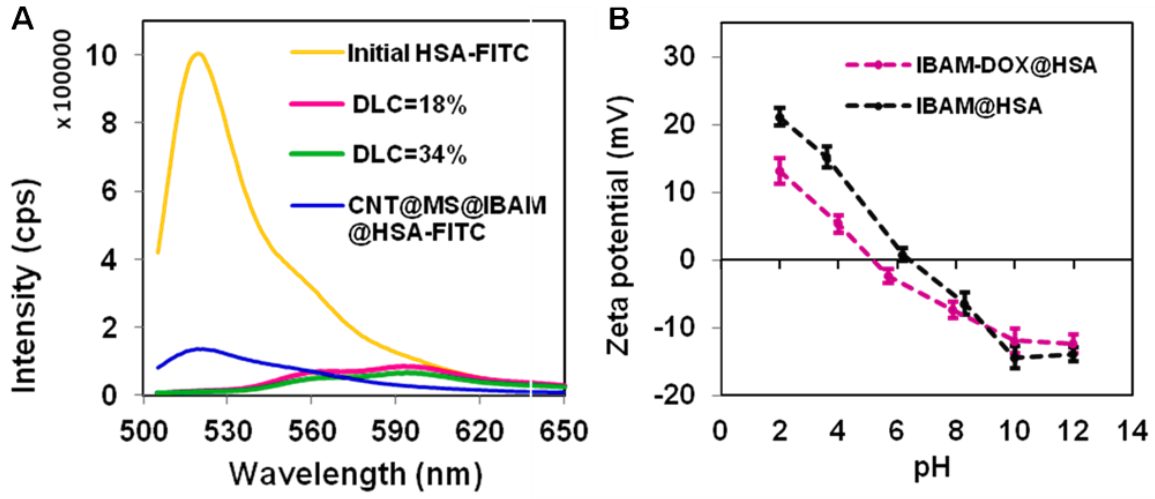

Fig.2-5 (A) Fluorescence spectra of supernatant of CNT@MS@IBAM-DOX@HSA^{FITC}

(DLC = 18% and 34%), CTRL (CNT@MS@IBAM@HSA^{FITC}) and HSA^{FITC} solution at 0.21 mg/mL. (B) Zeta potential curves as a function of pH for CNT@MS@IBAM-DOX@HSA and CNT@MS@IBAM@HSA.

Then, once the composite was suitably loaded with DOX, an HSA coating was directly added just after removing the impregnation supernatant. The adsorption of HSA in aqueous solution at a concentration of *ca.* 0.21 mg/mL was performed on two CNT@MS@IBAM-DOX nanocomposites with initial DOX loading measured at DLC = 18% and 34%. The quantification of the amount of HSA coated on the CNT@MS@IBAM-DOX composites was achieved and followed by spectrofluorimetry analysis of the supernatant. For that, HSA was labeled with the fluorophore FITC and a spectrofluorimetry calibration curve of HSA^{FITC} (Exc/Em : 480/520 nm) in water measuring the fluorescence intensity emission at 520 nm at different HSA^{FITC} concentrations was traced (**S.2-4**). Fluorescence spectra in **Fig.2-5 A** showed the complete disappearance in fluorescence at 520 nm of the supernatants after the HSA adsorption on both systems, which is compared to an HSA-FITC solution at 0.21 mg/mL. This data showed that in the conditions of HSA adsorption, almost all the HSA brought in contact with the CNT@MS@IBAM-DOX composites was coated onto their surfaces, which was attributed to the non-covalent bonds between HSA and isobutyramide (IBAM) functional groups. This allowed us estimating that ca. 98 µg HSA was adsorbed per mg of CNT@MS composite. As observed above, some slight natural DOX leakage arose in both samples as DOX is highly soluble in water (cf slight signals at ca. 560 and 590 nm). After evaluation of the DOX amount loss by using the absorbance calibration curve, the final DLC of the drug tightly retained in the system after HSA coating and washing were found of 16 and 31% as compared to initial DOX loadings during DOX impregnation (DLC = 18% and 34%).

Regarding the surface charge, Zeta potential measurements as a function of the pH were performed on CNT@MS@IBAM@HSA and CNT@MS@IBAM-DOX@HSA systems (**Fig.2-5 B**) and very similar trends with and without DOX loading were found. The isoelectric point values for CNT@MS@IBAM@HSA and CNT@MS@IBAM-DOX@HSA (DLC = 56 %) composites were found at pH *ca*. 6 and 5, respectively. These data indicated that despite of the very high amount of DOX introduced, the surface charge is probably the same without and with DOX, which/and is mainly determined by the HSA coating. This confirms the good coverage of composites by HSA and its efficiency as gate-keeper.

2.3.4 DOX Release

CNTs have strong absorbance in NIR region (in the range 750-1400 nm) and can convert the NIR light into local heat. By adding to their surface a thermally responsive coating, they become suitable photo-responsive nanostructures for the remote release of drugs. In this paragraph, we investigated the possibility to deliver DOX upon NIR photothermal effect. We assumed the generated heat would disturb intermolecular interactions between DOX and IBAM facilitating the DOX release.

To evaluate the photothermal properties, aqueous solutions (1 mL) of various concentrations of CNT@MS@IBAM-DOX@HSA (DLC ca. 56%) ranging from 0.32 to 2.5 mg/mL (0.32; 0.63; 1.25 and 2.5 mg/mL) were exposed to 1064 nm NIR laser with power densities at 2.5 and 1 W/cm^2. The temperature changes were then recorded as a function of time during the 15 min irradiation time of NIR light, as shown in **Fig.2-6 A** (2.5 W/cm^2) and **B** (1 W/cm^2). As expected, obvious photothermal heating of the suspensions was observed but with differences in term of temperature profiles between the two powers used. At the highest NIR power density of 2.5 W/cm^2 (**Fig.2-6 A)**, the temperature profiles of the suspensions were shown not to depend on the nanocomposite concentration and increased rapidly from ca. 31 to 68 ℃ at the early stage (over the first 5 min) and then remained substantially constant with extending exposure time. The effect of the NIR light in water (without CNTs composites) showed a slight increase of the T from 22 to 30 ℃ when exposure to the 2.5 W/cm^2 NIR laser, confirming a temperature effect of the composites. Oppositely, the temperature of the solution under 1 W/cm^2 NIR irradiation (**Fig.2-6 B**) increased slowly throughout the run and was found to be finely tunable with concentrations and irradiation times so that temperature could be raised in a controlled manner from 28 to 41 ℃. The power effect is important when applied to cells to avoid their necrosis which is expected above 45 ℃[59–61]. In contrast, by looking at the effect of the NIR light in the solution without composites, the temperature of pure water showed almost no changes under the same power condition. The excellent photothermal performances of CNTs whatever the power make them thusly an effective photothermal agent and we have now to demonstrate that it is efficient for drug delivery.

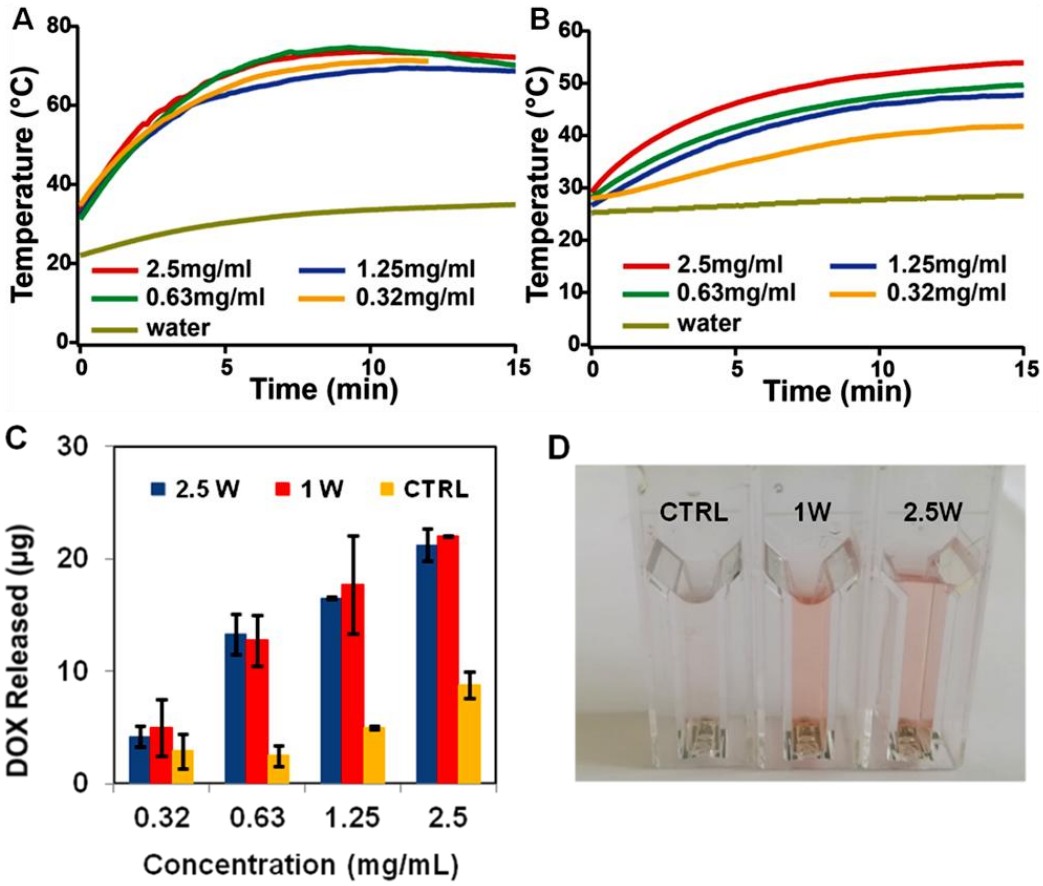

Fig.2-6 Changes in temperature of 1 mL of CNT@MS@IBAM-DOX@HSA (DLC = 56%) at various concentrations upon irradiation by the 1064 nm NIR laser at power densities of (A) 2.5 W/cm^2 and (B) 1 W/cm^2. (C) Mass of DOX released from various concentrations of CNT@MS@IBAM-DOX@HSA (DLC = 56%) upon NIR laser irradiation at power densities of 2.5 and 1 W/cm^2, and ambient T (CTRL). (D) Photograph of the DOX released from the composite concentration of 2.5 mg/mL (DLC = 56%) after NIR exposure at the two power densities (1 W/cm^2 and 2.5 W/cm^2) or when exposed to room T (CTRL)

Then, the NIR-light controlled drug release properties of CNT@MS@IBAM-DOX@HSA were investigated by measuring the DOX amount released from the exposed suspensions (DLC = 58%) at various concentrations of (0.32 - 2.5 mg/mL) under NIR laser for 15 min (followed by three days at rest at 4 ℃) at power densities of 1 and 2.5 W/cm^2. For each concentration, a control sample (CTRL) not exposed to NIR light at room temperature was also considered. The supernatants of the centrifuged suspensions after NIR treatment (and rest time) were monitored by UV/Vis absorption spectroscopy at 480 nm to determine the amount of DOX released during this period. As shown in **Fig.2-6 C**, the increased sample concentration resulted in an increased DOX release under NIR light stimulation at both power densities 1 and 2.5 W/cm^2, with very similar DOX release trends

for both power densities. Hence after the first 15 min NIR irradiation trail, respectively ca. 21 and 22 µg of DOX were released at the concentration of 2.5 mg/mL under NIR power densities of 2.5 and 1 W/cm^2, respectively, which correspond to almost three times that of the control sample (natural leakage) of 8 µg. This natural release is attributed to a spontaneous desorption of DOX that occurs with time which remains however lower than that of the photo-induced one. A photograph of the supernatants (**Fig.2-6 D**) illustrated the differences in contrast of DOX between the samples submitted to NIR light and the control. Finally, regarding the results obtained in **Fig.2-6 A** and **B** for the T profiles and the results obtained in drug release in **Fig.2-6 C** and **D**, we can conclude that the NIR exposure at 1W/cm^2 condition is optimal as it ensures a better T control and efficient drug release.

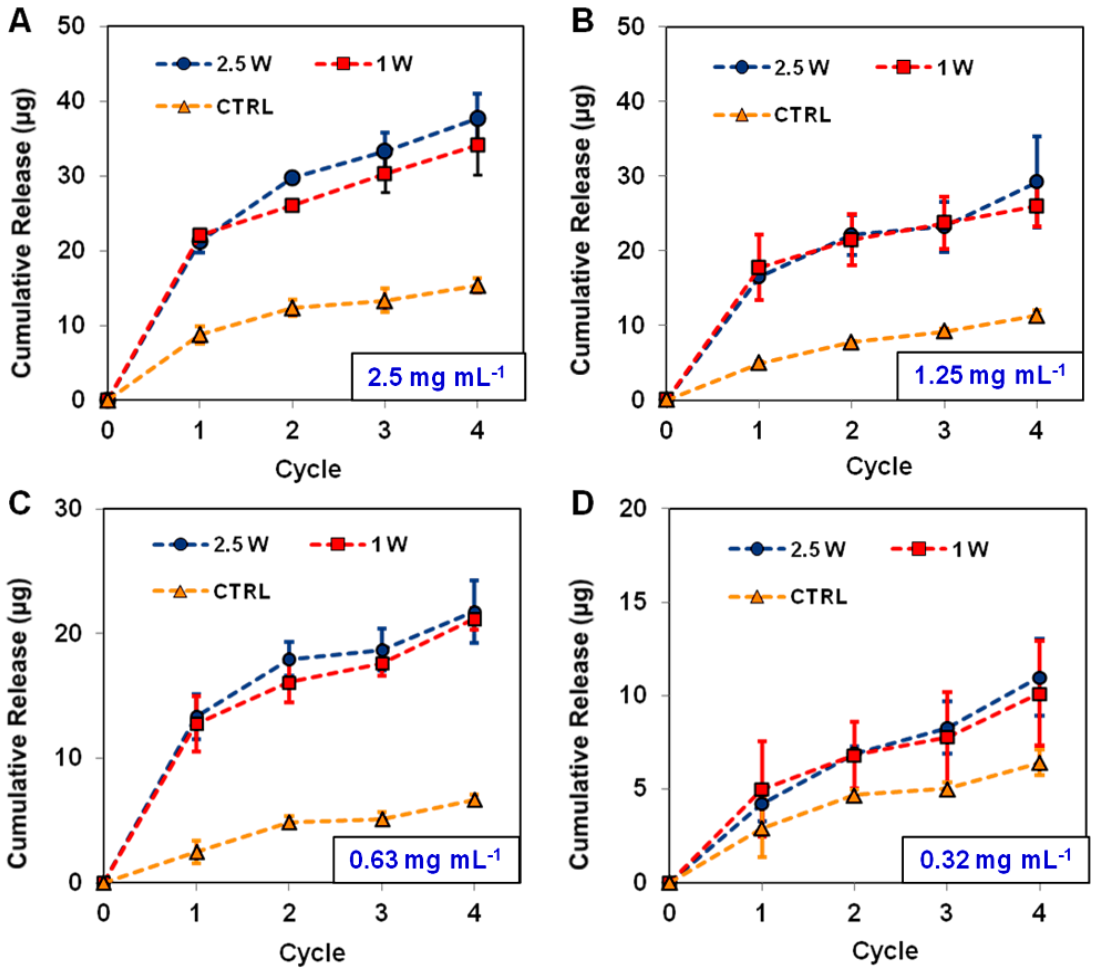

Fig.2-7 Cumulative DOX release from various concentrations of CNT@MS@IBAM-DOX@HSA: (A) 2.5 mg/mL, (B) 1.25 mg/mL, (C) 0.63 mg/mL and (D) 0.32 mg/mL (DLC = 58%) upon four consecutive NIR laser irradiation cycles at power densities of 2.5 and1 W/cm^2 (15 min ON, 3 days OFF), and at ambient T (CTRL).

We also investigated the effect of pulsatile release by performing four cycles of NIR

laser irradiation to the four batches at various concentrations (0.32; 0.63; 1.25 and 2.5 mg/mL). Pulsatile release is a very attractive approach because triggering the drug release in several pulses with chosen periods could be beneficial for a treatment needing dosing in several sequential steps of the drug administration.[62–65] As observed above, this system is supposed to have a continuous, rather slow release of DOX in the absence of NIR light, and the pulsatile release would ensure bursts of DOX released upon NIR irradiations. As shown in **Fig.2-7 A**, for nanocomposites at a concentration of 2.5 mg/mL (DLC = 58%), along four consecutive NIR treatment cycles, the DOX release enhancement was found to be lower than for the first pulse reaching nevertheless a rate ca. 5 ug DOX/pulse. This can be explained by the observed agglomeration of the CNT@MS@IBAM-DOX@HSA composite induced by NIR irradiation at the power density of 2.5 W/cm^2. Finally, the cumulative amount of DOX released was found to be of *ca.* 37 and 34 μg upon NIR laser application at 2.5 and 1 W/cm^2, respectively. For 1.25, 0.63 and 0.32 mg/mL **(Fig.2-7 B-D)**, the cumulative DOX release showed also a moderate though progressive increase after each cycle of NIR irradiation with the following slopes after the first pulse: ca. 4, 3, 2 ug DOX/NIR pulse. Percentages of the cumulative release of DOX as compared to the initial loading of DOX in the CNT@MS@IBAM-DOX@HSA nanocomposites for all of these graphs are provided in **S.2-5**. Even if the DOX loading (58% *i.e.* 580 μg/mg CNTS@MS) is very high as compared to the literature and the amount released in **Fig.2-7** are suitable for cancer cell toxicity, the % DOX amount released indicate that only less than 10% of the total DOX loaded amount is released. Nevertheless, this lets envision using these systems for long term and sustained pulsatile release. Altogether, these results showed that the amount of DOX released upon NIR is proportional to the composite concentration (at equal DLC). Moreover, since power of NIR had no substantial benefit on the amount of DOX that is released (see **S.2-5 A** and **B)**, using low power (1W) allows to preserve a better temperature control below the inflammation/necrotic temperature of 45 ℃ [59–61].

2.3.5 Uptake of DOX and cytotoxicity upon NIR excitation

Here, we aimed at testing the cytotoxic potential of our functionalized nanocomposites using a classical breast carcinoma tumor cell line. We tested their cytotoxic effect using either (i) a classical cell culture where CNTs were supplemented to the cell culture medium, or (ii) a hydrogel-composite formulation where the nanocomposites were dispersed in the hydrogel (Matrigel), on top of which cells are seeded.

Cytotoxicity of CNT@MS@IBAM@HSA (without DOX) and CNT@MS@IBAM-DOX@HSA-loaded cells without and with NIR irradiation was estimated

at various concentrations (**Fig.2-8)**. First, we observed a very little cytotoxicity of CNT@MS@IBAM@HSA on tumor cells when no NIR was applied (**Fig.2-8 A**, yellow curve), independent of the nanocomposite concentration. Indeed, without any irradiation, D2A1 cells treated with CNT@MS@IBAM@HSA are only poorly affected with an average viability that remains for the 4 concentration conditions over 90%. Interestingly, a dose-dependent cytotoxicity was observed when tumor cells were subjected to CNT@MS@IBAM-DOX@HSA (**Fig.2-8 A**, blue curve), that could arise from previously observed DOX leaking from the nanocomposites.

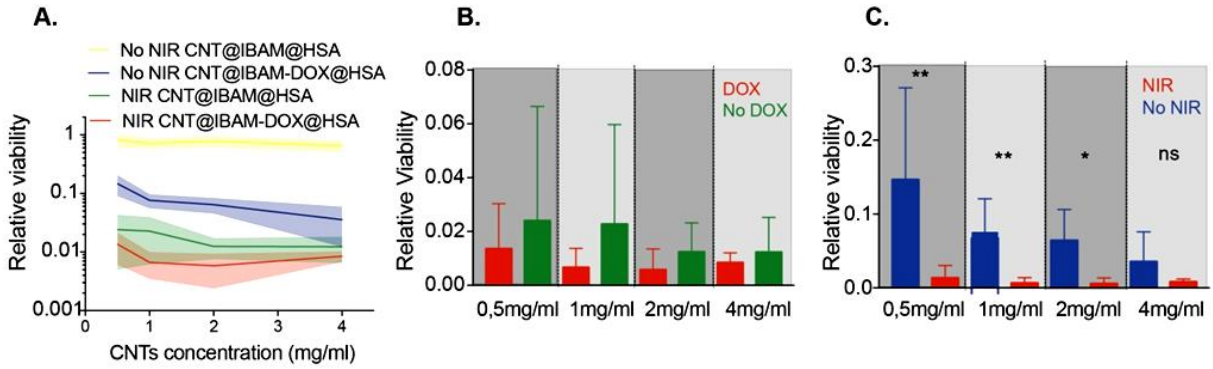

Fig.2-8 Viability assay results. (A) The relative emission values in semi logarithmic scale as compared to the control (cells grown without nanocomposites) after 24 h of incubation with the nanocomposites followed by 15 min NIR irradiation. CNT@MS@IBAM@HSA (no DOX) and CNT@MS@IBAM-DOX@HSA (DOX) composites at concentrations 0.5, 1, 2, and 4 mg/mL were considered. Represented on the graph are the average values and the SEM. (B) Relative cellular viability extracted from graph A with and without DOX, upon 15 min of NIR exposure for CNT@MS@IBAM@HSA (no DOX) and CNT@MS@IBAM-DOX@HSA (DOX) at concentrations of 0.5, 1, 2, and 4 mg/mL. (C) Relative cellular viability with and without 15 min of NIR light exposure on CNT@MS@IBAM-DOX@HSA at the concentrations of 0.5, 1, 2 and 4 mg/mL.

Upon NIR light, cytotoxicities of CNT@MS@IBAM@HSA and of CNT@MS@IBAMDOX@HSA were significantly increased suggesting that T increase is sufficient to promote a cytotoxic effect of the CNTs (**Fig.2-8 A** green and red curves). Indeed, if we compare nanocomposites loaded with DOX, CNT@MS@IBAM-DOX@HSA, under NIR irradiation with the one without DOX, the release of DOX appears to moderately enhance cellular death (DOX vs NO DOX under NIR light). However it can be observed that, we reached a very efficient cytotoxic effect when both NIR and CNT@MS@IBAM-DOX@HSA were applied, demonstrating the synergistic effects of

photothermia and DOX release (**Fig.2-8 C**).

Noteworthy, as a control, we investigated also the NIR irradiation effect onto cells without the composites. NIR irradiation showed no significant cytotoxicity further indicating that the locally increase heat from the nanocomposites is required to induce subsequent cell death **(S.2-7 A)**. In conclusion, cytotoxicity is predominantly mediated by CNTs-dependent local T increase and it can be enhanced with DOX release.

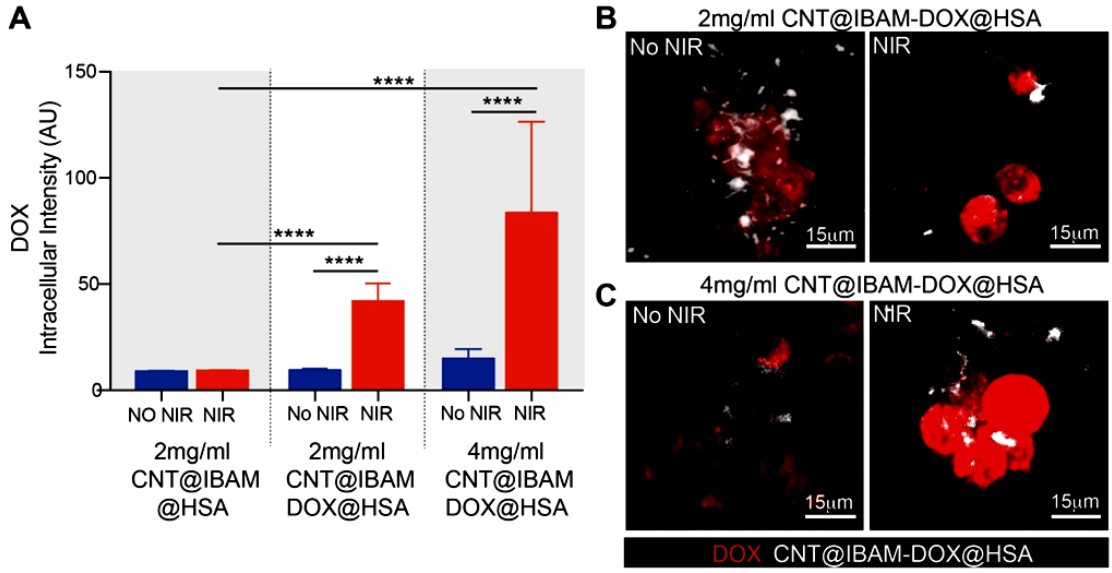

Fig.2-9 (A) Intracellular DOX intensity. Average and standard deviation from the red DOX fluorescence signal in the different scaffold conditions. *P* values were calculated by the Mann Whitney test (**** p <0.0001). *Z*-projection of the fluorescent stack of images taken on D2A1 cells grown in CNT@IBAM-DOX@HSA composite at the concentrations of (B) 2 mg/mL and (C) 4 mg/mL without and with NIR irradiation, respectively.

With the aim to evidence that the DOX loaded in the CNT@MS@IBAM-DOX@HSA nanocomposites can be efficiently delivered to the cancer cells following NIR light application, thereby enhancing cytotoxic activity, we decided to incorporate the composites inside a 3D hydrogel scaffold. Additionally, this allows shielding cells from the unwanted non-specific adsorption of heat-inducing composite particles. Hence, the CNT@MS@IBAM-DOX@HSA nanocomposites were formulated within a commercially-available biocompatible protein-based hydrogel (Matrigel) that mimics a biocompatible implantable scaffold. Indeed, the development of activable nanocomposite scaffolds has become an emerging field in nanomedecine and biomaterials which allows to solve issues associated with the use of injectable scaffolds (such as local injection, controlled release, limited loss of therapeutics). To build such nanocomposite scaffolds,

CNT@MS@IBAM-DOX@HSA suspensions at 2 and 4 mg/mL were mixed with Matrigel as substrates for the growth of the tumor cells and CNT@MS@IBAM@HSA were mixed to Matrigels to be used as controls. DOX release and uptake upon NIR was followed by confocal microscopy and the results showed significantly increased red fluorescence signals when cells were treated with CNT@MS@IBAM-DOX@HSA (**Fig.2-9 A-C**). The procedure allowing us to visualize the cellular DOX uptake (red color) and the CNT@MS@IBAM-DOX-HSA nanocomposites (white color) distribution is detailed in **S.2-8**. While absence of NIR led to backgrounds levels of DOX, we observed a dose-dependent NIR-stimulated DOX release in tumor cells (**Fig.2-9 A**). Overall, this confirms that DOX is released from the CNT@MS@IBAM-DOX@HSA nanocomposites upon NIR light application and it contributes to the synergistic effect of photothermia and DOX release observed in the 2C cell culture in the previous paragraph.

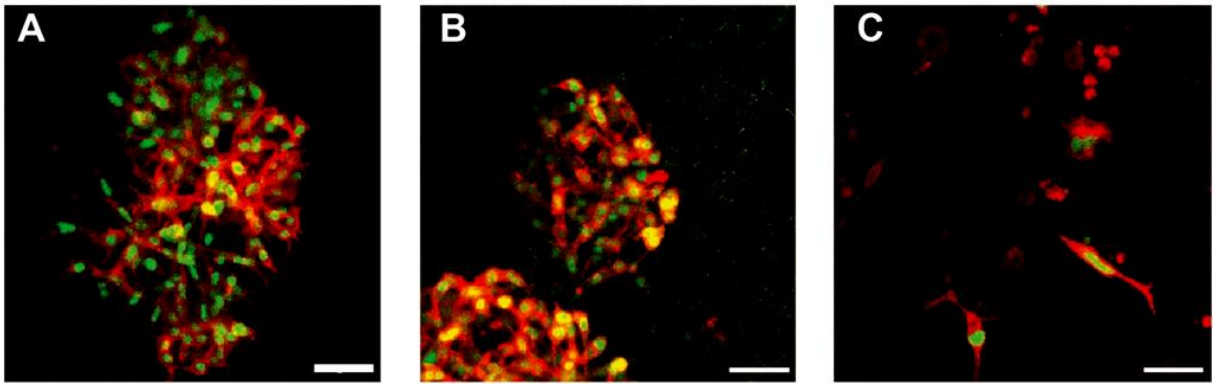

Fig.2-10 Confocal microscopy imaging of 3D tumoral D2A1 cancer cell growth in Matrigel over 5 days in the absence or in the presence of the nanocomposites. D2A1 grown in Matrigel (A) in the absence of nanocomposites (B) treated with 2.5 mg/mL CNT@MS@IBAM@HSA and (C) treated with 2.5 mg/mL CNT@MS@IBAM-DOX@HSA. (Scale bars 50 µm). In green: the nuclear localization signal and in red: the actin filaments.

At last, in order to assess whether this hydrogel system loaded with CNTs@MS@IBAM-DOX@HSA nanocomposite displays cytotoxicity towards murine breast cancer cells in 3D conditions, we assessed cellular growth in presence of different nanocomposites (**Fig.2-10**). The cells were grown over 5 days in either Matrigel (control without nanocomposites) or in a mixture of Matrigel added with the nanocomposites at 2.5 mg/mL. While CNT@MS@IBAM@HSA had no effect on cellular growth as compared to the control without nanocomposites (**Fig.2-10 A-B**), CNT@MS@IBAM-DOX@HSA significantly led to cell death in these conditions (**Fig.2-10 C**). Thus, when incorporated into a

matrix, CNT@MS@IBAM@HSA composites are not cytotoxic. When functionalized with DOX, its release would favor cytotoxicity (as expected upon NIR light). Such property could be beneficial for antitumor applications where drug release could be potentiated with external stimulus such as NIR light.

2.4 Conclusion

In this work, we have designed new NIR light-responsive nanocomposites made of MS shell coated CNTs, loaded with the antitumor drug doxorubicin (DOX), and capped with plasma protein human serum albumin (HSA) as a biocompatible interface and gate keeper. We have developed here a novel way to immobilize DOX with a DLC up to 80%, (a very high amount as compared to the literature), via the powerful strategy based on IBAM versatile non-covalent binders grafted on CNT@MS shells which additionally allow the tight anchoring of HSA.

The photothermal properties of these composites were investigated as a function of their concentration and of the laser power. We found that adjusting the power at $1W/cm^2$ is well suited to control the temperature under the necrosis temperature (45 ℃). These drug-loaded CNT@MS@IBAM-DOX@HSA nanocomposites were shown to release DOX in response to NIR light applied. We demonstrated that this release occurs first by a burst that depends on the concentration of the composites but can also be controlled on a pulsatile fashion as a regular increase of DOX after each NIR light application. We demonstrated that a NIR power of $1\ W/cm^2$ is efficient to control the release of DOX dose on time.

We further demonstrated the cytotoxic potential of DOX-loaded nanocomposites and highlighted a potentially interesting feature of our nanocomposites: even if photothermic effect from the CNTs composites allows an important cancer cell cytotoxicity, the DOX –mediated release ensure an additional cytotoxicity allowing synergy of both effect to kill cancer cells. Finally, another originality of this work is the integration of such nanocomposites into a hydrogel mimicking the extracellular matrix which can have potential applications in the field of antitumoral scaffolds or polymer matrices for tissue engineering (if DOX is replaced by another molecule). We showed here that the application of NIR light on such nanocomposite hydrogel scaffold covered with D2A1 murine breast cancer cells allows triggering the release of DOX to the cellular media, which results in cell toxicity over time.

Hence, such nanosystems may be of huge interest as components of implantable scaffolds for antitumor or tissue engineering applications. This approach would make it possible the development of new (nano) medical devices for the medicine of tomorrow.

Acknowledgements

D.M. acknowledges the Materials Institute Carnot Alsace (project ProtRemote) and the Cancerop ôle Est (project VIVIRMAG) for the financial supports. Bing LI would like to thank the Chinese Scholarship Council (CSC) for the grant during her PhD at the University of Strasbourg. M.T. acknowledges CONICET for funding and support for researchers' exchange, as well as the EU project Hygraphen for researchers' mobility allowances. Work in the Goetz lab (VG, SH, JGG) is supported by institutional funds from INSERM and University of Strasbourg as well as by Cancerop ôle Est (project VIVIRMAG). V.G. funded by an INSERM/RegionEst *Ph.D.* fellowship.

2.5 References

[1] S. Augustine, J. Singh, M. Srivastava, M. Sharma, A. Das, B.D. Malhotra, Recent advances in carbon based nanosystems for cancer theranostics, Biomater. Sci. 5 (2017) 901–952.

[2] E. Cazares-Cortes, S. Cabana-Montenegro, C. Boitard, E. Nehling, N. Griffete, J. Fresnais, C. Wilhelm, A. Abou-Hassan, C. Ménager, Recent insights in magnetic hyperthermia: From the "hot-spot" effect for local delivery to combined magneto-photo-thermia using magneto-plasmonic hybrids, Adv. Drug Deliv. Rev. 138 (2019) 233-246.

[3] S. Kralj, T. Potrc, P. Kocbek, S. Marchesan, D. Makovec, Design and fabrication of magnetically responsive nanocarriers for drug delivery, Curr. Med. Chem. 24 (2017) 454–469.

[4] D. Mertz, O. Sandre, S. Bégin-Colin, Drug releasing nanoplatforms activated by alternating magnetic fields, Biochim. Biophys. Acta BBA - Gen. Subj. 1861 (2017) 1617–1641.

[5] S. Mura, J. Nicolas, P. Couvreur, Stimuli-responsive nanocarriers for drug delivery, Nat. Mater. 12 (2013) 991–1003.

[6] M.A.C. Stuart, W.T.S. Huck, J. Genzer, M. Müller, C. Ober, M. Stamm, G.B. Sukhorukov, I. Szleifer, V.V. Tsukruk, M. Urban, F. Winnik, S. Zauscher, I. Luzinov, S. Minko, Emerging applications of stimuli-responsive polymer materials, Nat. Mater. 9 (2010) 101–113.

[7] A.K. Gaharwar, N.A. Peppas, A. Khademhosseini, Nanocomposite hydrogels for biomedical applications, Biotechnol. Bioeng. 111 (2014) 441–453.

[8] L. Gao, L. Xia, R. Zhang, D. Duan, X. Liu, J. Xu, L. Luo, Enhanced antitumor efficacy of poly (D, L-lactide-co-glycolide)-based methotrexate-loaded implants on sarcoma 180 tumor-bearing mice, Drug Des. Devel. Ther. 11 (2017) 3065.

[9] N.S. Satarkar, D. Biswal, J.Z. Hilt, Hydrogel nanocomposites: a review of applications as remote controlled biomaterials, Soft Matter. 6 (2010) 2364–2371.

[10] S. Talebian, J. Foroughi, S.J. Wade, K.L. Vine, A. Dolatshahi‐Pirouz, M. Mehrali, J. Conde, G.G. Wallace, Biopolymers for Antitumor Implantable Drug Delivery Systems: Recent Advances and Future Outlook, Adv. Mater. 30 (2018) 1706665.

[11] B.D. Weinberg, E. Blanco, J. Gao, Polymer implants for intratumoral drug delivery and cancer therapy, J. Pharm. Sci. 97 (2008) 1681–1702.

[12] Y. Zhang, J. Yu, H.N. Bomba, Y. Zhu, Z. Gu, Mechanical Force-Triggered Drug Delivery, Chem. Rev. 116 (2016) 12536–12563.

[13] D. Mertz, S. Harlepp, J. Goetz, D. Bégin, G. Schlatter, S. Bégin‐Colin, A. Hébraud, Nanocomposite Polymer Scaffolds Responding under External Stimuli for Drug Delivery and Tissue Engineering Applications, Adv. Ther. n/a (n.d.) 1900143.

[14] S. Merino, C. Martín, K. Kostarelos, M. Prato, E. Vázquez, Nanocomposite Hydrogels: 3D Polymer–Nanoparticle Synergies for On-Demand Drug Delivery, ACS Nano. 9 (2015) 4686–4697.

[15] A.A. Adedoyin, A.K. Ekenseair, Biomedical applications of magneto-responsive scaffolds, Nano Res. 11 (2018) 5049–5064.

[16] A. Battigelli, C. Ménard-Moyon, T. Da Ros, M. Prato, A. Bianco, Endowing carbon nanotubes with biological and biomedical properties by chemical modifications, Adv. Drug Deliv. Rev. 65 (2013) 1899–1920.

[17] H. Gong, R. Peng, Z. Liu, Carbon nanotubes for biomedical imaging: the recent advances, Adv. Drug Deliv. Rev. 65 (2013) 1951–1963.

[18] H. Dai, Carbon nanotubes: synthesis, integration, and properties, Acc. Chem. Res. 35 (2002) 1035–1044.

[19] A. Bianco, K. Kostarelos, C.D. Partidos, M. Prato, Biomedical applications of functionalised carbon nanotubes, Chem. Commun. (2005) 571–577.

[20] K. Kostarelos, A. Bianco, M. Prato, Promises, facts and challenges for carbon nanotubes in imaging and therapeutics, Nat. Nanotechnol. 4 (2009) 627–633.

[21] Z. Liu, J.T. Robinson, S.M. Tabakman, K. Yang, H. Dai, Carbon materials for drug delivery & cancer therapy, Mater. Today. 14 (2011) 316–323.

[22] R. Singh, S.V. Torti, Carbon nanotubes in hyperthermia therapy, Adv. Drug Deliv. Rev. 65 (2013) 2045–2060.

[23] B.S. Wong, S.L. Yoong, A. Jagusiak, T. Panczyk, H.K. Ho, W.H. Ang, G. Pastorin, Carbon nanotubes for delivery of small molecule drugs, Adv. Drug Deliv. Rev. 65 (2013) 1964–2015.

[24] C. Ge, J. Du, L. Zhao, L. Wang, Y. Liu, D. Li, Y. Yang, R. Zhou, Y. Zhao, Z. Chai, Binding of blood proteins to carbon nanotubes reduces cytotoxicity, Proc. Natl. Acad. Sci. 108 (2011) 16968–16973.

[25] B. Koh, W. Cheng, Mechanisms of Carbon Nanotube Aggregation and the Reversion of Carbon Nanotube Aggregates in Aqueous Medium, Langmuir. 30 (2014) 10899–10909.

[26] X. Wang, T. Xia, S.A. Ntim, Z. Ji, S. George, H. Meng, H. Zhang, V. Castranova, S. Mitra, A.E. Nel, Quantitative Techniques for Assessing and Controlling the Dispersion and Biological Effects of Multiwalled Carbon Nanotubes in Mammalian Tissue Culture Cells, ACS Nano. 4 (2010) 7241–7252.

[27] H.B. Chew, M.-W. Moon, K.R. Lee, K.-S. Kim, Compressive dynamic scission of carbon nanotubes under sonication: fracture by atomic ejection, Proc. R. Soc. A 467 (2011), 1270–1289.

[28] J. Liu, A.G. Rinzler, H. Dai, J.H. Hafner, R.K. Bradley, P.J. Boul, A. Lu, T. Iverson, K. Shelimov, C.B. Huffman, Fullerene pipes, Science. 280 (1998) 1253–1256.

[29] X. Liu, R.H. Hurt, A.B. Kane, Biodurability of single-walled carbon nanotubes depends on surface functionalization, Carbon. 48 (2010) 1961–1969.

[30] Z. Liu, X. Sun, N. Nakayama-Ratchford, H. Dai, Supramolecular chemistry on water-soluble carbon nanotubes for drug loading and delivery, ACS Nano. 1 (2007) 50–56.

[31] Z. Liu, K. Chen, C. Davis, S. Sherlock, Q. Cao, X. Chen, H. Dai, Drug delivery with carbon nanotubes for in vivo cancer treatment, Cancer Res. 68 (2008) 6652–6660.

[32] Z. Liu, A.C. Fan, K. Rakhra, S. Sherlock, A. Goodwin, X. Chen, Q. Yang, D.W. Felsher, H. Dai, Supramolecular stacking of doxorubicin on carbon nanotubes for in vivo cancer therapy, Angew. Chem. Int. Ed. 48 (2009) 7668–7672.

[33] M. Zheng, A. Jagota, E.D. Semke, B.A. Diner, R.S. Mclean, S.R. Lustig, R.E. Richardson, N.G. Tassi, DNA-assisted dispersion and separation of carbon nanotubes, Nat. Mater. 2 (2003) 338–342.

[34] M. Zhang, X. Zhang, X. He, L. Chen, Y. Zhang, A facile method to coat mesoporous silica layer on carbon nanotubes by anionic surfactant, Mater. Lett. 64 (2010) 1383–1386.

[35] K. Ding, B. Hu, Y. Xie, G. An, R. Tao, H. Zhang, Z. Liu, A simple route to coat mesoporous SiO 2 layer on carbon nanotubes, J. Mater. Chem. 19 (2009) 3725–3731.

[36] S.-W. Bian, Z. Ma, L.-S. Zhang, F. Niu, W.-G. Song, Silica nanotubes with mesoporous walls and various internal morphologies using hard/soft dual templates, Chem. Commun. (2009) 1261–1263.

[37] P. Yang, S. Gai, J. Lin, Functionalized mesoporous silica materials for controlled drug delivery, Chem. Soc. Rev. 41 (2012) 3679–3698.

[38] M. Ménard, F. Meyer, K. Parkhomenko, C. Leuvrey, G. Francius, S. Bégin-Colin, D. Mertz, Mesoporous silica templated-albumin nanoparticles with high doxorubicin

payload for drug delivery assessed with a 3-D tumor cell model, Biochim. Biophys. Acta BBA - Gen. Subj. 1863 (2019) 332–341.

[39] F. Perton, S. Harlepp, G. Follain, K. Parkhomenko, J.G. Goetz, S. Bégin-Colin, D. Mertz, Wrapped stellate silica nanocomposites as biocompatible luminescent nanoplatforms assessed in vivo, J. Colloid Interface Sci. 542 (2019) 469–482.

[40] M. Ménard, F. Meyer, C. Affolter-Zbaraszczuk, M. Rabineau, A. Adam, P.D. Ramirez, S. Bégin-Colin, D. Mertz, Design of hybrid protein-coated magnetic core-mesoporous silica shell nanocomposites for MRI and drug release assessed in a 3D tumor cell model, Nanotechnology. 30 (2019) 174001.

[41] V. Fiegel, S. Harlepp, S. Begin-Colin, D. Begin, D. Mertz, Design of Protein-Coated Carbon Nanotubes Loaded with Hydrophobic Drugs through Sacrificial Templating of Mesoporous Silica Shells, Chem. – Eur. J. 24 (2018) 4662–4670.

[42] C. Wells, O. Vollin‐Bringel, V. Fiegel, S. Harlepp, B.V. der Schueren, S. Bégin‐Colin, D. Bégin, D. Mertz, Engineering of Mesoporous Silica Coated Carbon-Based Materials Optimized for an Ultrahigh Doxorubicin Payload and a Drug Release Activated by pH, T, and NIR-light, Adv. Funct. Mater. 28 (2018) 1706996.

[43] F. Perton, M. Tasso, G.A. Muñoz Medina, M. Ménard, C. Blanco-Andujar, E. Portiansky, M.B.F. van Raap, D. Bégin, F. Meyer, S. Begin-Colin, D. Mertz, Fluorescent and magnetic stellate mesoporous silica for bimodal imaging and magnetic hyperthermia, Appl. Mater. Today. 16 (2019) 301–314.

[44] D. Mertz, P. Tan, Y. Wang, T.K. Goh, A. Blencowe, F. Caruso, Bromoisobutyramide as an Intermolecular Surface Binder for the Preparation of Free-standing Biopolymer Assemblies, Adv. Mater. 23 (2011) 5668–5673.

[45] D. Mertz, J. Cui, Y. Yan, G. Devlin, C. Chaubaroux, A. Dochter, R. Alles, P. Lavalle, J.C. Voegel, A. Blencowe, Protein capsules assembled via isobutyramide grafts: sequential growth, biofunctionalization, and cellular uptake, ACS Nano. 6 (2012) 7584–7594.

[46] D. Mertz, H. Wu, J.S. Wong, J. Cui, P. Tan, R. Alles, F. Caruso, Ultrathin, bioresponsive and drug-functionalized protein capsules, J. Mater. Chem. 22 (2012) 21434–21442.

[47] S.H. Lü, Q. Lin, Y.N. Liu, Q. Gao, T. Hao, Y. Wang, J. Zhou, H. Wang, Z. Du, J. Wu, C.Y. Wang, Self-assembly of renal cells into engineered renal tissues in collagen/Matrigel scaffold in vitro, J. Tissue Eng. Regen. Med. 6 (2012) 786–792.

[48] Y. Kimura, M. Ozeki, T. Inamoto, Y. Tabata, Time Course of de Novo Adipogenesis in Matrigel by Gelatin Microspheres Incorporating Basic Fibroblast Growth Factor, Tissue Eng. 8 (2002) 603–613.

[49] M.W. Laschke, M. Rücker, G. Jensen, C. Carvalho, R. Mülhaupt, N.-C. Gellrich, M.D. Menger, Incorporation of growth factor containing Matrigel promotes vascularization of porous PLGA scaffolds, J. Biomed. Mater. Res. A. 85A (2008) 397–407.

[50] G. Follain, N. Osmani, A.S. Azevedo, G. Allio, L. Mercier, M.A. Karreman, G. Solecki, M.J. Garcia León, O. Lefebvre, N. Fekonja, C. Hille, V. Chabannes, G. Dollé, T. Metivet, F.D. Hovsepian, C. Prudhomme, A. Pichot, N. Paul, R. Carapito, S. Bahram, B. Ruthensteiner, A. Kemmling, S. Siemonsen, T. Schneider, J. Fiehler, M. Glatzel, F. Winkler, Y. Schwab, K. Pantel, S. Harlepp, J.G. Goetz, Hemodynamic Forces Tune the Arrest, Adhesion, and Extravasation of Circulating Tumor Cells, Dev. Cell. 45 (2018) 33-52.e12.

[51] N. Osmani, G. Follain, M.J. García León, O. Lefebvre, I. Busnelli, A. Larnicol, S. Harlepp, J.G. Goetz, Metastatic Tumor Cells Exploit Their Adhesion Repertoire to Counteract Shear Forces during Intravascular Arrest, Cell Rep. 28 (2019) 2491-2500.e5.

[52] M. Vinci, S. Gowan, F. Boxall, L. Patterson, M. Zimmermann, W. Court, C. Lomas, M. Mendiola, D. Hardisson, S.A. Eccles, Advances in establishment and analysis of three-dimensional tumor spheroid-based functional assays for target validation and drug evaluation, BMC Biol. 10 (2012) 29.

[53] X.-Y. Wang, D. Mertz, C. Blanco-Andujar, A. Bora, M. Ménard, F. Meyer, C. Giraudeau, S. Bégin-Colin, Optimizing the silanization of thermally-decomposed iron oxide nanoparticles for efficient aqueous phase transfer and MRI applications, RSC Adv. 6 (2016) 93784–93793.

[54] D. Mertz, C. Affolter-Zbaraszczuk, J. Barthès, J. Cui, F. Caruso, T.F. Baumert, J.-C. Voegel, J. Ogier, F. Meyer, Templated assembly of albumin-based nanoparticles for simultaneous gene silencing and magnetic resonance imaging, Nanoscale. 6 (2014) 11676–11680.

[55] N.Ž. Knežević, I.I. Slowing, V.S.-Y. Lin, Tuning the release of anticancer drugs from magnetic iron oxide/mesoporous silica core/shell nanoparticles, ChemPlusChem. 77 (2012) 48–55.

[56] L. Yuan, Q. Tang, D. Yang, J.Z. Zhang, F. Zhang, J. Hu, Preparation of pH-responsive mesoporous silica nanoparticles and their application in controlled drug delivery, J. Phys. Chem. C. 115 (2011) 9926–9932.

[57] J. Shen, Q. He, Y. Gao, J. Shi, Y. Li, Mesoporous silica nanoparticles loading doxorubicin reverse multidrug resistance: performance and mechanism, Nanoscale. 3 (2011) 4314–4322.

[58] J. Liu, C. Detrembleur, M.-C. De Pauw-Gillet, S. Mornet, L. Vander Elst, S. Laurent, C. Jérôme, E. Duguet, Heat-triggered drug release systems based on mesoporous silica nanoparticles filled with a maghemite core and phase-change molecules as gatekeepers, J. Mater. Chem. B. 2 (2014) 59–70.

[59] B.V. Harmon, A.M. Corder, R.J. Collins, G.C. Gobé, J. Allen, D.J. Allan, J.F.R. Kerr, Cell Death Induced in a Murine Mastocytoma by 42–47 °C Heating in Vitro: Evidence that the Form of Death Changes from Apoptosis to Necrosis Above a Critical Heat Load, Int. J. Radiat. Biol. 58 (1990) 845–858.

[60] S. Li, S. Chien, P.-I. Brånemark, Heat shock-induced necrosis and apoptosis in osteoblasts, J. Orthop. Res. 17 (1999) 891–899.

[61] S.S. Mambula, D. >Stuart K. Calderwood, Heat induced release of Hsp70 from prostate carcinoma cells involves both active secretion and passive release from necrotic cells, Int. J. Hyperthermia. 22 (2006) 575–585.

[62] J. Wu, A. Chen, M. Qin, R. Huang, G. Zhang, B. Xue, J. Wei, Y. Li, Y. Cao, W. Wang, Hierarchical construction of a mechanically stable peptide–graphene oxide hybrid hydrogel for drug delivery and pulsatile triggered release in vivo, Nanoscale. 7 (2015) 1655–1660.

[63] J. Liu, C. Wang, X. Wang, X. Wang, L. Cheng, Y. Li, Z. Liu, Mesoporous Silica Coated Single-Walled Carbon Nanotubes as a Multifunctional Light-Responsive Platform for Cancer Combination Therapy, Adv. Funct. Mater. 25 (2015) 384–392.

[64] W.-L. Chiang, C.-J. Ke, Z.-X. Liao, S.-Y. Chen, F.-R. Chen, C.-Y. Tsai, Y. Xia, H.-W. Sung, Pulsatile drug release from PLGA hollow microspheres by controlling the permeability of their walls with a magnetic field, Small. 8 (2012) 3584–3588.

[65] K Katagiri, M Nakamura, K Koumoto, Magnetoresponsive smart capsules formed with polyelectrolytes, lipid bilayers and magnetic nanoparticles, ACS Appl. Mater. Interfaces 2 (2010) 768–773.

2.6 Supporting information

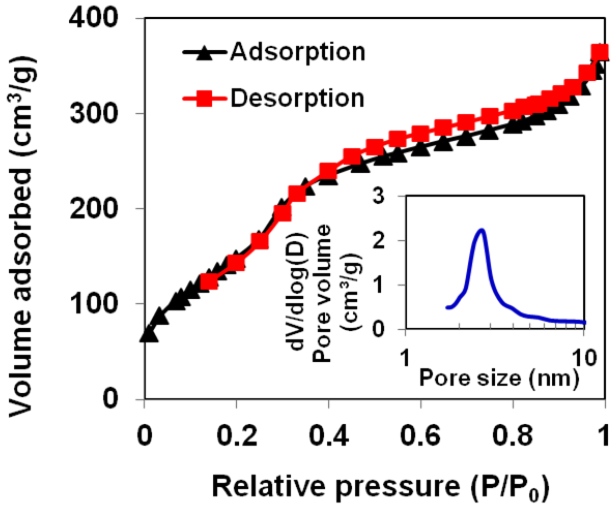

S.2-1 Nitrogen adsorption-desorption isotherms of CNT@MS composite associated with the pore size distribution

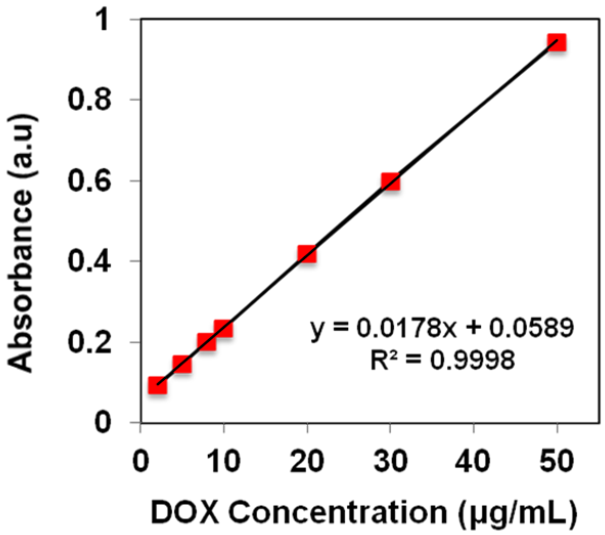

S.2-2 DOX calibration curve Absorbance at 480 nm *vs* [DOX] by UV visible spectrophotometry

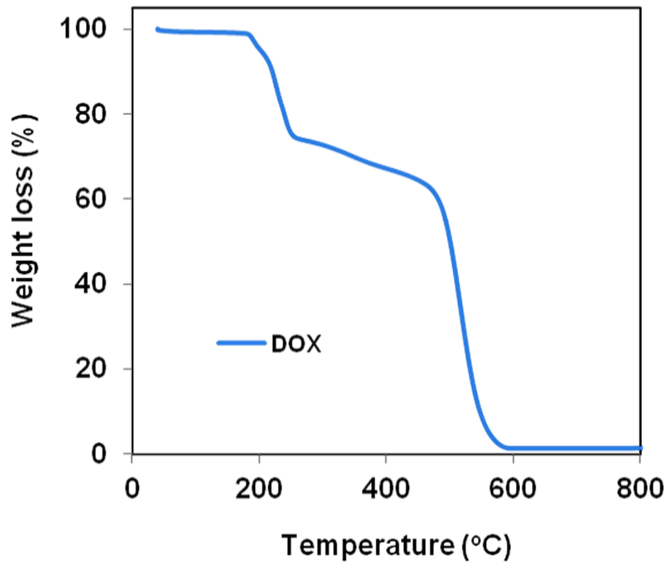

S.2-3 TGA curve of pure DOX

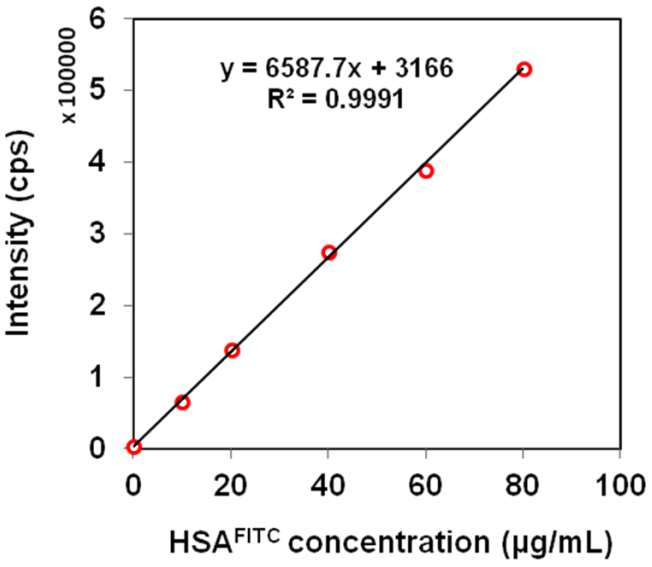

S.2-4 Calibration curve of HSA^{FITC} solutions in water representing maximum fluorescence intensity at 520 nm *vs* [HSA^{FITC}] by spectrofluorimetry

Table S2-1 Summary of calculating the proportion of each component based on the TGA results

Sample	SiO_2 (wt%)	Carbon (wt%)	APTS (wt%) [1]	IBAM (wt%) [2]	DOX (wt%) [3]	APTS/CNT@MS (wt%) [4]	IBAM/CNT@MS (wt%) [4]	DOX/CNT@MS (wt%) [4]
CNT@MS	37.20	62.80						
CNT@MS@APTS	33.70	56.89	9.41			10.4		
CNT@MS@IBAM	31.68	53.48	8.84	5.99		10.4	7.0	
CNT@MS@IBAM-DOX	21.47	36.25	5.99	4.06	32.23	10.4	7.0	55.8

[1] The calculation of APTS (wt%) is based on the constant of carbon/SiO_2.

[2] The calculation of IBAM (wt%) is based on the constant of carbon/SiO_2 and APTS/SiO_2.

[3] The calculation of DOX (wt%) is based on the constant of carbon/SiO_2, APTS/SiO_2 and IBAM/SiO_2.

[4] CNT@MS is considered as the sum of SiO_2 and carbon components.

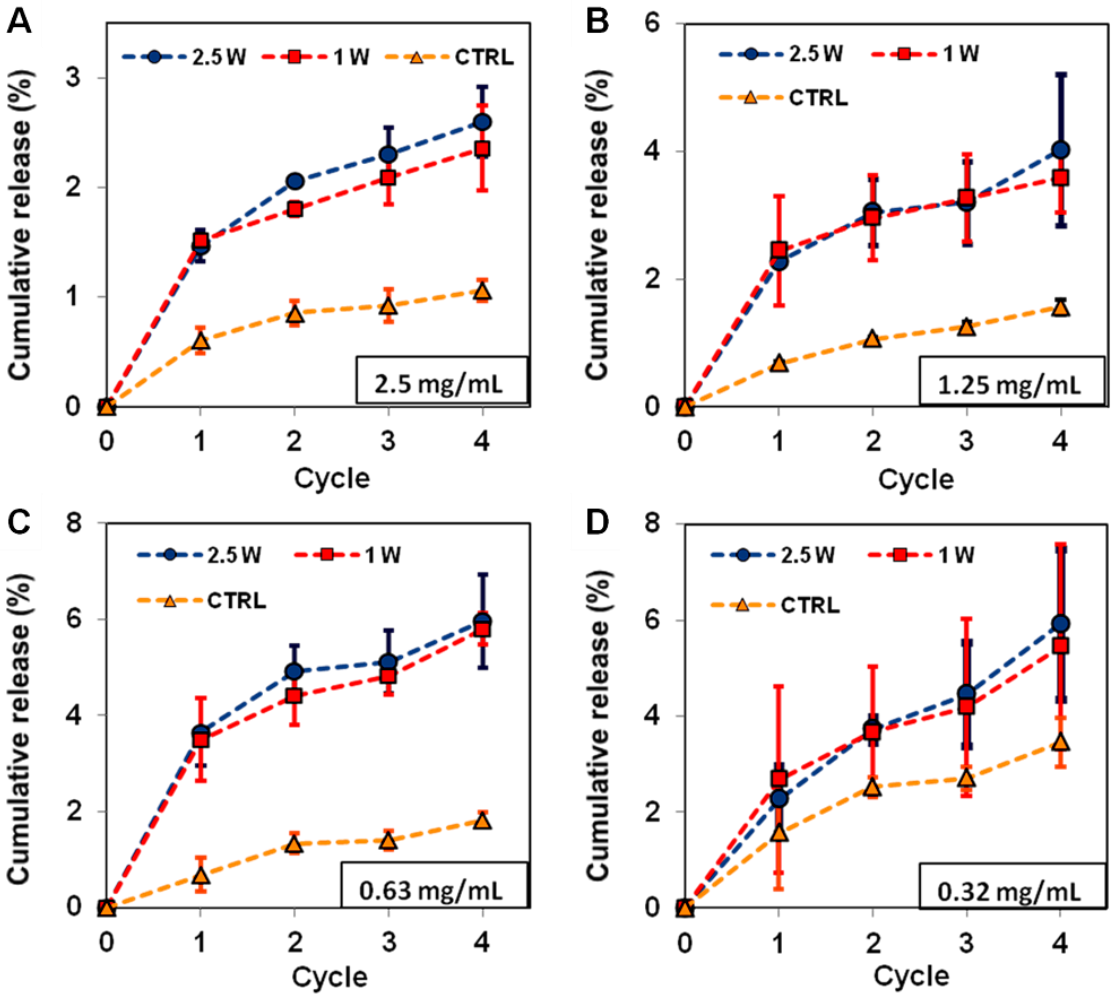

S.2-5 Cumulative DOX release from Figure 7 expressed in % of the DOX amount released as compared to the initial loading.

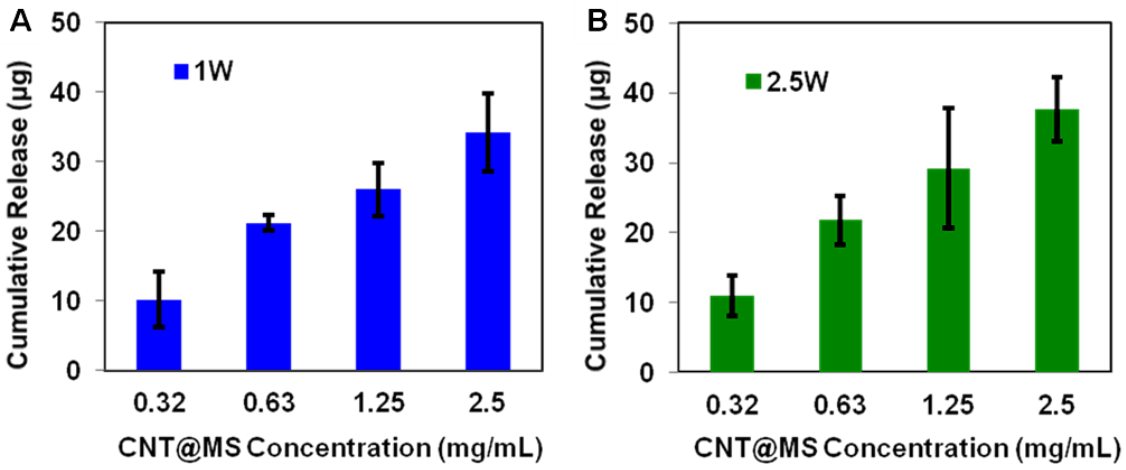

S.2-6 Cumulative DOX release from various concentrations of CNT@MS@IBAM-DOX@HSA upon four times of NIR laser irradiation at a power density of (A) 1 W/cm^2 and (B) 2.5 W/cm^2. Irradiation cycle was 15 min ON, 3 days OFF.

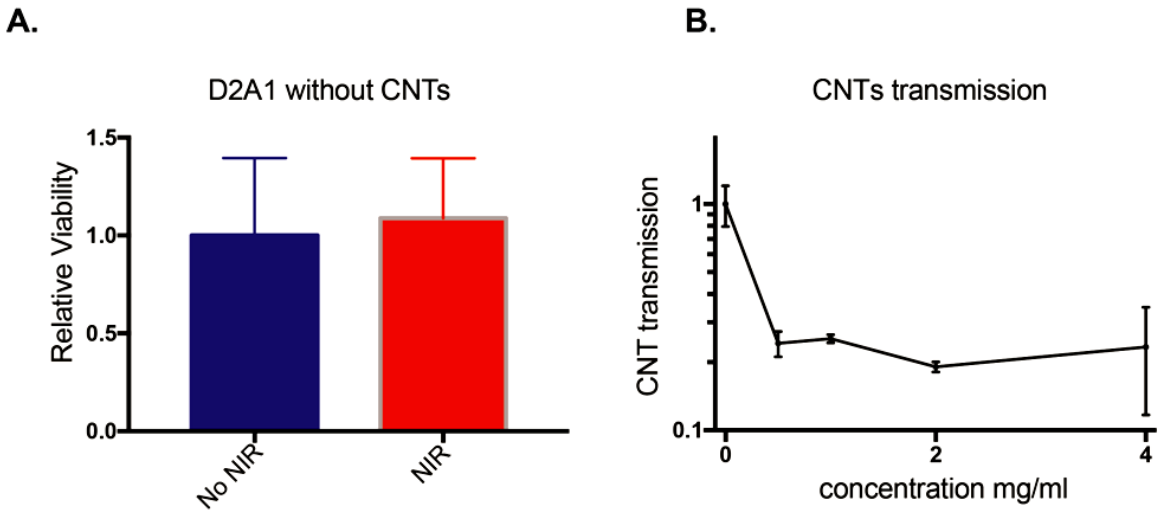

S.2-7 (A) Effect of the NIR light by itself (without CNT@MS nanocomposite) on the cell viability of the 2D cultured cells. (B) Cells grown for 48h in DMEM, CNT@MS@IBAM@HSA added before viability test to quantify absorption.

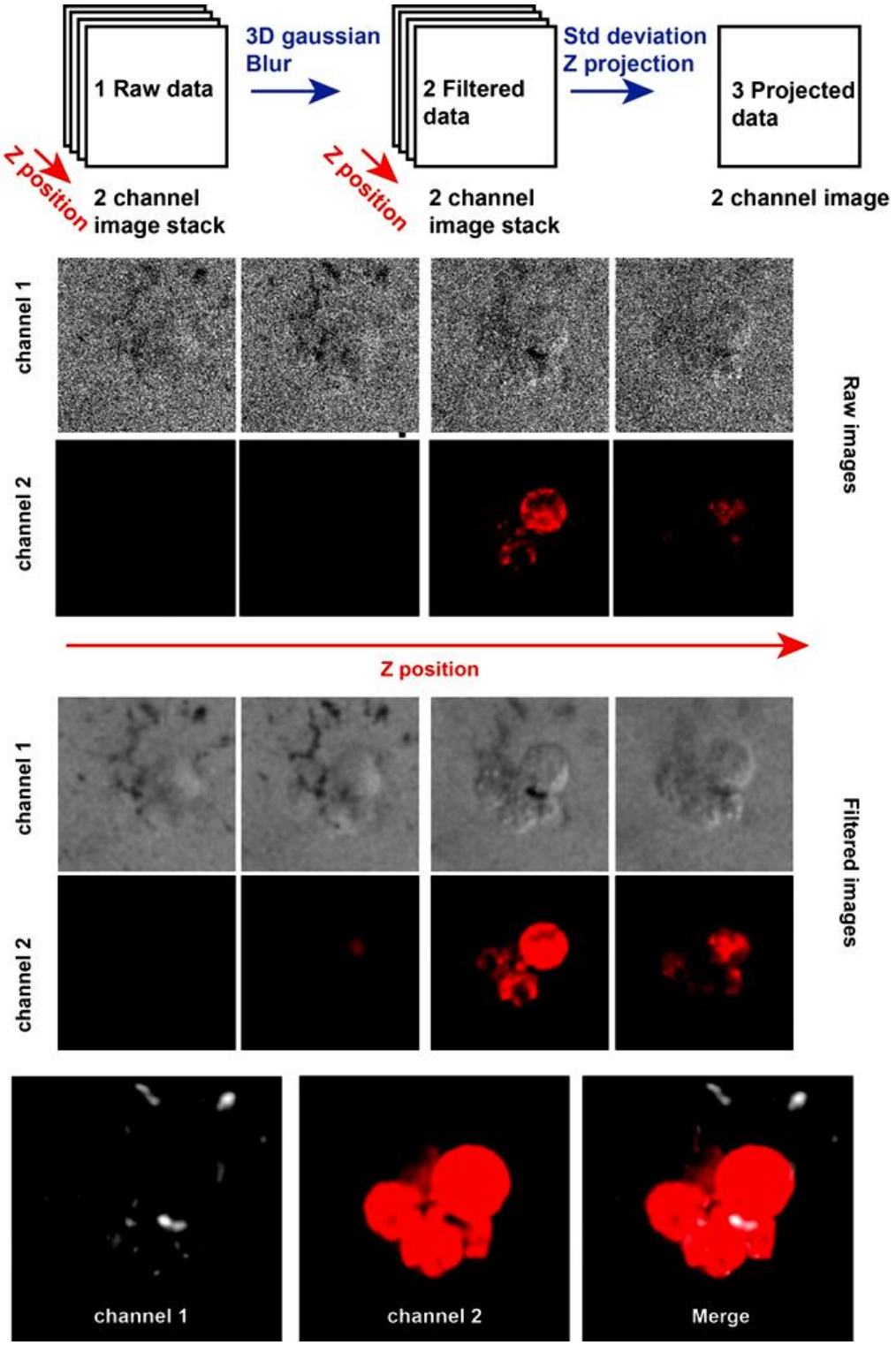

S.2-8 Procedure allows visualization of the cellular DOX uptake and the CNT@MS@IBAM-DOX-HSA nanocomposite distribution**.** The Matrigel and the nanocomposites were first polymerized before adding cells on the gel. The nanocomposites, thus, appear on different layers compared to the cells. The standard deviation *Z* projection allows the nanocomposites to appear white due to the high contrast from background.

Chapter 3 Nanocomposite supramolecular hydrogels assembled through enzyme-loaded carbon nanotubes@large pore mesoporous silica for thermally induced drug release

Bing Li[1,2], Miryam Criado-Gonzalez[3], Lo ïc Jierry[3], Christophe M édart[2], Sylvie Begin-Colin[1], Dominique Begin[2], Damien Mertz[1]

[1] *Institut de Physique et Chimie des Mat ériaux de Strasbourg (IPCMS), UMR-7504 CNRS-Universit éde Strasbourg, 23 rue du Lœss, BP 34 67034, Strasbourg Cedex 2, France, §*

[2] *Institut de Chimie et Proc édés pour l'Energie, l'Environnement et la Sant é (ICPEES), UMR-7515 CNRS-Universit é de Strasbourg, 25 rue Becquerel, 67087 Strasbourg, Cedex 2, France*

[3] *Institut Charles Sadron (ICS) CNRS UPR 22, 23 rue du Loess BP 84407, 67034 Strasbourg cedex*

Abstract

The controlled synthesis of nano-sized objects with tailored features is an important challenge for the design of powerful functional nanocomposite macromolecular scaffolds. Achieving chemical and mechanical robustness of these materials require a strong crosslinking of the nano-objects within its 3D environment. In this way, the surface modification of the nano-object is a *sine qua none* step to ensure the crosslinking within the material. Herein, we have developed an efficient process to get large pore mesoporous silica coating around carbon nanotubes (CNT@LPMS). This inorganic layer exhibits large nanopores (ca. 10 nm size) particularly suitable for the loading of proteins. Based on the isobutyramide (IBAM)-mediated coating approach, a huge amount of alkaline phosphatase (more than 100% wt payload) was immobilized within the large pore MS surface allowing the localized growth of peptide self-assembled nanofibers architecture resulting in supramolecular hydrogel. This assembly is also shown on (carbon free) stellate large pore silica spherical nanoparticles having a similar surface engineering to the CNT@LPMS, emphasizing the versatility of the approach by changing the nanoparticle morphology but not the interface. Furthermore, the incorporation of Doxorubicin (DOX) during the hydrogelation process leads to a reservoir material of anti-cancer agents whose release is thermally triggered at hyperthermia temperature (T ca. 42 ℃).

Keywords:

Large pore mesoporous silica, Mesoporous silica coated carbon nanotubes, Enzymatic catalysis, Hydrogel peptide, Drug delivery

3.1 Introduction

Today, the meeting between macromolecular science and nanomaterial synthesis lets envision the development of new and powerful stimuli-responsive advanced composite materials[1, 2] for a wide range of technological applications such as energy storage[3], self-repairing materials[4], catalysis[5] or sensing[6]. Especially, in the field of nanomedecine and tissue engineering, the development of such nano-engineered smart composite materials has become blossoming these last years.[7-9] The polymer matrix of such nanocomposite assemblies ensures features such as reinforced controlled mechanical properties, biocompatibility, and a suitable macroscopic support for cell adhesion/interaction, and the nanocomposites ensure the role of mechanical fillers, anchoring local points and eventually, response under external fields. Indeed, usual nanomaterials such as gold or iron oxide nanoparticles (NPs) are particularly attractive nanocomponents of smart remotely responsive polymer scaffold materials given respectively their response to external fields such as NIR light[10, 11] or magnetic fields[12-14] due their plasmonic or magnetization properties.

However, designing such smart functional scaffolds is actually an important challenge since their internal architecture needs to be built on a very controlled fashion. To achieve this aim, a fine engineering of the surface of nanomaterials is highly required. An ideal surface should have a high surface area to ensure high linker surface grafting and multiple connection points with the network polymer. Moreover, the surface should be easily chemically modified with suitable surface binders ensuring tight and strong contacts with the polymer network. Indeed, though many studies report the insertion of nanoparticles within a polymer matrix, there is still few studies reporting the use of surface engineered nanoparticles to finely crosslink the polymer network which is the challenge addressed here.

Among the possible nanomaterials choices, carbon nanotubes (CNTs) are particularly attractive to design nanocomposite scaffolds because they bring particularly high mechanical properties, high electrical conductivity and NIR light induced thermal activation properties.[15, 16] However, for biomedical applications, given their intrinsic surface hydrophobicity, the capping of such carbon materials with hydrophilic coating is necessary.[17, 18] Among the various capping possibilities described in the literature, which encompasses molecules or polymer coatings[19, 20], mesoporous silica (MS) is a particularly suitable coating of CNTs[21-23]. Indeed, in addition to provide a great dispersion in aqueous buffer, the silanol groups can be easily chemically modified with a range of silane precursors and the high surface area allow the loading with various types of drugs.[24-26] Besides, the vast majority of such design concern

small pore silica and the design of large pore silica around CNTs (or other nanomaterial) is very few reported.[27] Especially such large pore design is particularly suitable for the immobilization of high MW biomolecules such as enzyme, DNA or other biopolymer of therapeutic interest. As compared to strategies to anchor polymer or molecules, the advantages of MS rely on better grafting density and better colloidal stability. Some works have reported different ways allow to immobilize biofunctional proteins such as enzymes in CNTs by chemical strategies[28, 29], however a better coverage density coverage is currently needed and the chemical crosslinking/coupling may induce loss of the enzymatic activity.

Among the polymer matrix possibilities, hydrogels are particularly interesting systems as their chemistry and their physicochemical features can be easily controlled by the polymer chemistry and the gel formation process. Even if main hydrogel development concern synthetic polymers such as PEG, Pluronics etc., there are important developments towards natural polymer building blocks such as peptides to constitute a biocompatible/biologically favorable hydrogel. Recently, a new biocompatible and effective approach has been developed to initiate locally the formation of hydrogel exclusively from any kind of surface[30], in particular from nano-objects[31-33]. It is based on the concept of enzyme-assisted self-assembly[34] of peptides where the enzyme is immobilized onto the surface of a nano-object and transforms the precursor peptides into hydrogelators. This strategy ensures the growth of a fibrous network of self-assembled peptide nanofibers from the surface of the enzyme-modified nano-objects. Thus, it allows the generation of a composite nanomaterial, where the nano-objects are specifically located at the nodes of its internal architecture. Herein, the assembly chosen is based on a tripeptide, *i.e.* Fmoc-FFY, exhibiting antimicrobian properties.[35]

In this work, we propose a powerful and facile strategy to trigger the self-assembly of a peptide hydrogel from enzyme-coated CNT@LPMS composites, which act as initiators of the peptide self-assembly and cross-linking points of the resulting nanocomposite hydrogel (**Fig.3-1**). The self-assembly by enzyme-coated carbon free stellate spherical large pore silica NPs (STMS) is also achieved in parallel to demonstrate the versatility of the surface engineering approach. The association of CNT@LPMS with the self-assembled peptide hydrogel as a polymer scaffold appears as an innovative strategy for the development of a new generation of stimuli responsive hydrogel nanocomposites having suitable and innovative features for nanomedecine applications. In this work, we address several originalities as compared to the literature. Firstly, the design of new carbon-based nanocomposites made of large pore MS surrounding CNTs is achieved which is few reported in the literature. The

LPMS design is well adapted for loading high molecular weight molecules such as enzymes with suitable surface binders. Secondly, the immobilization of enzyme alkaline phosphatase (AP) with very high loading capacity (sup 100%) within the porous shell thanks to the use of isobutyramide (IBAM) grafts is demonstrated. Previously, IBAM binders grafted at silica surface were already shown efficient to immobilize range of biopolymers of therapeutic interest including: nucleic acids[36], polysaccharides[37], or serum albumin[38, 39], and their use to immobilize enzymes on plain silica was shown with preservation of their enzymatic catalysis functionality[40, 41]. Here, the biocatalytic activities of such AP-coated CNT@LPMS and AP-coated STMS are then assessed by following the conversion of AP enzymatic substrate paranitrophenylphosphate (PNP) into paranitrophenol (PN). Thirdly, with the aim to create new and powerful self-assembled peptide hydrogel nanocomposites whose assembly is triggered by the dephosphorylation catalytic activity of AP, the self-assembly of Fmoc−FF*p*Y peptide (Fmoc: fluorenylmethyloxycarbonyl; F: phenylalanine; Y: tyrosine; p: phosphate group) is assessed in the presence of AP-coated STMS or AP-coated CNT@LPMS. The mechanical properties of such nanocomposite hydrogels are investigated without/with the two types of NPs through rheological studies and depending on its nature and without/with the loading of doxorubicin (DOX), an antitumor drug. Finally, the ability to release DOX upon T elevation is investigated.

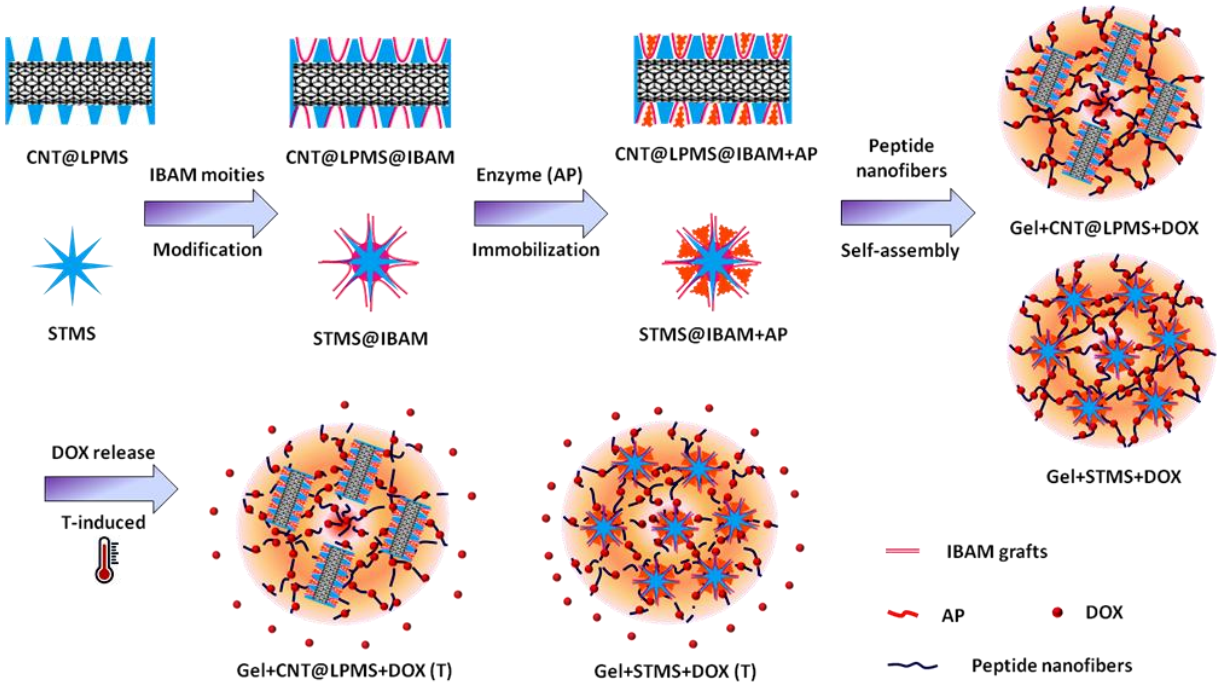

Fig.3-1 Schematic representations of hydrogel self-assembled from AP immobilized CNT@LPMS and STMS composites and the thermally induced release of DOX

3.2 Materials and methods

3.2.1 Chemicals

Carbon nanotubes PR-24-XT-PS (CNTs) were purchased from Pyrograf-III. Cetyltrimethylammonium bromide (CTAB) was purchased from Roth (France). Nitric acid (HNO_3), sulfuric acid (H_2SO_4), ethanol (EtOH), tetraethyl orthosilicate (TEOS), sodium hydroxide (NaOH), ammonium nitrate (NH_4NO_3, >99%), 3-aminopropyltriethoxysilane (APTS), isobutyryl chloride (IBC), triethylamine (Et_3N), dimethylformamide (DMF), dimethylsulfoxide (DMSO), sodium bicarbonate ($NaHCO_3$), fluorescein isothiocyanate (FITC), cetyltrimethylammonium p-toluenesulfonate (CTATos), 2-Amino-2-(hydroxymethyl)-1,3-propanediol (AHMPD), ethylene glycol (EG, 99.8%), decane (≥99%), bovine alkaline phosphatase (AP) and 4-Nitrophenyl phosphate disodium salt hexahydrate (pNPP-Na) were purchased from Sigma-Aldrich (France). Ammonium hydroxide solution (25% in H_2O) was purchased from Fluka. Doxorubicin hydrochloride (DOX, purity 99%) was purchased from OChem Incorporation (USA). Sodium tetraborate anhydrous (borax) and 1, 3, 5-Triisopropylbenzene (TIB, 95%) were supplied by Acros Organics. Fmoc−FF*p*Y peptide (Fmoc: fluorenylmethyloxycarbonyl; F: phenylalanine; Y: tyrosine; p: phosphate group) was purchased from PepMic.

3.2.2 Procedures

(1) Synthesis of large pore stellate mesoporous silica (STMS)

Typically, 200 mL of distilled water, 3.8 g of CTATos and 0.436 g of AHMPD were introduced into a 500 mL flask. Then the mixture was heated from room temperature to 75 ^{o}C with stirring at 250 rpm. 30.2 g of TEOS was added to the mixture when the temperature reached 75 ^{o}C, and stirred at 75 ^{o}C for 2h. After that, a white precipitate was formed and then was filtered under vacuum. The precipitate was washed with distilled water (3 x 20 mL) and then centrifuged. The resulted powder was calcinated at 550 ^{o}C for 6 h to remove the CTATos template.

(2) Synthesis of large pore mesoporous silica coated CNTs (CNT@LPMS)

First, the pristine CNTs were cleaved in a better-suited length. Typically, 0.75 g of pristine CNTs was added into 108 mL mixture of H_2SO_4/HNO_3 (Volume ratio = 3 : 1,) and sonicated at 0 ℃ for 24 h. The mixture was then monitored to neutrality with NaOH (1 M) solution. The sliced CNTs were washed with distilled water (3 x 25 mL), dried at room temperature, and then reduced at 900 ℃ for 2 h under argon. The resulting sliced CNTs were used as the initial material for the following silica layer coating step.

100 mg of sliced CNTs were well dispersed in 120 mL distilled water by ultrasonication (Vibracell 75043 from Bioblock Scientific, 2 x 10 min, Power = 750 W, Amplitude = 40%, Temperature = 30°C, runs: 50" ON, 50" OFF). 684 mg of CTAB was dissolved in 60 mL of distilled water and stirred at room temperature for 40 min at 250 rpm. Then, the CNTs solution was mixed with the CTAB solution, and the mixture was sonicated for 30 min. After that, 45 mL of ethylene glycol and 456 µL of NaOH (1 M) solution were added, and the mixture was stirred at 250 rpm at 70 ^{o}C. After 1 h, 1.095 mL of decane was added and kept stirring at 250 rpm at 70 ^{o}C. After continuous stirring for 2 h, 1.35 mL of TIB was added. Then, stirring was continued at 70 ^{o}C at 250 rpm for another 2 h, and finally 684 µL of TEOS was added, and stirring was continued for 3 h under the same conditions. After the sol gel reaction, LPMS coated CNTs product was obtained, followed by centrifugation (8000 g x 10 min) and washing with EtOH (2 x 20 mL).

(3) Surfactant extraction from the LPMS coated composite

The removal of CTAB template agent from the silica pores was achieved by redispersing the composite in 25 mL of NH_4NO_3 (20 mg/mL in EtOH), and extracting with stirring at 60 ℃ for 1 h. Then 10 µL of the mixture was diluted in 1 mL of water and measured its Zeta potential. The surface charge of the composite measured by ZP allows determining when all the CTAB templates were removed. The procedure was repeated until almost all the CTAB templates were extracted from the composite (approximately 5 extractions were required). At this point, the composite was denoted as CNT@LPMS.

(4) FITC labeling

AP was fluorescently labeled with FITC using a stoichiometry of 2 moles of fluorescent dye per mole of enzyme. 100 mg of AP was first dissolved in 10 mL of sodium bicarbonate buffer ($NaHCO_3$ 50 mM, pH 8.5) and then 212 µL of FITC (10 mg/mL in DMSO) was added into the AP solution. The mixture was stirred on the wheel for 24 h and then dialyzed for 2 days (membrane pore size: 10 kDa) in distilled water at room temperature to remove the free FITC. The water was changed every 2 h. Finally, the resulting AP^{FITC} was adjusted to a concentration of 10 mg/mL for further use.

(5) APTS functionalization of silica surface

Firstly, 20 mg of STMS or CNT@LPMS composites were dispersed in 6 mL of EtOH. Then 0.3 mL of ammonium hydroxide (25%) was added and the mixture was vortexed for 10 s, followed with the addition of 1.25 mL of APTS. After 2 h of stirring on the wheel at room temperature, the amino modified composites were centrifuged (13 000g x 10 min) and washed with EtOH (1 x 10 mL) and DMF (2 x 10 mL).

(6) IBAM modification

The resulting amino-modified composites were firstly dispersed in a mixed solution of 0.24 mL of Et_3N and 3 mL of DMF, and vortexed for 10 s. After that, a solution containing of 0.55 mL of IBC and 3 mL of DMF was added. After stirring on the wheel for 2 h at room temperature, about 1 mL of distilled water was added to dissolve the inorganic salt formed from the reaction, and finally a clear orange solution was obtained. The resulting IBAM-modified composites were separated via centrifugation (13 000g x 10 min) and then washed with DMF (1 x 5 mL). Finally, the IBAM moieties functionalized composites were dispersed in DMF and stored on the wheel with stirring at room temperature.

(7) AP immobilized on the STMS@IBAM and CNT@LPMS@IBAM composites

4 mg of chemically modified STMS@IBAM or CNT@LPMS@IBAM was isolated by centrifugation (13 000g x 10 min) to remove the DMF, then washed with distilled water (1 x 1 mL). After that, the composite was dispersed in 1 mL of a certain concentration (from 500 μg/mL to 25 000 μg/mL) of AP^{FITC} aqueous solution and sonicated for 10 s. The mixture was stirred on the wheel for 1 h at room temperature and then centrifuged (13 000g x 10 min). The supernatant was collected and diluted with water to a certain multiple in order to quantify AP^{FITC} remaining in the supernatant through the calibration curve of AP^{FITC} (e.g. the supernatant of 500 μg/mL impregnating solution is diluted by 2 times, and the supernatant of 25 000 μg/mL impregnating solution is diluted by 160 times). The diluted supernatant was measured by spectrofluorimetry. By recording the maximum fluorescence intensity at 520 nm, the AP^{FITC} remaining in the supernatant could be calculated, which allow us determining the mass of AP^{FITC} adsorbed on the chemically modified STMS@IBAM or CNT@LPMS@IBAM composites. The AP^{FITC} immobilized composites were washed with water (1 mL) to remove the loosely bound enzyme, centrifuged (13 000g x 10 min) and then dried at 40 ^{o}C for 3 days. The dry AP^{FITC} immobilized composites were analyzed by TGA to confirm the actual immobilization amount of AP^{FITC}.

(8) Enzymatic activity measurement of the immobilized AP

The enzymatic activity of the immobilized AP was performed on the composites loaded with 100 wt% AP relative to STMS and CNT@LPMS, which were denoted as STMS@IBAM+AP (100 wt%) and CNT@LPMS@IBAM+AP (100 wt%), respectively. The assay was performed using p-Nitrophenyl phosphate disodium hexahydrate (pNPP-Na) as the substrate. Firstly, 20 μL of AP immobilized-composites (0.1 mg/mL in 50 mM $NaHCO_3$ buffer) was dispersed in 0.98 mL $NaHCO_3$ buffer (50 mM, pH = 8.5) and sonicated for 10 s. Then 1 mL of pNPP-Na substrate solution (0.1 mg/mL in 50 mM $NaHCO_3$ buffer) was added

and the mixture was vortexed for 10 s. That is, the final concentration of pNPP-Na substrate was 0.05 mg/mL. After that, the mixture was covered with aluminum foil and placed in the 25, 37 and 42 ^{o}C water baths. The subsequent conversion of pNPP-Na into p-nitrophenol (pPN) and disodium phosphate was catalyzed by the immobilized AP. The enzymatic hydrolysis of pNPP-Na was detected by the presence of the yellow color product pNP using a UV-vis spectrometry. After reacting for 10, 20, 30, 40, 60, 90 and 120 min, the mixture was transferred to a 1 cm path length cell. The hydrolysis product pNP was monitored by the UV-vis spectroscopy, and the maximum absorbance at λ = 405 nm was recorded.

(9) Formation of supramolecular hydrogels

The peptide self-assembly process was synthesized according to the reported procedure.[42] Firstly, 1 mg of Fmoc-FF*p*Y peptide was dissolved in 155 μL borax buffer (25 mM, pH = 9.5) by vortex for 60 s. Then, 25 μL of DOX aqueous solution at 4 mg/mL was added into the peptide solution and the mixture was vortexed for 20 s. Finally, 20 μL of STMS@IBAM+AP (100 wt%) or CNT@LPMS@IBAM+AP (100 wt%) composites (1 mg/mL) was added into the mixture of peptide and DOX. The mixture was vortexed for 20 s, and then allowed to stand at room temperature for 24 h to self-assemble to form hydrogel. The same procedure was used to prepare hydrogels without DOX, except that 1 mg of Fmoc-FF*p*Y peptide was dissolved in 180 μL borax buffer (25 mM, pH = 9.5). The hydrogels with and without DOX assembly formed from STMS@IBAM+AP and CNT@LPMS@IBAM+AP composites are denoted as: Gel+STMS+DOX, Gel+CNT@LPMS+DOX, Gel+STMS and Gel+CNT@LPMS, respectively. The gel prepared from free AP is denoted as Gel, which was obtained by dissolving 1 mg of Fmoc-FF*p*Y peptide in 180 μL of borax buffer and contacting with 20 μL of AP solution in 1 mg/mL for 24 h. The final concentrations of Fmoc-FF*p*Y, STMS@IBAM+AP or CNT@LPMS@IBAM+AP composite or free AP, and DOX in the hydrogel were maintained respectively 5 mg/mL, 0.1 mg/mL and 0.5 mg/mL.

(10) DOX release from hydrogel

After the hydrogel formation, 1 mL of distilled water was added slowly along the tube wall. The tubes were then covered with aluminum foil and placed in the water baths for 24 h. Thereafter, the supernatant containing the released DOX was collected and then measured by UV-vis spectrometry. The amount of DOX released in the supernatant was then calculated by the DOX calibration curve. The calibration curve of DOX aqueous solution was obtained by measuring the absorbance of different DOX concentrations at 480 nm. An inverted tube test was conducted after to detect the stability of the hydrogel.

3.2.3 Characterization Methods

(1) Nitrogen adsorption-desorption analysis

The Nitrogen adsorption-desorption isotherms were measured on a Tristar 3000 Gas Adsorption Analyzer (Micromeritics). Before each measurement, the sample was outgassed under vacuum at 150 ℃ for 4 h. The specific surface area was calculated by Brunauer-Emmett-Teller (BET) method, the pore size and pore volume was calculated by Barrett-Joyner-Halenda model (BJH).

(2) Zeta potential and dynamic light scattering measurements

Zeta potential and dynamic light scattering (DLS) measurements were carried out using Zetasizer nano ZS manufactured by Malvern Instruments. Zeta potential measurements were performed by diluting 10 μL of the stock suspensions in 1 mL of water using a DTS1070 folded capillary cell. The measurements were carried out at 25 ℃ in triplicate. The DLS measurements were carried out by measuring the particle size distribution at concentration of 0.5 mg/mL in water in triplicate.

(3) Thermal gravimetric analysis

The thermogravimetric analysis (TGA) was performed on a Q5000 Automatic Sample Processor (TA Instruments). The runs were started from room temperature to 800 ℃ with a heating rate of 10 ℃/min, under an air flow rate of 25 mL/min.

(4) Scanning electron microscopy

The morphology of STMS and CNT@LPMS composites were characterized by scanning electron microscopy (SEM) on the JEOL F2600 microscope equipped with a CCD camera. The tested composites were firstly dispersed in EtOH and a drop of the suspension was dropped on a copper grid for observation.

(5) Transmission electron microscopy

Transmission electron microscopy (TEM) images were taken via a JEOL 2100 apparatus with high resolution operating at an acceleration voltage of 200 kV. The STMS and CNT@LPMS composites were firstly dispersed in EtOH, while the STMS@IBAM+AP and CNT@LPMS@IBAM+AP composites were dispersed in distilled water. Then a few drops of the suspension were deposited on a carbon-coated copper grid and then dry at room temperature before observation.

(6) Cryo-SEM

The morphology of the obtained peptide fibers was observed through a Cryo-SEM designed and manufactured by the mechanical facility of the Charles Sadron Institute. The supramolecular hydrogel was plunged quickly into liquid ethane and then fixed vertically into a cryo-holder which was previously placed inside a nitrogen bath. During the plunging, the

sample is rapidly frozen by direct contact with the liquid ethane. The specific cryo-holder was designed and manufactured by the mechanical facility of the Charles Sadron Institute. The cryo-holder was then placed under vacuum into the cryo preparation chamber of the Quorum PT 3010 machine attached to the microscope. The sample was fractured with a razor blade and a slight etching at -90 ℃ for 3 min was performed to render the fibers more visible. The sample was eventually transferred in the FEG-cryoSEM (Hitachi SU8010) and observed at 1kV at -150 ℃.

(7) Fluorescence spectroscopy

The fluorescence spectra of AP^{FITC} were obtained on a Horiba scientific Fluorolog spectrophotometer using a 1 cm path length cell. The emission spectra were recorded from 505 to 600 nm upon an excitation wavelength of 495 nm.

(8) UV-Vis spectroscopy

UV-vis spectroscopy was used to determine the enzymatic activity of the immobilized AP and the amount of drug released in the supernatant. The UV-vis spectra were recorded by a Lambda 950 UV/vis Spectrometer (Perkin Elmer). The colorless substrate pNPP-Na resulted in a yellow product by enzymatic hydrolysis of pNPP-Na in the presence of AP, with absorbance at $\lambda = 405$ nm. The relative enzymatic activity of immobilized AP was determined by recording the absorbance of pNPP-Na solution at $\lambda = 405$ nm. The concentration of DOX was obtained by measuring the absorbance at 480 nm.

(9) Rheological measurements

Rheological properties were measured in a NAME OF THE EQUIPMENT rheometer using a Peltier plate aluminium geometry of 10 mm diameter and a gap of 1.2 mm. Strain measurements were performed from 1% to 100% at a fixed frequency of 1 Hz at 25°C. Frequency sweeps were carried out from 1 Hz to 10 Hz at a fixed strain of 1% at 25°C. Temperature sweeps were performed from 25°C to 42°C with a heating rate of 3 ^{o}C/min at fixed 1% strain and 1 Hz. Gels were previously prepared in teflon molds of 10 mm diameter before the measurements.

3.3 Results and discussion

3.3.1 Synthesis and characterization of STMS and CNT@LPMS

Large pore stellate mesoporous silica (STMS) nanoparticles were synthesized by using TEOS as a silica precursor and CTATos as a structure-directing agent. TEM and SEM were used to characterize the structures of synthesized STMS particles, as shown in **S.3-1 A** and **B**. It can be clearly observed from the TEM image that the silica nanoparticles are highly

monodisperse showing a homogenous radial stellate mesoporous structure with an average size of 90±7 nm. The SEM image displays the presence of spherical and porous particles (**S.3-1 B**). Specially, the open large pore channels in the porous silica matrix of STMS are revealed both by TEM and SEM images. The nitrogen adsorption-desorption isotherms and the corresponding pore size distribution of STMS are shown in **S.3-2 A**. The specific surface area value for STMS was determined using an adsorption model. The pore volume was calculated based on the amount of nitrogen adsorbed at relative pressure of about 0.98. The pore size distribution was calculated using the Barrett-Joyner-Halenda model (BJH) (**S.3-2 A**, inset). According to IUPAC classification, type IV isotherms with a narrow hysteresis loop could be classified on STMS material. According to the Brunauer-Emmett-Teller (BET) analysis, a BET surface area of 393 m^2 /g associated with a pore volume of 1.06 cm^3/g was obtained. The BJH pore size distribution indicates that STMS exhibits an average pore size ca. 11.2 nm.

The pristine CNTs were firstly cleaved through acid treatment and a sol-gel procedure was performed to coat the sliced CNTs with a homogeneous MS shell. **Fig.3-2 A-C** show the TEM and SEM images of LPMS layer coated CNTs. It can be seen that the MS layer is composed of numerous large pore channels, which are uniformly surrounded on the outer surface of the CNTs. TEM image reveals that the silica layer surrounding the CNTs was characterized with a shell thickness of ca. 50 nm. The silica content and the CNT content of CNT@LPMS composite were evaluated by a TGA measurement (**Fig.3-3 B**). Based on the combustion of CNTs at about 500℃, the proportion of silica is estimated to 56 wt%. After CTAB extraction, the CNT@LPMS composite was characterized by nitrogen adsorption-desorption isotherms. The isotherms of CNT@LPMS are classified as type IV with a type H3 hysteresis loop, which indicates the mesoporous structure of the silica layer. The BET surface area of CNT@LPMS (**Fig.3-2 D**) shows a high value of the surface area (672 m^2/g), which is much larger than that of the pristine CNT (80 m^2/g) (in **S.3-2 B**). The pore volume of pristine CNTs is 0.14 cm^3/g, which is increased to 2.12 cm^3/g after LPMS layer coating. The pore size distribution of CNT@LPMS shows a peak near 12 nm, which again indicates the formation of a LPMS layer on the CNTs surface. The formation of mesoporous structure of the MS layer greatly improved the specific surface area and the pore volume, making these nanocomposites as ideal supports to host guest molecules.

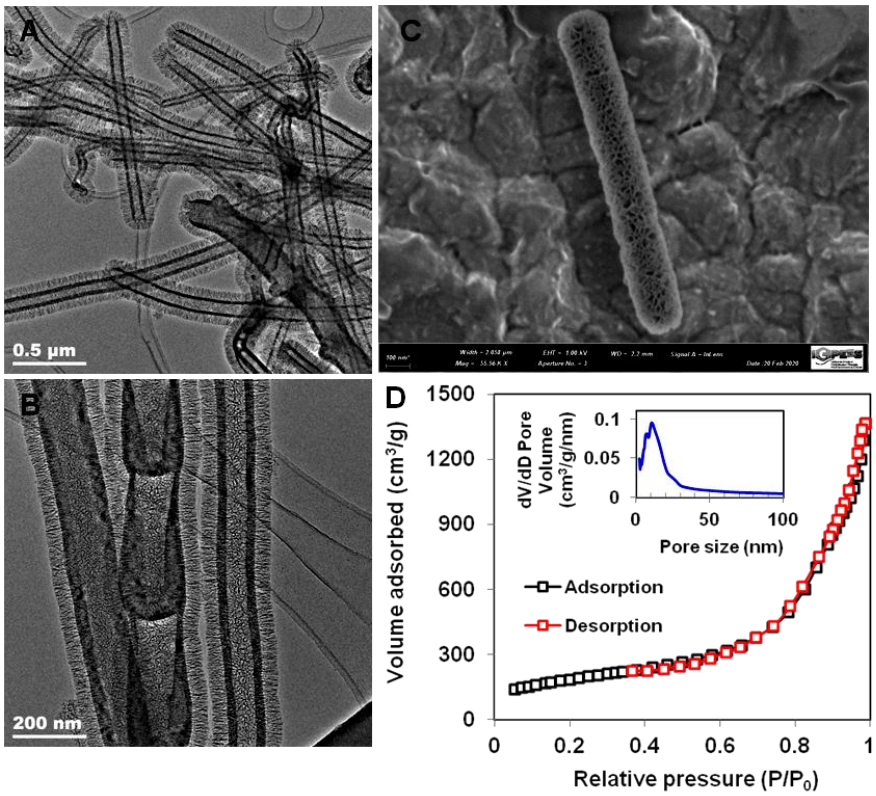

Fig.3-2 (A-C) TEM and SEM images of CNT@LPMS composite. (D) N_2 adsorption-desorption isotherms of CNT@LPMS associated with the pore size distribution.

3.3.2 Functionalization of silica surface

Surface functionalization of STMS was carried out before enzyme immobilization. First, the silica surface was "silanized" by NH_4OH catalyzing 3-aminopropyltriethoxysilane (APTS) condensation on their surface. Therefore, the amine modified silica surface was further functionalized by isobutyryl chloride (IBC), and finally, isobutyramide (IBAM) terminal functional groups were formed on the MS surface. The extent of APTS and IBAM functional groups was studied using thermogravimetric analysis. TGA curves depicting thermal decomposition of STMS, STMS@APTS and STMS@IBAM are showed in **Fig.3-3 A**. In the case of bare STMS, the TGA curve shows that there is a slightly negligible weight loss below 200 ℃, which corresponds to the evaporation of physically adsorbed water. The greater weight loss on STMS@APTS and STMS@IBAM curves occurs in the range of 250-400 ℃ and is due to the removal of organic moieties from the composite. Using STMS as a baseline, the amount of grafting APTS and IBAM groups were estimated to 11.9 wt% and ca. 13.2 wt% of STMS, respectively. This allows us determining the graft density of APTS and IBAM groups on the silica surface. Finally, the density of APTS and IBAM moieties grafted on the silica surface was estimated to 3.3 per nm^2 and 2.6 per nm^2, respectively.

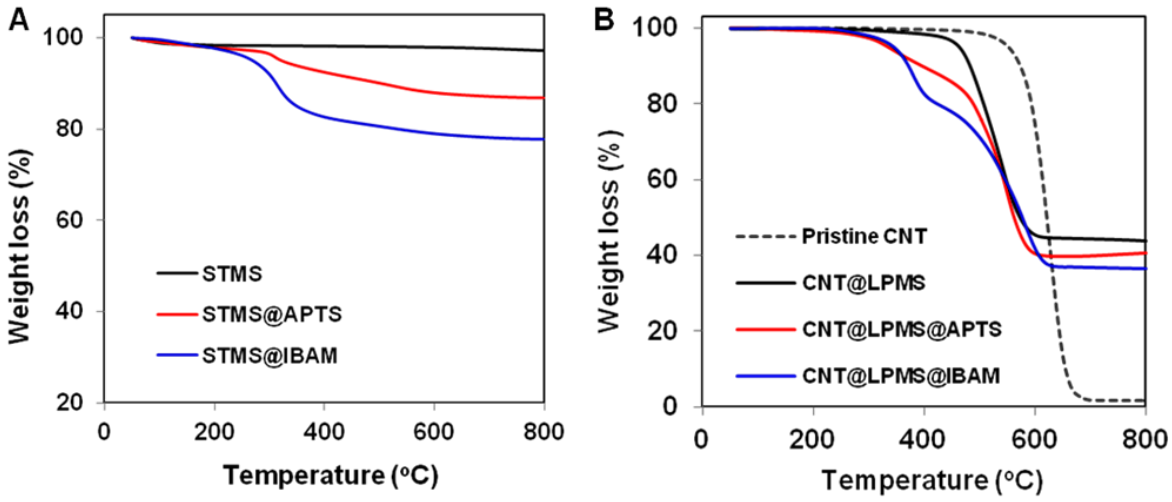

Fig.3-3 (A) TGA curves of STMS, STMS@APTS and STMS@IBAM. (B) TGA curves of pristine CNT, CNT@LPMS, CNT@LPMS@APTS and CNT@LPMS@IBAM.

The TGA tests were also performed on the pristine CNTs and functionalized samples: CNT@LPMS, CNT@LPMS@APTS and CNT@LPMS@IBAM from 50 ℃ to 800 ℃ under air flow, the results are shown in **Fig.3-3 B**. The pristine CNTs remained fairly stable at temperatures up to 500 °C, after which they quickly began to oxidize and burn. It is worth noting that the decomposition of carbon in CNT@LPMS started from 400 ℃, which was lower than the combustion of pristine CNT. This is most likely due to more defects generated on the sliced CNTs during acid treatment. The TGA curves of the functionalized CNT@LPMS are significantly different from that of bare CNT@LPMS. The TGA curves of CNT@LPMS@APTS and CNT@LPMS@IBAM show two distinct weight loss regions. The functional groups started to decompose at 250 ℃ due to the elimination of APTS and IBAM groups, from which the approximate amount of functional groups grafted on the MS surface could be determined. The second region weight loss in the temperature range of 400 ℃ to 600 ℃ corresponds to the combustion of carbon. It was calculated that the fixed APTS and IBAM functional groups were respectively ca. 10.4 wt% and 9.2 wt% of CNT@LPMS.

The characteristics of the porous structure of the functionalized STMS@IBAM and CNT@LPMS@IBAM were also studied by nitrogen adsorption-desorption analysis, the results are showed in **S. 3-2** and **Table 1**. As expected, the introduction of the IBAM moieties resulted in the reduction in specific surface area, pore volume and average pore size. The changes of the structural properties of STMS@IBAM and CNT@LPMS@IBAM composites indicate the fact that the functional groups are partially located in the pore channels of the silica matrix, resulting in a reduction of these textural structure parameter values, which can also indirectly confirm the effectiveness of the modification process.

Table 1 Relevant parameters characterizing the textural features of supports and after surface functionalization

Sample	BET surface area (m^2/g)	Pore volume (cm^3/g)	Pore size (nm)
STMS	393	1.06	11.2
STMS@IBAM	110	0.45	7.6
CNT@LPMS	672	2.12	12.0
CNT@LPMS@IBAM	218	0.70	7.7

Zeta potential measurements were measured in water at pH=6.5 to characterize the surface charge of the prepared samples. **Fig.3-4** shows the zeta potentials of the naked STMS and CNT@LPMS, IBAM-functionalized STMS and CNT@LPMS dispersed in pure water (pH 6.5). The ZP value, which corresponds theoretically to the potential at the sliding plane of the double ion layer on the coated surface, indicates the surface charge of the nanocomposite. ZP measurement results show that for the bare STMS and CNT@LPMS, they are negatively charged on MS surfaces with zeta potential of -28.7±0.9 mV and -14.2±1.2 mV, respectively. As IBAM groups are introduced on the silica surface, the ZP values recorded for the modified STMS@IBAM and CNT@LPMS@IBAM are significantly different. ZP values of +10.1±0.7 mV and +24.3±0.9 mV corresponding to STMS@IBAM and CNT@LPMS@IBAM were found, respectively. There are still remaining APTS groups exposed after the IBAM modification which probably result in these positive ZP values. The successful functionalization with IBAM on the silica surface of STMS@IBAM and CNT@LPMS@IBAM is beneficial to the high loading capacity for enzyme immobilization.

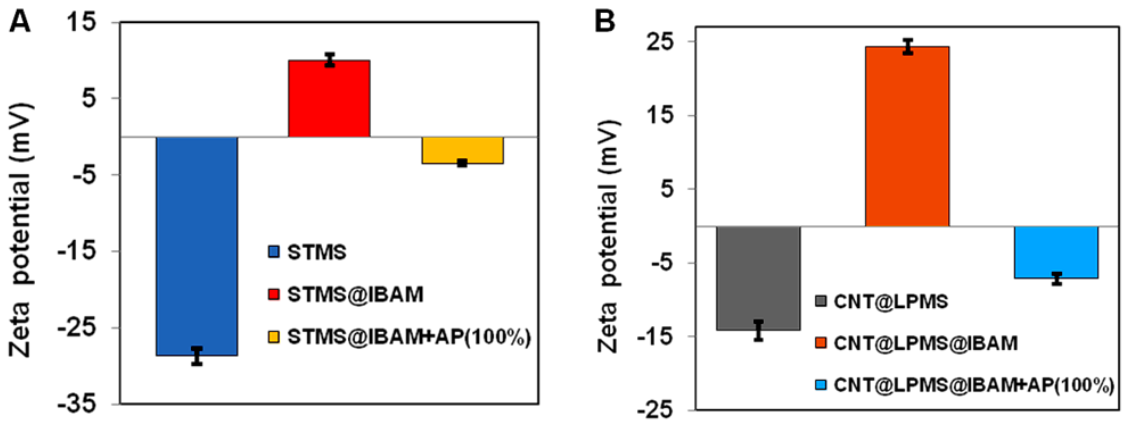

Fig.3-4 (A) Zeta potential of STMS, STMS@IBAM and STMS@IBAM+AP (100 wt%) in water (pH=6.5). (B) Zeta potential of CNT@LPMS, CNT@LPMS@IBAM and

CNT@LPMS@IBAM+AP (100 wt%) in water (pH = 6.5).

3.3.3 Immobilization of AP on functionalized composites

In order to study the ability and efficiency of the functionalized composites for enzyme immobilization, and to determine the maximum immobilization capacity, AP adsorption tests at various concentrations were investigated. The enzyme immobilization capacity q represents the mass of the adsorpted AP (mg) versus the mass of composite (mg), and the enzyme loading efficiency represents the mass of the absorbed AP versus the initial mass of AP introduced. AP was firstly labeled with fluorescent FITC for subsequent quantitative measurements. For the enzyme adsorption process, AP^{FITC} was first incubated with the composite under continuous stirring for 1 hour, then the AP-immobilized composites were separated by centrifugation. The supernatant was collected and measured after dilution with water by spectrofluorimetry. Thereafter, the mass of AP^{FITC} remaining in the supernatant (ie, AP^{FITC} that has not yet been adsorbed) could be determined using the calibration curve of AP^{FITC} (**S.3-3**), which allows us calculating the actual amount of adsorbed enzyme.

The immobilization and efficiency capacities of AP on the functionalized STMS@IBAM and CNT@LPMS@IBAM were traced as a function of the initial enzyme concentration and compared with the naked STMS and CNT@LPMS (**Fig.3-5**). The results show that for the naked STMS and CNT@LPMS, the immobilization capacities of AP increase with increasing initial enzyme concentration ranging from 0.1 to 4 mg/mL and reach maxima loading capacity at ca. 39 μg and 127 μg AP per mg of STMS and CNT@LPMS, respectively (at concentration of 1 mg/mL). Although the immobilization capacity increased with increasing AP concentration, the loading efficiency decreased as the AP concentration increased. It is worth noting that the maximum immobilization capacity and efficiency of AP on CNT@LPMS is much higher that of STMS, which probably benefits from the larger specific surface area of CNT@LPMS.

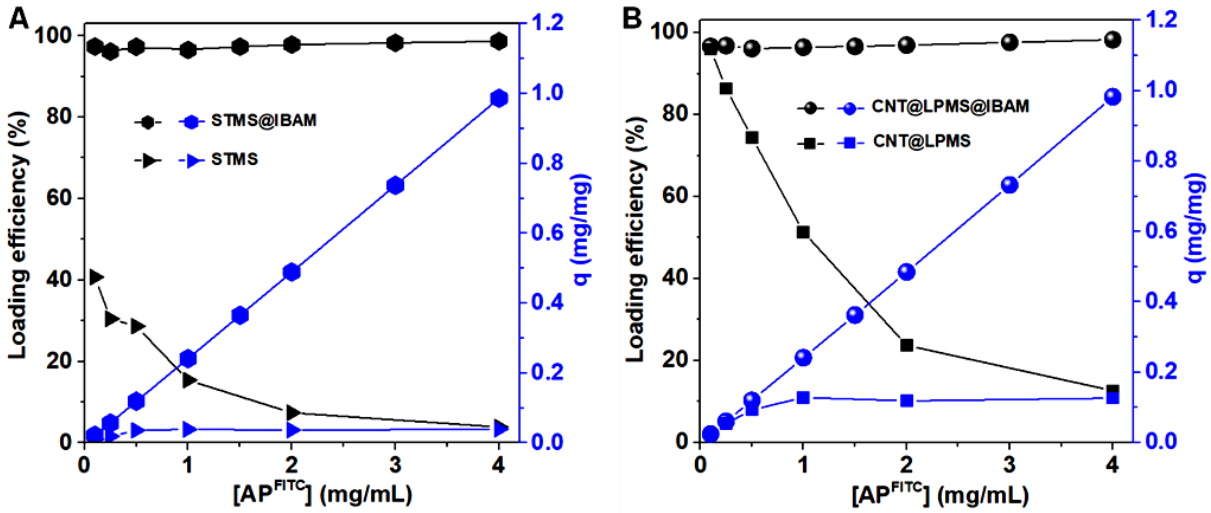

Fig.3-5 Enzyme immobilization capacity q (mg of AP adsorbed per mg of composite, blue curves) and loading efficiency (in %, black curves) on (A) STMS and STMS@IBAM, (B) CNT@LPMS and CNT@LPMS@IBAM, as a function of the initial enzyme concentration.

The immobilization capacity and loading efficiency of AP were then investigated on the functional STMS@IBAM and CNT@LPMS@IBAM composites as a function of the initial AP concentration of from 0.1 mg/mL to 4 mg/mL (increasing initial AP concentration up to 25 mg/mL are shown in **S.3-4**). The results (**Fig.3-5**) indicate that the immobilization capacities of AP on both STMS@IBAM and CNT@LPMS@IBAM composites are greatly improved and the maximum immobilization plateau was reached when at the concentration of AP 22 mg/mL. The photographs of different composites with different amounts of AP^{FITC} immobilized at various concentration show (**S.3-5**) that with the increase of AP^{FITC} adsorbed, the composites become more and more yellow. The maximum immobilization capacities of AP on the STMS@IBAM and CNT@LPMS@IBAM composites are calculated to be 4 mg and 4.3 mg of AP adsorbed per mg of STMS@IBAM and CNT@LPMS@IBAM composite (ie. 400 wt% and 430 wt%), respectively. The STMS@IBAM and CNT@LPMS@IBAM composites after AP adsorption were washed with water and then TGA measurements were performed to confirm the amount of immobilized AP. TGA profiles in **S.3-6** show that the amount of AP^{FITC} immobilized on the composite is consistent with the value obtained by fluorescence spectrometry.

The effect of the initial concentration of AP on the loading efficiency on STMS@IBAM and CNT@LPMS@IBAM indicates that the loading efficiency remains ca. 97% at the studied concentration below 8 mg/mL. A continuous decrease in the loading efficiency was observed with the continuous increase of the impregnation concentration of AP. Whatever their

concentrations, the immobilization capacities of AP on functionalized STMS@IBAM and CNT@LPMS@IBAM are far higher than in the case of naked STMS and CNT@LPMS. The high loading capacity of AP on the IBAM-modified composites could be attributed to the presence of non-covalent bonds of isobutyramide (IBAM), the high density of functional groups and the strong chemical bonding interactions with AP, which could provide abundant binding sites for the adsorption of AP.

After immobilization of AP, ZP measurements were performed on STMS@IBAM+AP(100 wt%) and CNT@LPMS@IBAM+AP(100 wt%) composites in water at pH 6.5 (**Fig.3-4**), and it was found that the ZP values changed from positive to slightly negative (–3.5±0.3 mV and –7.1±0.8 mV, respectively). The decrease in zeta potential value was likely due to the introduction of AP on the outer surface, which confirmed the effective immobilization of AP on the functionalized composites.

The resulting STMS@IBAM+AP nanocomposites were then imaged by TEM. It is observed from **Fig.3-6 A** that the grafting of IBAM resulted in obtaining silica particles with a rough surface. The TEM images of STMS@IBAM+AP composites in **Fig.3-6 B** and **C** reveal that due to the presence of the AP, dense and sticky organic matrix links were found on the surface of STMS. The yellow arrows highlight that the adsorbed AP acts like “glue” to connect the nearby NPs. As the AP loading capacity increases from 25 wt% to 100 wt%, these organic links between STMS becomes more apparent. The size distribution and colloidal stability of STMS@IBAM+AP systems with different amounts of AP was measured by DLS in water at pH 6.5, as shown in **S.3-7**. The results show that the hydrodynamic diameter of the IBAM-modified STMS determined by DLS is 164 nm (from TEM the mean size of STMS is ca. 90 nm), showing a monomodal dispersion of the IBAM-modified STMS. Meanwhile, the hydrodynamic diameter of the nanoparticles increases with the increasing immobilization amount of AP, which can be explained by the aggregation of the nanoparticles due to the enhanced interconnection among the silica NPs. The larger nanoparticle aggregates appeared when more AP was adsorbed on STMS@IBAM (200 wt% of AP), with a size of several microns.

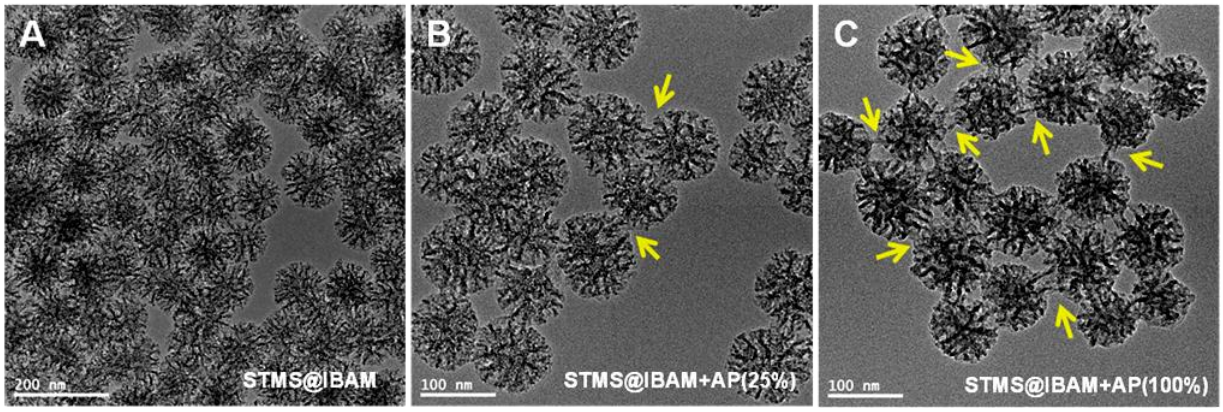

Fig.3-6 TEM images of (A) STMS@IBAM, (B) STMS@IBAM with 25 wt% AP immobilized and (C) STMS@IBAM with 100 wt% AP immobilized

3.3.4 Biocatalytic performance of the immobilized AP

The biological functionality of the immobilized enzyme was assessed by investigating the biocatalytic property of the AP loaded composites meaning their enzymatic activity to turn a molecular substrate to its product. The enzymatic activity measurements were performed using a conventional spectrophotometric method based on the ability of phosphatase enzymes to hydrolyse the p -Nitrophenyl phosphate disodium hexahydrate (pNPP-Na) into p-nitrophenol (pPN), a chromogenic product with a maximum absorbance at 405 nm. In the presence of AP, the hydrolysis of pNPP-Na substrate was quickly catalyzed to obtain the pPN with a yellow colour, which was recorded by the UV-visible spectrum. The auto-hydrolysis process of pNPP-Na (in the absence of AP) is extremely slow at room temperature (**S.3-8**), which is negligible. The mixture of AP-immobilized composites and substrate was directly subjected to UV visible spectrometry detection without centrifugation (the effect of the composites on the absorbance has shown to be negligible (**S.3-9**)).

In order to study the enzymatic activity of the immobilized AP, 2 mL of pNPP-Na (0.05 mg/mL in 50 mM $NaHCO_3$ buffer) was brought in contact with 2 µg of AP immobilized composites in water baths set at different temperatures: 25, 37 and 42 ℃ for 2 h. **Fig.3-7** shows the absorbance of the mixture versus time, revealing the conversion of pNPP-N into pPN catalyzed by the immobilized AP. The results show that under the temperature conditions studied, the absorbance of both mixtures with STMS@IBAM+AP(100 wt%) or CNT@LPMS@IBAM+AP(100 wt%) composite increased with the extension of the contact time, indicating that the immobilized AP continuously catalyzed the hydrolysis of pNPP-Na into the pPN product within 2 h. No conversion was observed in the absence of immobilized AP (Control). The highest activity of the immobilized enzyme was observed at the

temperature of 37 ℃ and 42 ℃. Similar results have been reported in other literature, showing that the the optimal enzymatic activity of AP is around 40 ℃.[43, 44] A faster catalytic effect was obtained when 5 μg of AP immobilized composites were used to catalyze the hydrolysis of pNPP-Na (**S.3-10**). Photographs of different amounts of immobilized AP catalyzed the hydrolysis of pNPP-Na to the yellow product pPN are showed in **S.3-11**.

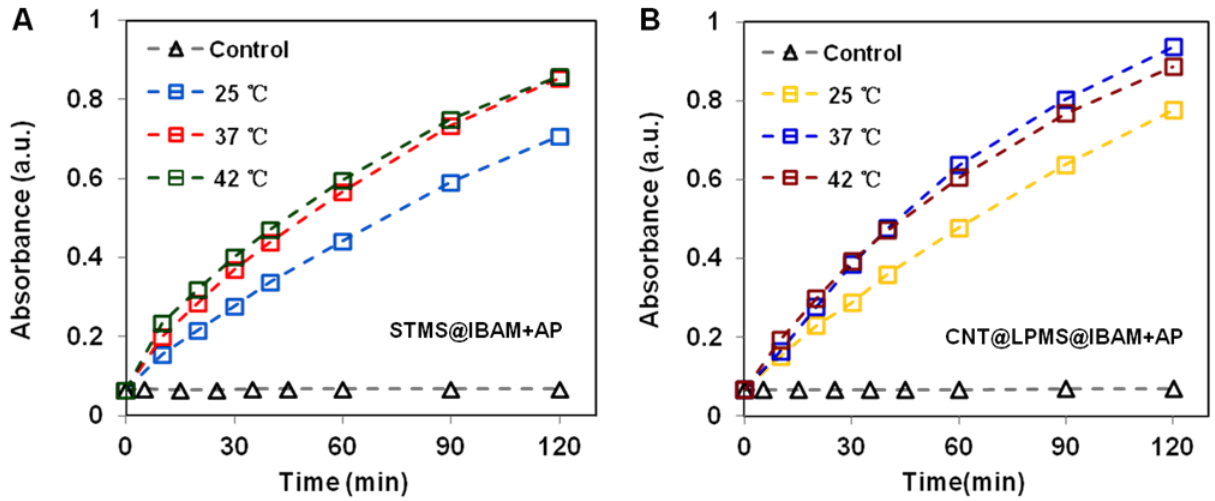

Fig.3-7 Absorbance of p-nitrophenol (pPN) as a function of time, converted from 2 mL of p-Nitrophenyl phosphate disodium hexahydrate (pNPP-Na) in the presence of 2 μg of: (A) STMS@IBAM+AP(100 wt%) and (B) CNT@LPMS@IBAM+AP(100 wt%). The absorbance was measured at λ= 405 nm by UV visible spectrometry.

3.3.5 Hydrogel formation and DOX release

In this paragraph, we describe the driven assembly of a peptide hydrogel mediated by the enzyme immobilized nanocomposites to yield a novel generation of nanocomposite hydrogel. The hybrid supramolecular hydrogel is prepared from the Fmoc-FF*p*Y tripeptide, which is dephosphorylated into Fmoc-FFY by the catalytic action of immobilized alkaline phosphatase (AP) (**Fig.3-8 A**). This mechanism induces the localized growth of self-assembled Fmoc-FFY peptide nanofibers from the silica surface of STMS and CNT@LPMS, leading to the formation of homogeneous hydrogels with fibrillary nanoarchitecture. The self-assembled peptide nanofibers are also cross-linked with the AP-immobilized STMS and CNT@LPMS as the intersection points. The drug-loaded hydrogel was prepared by pre-mixing the Fmoc-FF*p*Y peptide precursor solution and the anticancer drug doxorubicin aqueous solution to yield a suitable hydrogel system for drug delivery. The effect of temperature as a stimulus to release of DOX from the hydrogel system was then investigated, with the aim to establish a temperature-responsive hydrogel system for DOX delivery.

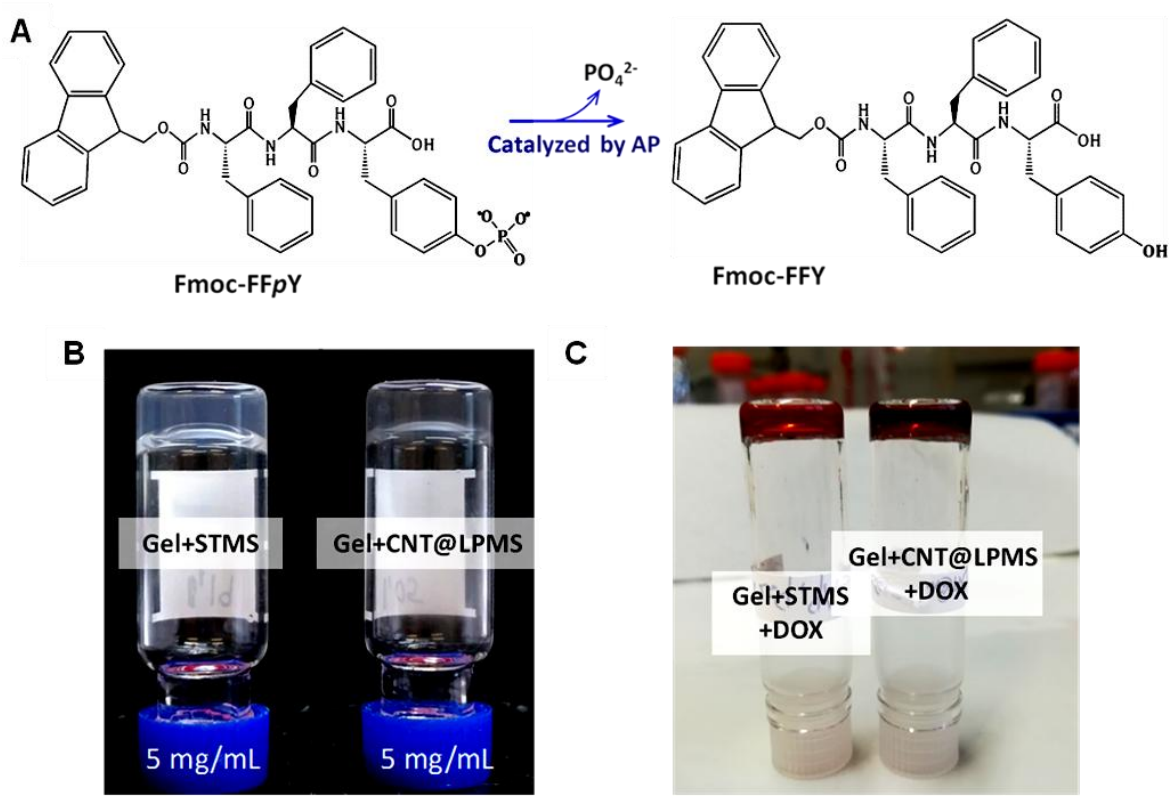

Fig.3-8 (A) Schematic diagram showing that Fmoc-FF*p*Y peptide is converted to Fmoc−FFY by the dephosphorylation of AP. Inverted tube tests of self-assembled hydrogels from AP-immobilized composites: (B) without DOX and (C) with DOX.

The Fmoc-FFY self-assembled hydrogels with and without DOX obtained from STMS@IBAM+AP (100 wt%) and CNT@LPMS@IBAM+AP(100 wt%) were obtained by mixing the AP-immobilized nanocomposites with Fmoc−FF*p*Y peptide. The concentrations of Fmoc-FF*p*Y, STMS@IBAM+AP or CNT@LPMS@IBAM+AP and DOX components in the hydrogel were set at 5 mg/mL, 0.1 mg/mL, and 0.5 mg/mL, respectively. Before the formation of the hydrogel, the mixture of AP-immobilized composites, DOX and Fmoc-FF*p*Y peptide showed a solution state (**S.3-12 A**). After contacting the AP-immobilized composites with Fmoc-FF*p*Y peptides at room temperature for 24 h, the gels were formed and test of inverted tubes was performed. As can be seen from **Fig.3-8 B**, homogeneous, opaque and dense hydrogels were obtained from these two AP-immobilized composites. The hydrogel containing CNT@LPMS appeared a dark gray color due to the blackness of CNTs. When in the presence of DOX, the resulting hydrogels appeared a uniform red color and adhered stably monolithic on the wall of the tubes (**Fig.3-8 C**), indicating that the DOX was uniformly distributed in the hydrogel. A dark red color was found on the hydrogel with CNT@LPMS composite.

The internal nanoarchitecture of the composite supramolecular hydrogel generated from AP immobilized composites STMS@IBAM+AP (100 wt%) and CNT@LPMS@IBAM+AP(100 wt%), as well as free AP (equivalent to the immobilized AP) were visualized by Cryo-SEM (**Fig.3-9**). The images confirmed the formation of nanofibrous architecture in all cases. Because AP is localized on STMS or CNT@LPMS through the IBAM's chemistry, the self-assembly process is initiated specifically from the surface of the nanoojects involved. The diameter of the self-assembled nanofibres is around ~15 nm, close to those observed when the hydrogel is formed using free AP. In addition, dark gray isolated STMS can be easily observed from Gel+STMS sample (**Fig.3-9 A-B**) because they are exclusively located at the nodes of the network, and the uniform and interweaved long nanofibers are distributed around the AP-immobilized STMS nanoparticles. Indeed, free STMS nanoparticles meaning not included in the fibrous network, are not observed. The AP-immobilized STMS acts as a cross-linking point in the 3D nanofibrous network, which suggests that the immobilized enzyme maintains good biocatalytic to convert Fmoc-FF*p*Y into Fmoc-FFY nanofibers. Similarly, cryo-SEM images taken from the composite supramolecular hydrogel formed from AP-immobilized CNT@LPMS (**Fig.3-9 C-D**), show equivalent fibrous network as the one observed with STMS@IBAM+AP or free AP. It can clearly observed that the self-assembled peptide nanofibres grew from the CNT@LPMS nanotubes and the CNT@LPMS are embedded within the fibrous network. For comparison, the hydrogel formed from free AP was prepared by directly mixing 5 mg/mL of Fmoc-FFpY and free AP (1 mg/mL), where the amount of free AP is the same as the immobilized AP on STMS and CNT@LPMS. The cryo-SEM images of the fibrous scaffold formed by free AP are shown in **Fig.3-9 E-F**, showing a homogeneous fibrillary structure. During the gelation process, Fmoc-FFpY is dephosphorylated by the free AP or immobilized AP on STMS and CNT@LPMS composites leading to the formation of Fmoc-FFY nanofibers, and the formed 3D networks of peptide nanofiber constructed the self-supporting homogeneous hydrogels. In the presence of STMS and CNT@LPMS composites, peptide nanofibers are guided by the immobilized AP generate from the surface of STMS and SNT@LPMS. The AP-immobilized STMS and CNT@LPMS composites play the role of cross-linking points within the nanofibrous hydrogel network, which has the potential to enhance the mechanical properties of the hydrogel network.

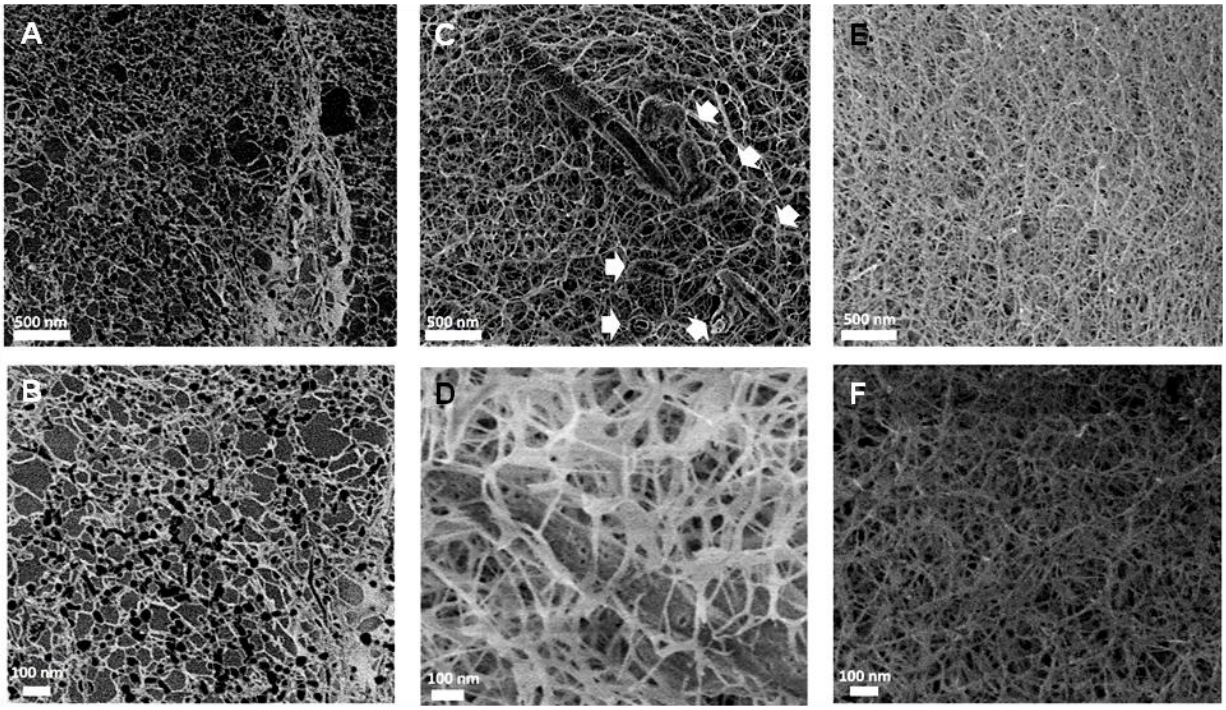

Fig.3-9 Typical Cryo-SEM images taken from supramolecular hydrogel prepared from: (A, B) STMS@IBAM+AP (100 wt%), (B, C) CNT@LPMS@IBAM+AP(100 wt%), and (E, F) free AP in the presence of the tripeptide Fmoc-FFpY. White arrows show CNT@LPMS perpendicular to the image section.

After the formation of hydrogel with DOX with a concentration of 0.5 mg/mL, 1 mL of water was added along the tube wall and the release of DOX was carried out at 25 ℃ and 42 ℃ for 24 h. After 24 h of treatment, the supernatant was removed and the amount of DOX released in the solution was detected by the UV-vis spectrometry, and calculated by the DOX calibration curve (**S.3-13**). **Fig.3-10 A** shows the release of DOX from hydrogels after 24 h of heating. In the case of the hydrogels treated at 25 ℃, only a small amount of DOX was released from the hydrogels after 24 h (ca. 3%). Conversely, the amount of DOX released from Gel+STMS+DOX and Gel+CNT@LPMS+DOX hydrogels was increased when the gels were heated at 42 ℃ for 24 h, with the release reaching 15.9% and 13.8%, respectively. The photographs (**Fig.3-10 B**) show the hydrogels before heating and a significant difference in contrast of the supernatants under different treatments.

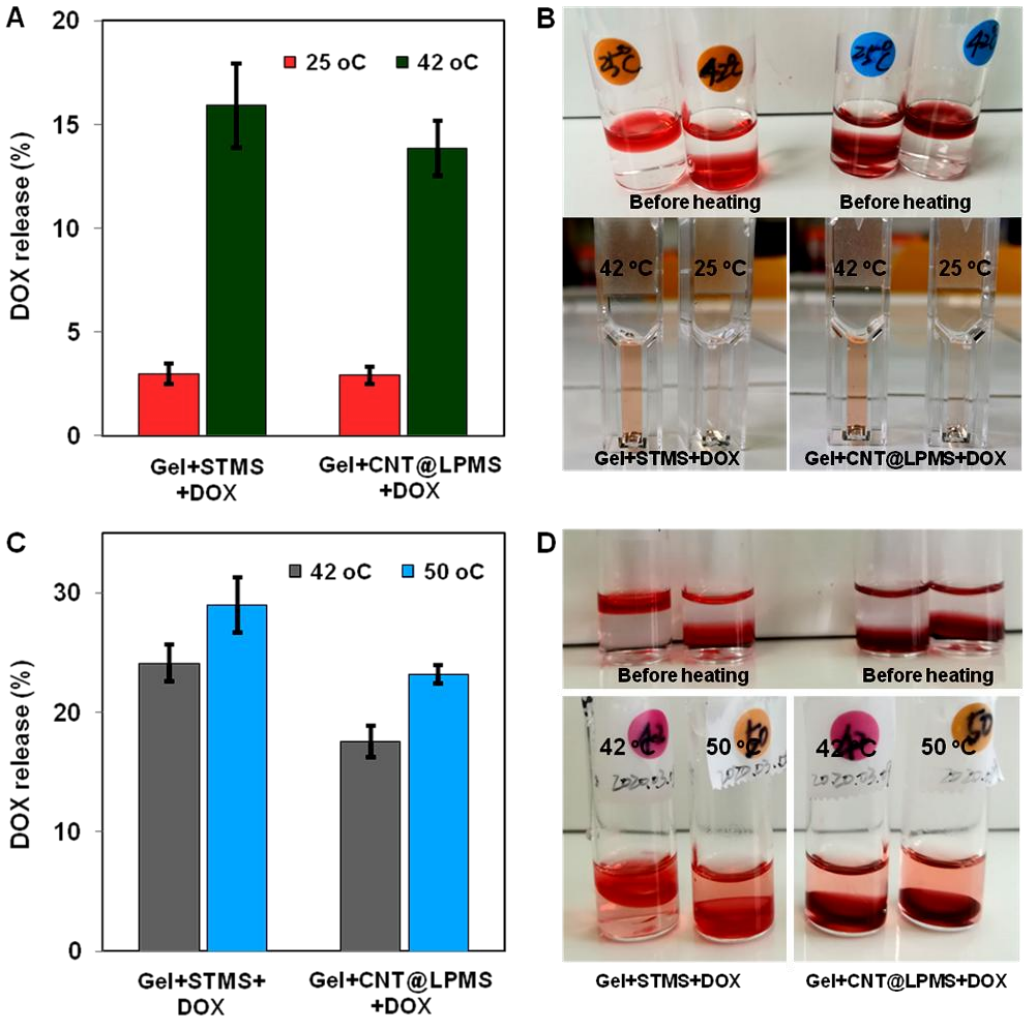

Fig.3-10 (A) DOX release from Gel+STMS+DOX and Gel+CNT@LPMS+DOX after heating at 25 ℃ and 42 ℃ for 24 h. (B) Photographs showing hydrogels before heating and DOX released into the aqueous solution after treated at 25 ℃ and 42 ℃ for 24 h. (C) DOX release from hydrogels after treated at 42 ℃ and 50 ℃ for 48 h. (D) Photographs showing hydrogels before heating and DOX released into the aqueous solution after treated at 42 ℃ and 50 ℃ for 48 h.

We then studied the drug release of these DOX-encapsulated hydrogels over a longer period of 48 hours at 42 ℃ and a higher stimulation temperature (50 ℃). The results are shown in **Fig.3-10 C**. As expected, we observed that the DOX-gel systems release more DOX over extended treatment time. The Gel+STMS+DOX and Gel+CNT@LPMS+DOX gel systems reached 24.1% and 17.6% of DOX release, respectively, at 42 ℃ over 48 h. When a higher stimulus temperature was applied (50 ℃), DOX release of 28.9% and 23.2% were obtained from the Gel+STMS+DOX and Gel+CNT@LPMS+DOX systems, respectively. Photographs in **Fig.3-10 D** show the hydrogels before heating and DOX released into the

aqueous solution after treated at 42 ℃ and 50 ℃ for 48 h. In addition, inverted tube tests for the hydrogels after heat treatment under the above conditions were performed. The result in **S.13 B-C** show that these hydrogels were somewhat damaged after treatment under 42 ℃ and 50 ℃, while the hydrogels treated at 25 ℃ stayed intact. The destroyed hydrogels with STMS@IBAM+AP or CNT@LPMS@IBAM+AP composites fell off from the bottom of the tube after being inverted, forming small pieces in the solution. These DOX-loaded hydrogel systems show great interest in releasing drugs in living systems and are expected to be used as biocompatible components of smart implantable systems.

The mechanical properties were determined by dynamic oscillatory rheology providing information about storage modulus (G') and loss modulus (G'') of studied hydrogels. G' is an indicator of the elastic behaviour of the material by measuring the ability to store deformation energy which can be recovered after removing the applied load. G'' measures the deformation energy that is dissipated as heat and friction during the shearing process. Strain sweeps from 0.1-100 % at a fixed frequency of 1 Hz were carried out in order to determine the linear viscoelastic region, defined as the region where the elastic modulus (G') and loss modulus (G") are parallel and independent of the strain amplitude. As shown in **Fig.3-11 A**, G' and G'' remained constant up to 10% of strain was applied and then decreased when strain was further increased. In order to get further insight on the elastic properties of the formed hydrogels, G' and G″ were measured as a function of frequency (0.01-10 Hz) and the results are depicted in **Fig.3-11 B**. The values of the elastic modulus were higher than the corresponding to the viscous modulus (G′ > G″) in all the frequency range indicating the gel-like behavior for all samples under study. At a frequency of 1 Hz and a stain of 1%, G' (**Fig.3-11 D**) (resp. G") of the bare gel (Gel) formed by dephosphorylation of Fmoc-FFpY peptide in contact with AP reached a value of 9.5 ± 2.5 Pa (resp. 2.0 ± 0.2 Pa). The formation of hydrogels by the action of AP immobilized on the surface of STMS@IBAM and CNT@LPMS@IBAM, resulting in the increase of elastic modulus up to 43.9 ± 2.7 Pa (resp. 6.3 ± 1.2 Pa) and 55.9 ± 7.5 Pa (resp. 10.0 ± 0.4 Pa), respectively. Functional STMS and CNT@LPMS composites, employed as supports for the grafting of AP and subsequently triggering gel formation, allow a larger number of immobilized enzymes were enriched on STMS and CNT@LPMS as interaction points for Fmoc-FF*p*Y peptide self-assembly to form the cross-linked fiber network, which gives rise to an increase of shear stiffness enhancing the mechanical properties of the self-assembled hydrogels. The increase in elastic modulus was even higher when DOX was introduced in those hydrogels, resulting in a value of 72.7 ± 1.3 Pa (resp. 7.9 ± 1.1 Pa) in the case of Gel+STMS+DOX and 75.8 ± 1.8 Pa (resp. 7.5 ± 0.4 Pa) for Gel+CNT@LPMS+DOX.

This phenomenon can be attributed to the fact that DOX is positively charged and could interact electrostatically with the phosphate groups of the peptide, Fmoc-FF*p*Y or the C-terminal carboxylate group of the self-assembled Fmoc-FFY fibres. Hydrogels containing DOX treated at 42 ℃ for 24 h were then characterized by rheological measurements (**Fig.3-11 C**), which helped to gain insight into the properties of the hydrogels after heat treatment. It is obviously seen that the G' of the heated hydrogels: Gel+STMS+DOX(T) and Gel+CNT@LPMS+DOX(T) were considerably lower than that of Gel+STMS+DOX and Gel+CNT@LPMS+DOX samples. Storage modulus G′ (resp. G") of heated hydrogels were measured to be 24.4 ± 0.3 Pa (resp. 5.4 ± 0.1 Pa) for Gel+STMS+DOX(T) and 31.5 ± 6.1 Pa (resp. 5.6 ± 0.2 Pa) for Gel+CNT@LPMS+DOX(T), which were highly reduced 66% and 58% respectively. The results indicate that the treatment of T (42 ℃) results in appreciable loss of the storage modulus of the hydrogels, which can be attributed to the hydrolytic cleavage of the assembly fibers.

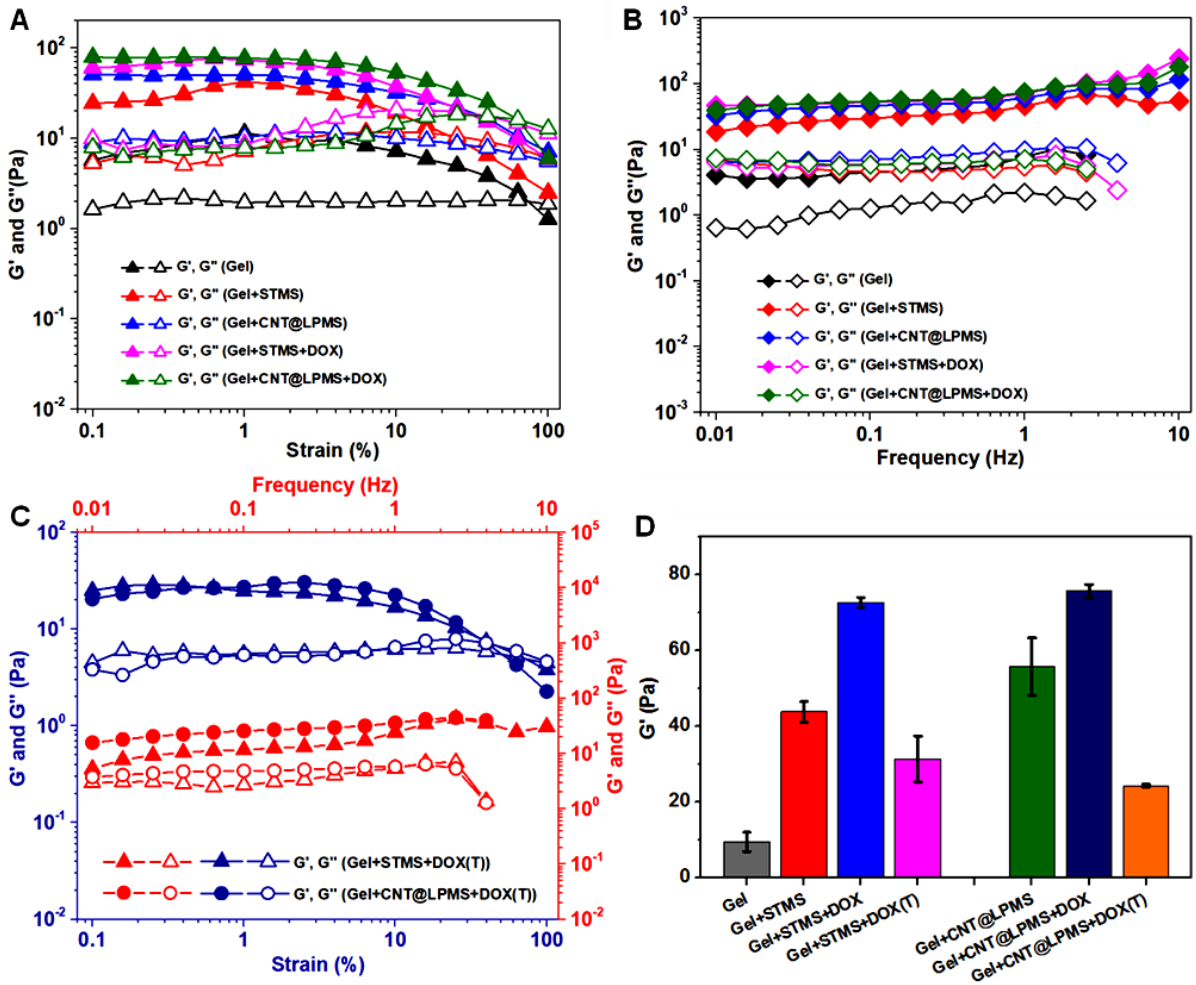

Fig.3-11 Storage modulus (G' –solid symbols) and loss modulus (G" – hollow symbols) of bare hydrogel (Gel), Gel+STMS, Gel+CNT@LPMS, Gel+STMS+DOX and

Gel+CNT@LPMS+DOX on: (A) strain sweeps and (B) frequency sweep. (C) G' (solid symbols) and G" (hollow symbols) of Gel+STMS+DOX(T) and Gel+CNT@LPMS+DOX(T) (after heating at 42 ℃ for 24 h) on strain sweeps (blue curves) and frequency sweep (red curves). (D) Storage modulus (G') at 1 Hz, 1% of the studied samples.

3.4 Conclusion

In summary, a facile strategy to trigger the self-assembly of a peptide hydrogel from enzyme-coated CNT@LPMS composites has been designed for thermal-induced drug delivery. Firstly, CNTs were coated with a homogeneous large pore mesoporous silica layer, making them particularly suitable for loading high MW biomolecules. It is found that an ultra-high AP loading capacity (up to 400 wt%) was achieved within the porous with the IBAM binders grafted on the silica surface. The excellent AP loading capacity of CNT@LPMS@IBAM composites enabled them to act as initiators of the peptide self-assembly and cross-linking points of the resulting nanocomposite supramolecular hydrogel, allowing local growth of peptide self-assembled nanofibers architecture from the silica surface. In addtion, the self-assembly of peptide hydrogel on AP-immobilized carbon-free silica NPs (STMS) with similar pore sizes was also performed, demonstrating the versatility of this surface engineering approach. Furthermore, significant DOX release from these hydrogels was obtained when the DOX-loaed hydrogels were submitted to external high temperature (42 ℃) stimulation. Rheological studies showed that the elastic modulus of these hydrogels increased with the introduction of DOX, while the storage modulus decreased significantly after T (42 ℃) treatment, indicating that the mechanical properties of hydrogels changed after T stimulation and led to the release of DOX. The above results indicate that this nanocomposite supramolecular hydrogels assembled from enzyme-coated large pore mesoporous materials can be used as T-induced thermally responsive controlled release nanoplatforms. The association of CNT@LPMS nanocomposites and self-assembled peptide supramolecular hydrogel as scaffold is an innovative strategy, which is expected to be used to develop a new generation of stimuli-responsive drug delivery systems suitable for the biomedical applications.

3.5 References

1. M. A. C. Stuart, W. T. S. Huck, J. Genzer, M. Müller, C. Ober, M. Stamm, G. B. Sukhorukov, I. Szleifer, V. V. Tsukruk, M. Urban, F. Winnik, S. Zauscher, I. Luzinov and S. Minko, *Nat. Mater.*, 2010, **9**, 101-113.
2. D. Roy, J. N. Cambre and B. S. Sumerlin, *Prog. Polym. Sci.*, 2010, **35**, 278-301.
3. F. Alvia, M. K. Ramc, P. A. Basnayakab, E. Stefanakosa, Y. Goswamid and A. Kumar, *Electrochimica Acta*, 2011, **56**, 9406-9412.
4. V. K. Thakur and M. R. Kessler, *Polymer*, 2015, **69**, 369-383.
5. A. Döring, W. Birnbaum and D. Kuckling, *Chem. Soc. Rev.*, 2013, **42**, 7391-7420.
6. Alamusi, N. Hu, H. Fukunaga, S. Atobe, Y. Liu and J. Li, *Sensors*, 2011, **11**, 10691-10723.
7. S. Merino, C. Martın, K. Kostarelos, M. Prato and E. Vázquez, *ACS Nano*, 2015, **9**, 4686-4697.
8. A. A. Adedoyin and A. K. Ekenseair, *Nano Res.*, 2018, **11**, 5049-5064.
9. D. Mertz, S. Harlepp, J. Goetz, D. Bégin, G. Schlatter, S. Bégin-Colin and A. Hébraud, *Adv. Therap.*, 2019, **3**, 1900143.
10. P. M. Bendix, S. N. S. Reihani and L. B. Oddershede, *ACS Nano*, 2010, **4**, 2256-2262.
11. E. C. Dreaden, A. M. Alkilany, X. Huang, C. J. Murphy and M. A. El-Sayed, *Chem. Soc. Rev.*, 2012, **41**, 2740-2779.
12. E. A. Périgo, G. Hemery, O. Sandre, D. Ortega, E. Garaio, F. Plazaola and F. J. Teran, *Appl. Phys. Rev.*, 2015, **2**, 041302.
13. D. Mertz, O. Sandre and S. Bégin-Colin, *Biochim. Biophys Acta*, 2017, **1861**, 1617-1641.
14. S. Dutz and R. Hergt, *Nanotechnology*, 2014, **25**, 452001.
15. A. K. Geim and K. S. Novoselov, *Nat. Mater.*, 2007, **6**, 183–191.
16. H. Dai, *Acc. Chem. Res.*, 2002, **35**, 1035-1044.
17. K. Kostarelos, A. Bianco and M. Prato, *Nat. Nanotechnol*, 2009, **4**, 627-633.
18. A. Bianco, K. Kostarelos, C. D. Partidos and M. Prato, *Chem. Commun.*, 2005, 571-577.
19. Z. Liu, X. Sun, N. Nakayama-Ratchford and H. Dai, *ACS Nano*, 2007, **1**, 50-56.
20. C. Samorì, H. Ali-Boucetta, R. Sainz, C. Guo, F. M. Toma, C. Fabbro, T. d. Ros, M. Prato, K. Kostarelos and A. Bianco, *Chem. Commun.*, 2010, **46**, 1494-1496.
21. M. Zhang, X. Zhang, X. He, L. Chen and Y. Zhang, *Mater. Lett.*, 2010, **64**, 1383-1386.
22. S. W. Bian, Z. Ma, L. S. Zhang, F. Niu and W. G. Song, *Chem. Commun.*, 2009, 1261-1263.

23. C. Wells, O. Vollin-Bringel, V. Fiegel, S. Harlepp, B. V. d. Schueren, S. Bégin-Colin, D. Bégin and D. Mertz, *Adv. Funct. Mater.*, 2018, **28**, 1706996.
24. Z. Li, J. C. Barnes, A. Bosoy, J. F. Stoddartbc and J. I. Zink, *Chem. Soc. Rev.*, 2012, **41**, 2590-2605.
25. S. H. Wu, C. Y. Mou and H. P. Lin, *Chem. Soc. Rev.*, 2013, **42**, 3862-3875.
26. P. Yang, S. Gai and J. Lin, *Chem. Soc. Rev.*, 2012, **41**, 3679-3698.
27. N. Ž. Knežević and J.-O. Durand, *Nanoscale*, 2015, **7**, 2199-2209.
28. R. J. Chen, Y. Zhang, D. Wang and H. Dai, *J. Am. Chem. Soc.*, 2001, **123**, 3838-3839.
29. K. Besteman, J.-O. Lee, F. G. M. Wiertz, H. A. Heering and C. Dekker, *Nano Lett.*, 2003, **3**, 727-730.
30. C. Vigier‐Carrière, F. Boulmedais, P. Schaaf and L. Jierry, *Angew. Chem. Int. Ed.*, 2018, **57**, 1448-1456.
31. M. P. Conte, J. K. Sahoo, Y. M. Abul-Haija, K. H. A. Lau and R. V. Ulijn, *ACS Appl. Mater. Interfaces*, 2018, **10**, 3069-3075.
32. C. Wu, W. Hu, Q. Wei, L. Qiao, Y. Gao, Y. Lv, M. Liu, C. Li, X. Wang and Q. Wang, *J. Biomed. Nanotechnol.*, 2018, **14**, 354-361.
33. M. Criado-Gonzalez, J. R. Fores, A. Carvalho, C. Blanck, M. Schmutz, Leyla Kocgozlu, P. Schaaf, L. Jierry and F. Boulmedais, *Langmuir : the ACS journal of surfaces and colloids*, 2019, **35**, 10838-10845.
34. Z. Yang, H. Gu, D. Fu, P. Gao, J. K. Lam and B. Xu, *Adv. Mater.*, 2004, **16**, 1440-1444.
35. M. Criado-Gonzalez, M. Schmutz, L. Jierry, M. H. Iqbal, P. Schaaf and F. Boulmedais, *Front. Bioeng. Biotechnol.*, 2020, **8**, 938.
36. D. Mertz, C. Affolter-Zbaraszczuk, J. Barthès, J. Cui, F. Caruso, T. F. Baumert, J.-C. Voegel, J. Ogier and F. Meyer, *Nanoscale*, 2014, **6**, 11676-11680.
37. F. Perton, S. Harlepp, G. Follain, K. Parkhomenkoc, J. G. Goetz, S. Bégin-Colin and D. Mertz, *J. Colloid Interf. Sci.*, 2019, **542**, 469-482.
38. M. Ménard, F. Meyer, C. Affolter-Zbaraszczuk, M. Rabineau, A. Adam, P. D. Ramirez, S. Bégin-Colin and D. Mertz, *Nanotechnology*, 2019, **30**, 174001.
39. V. Fiegel, S. Harlepp, S. Begin-Colin, D. Begin and D. Mertz, *Chem. Eur.J.*, 2018, **24**, 4662-4670.
40. D. Mertz, J. Cui, Y. Yan, G. Devlin, C. Chaubaroux, A. Dochter, R. Alles, P. Lavalle, J. C. Voegel, A. Blencowe, P. Auffinger and F. Caruso, *ACS Nano*, 2012, **6**, 7584-7594.
41. D. Mertz, P. Tan, Y. Wang, T. K. Goh, A. Blencowe and F. Caruso, *Adv. Mater.*, 2011, **23**, 5668-5673.

42. C. Vigier‐Carrière, T. Garnier, D. Wagner, P. Lavalle, M. Rabineau, J. Hemmerlé, B. Senger, P. Schaaf, F. Boulmedais and L. Jierry, *Angew. Chem. Int. Ed.*, 2015, **127**, 10336-10339.
43. H. T. Wu, D. M. Li, J. H. Cheng, Y. Yang, Y. K. Song, B. W. Zhu, J. J. Sun, F. L. Wang and C. X. Yu, *Fish. Sci.*, 2013, **79**, 477-485.
44. D. H. Lee, S. L. Choi, E. Rha, S. J. Kim, S. J. Yeom, J. H. Moon and S. G. Lee, *BMC Biotechnol.*, 2015, **15**, 1.

3.6 Supporting information

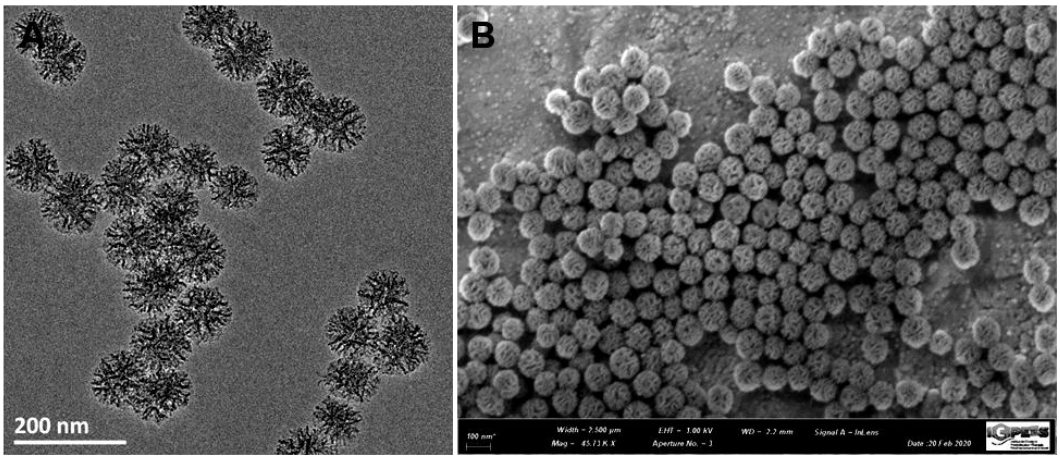

S.3-1 (A) TEM and (B) SEM images of STMS

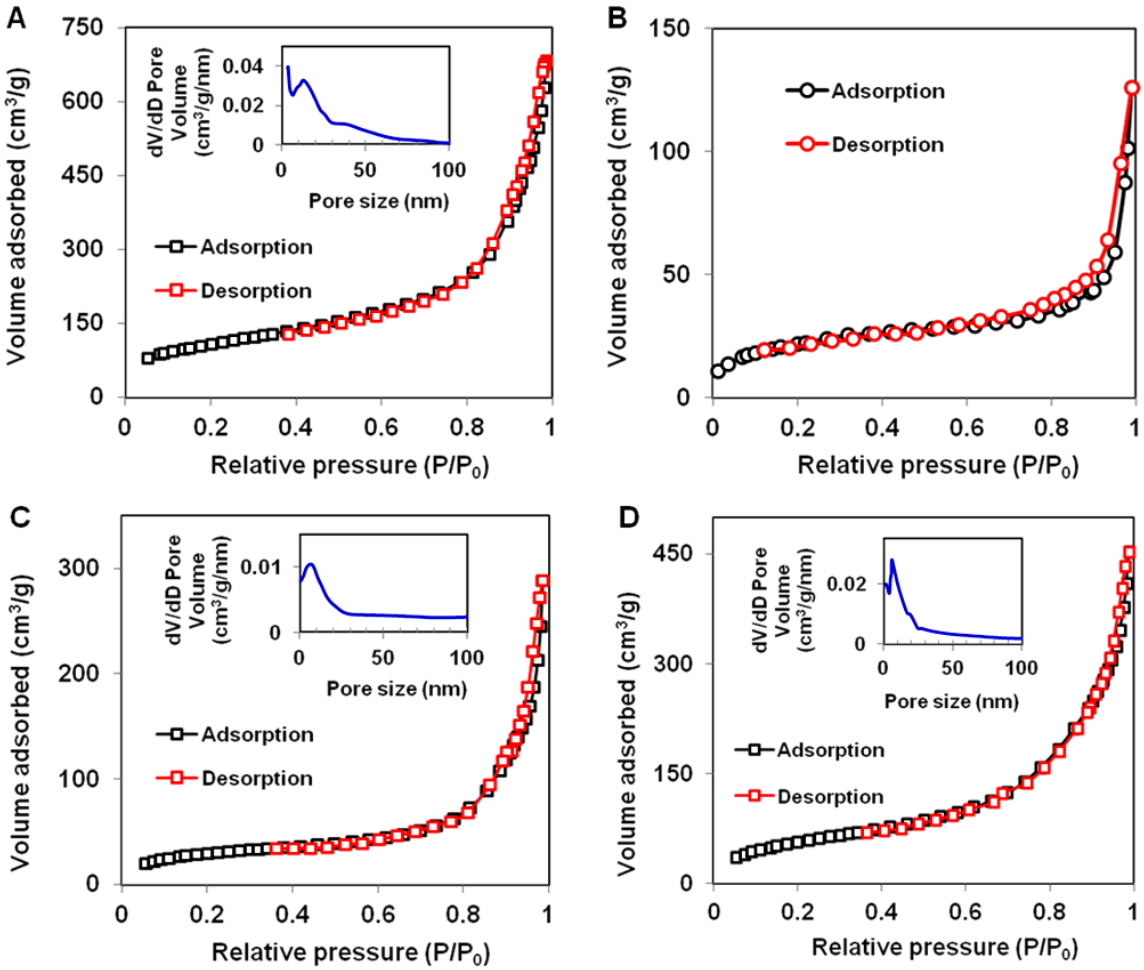

S.3-2 N_2 adsorption-desorption isotherm associated with the pore size distribution of (A) STMS, (B) pristine CNTs, (C) STMS@IBAM and (D) CNT@LPMS@IBAM

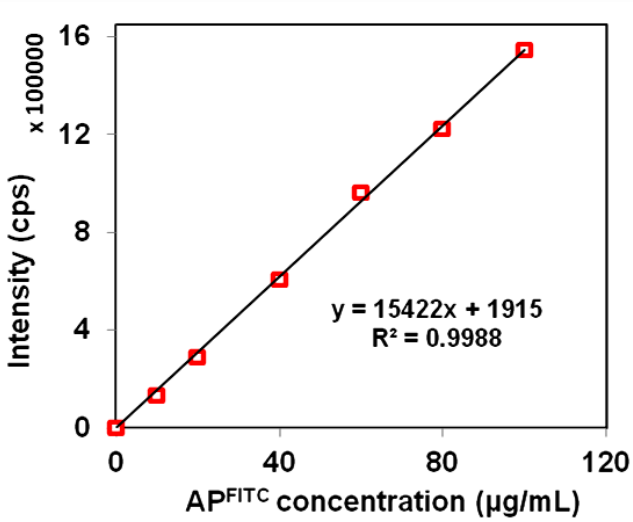

S.3-3 Calibration curve of AP^{FITC} in water representing fluorescence intensity at 520 nm *vs* [AP^{FITC}] by spectrofluorimetry

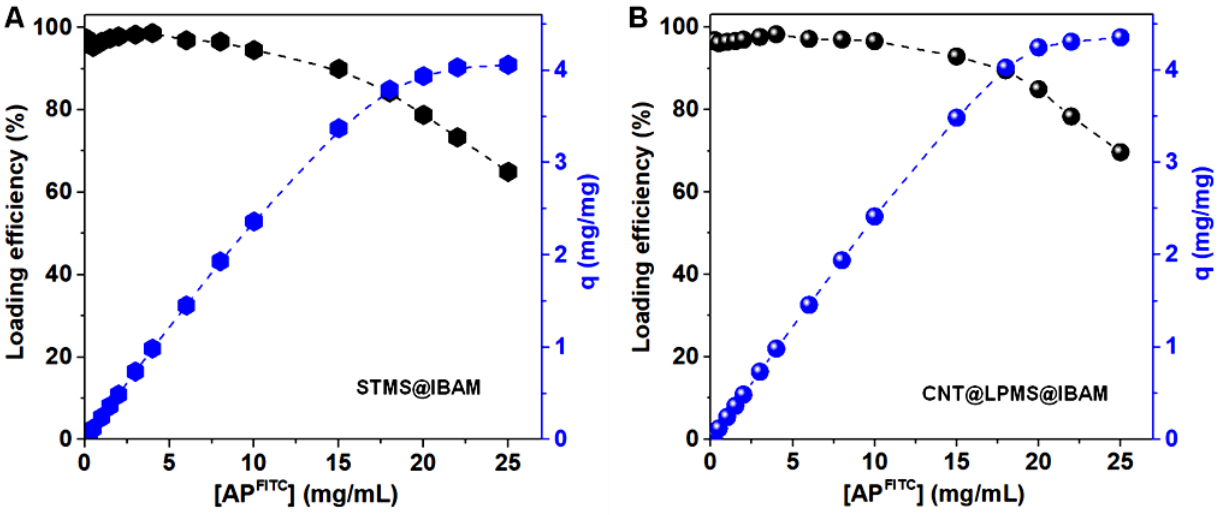

S.3-4 Enzyme immobilization capacity q (mg of AP adsorbed per mg of composite, blue curves) and loading efficiency (in %, black curves) on (A) STMS@IBAM and (B) CNT@LPMS@IBAM composites, as a function of the initial enzyme concentration.

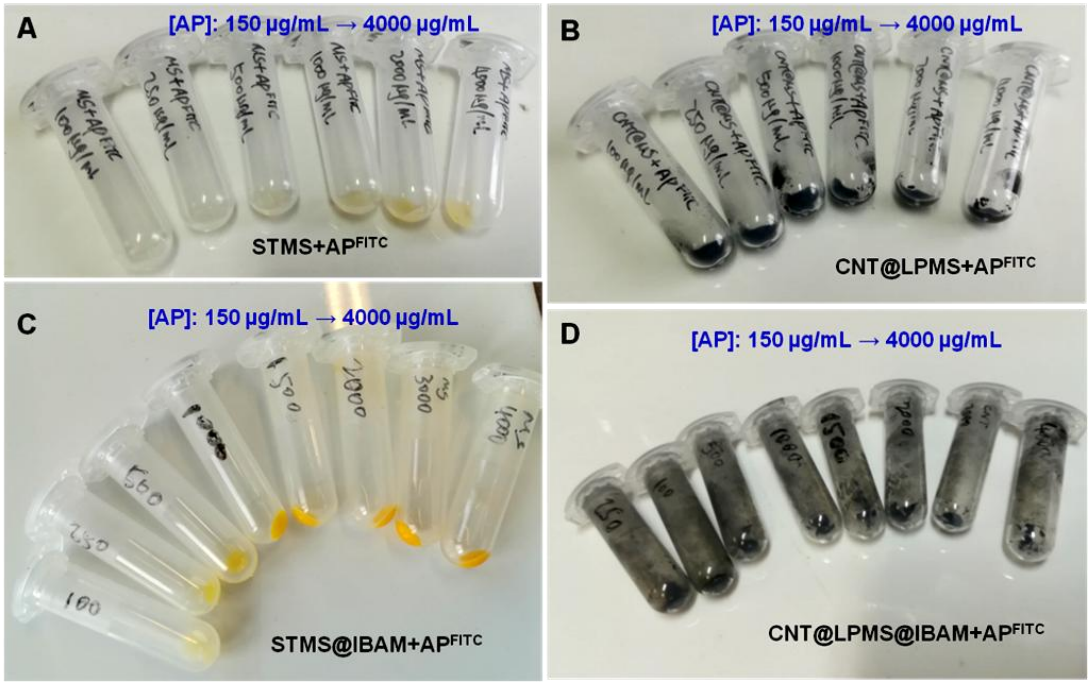

S.3-5 Photographs of (A) STMS+AP^{FITC}, (B) CNT@LPMS+AP^{FITC}, (C) STMS@IBAM+AP^{FITC} and (D) CNT@LPMS@IBAM+AP^{FITC} with different amount of AP^{FITC} immobilized at various concentrations

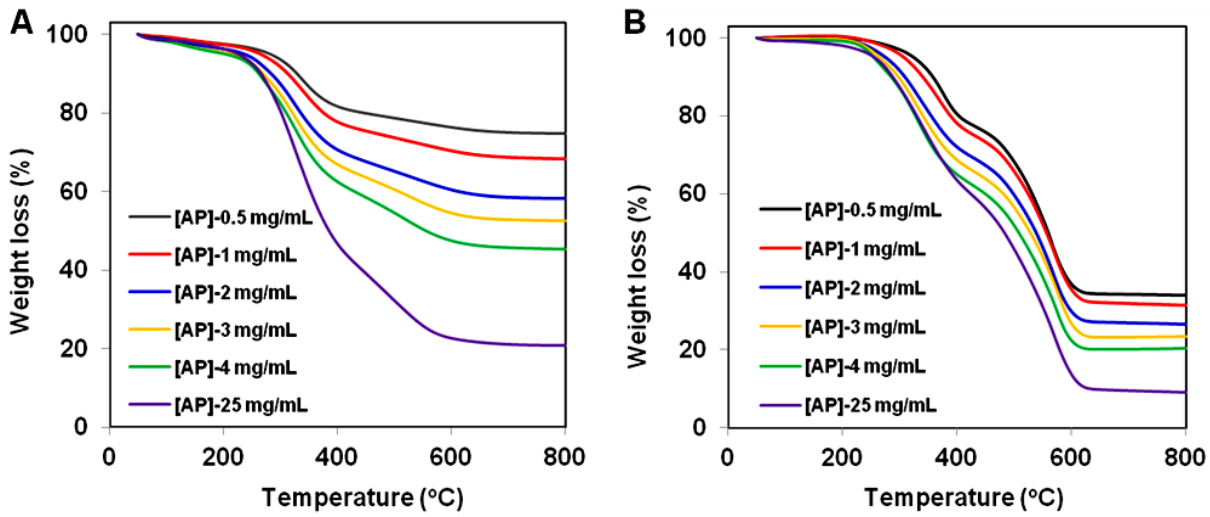

S.3-6 TGA profiles of (A) STMS@IBAM and (B) CNT@LPMS@IBAM immobilized with different amount of AP^{FITC} at different initial concentrations

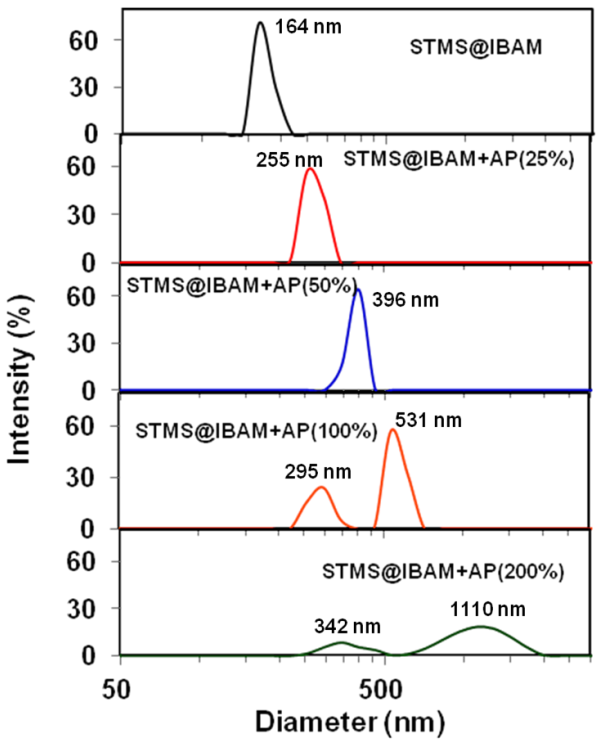

S.3-7 DLS size distributions of STMS and STMS@IBAM+AP with different amounts of AP immobilized in water (pH = 6.5).

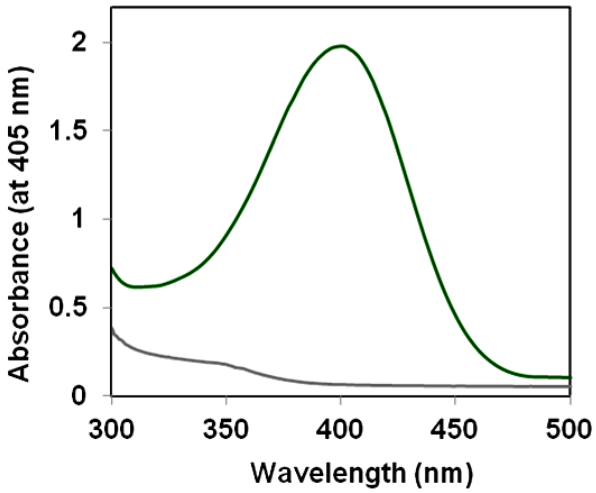

S.3-8 The UV visible spectra of pNPP-Na solution in the absence of immobilized AP (grey) and in the presence of immobilized AP (green) after 24 h at room temperature

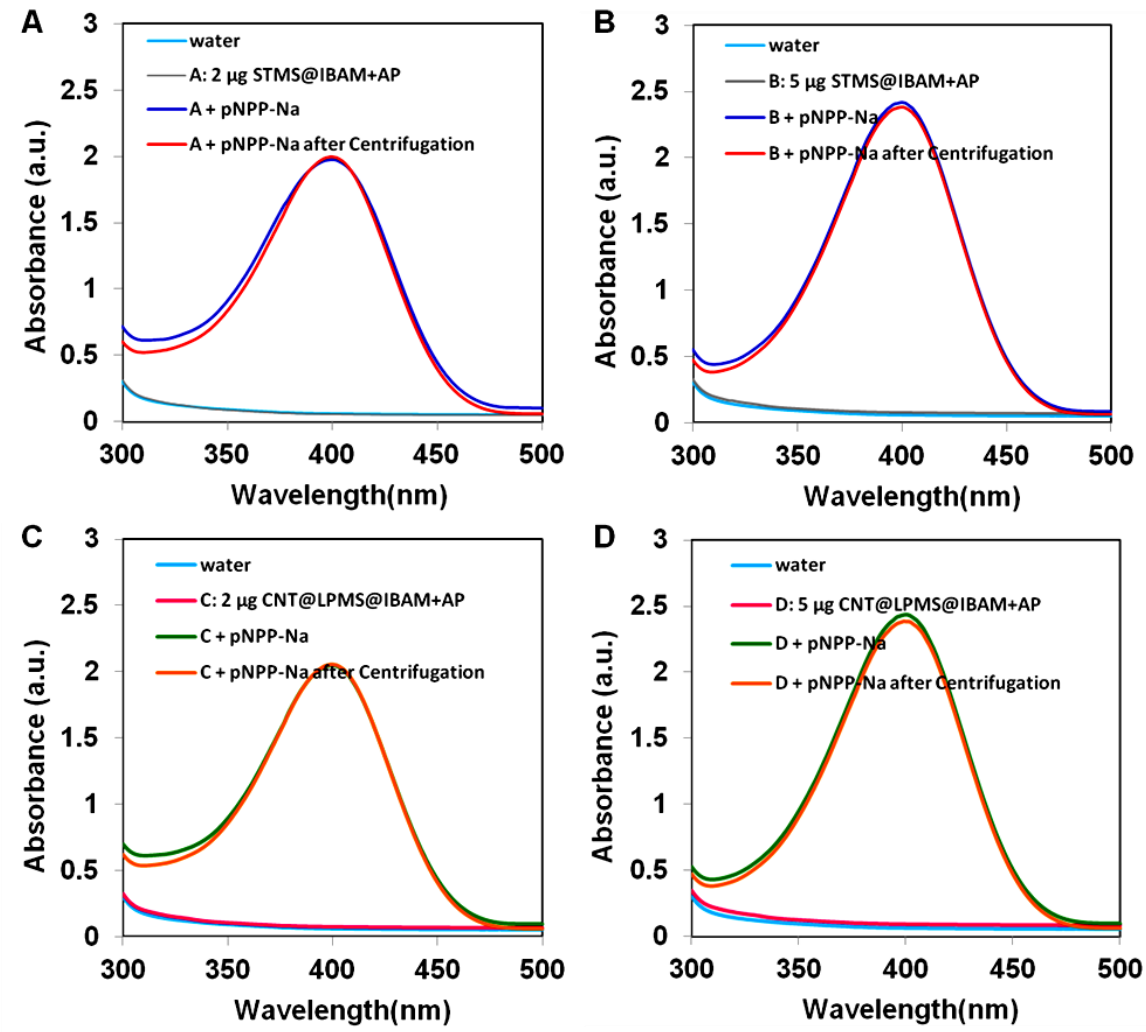

S.3-9 The UV visible spectra of 2 mL of pNPP-Na solution after 24 h of contact with STMS@IBAM+AP (100 wt%) and CNT@LPMS@IBAM+AP (100 wt%). The results show that the existence of 2 µg and 5 µg STMS@IBAM+AP or CNT@LPMS@IBAM+AP hardly changed the maximum absorbance of the solution, which was almost the same as the absorbance of the solution after removing the composites by centrifugation.

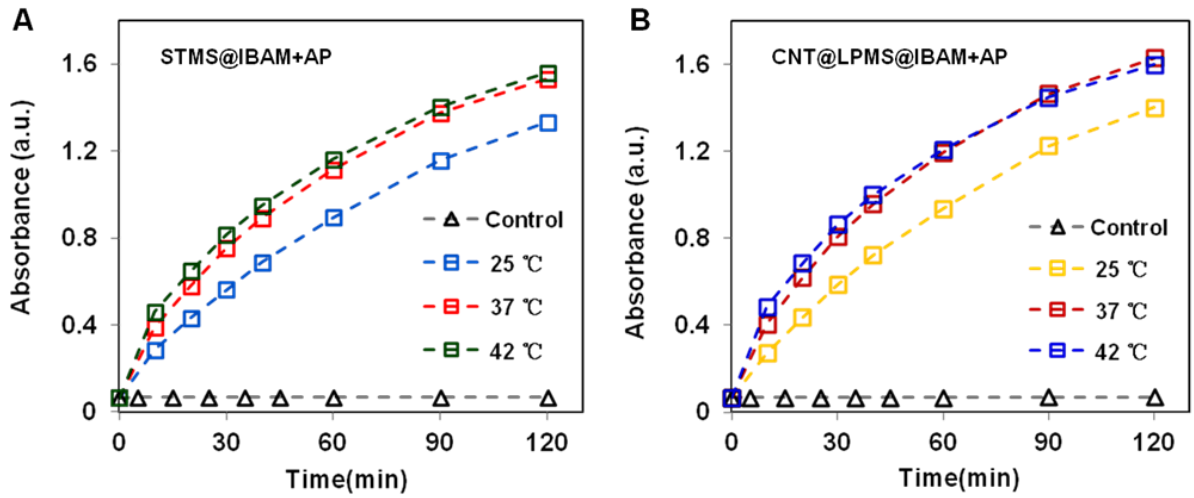

S.3-10 The absorbance of p-nitrophenol (pPN) as a function of time, converted from 2 mL of p-Nitrophenyl phosphate disodium hexahydrate (pNPP-Na) in the presence of 5 µg of (A) STMS@IBAM+AP(100 wt%) and (B) CNT@LPMS@IBAM+AP(100 wt%). The absorbance was measured at λ= 405 nm by UV visible spectrometry

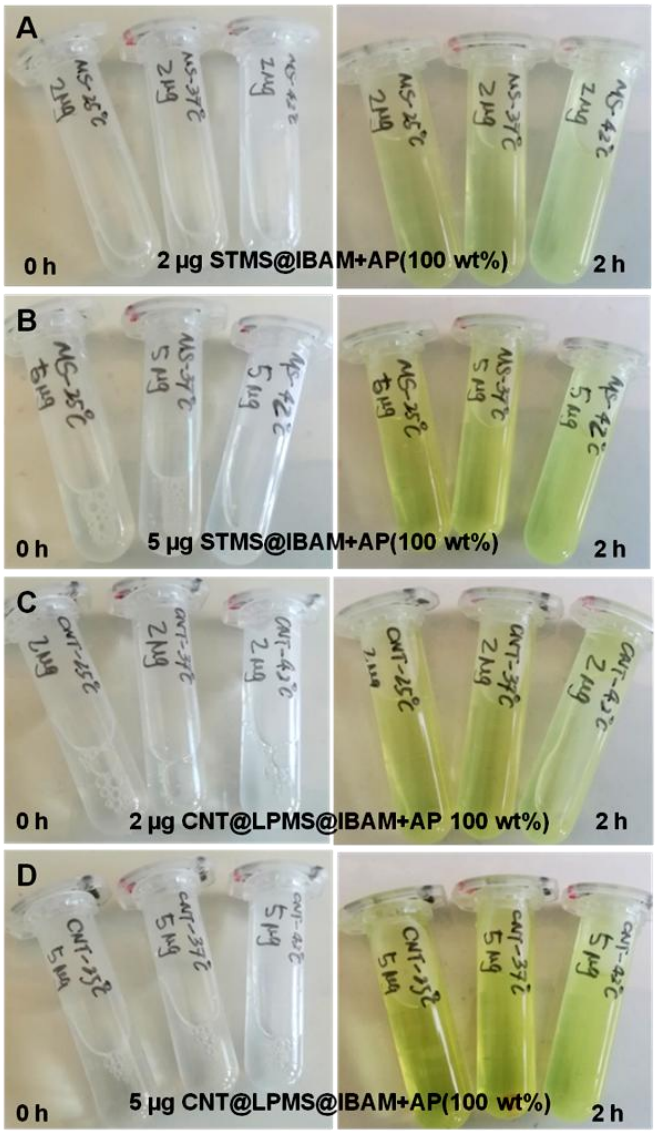

S.3-11 Photographs show that different amounts of immobilized AP catalyzed the hydrolysis of pNPP-Na to the yellow product pPN

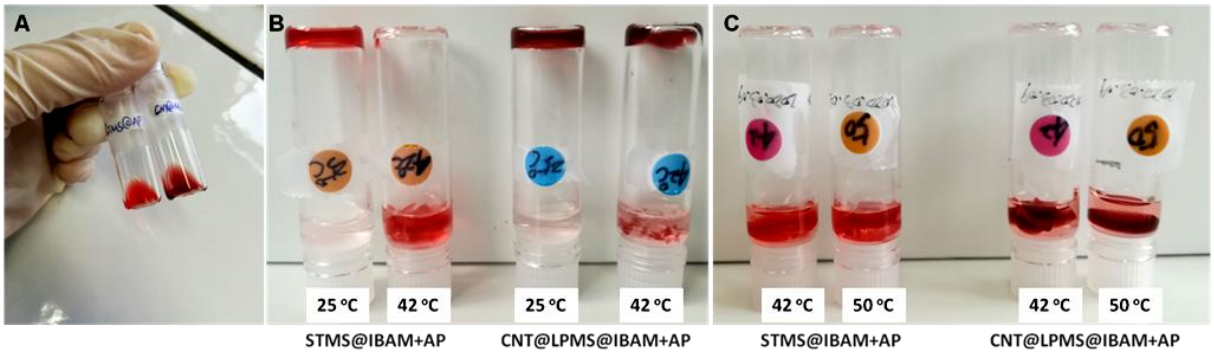

S.3-12 (A) The mixture of AP-immobilized composite, DOX and Fmoc-PP*p*Y peptide before gel formation. Inverted tube tests for the hydrogels after treated (B) at 25 and 42 ℃ for 24 h and (C) at 42 and 50 ℃ for 48 h

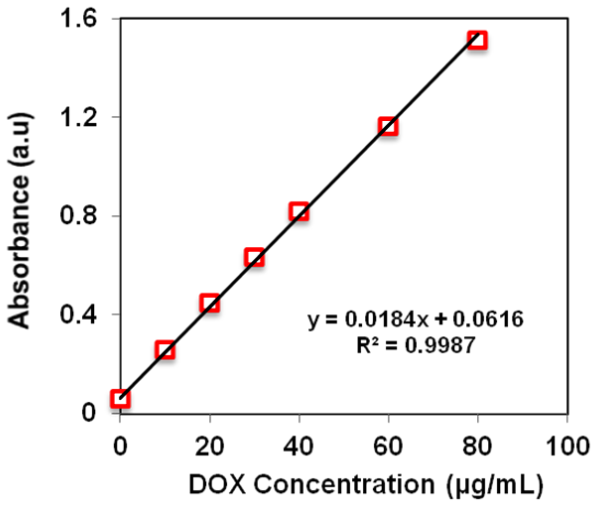

S.3-13 Calibration curve of DOX in water representing the maximum absorbance at 480 nm vs [DOX] by UV visible spectrophotometry

Chapter 4 Electrospun nanofiber composite scaffolds incorporated with carbon nanotubes@mesoporous silica: fabrication, properties and biological evaluation

Abstract

The biocompatible alginate and polylactic acid (PLA) hybrid nanofiber scaffolds are fabricated through electrospinning technique, in which mesoporous silica shell coated-CNTs (CNT@MS) were incorporated. Detailed optimizations were made to produce continuous and uniform nanofibers without beads or drops. The topographical features and the distribution of CNT@MS composites in nanofiber are observed by SEM. The tensile mechanical properties of the manufactured fibrous membranes are then investigated to comfirm that CNT@MS composites play a role in improving the mechanical properties of the electrospun scaffolds. The synthesized hybrid CNT@MS-incorporated alginate and PLA platforms are further shown to photothermal performance under NIR laser irradiation. Finally, in vitro biological evaluation of the CNT@MS-incorporated alginate and PLA nanofiber scaffolds was investigated to study the potential use of these electrospun nanofibrous systems as substrates for cell/tissue culture. It is expected that these CNT@MS-incorporated alginate and PLA electrospun nanofiber mats can be used as potential scaffolds for tissue engineering.

Keywords:

Carbon nanotubes, Mesoporous silica, Electrospinning technique, Nanofibous scaffold, Biolodical evaluation

4.1 Introduction

Over the years, tissue engineering has been regarded as a promising area allowing for the foreseen high advances for the regeneration of human tissues and organs, which has attracted widespread attention.[1-4] The design and manufacture of bioactive scaffolds plays a key role in the tissue engineering process because they must have the ability to provide physical environment and mechanical support for cell growth, to guide the cell growth, allow cells to produce their own extracellular matrix (ECM), and promote the formation of new functional tissues.[5-7] Polymers have a long history of being used as biomaterials for the fabrication of medical devices and tissue engineering scaffolds. They can potentially mimic many functions of the native ECM that induce synthesis of tissues and organs.[8, 9] Biomimetic polymer scaffolds, ranging from natural biopolymers to synthetic polymers, can be used as a matrix for tissue regeneration or as an implant for cell transplantation.[10-12] They have been shown to achieve many specific functions, such as allowing the transportation of nutrients and diffusion of active components[13, 14], regulating cell adhesion and migration[15, 16] and directing specific cellular functions and responses[17, 18].

Carbon nanotubes (CNTs) possess many promising physical and chemical properties and have been widely explored in the field of tissue engineering.[19-21] They exhibit high strength, elasticity and fatigue resistance properties, and are excellent candidates for reinforcement material in bone tissue engineering scaffolds.[22, 23] Moreover, CNTs show strong optical absorption from visible light to NIR region and convert it into local heat, which can be used as a stimulus to remotely control and induce the release of bioactive agents (such as growth factors) to elicit favorable cellular behavior.[24] The nanoscale characteristics of CNTs are also essential for regulating cell hierarchy level behaviors.[25] However, CNTs are difficult to uniformly disperse in solvent due to their easy agglomeration nature and this effect is reported to promote cytotoxicity and greatly limits their applications.[26-28] Therefore, for their applications in the biomedical field, many strategies have been reported for the surface functionalization of CNTs to improve their biocompatibility and dispersibility.[29, 30] The coating of mesoporous silica (MS) shell on CNTs has been reported in our previous work, which could effectively generate a highly biocompatible and hydrophilic MS layer to facilitate the dispersion of CNTs in liquid medium.[31, 32] The MS shell of CNTs also offers many other outstanding properties, such as stable porous structure, large specific surface area, tunable pore size, and easy-to-modify surface, providing more possibilities for the application of CNTs in tissue engineering.[33, 34]

On the other hand, considering the potential applications where the release of CNTs may be harmful, it is necessary to incorporate nanoscale structured CNTs inside or bond to a macroscopic level matrix. Currently, one area under active research is to embed CNTs within a polymer matrix that is very suitable as tissue scaffolds.[35] While reducing the potential toxicity of CNTs, it can also reinforce conventional polymer with enhanced physical properties. Polymer/CNTs composites have been synthesized through a variety of manufacturing methods, such as melt-mixing techniques[36], shear mixing[37], in-situ polymerization[38], and physical vapor deposition (PVD)[39]. Deka et al. prepared a hyperbranched polyurethane (HBPU)/MWCNTs composite by in situ technique, which displayed enhanced displayed biocompatibility in terms of non-toxicity at the cellular level and biodegradability.[40] It has recently been reported that MWCNTs-polymer (poly(maleic-*alt*-1-octadecene)) composites prepared by spin-coating technique provided good support for cellular growth and spreading, and was promising for in vitro screening for biomedical applications, including conductive tissues regeneration.[41]

Another effective synthesis technique for making polymer/CNT composite nanofibers is electrospinning (ES) or combined electrospinning/electrospray technique. Recently, there has been a rapid increase in the study of using ES technology to produce polymer nanofibers. Electrospinning (ES) is a very effective technology for manufacturing nanofiber scaffolds in the field of tissue regeneration, because it can produce continuous electrospun nanofibers with diameters ranging from tens of nanometers to several microns by simply projecting a single or blend polymer solution under a high electric field.[42, 43] It is well known that the ECM is made of collagen nanofibers, so the specific fiber morphology of the ES scaffold will help imitate the natural structure of ECM. Combined electrospining/electrospray technique is also an effective and flexible way for dispersing nano-objects in the polymer nanofiber scaffold, which combines the ES process while spraying liquid containing nano-objects in the form of droplets in a high voltage electric field.[44, 45] Therefore, the electrospun scaffolds are considered as a promising matrix for incorporating CNTs because it can assembly manufactured continuous polymer/CNTs hybrid nanofibers, which is superior to other multi-step traditional discontinuous fiber manufacturing methods.

There are many types of polymers suitable for tissue engineering scaffolds that can be prepared by the ES process. The most commonly used natural biopolymers include agarose[46-48], collagen[49], hyaluronan[50] and alginate[51], as well as synthetic polymers include polyglycolic acid (PGA)[52], polylactic acid (PLA)[53] and its copolymers, and poly(lactic-co-glycolic acid) (PLGA)[54], etc., have a long history of clinical application.

Among them, alginate is known for its good biocompatibility, biodegradability and non-toxic properties, and has been widely used in pharmaceutical and biomedical fields such as wound dressings[55], dental impressions[56] and pharmaceutical compositions[57]. Alginate is a general term for the polysaccharides family synthesized from brown algae and bacteria. It is a linear water-soluble binary copolymer and with sodium carboxylate on the chain, which can be cross-linked with divalent ions. Another polymer, PLA, is linear aliphatic polyester with excellent mechanical properties, thermal plasticity and biocompatibility. It has been approved by the FDA for specific human clinical applications including surgical sutures, substrates for tissue regeneration and long-term implantable devices.[58, 59]

In this work, alginate and PLA hybrid nanofibers containing homogeneously MS shell-coated CNTs (CNT@MS) that are aligned along the nanofibers axis were developed through the technology of ES (**Fig.4-1**). CNTs are very attractive additives for improving the mechanical properties of polymer matrix due to their high strength-to-weight ratio and the nano-scale size. CNTs have been proven to effectively transfer loads and improve the strength and toughness of different polymer scaffolds.[60, 61] Furthermore, the photothermal effect of these CNT@MS-incorporated alginate and PLA electrospun nanofiber composite scaffolds under NIR laser irradiation was studied. Finally, biological evaluation in vitro of these CNT@MS-incorporated electrospun nanofibers was conducted as a way of exploring their potential applications in tissue engineering. The formation of such nanofibous scaffold can further improve the biomedical compatibility of CNTs and expand their applications in the biomedical field, while enhancing the mechanical properties of the total electrospun nanofiber membrane.

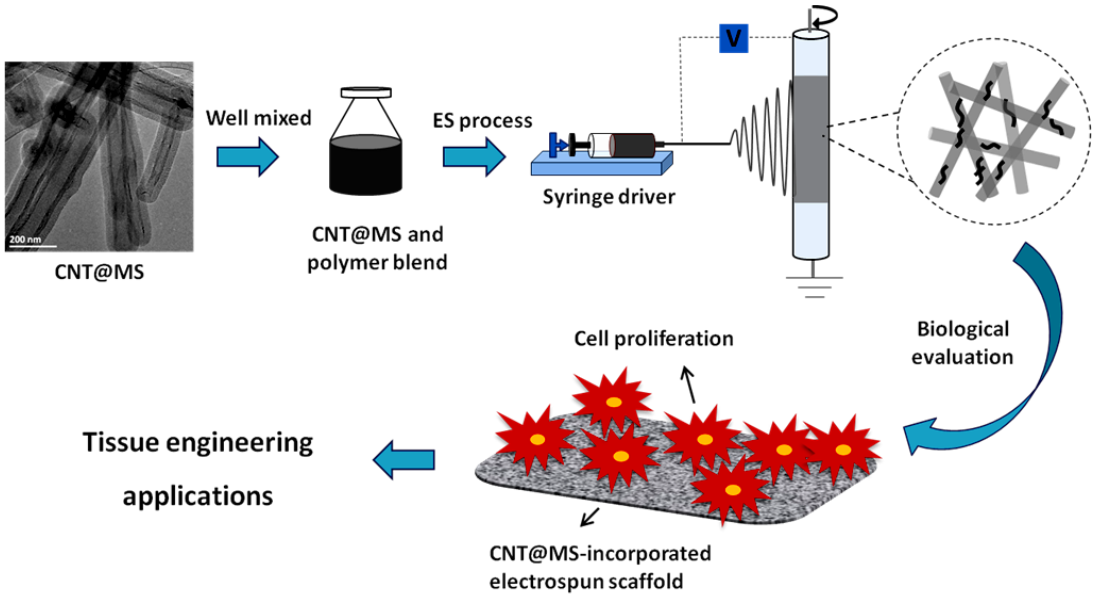

Fig.4-1 The schematic showing the preparation of CNT@MS-incorporated electrospun

nanofibers for biological applications

4.2 Materials and methods

4.2.1 Materials

Carbon nanotubes (CNTs, PR-24-XT-PS) were supplied by Pyrograf-III. Cetyltrimethylammonium bromide (CTAB) was obtained from Roth (France). Nitric acid (HNO_3), sulfuric acid (H_2SO_4), ethanol (EtOH), tetraethyl orthosilicate (TEOS), sodium hydroxide (NaOH), ammonium nitrate (NH_4NO_3, >99%), 3-aminopropyltriethoxysilane (APTS), dimethylformamide (DMF), polylactic acid (PLA, 7000 Da), alginic acid sodium salt from brown algae (low viscosity), poly(ethylene oxide) (PEO, 900 kDa), calcium chloride dehydrate ($CaCl_2 \cdot 2H_2O$, ≥99%), Pluronic F127, N,N-dimethyl formamide (DMF, 99.8%) and dichloromethane (DCM) were obtained from Sigma-Aldrich (France). Ammonium hydroxide solution (25% in H_2O) was obtained from Fluka.

4.2.2 Procedures

(1) Synthesis of cleaved CNTs

First, the pristine CNTs were cleaved in a better-suited length through acid treatment. Typically, 0.75 g of pristine CNTs was added into 108 mL mixture of H_2SO_4/HNO_3 (Volume ratio = 3 : 1,) and the mixture was sonicated at 0 ℃ for 24 h. The mixture was then monitored to neutrality with NaOH (1 M) solution. The sliced CNTs were washed with distilled water (3 x 25 mL), dried at room temperature, and then reduced at 900 ℃ for 2 h under argon. The resulting sliced CNTs were used as the initial material for the following silica layer coating step.

(2) Synthesis of mesoporous silica coated CNTs

In a typical procedure, 372 mg of CTAB was added into a mixture of H_2O (90 mL) and EtOH (60 mL) with stirring at 60 ℃ for 2 h. 72 mg of CNTs were dispersed in the CTAB solution by ultrasonication (2 x 20 min, power = 750 W, amplitude = 40%, temperature = 30 °C, runs: 50” ON, 50” OFF, Vibracell 75043 from Bioblock Scientific), yielding a black suspension. The sol gel process was initiated after addition of TEOS (180 µL) and NaOH (180 µL, 1M) into the above mixture. The mixture was stirred for 16 h at room temperature. Finally, the composite was centrifuged and washed with EtOH (2 x 25 mL, 12000 g, 12 min) and re-dispersed in EtOH. The process resulted in the formation of a uniform layer of MS on the surface of CNTs.

(3) CTAB extraction from CNT@MS composite

The removal of mesostructural templating agent CTAB from the silica pores was done by

mixing the CNT@MS composite with 25 mL NH_4NO_3 (20 mg/mL in EtOH) under 60 ℃ with stirring for 1 h. The surface charge of CNT@MS was measured by Zeta potential after each washing, in order to make sure that the majority of CTAB was removed. This process was repeated approximately 5 times.

(4) APTS functionalization of CNT@MS

50 mg of CNT@MS were dispersed in 27 mL of EtOH. Then, 1.2 mL of NH_4OH (25 % in water) and 5 mL of APTS were added respectively and the mixture was agitated on a mechanical wheel (40 rpm) at room temperature for 2 h. After that, the amino-modified composite was centrifuged and washed with EtOH (2 x 20 mL, 13000 g, 14 min). The composite after APTS modification was denoted as CNT@MS@APTS.

(5) Preparation of alginate-based nanofibers

a) Preparation of alginate nanofibers without CNT@MS (Algin/PEO/PF127)

A homogenously mixed solution was obtained by dissolving 0.4 g of alginate, 0.2 g of PEO and 0.2 g of Pluronic F127 in 9.2 g of deionized water and stirring continuously at 400 rpm at room temperature for 24 h. The mass fractions of alginate, PEO and Pluronic F127 in the suspension are 4 wt%, 2 wt% and 2 wt%, respectively. The mixed solution was added via a 5 mL plastic syringe attached to a circular shaped metal spinneret through a polyethylene catheter (inner diameter 1.5 mm). Algin/PEO/PF127 electrospun fiber scaffold was prepared under the optimized conditions: a distance of 15 cm between the spinneret and the fiber collector, a flow rate of 0.3 mL/h and an applied voltage of 18 kV. The thickness of the electrospun scaffold was controlled by adjusting the depositing time.

b) Preparation of CNT@MS-incorporated alginate nanofibers (Algin/PEO/PF127/CNT@MS)

A mixture containing 0.4 g of alginate, 0.2 g of PEO and 0.2 g of Pluronic F127 and 7.2 g of deionized water was stirred continuously at 400 rpm at room temperature for 24 h. After that, 42 mg of CNT@MS after APTS-modification in 2 g of deionized water was added to the mixture and stirring at 400 rpm for 24 h. The mass fractions of alginate, PEO, Pluronic F127 and CNT@MS in the suspension are 4 wt%, 2 wt% 2 wt% and 0.42 wt%, respectively, resulting in the proportion of CNT@MS in the Algin/PEO/PF127/CNT@MS scaffold being 5 wt%. The concurrent-ES process of Algin/PEO/PF127/CNT@MS electrospun scaffold was carried out using the same experimental setup and the same processing parameters as preparing Algin/PEO/PF127 nanofibers.

(6) Preparation of PLA-based nanofibers

a) Preparation of PLA nanofibers

4.5 g of PLA was dissolved in 20 mL of DCM and stirred continuously overnight at 400

rpm at room temperature. After that, 20 mL of DMF was added and then stirred continuously for 24 h. The mass fractions of PLA in the suspension is 9 wt%. The mixed solution was added via a 5 mL syringe attached to a circular shaped metal spinneret through a polyethylene catheter (inner diameter 1.5 mm). PLA fiber was prepared under the optimized conditions: a distance of 15 cm between the spinneret and the fiber collector, a flow rate of 1.4 mL/h and an applied voltage of 25 kV. The thickness of the electrospun scaffold was controlled in the range of 10-20 μm for subsequent use by adjusting the depositing time.

b) Preparation of CNT@MS-incorporated PLA nanofibers (PLA/CNT@MS)

Firstly, 78 mg of CNT@MS was modified by APTS to improve the dispersion of CNT@MS in the suspension according to our previous description. After that, the amino-modified CNT@MS was dispersed in 7 mL of DMF (good solvent for dissolving PLA) with the assistance of ultra-sonication and stirred continuously on the wheel overnight at 40 rpm at room temperature. At the same time, 1.57 g of PLA was dissolved in 7 mL of DCM and stirred continuously overnight at 400 rpm at room temperature. Finally, the PLA/CNT@MS suspension was obtained by adding well dispersed amino-modified CNT@MS to PLA solution drop by drop and then stirred continuously for 24 h before ES. The concurrent-ES process of PLA/CNT@MS electrospun scaffold was carried out using the same experimental setup and the same processing parameters as preparing PLA nanofibers. The mass fractions of PLA and CNT@MS in the suspension were controlled to 9 wt% and 0.44 wt%, respectively, resulting in the proportion of CNT@MS in the PLA/CNT@MS scaffold being 5 wt%.

c) Preparation of PLA/CNT@MS (spray) scaffold

The synthesis was a multi-step process incorporating CNT@MS clusters produced by electrospray into the electrospun PLA fibers. 50 mg of APTS-modified CNT@MS was dispersed in 10 mL of EtOH to form a 5 mg/mL solution by ultrasonic treatment for 30 min. The 9 wt% PLA blend and CNT@MS@APTS solution were loaded into two syringes, which were adjusted by two separate syringe pumps to control the flow rate. The PLA/CNT@MS (spray) scaffold was obtained by alternately performing electrospinning of PLA and electrospraying of CNT@MS. The electrospinning of PLA was performed under the same conditions as preparing PLA nanofibers. The parameters for electrospray of CNT@MS: distance of collector-to-needle was 25 cm, the working voltage was 18 kV, and the flow rate was 0.3 mL/h. In this work, PLA/CNT@MS (spray) scaffold was prepared by the following steps: 40 min of PLA electrospinning, then 10 min of CNT@MS electrospray, then 40 min of PLA electrospinning, and finally 10 min of CNT@MS electrospray (10 min -40 min - 10 min

- 40 min).

(7) Crosslinking of the composite membranes

The resulting Algin/PEO and Algin/PEO/CNT@MS samples were cross-linked by immersing the electropun scaffold in 100 ml of $CaCl_2$ (1 M) aqueous solution for 60 min under slow stirring. The crosslinked scaffolds were rinsed with deionized water three times to remove any residual chemicals, and then dried in the fume hood at room temperature for 2 days.

4.2.3 In vitro biological evaluation

For the biological tests, the membranes of 1 cm^2 were deposited in a 24-well plate, and the bottom of the plate was treated with a hydrophobic poly-HEMA coating to prevent cells from adhering to the bottom of the wells. To prevent the membrane from floating in the medium, a stainless steel cylinder was made to press the membrane on the bottom of the well. Then it was sterilized by UV treatment and rinsed with 70% ethanol. Each type of membrane was tested with 3 samples (replicas) and 1 material-free control sample was used. An additional sample used as a control consisted of a solution of chlorhexidine, an antiseptic known for its high-dose toxicity. Then 20,000 cells per well were deposited using a DMEM (High Glucose, Dutscher) medium with 10% serum (FBS, Dutscher) and 1% antibiotic (Pencillin/Streptomycin). The samples were then placed in the incubator at 37℃ with 5% CO_2. After 1, 3 and 7 days incubation, measurements of cell activity were performed using a fluorimetric Alamar Blue kit that will measure the mitochondrial activity of the cells. For environmental scanning electron microscopy analyses, the samples were previously fixed with 2.5% glutaraldehyde and 4% paraformaldehyde in a cacodylate buffer.

4.2.4 Characterization Methods

(1) Scanning electron microscopy (SEM)

The electrospun nanofibers were gold-coated using sputter coating to observe the surface topographies by SEM on the JEOL F2600 microscope equipped with a CCD camera. The electron accelerating voltage for SEM was 5.0 kV. SEM micrographs were digitized and analyzed with Image Tool to determine the average fiber diameter of the produced nanofibers.

(2) Transmission electron microscopy (TEM)

TEM images of electrospun fibers were taken via a JEOL 2100 apparatus with high resolution operating. The nanofibers were prepared by ES onto the carbon-coated copper grids directly for about 10 s. Then they were dried i n the fume hood over 24 h to remove residual solvent completely.

(3) Thermal gravimetric analysis (TGA)

TGA was performed on a Q5000 Automatic Sample Processor (TA Instruments). The runs were started from room temperature to 800 ℃ at a heating rate of 10 ℃/min under an air flow rate of 25 mL/min.

(4) Nitrogen adsorption / desorption analysis

Specific surface area of CNT@MS was characterized by nitrogen adsorption/desorption analysis and was calculated by the Brunauer-Emmett-Teller (BET) method. The pore size and pore volume were calculated by the Barrett-Joyner-Halenda (BJH) method. All the measurements were done on a Tristar 3000 Gas Adsorption Analyzer by Micromeritics Instruments. Before the tests, the samples were outgassed under vacuum at 150 ℃ for about 4h.

(5) Mechanical properties

The tensile stress-strain behavior of the electrospun nanofiber scaffolds was performed using a MCR301 rheometer from Anton-Paare (quipped with the Universal Extensional Fixture), which contains two drums allowing the fixation of a rectangular film sample. The samples were carefully trimmed to a size of 40 mm x 10 mm. The thickness of alginate-based samples was around 0.15 mm, and the thickness of PLA-based samples was around 0.10 mm. The distance between the gripping points is around 40 mm. The mechanical testing was conducted with the grips moving at a stretch speed of 10 mm/min at room temperature. The reported results represent an average result of five tests.

(6) Photothermal effect study

To study the photothermal effect of the CNT@MS-incorporated alginate and PLA nanofiber scaffolds under NIR irradiation, 2 mL of distilled water was added in a plastic cuvette containing a membrane with size of 1 cm x 1 cm. The cuvette was irradiated with the 1064 nm laser with a power density at 1 W/cm^2 for 15 min.

4.3 Results and discussion

4.3.1 Preparation of CNT@MS-incorporated alginate electrospun nanofiber scaffold

(1) Optimization of alginate-based electrospun nanofibers

Due to the polyelectrolyte nature of alginate, it is difficult to form electrospun nanofibers by ES with pure alginate solution, but it can be fibrillated with ES by combination with other polymers.[62] Polyethylene oxide (PEO) is usually selected to blend with polymers that cannot be electrospun alone to produce ES nanofibers. It has been previously showed that blending alginate with electrospinnable polymer PEO enables the formation of nanofibers by ES, and the nanofibers can be transformed from beaded nanofibers to non-beaded nanofibers.[63, 64]

Fig.4-2 shows the SEM images of alginate electrospun nanofibers after the addition of PEO with different concentrations in fixed concentrations of alginate (1.5 wt% and 2.0 wt%). When alginate was fixed at the concentration of 1.5 wt%, no electrospun fibers but only beaded morphology were obtained with 1.5 -2.0 wt% PEO addition (**Fig.4-2 A** and **B**). The degree of beading decreased as the PEO content increased from 1.5 to 4.0 wt% (**Fig.4-2 B-F**) with fixed alginate concentration at 2 wt%. When alginate was blended with PEO at the concentration of 2.0/4.0 wt%, uniform non-beaded electrospun nanofibers were obtained (**Fig.4-2 F**), and the maximum content of alginate in the resulting nanofibers was 33.3 wt %.

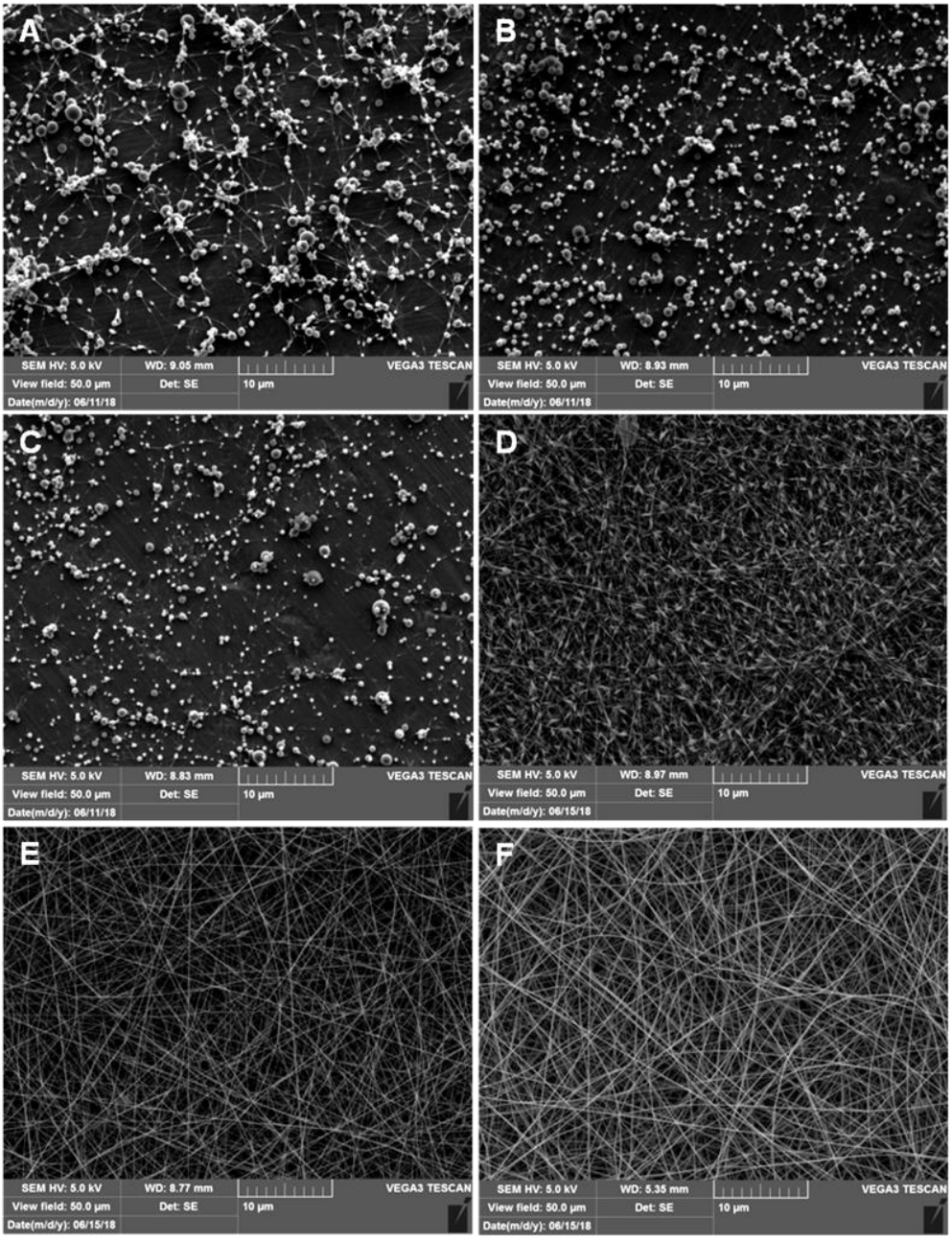

Fig.4-2 SEM images of Algin/PEO electrospun nanofibers with different concentrations alginate/PEO at (A)1.5 : 2.0 wt%, (B) 1.5 : 1.5 wt%, (C) 2.0 : 1.5 wt%, (D) 2.0 : 2.0 wt%, (E)

2.0 : 3.0 wt%, and (F) 2.0 : 4.0 wt%

Although it is possible to form blended nanofibers by ES alginate with PEO, it is worth noting that alginate electrospun nanofibers are soluble in water, which prevents them from being used as scaffolds for biological applications. Fortunately, the property of cross-linking of alginate with calcium chloride ($CaCl_2$) can overcome this issue. During the cross-linking process, the double positive charge Ca^{2+} takes the place of the Na^{+} ion on the chain and interacts with two CO^{2-} groups, thus forming a connection between the two alginate chains and creating a cross-linked network. Therefore, it is necessary to increase the amount of alginate in the electrospun scaffold for the subsequent cross-linking process.

The amount of alginate in the blended nanofibers can be increased by adding additional nonionic surfactant, such as Triton X-100 or Pluronic F127. In this work, the FDA-approved surfactant Pluronic F127 was chosen. The effect of Pluronic F127 on the morphologies of the Algin/PEO nanofibers was then investigated. The results are showed in **Fig.4-3**. Among them, the concentration of PEO was maintained at 2 wt%, and the concentration of alginate was controlled in the range of 2.0-5.0 wt%. We found that Algin/PEO blends (alginate% varied from 2 wt% to 4 wt%) with the addition of small amount (1 wt%) of Pluronic F127 produced beaded nanofibers **(Fig.4-3 A-C**). As the alginate content in the blend increases from 2 wt% to 4 wt%, the degree of beading of the electrospun nanofibers increases. When the concentration of Pluronic F127 was increased to 2 wt%, uniform bead-free nanofibers were generated (**Fig.4-3 D-E**), and the maximum content of alginate in the resulting nanofibers was 50 wt % in **Fig.4-3 E**. It has been reported that the addition of nonionic surfactant will cause a reduction in surface tension of the alginate solution, which contributes to the morphological transition from beaded to uniform non-beaded fibers.[65]

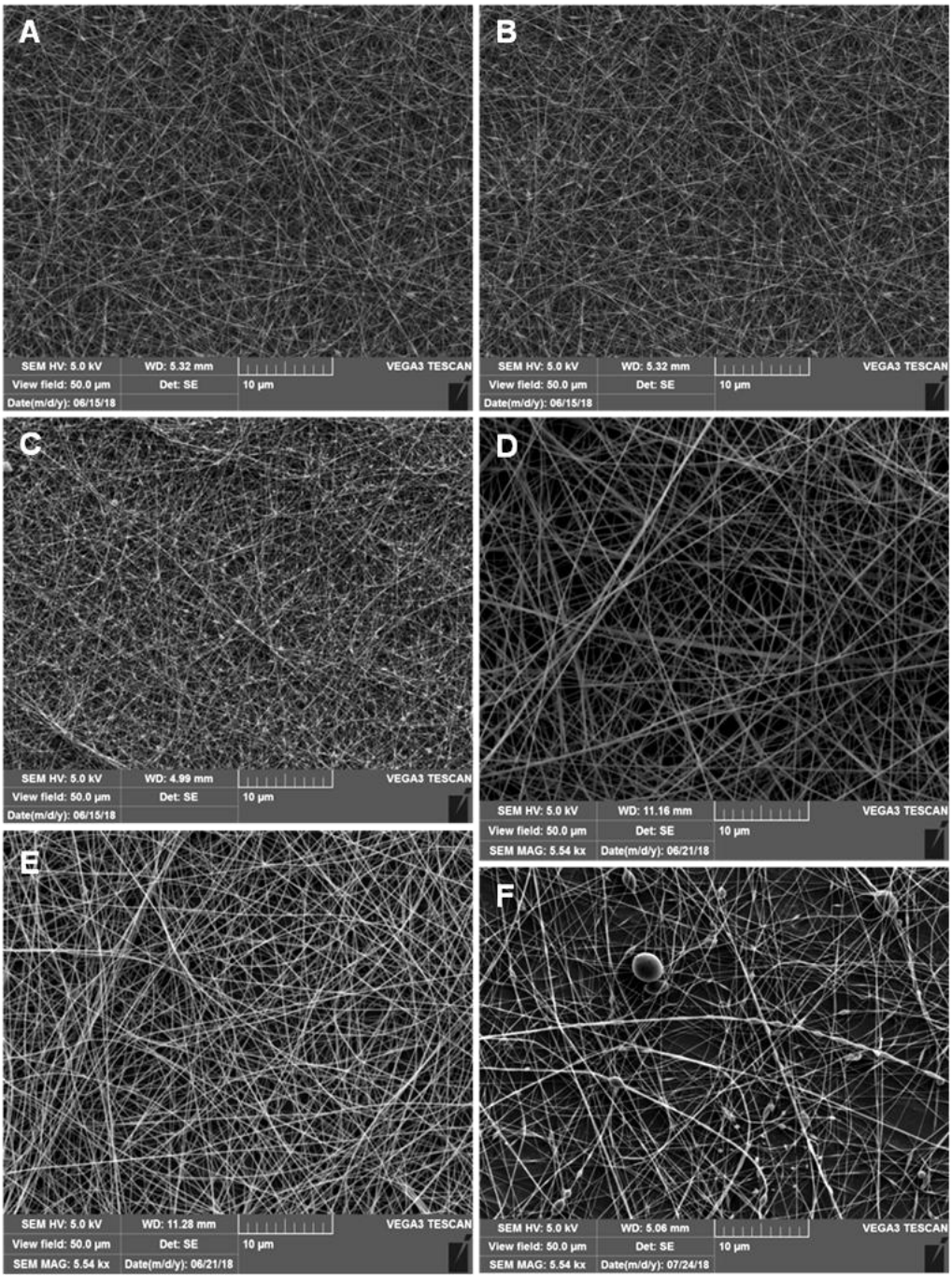

Fig.4-3 SEM images of Algin/PEO/PF127 electrospun nanofibers with the addition of 1 wt% of Pluronic F127 and alginate/PEO at (A) 2.0 : 2.0 wt%, (B) 3.0 : 2.0 wt%, and (C) 4.0 : 2.0 wt%. SEM images of Algin/PEO/PF127 electrospun nanofibers with the addition of 2 wt% of Pluronic F127 and alginate/PEO at (D) 3.0 : 2.0 wt%, (E) 4.0 : 2.0 wt%, and (F) 5.0 : 2.0 wt%.

Thus, the addition of Pluronic F127 enhances the electrospinnability of Algin/PEO solution and higher concentrations of alginate can be achieved in the electrospun system. However, as the concentration of alginate increased to 5 wt%, bead-nanofibers were formed at

the same Pluronic F127 concentration (**Fig.4-3 F**). Based on these studies, we decided to use the blend with fixed concentrations of 4 wt%, 2 wt% and 2 wt% corresponding to alginate, PEO and Pluronic F127 respectively, for the preparation of alginate-based electrospun scaffolds.

(2) Incorporation of CNTs@MS within alginate-based electrospun nanofibers

Then, the electrospun scaffold comprised of 5 wt% CNT@MS was fabricated by directly ES Algin/PEO/PF127 blend containing CNT@MS. The pristine CNTs were firstly cleaved into an appropriate length through acid treatment, and then a MS layer was uniformly coated on the CNTs surface, as described above. The characterization of CNT@MS is shown in **S.4-1**. TEM images showed a homogenous coverage of the MS on all the CNTs (**S.4-1 A** and **B**), indicated the well-organized mesoporous structure of the MS shell surrounding the CNTs. The thickness of the MS shell is around 30 ± 4 nm, and the diameter of CNT@MS is 147 ± 10 nm. The porosity was investigated by nitrogen adsorption-desorption isotherms (**S.4-1 C**) and the specific surface area was calculated to be 594 ± 14 m^2/g and the pore size was ca. 3.4 nm with a pore volume of 0.53 cm^3/g. The TGA analysis (**S.4-1 D**) indicated a C/SiO_2 mass ratio of 63%/37% for the CNT@MS composite system. Afterwards, CNT@MS was modified with APTS groups to improve its dispersion in aqueous solution or DMF.

Fig.4-4 presents the SEM images and the diameter distribution of Algin/PEO/PF127 and Algin/PEO/PF127/CNT@MS hybrid nanofibers. All the electrospun nanofibers with or without CNT@MS were well formed without beads, and formed uniform mats. Additionally, as can be seen from the nanofiber diameter distribution (**Fig.4-4 C** and **F**), the diameter distribution of Algin/PEO/PF127 nanofibers is relatively uniform, with an average diameter of 173 ± 15 nm. With the addition of CNT@MS in the Algin/PEO/PF127 blend, the average diameter of the resulting nanofibers was decreased slightly to 154 ± 29 nm. In this study, since alginate-based electrospun nanofibers were synthesized under the same ES conditions, the final nanofiber morphology should be determined by the characteristic parameters of the initial spinning solutions. Thus, the decisive factor leading to the difference in nanofiber morphology might be due to the addition of CNT@MS enhanced the conductivity of the spinning solution. The presence of CNTs in the polymer solution leads to an increase in surface charge in the jet, which affects the stretching process of the nanofiber, resulting in a smaller average diameter of nanofiber. Therefore, the nanofiber containing CNT@MS can be stretched thinner than those without CNT@MS under the same electrospun conditions. In addition, it can be clearly seen that CNT@MS is distributed on the surface of the polymer nanofibers along the nanofiber axis (in **Fig.4-4 E** marked with red circles), and no

agglomeration of CNT@MS were observed. Macroscopically, it can also be seen that the Algin/PEO/PF127/CNT@MS electrospun scaffold is uniformly black (**S.4-2**), indicating that CNT@MS was evenly distributed throughout the scaffold.

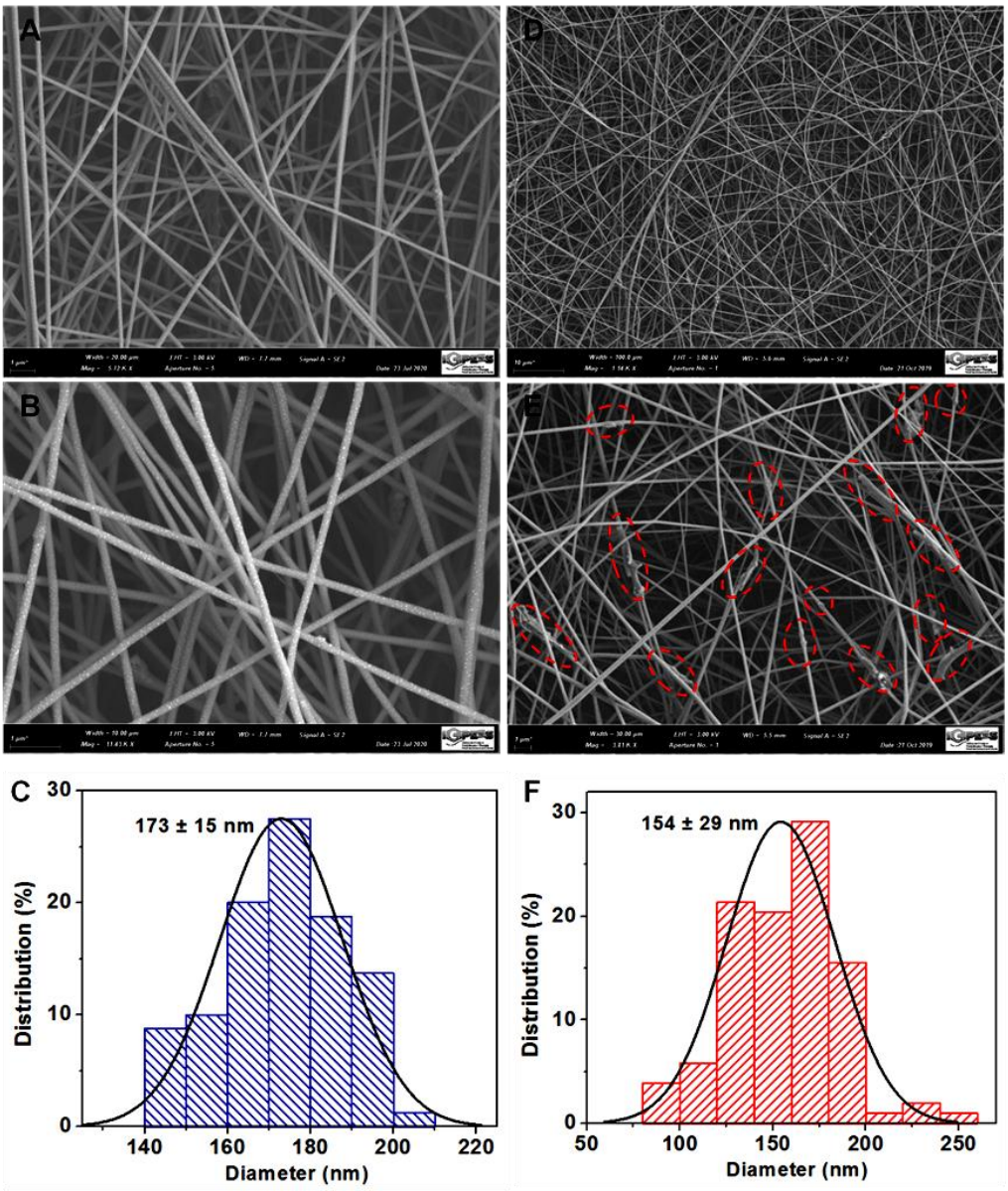

Fig.4-4 SEM images and fiber diameter distribution with average value of the obtained electrospun nanofibers: (A-C) Algin/PEO/PF127 nanofibers and (D-F) Algin/PEO/PF127/CNT@MS hybrid nanofibers.

TGA measurements were conducted to analyze the thermal decomposition behavior of these electrospun nanofibers and confirm the final amount of CNT@MS incorporated into alginate and PLA nanofibers. The TGA curves of alginate-based and PLA-based nanofibers are exhibit in **Fig.4-5**. There was a weight loss in the temperature range of 30-100 ^{o}C in the TGA curves of Algin/PEO/PF127 and Algin/PEO/PF127/CNT@MS, which could be

attributed to the removal of physically adsorbed water. The decomposition of the polymer started at 160 ℃ and was completed at 360 ℃, which corresponded to the decomposition of the three polymers: alginate, PEO and Pluronic F127 in Algin/PEO/PF127 matrix (TGA curves of the pure reagents are shown in **S.4-3**.). The TGA curves of Algin/PEO/PF127/CNT@MS presents a highly similar with Algin/PEO/PF127, except that there is a small mass loss corresponding to the combustion of CNTs in the range of 500-600 ℃ with a weight loss of 3.2%. According to the proportion of CNTs in CNT@MS being 63%, it can be calculated that the proportion of CNT@MS in Algin/PEO/PF127/CNT@MS scaffold is around 5.1 wt%. It is reliable to the quantity of 5 wt% CNT@MS that introduced initially. The remaining residual was 19.4% and 20.4% at 800 ℃ for Algin/PEO/PF127 and Algin/PEO/PF127/CNT@MS, respectively, which were mainly incombustible components from alginate and CNT@MS.

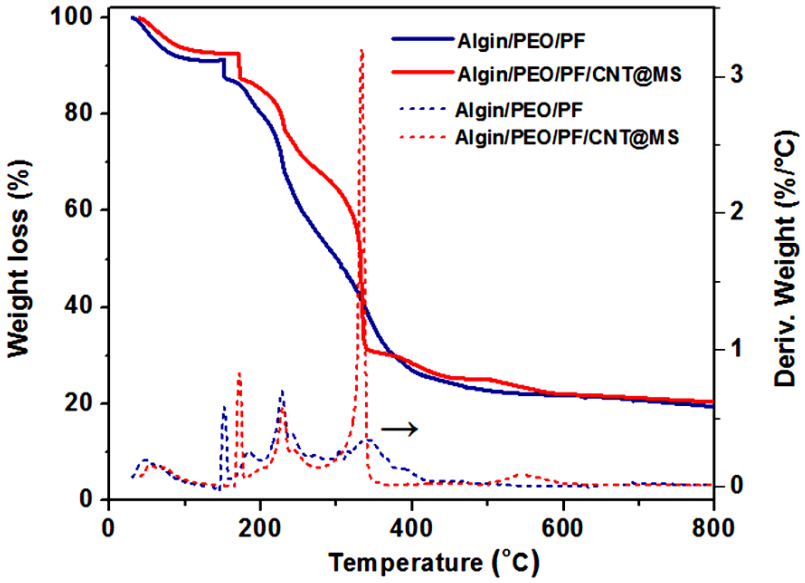

Fig.4-5 TGA and DTG curves of alginate-based electrospun scaffolds with and without CNT@MS

As expected, the as-prepared alginate based nanofibers were highly water-soluble. In order to be able to use the alginate electrospun nanofibers as a scaffold for biological applications, stabilization and cross-linking processes are required. The resulting alginate-based nanofibers are ionically cross-linked calcium chloride ($CaCl_2$) solution to obtain a water-insoluble scaffold while maintain their structure in an aqueous environment. The Ca^{2+} ions take the place of the Na^{+} ions on the alginate chain and the Ca^{2+} ions with double positive charges can interact with two CO^{2-} to form a cross-linked network. The SEM

images of the alginate based nanofibers after cross-linking in $CaCl_2$ solution of 1 M concentration (**Fig.4-6 A-D**) show that the morphology of the cross-linked nanofibers changed slightly, and they were found to be a little swelling and interfused inconsiderably. However, it is worth noting that the nanofibrous structure was maintained after crosslinking treatment. It was concluded that the alginate-based nanofibers were successfully ionically cross-linked in the calcium solution. Moreover, CNT@MS nanotubes can also be observed on the surface of Algin/PEO/PF127/CNT@MS nanofibers (**Fig.4-6 C** and **D**), indicating that CNT@MS composites are stably immobilized in the electrospun scaffold after cross-linking process.

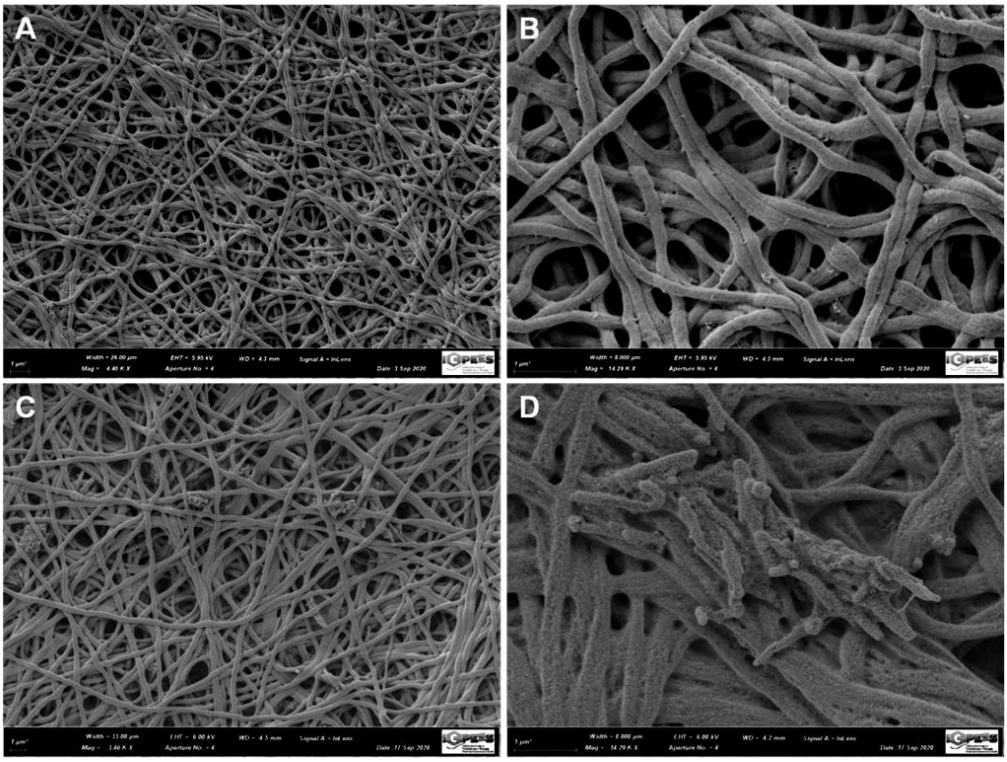

Fig.4-6 SEM images of (A, B) Algin/PEO/PF127 and (C, D) Algin/PEO/PF127/CNT@MS electrospun nanofibers after cross-linking

4.3.2 Preparation of CNT@MS-incorporated PLA electrospun nanofiber scaffold

(1) Preparation of CNT@MS-incorporated PLA nanofibers by electrospinning

To obtain PLA/CNT@MS hybrid nanofibers through ES process, APTS-modified CNT@MS was firstly dispersed in DMF and then thoroughly mixed with PLA solution. CNT@MS was well dispersed in DMF (one of the components of the PLA solution) before mixing with PLA solution, and its high dispersion in the PLA blend would be beneficial to the formation of uniform PLA/CNT@MS hybrid nanofibers. The ES process of PLA and PLA/CNT@MS nanofibers was conducted under the processing conditions as described

above. SEM images and fiber diameter distribution of the electrospun materials manufactured from PLA solution and PLA/CNT@MS blend are presented in **Fig.4-7**. All the electrospun nanofibers were uniformly formed and bead-free. The average diameter of PLA nanofibers is 369 ± 84 nm (**Fig.4-7 C**). Similarly, the average diameter of the nanofibers doped with CNT@MS decreased to 350 ± 84 nm (**Fig.4-7 F**). As discussed above, the reason for the change in fiber diameter was probably due to the increase in electrical conductivity of the PLA/CNT@MS blend after the addition of CNT@MS. Compared with that of the neat PLA nanofibers, the morphology of the PLA/CNT@MS composite fibers was more or less degraded because of the presence of CNT@MS. The image in **Fig.4-7 E** marks several typical distribution of the CNT@MS in the PLA/CNT@MS hybrid nanofibers with red circles. The CNT@MS fibers with shorter length and smaller diameter (147 ± 10 nm) were attached and dispersed along the outer surface of the electrospun nanofiber axis in the form of entanglements (composed by single to several of oriented CNT@MS). As a result, the obtained PLA/CNT@MS hybrid nanofibers show tortuous morphologies and a rough surface. Similar observations have also been reported on some other PLA-CNTs electrospun nanofibers.[60, 66] Similarly, the whole PLA/CNT@MS electrospun membrane showed a homogeneous black color (**S.4-4**), suggesting that CNT@MS was uniformly dispersed throughout the scaffold.

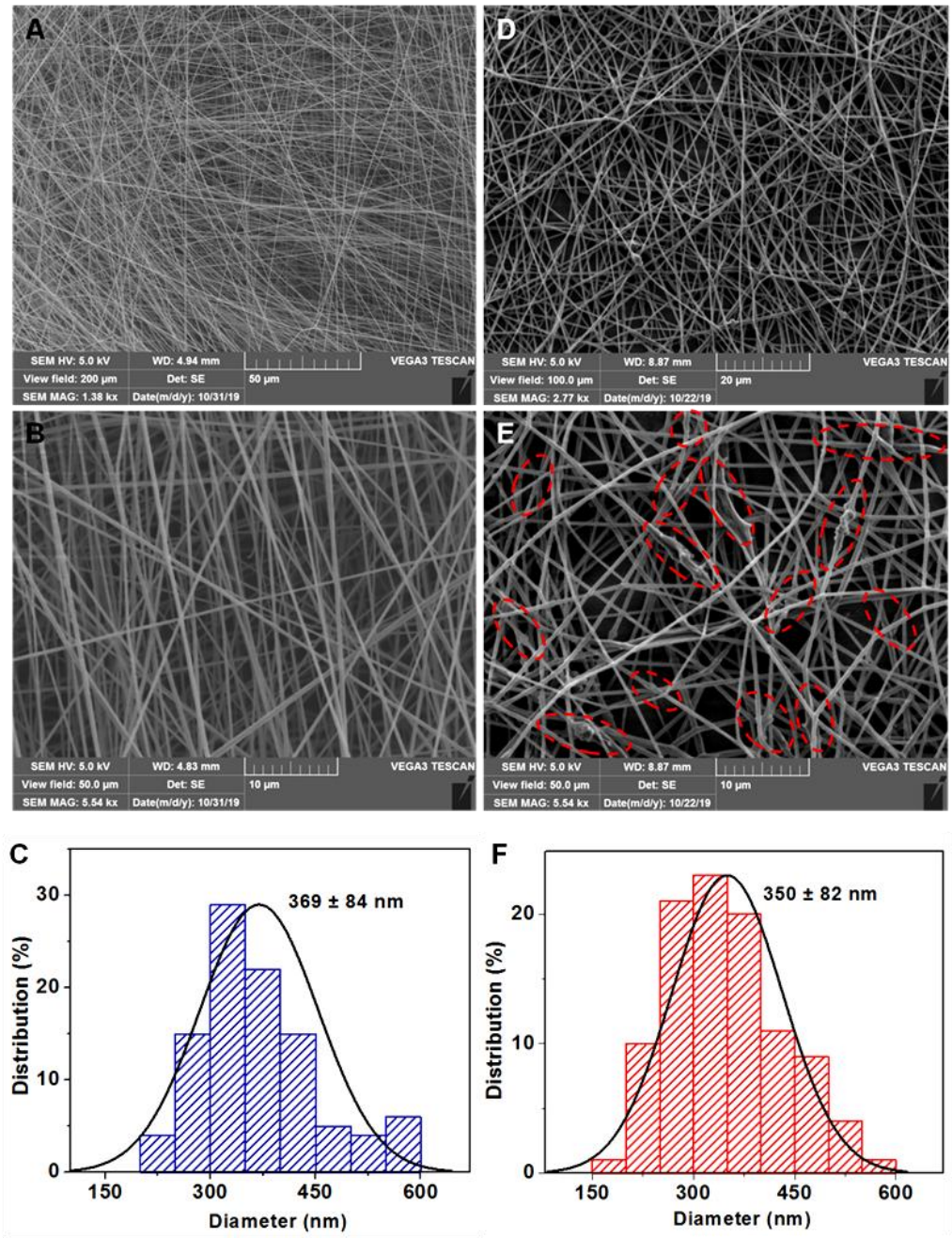

Fig.4-7 SEM images and fiber diameter distribution with average value of the obtained electrospun nanofibers: (A-C) PLA nanofibers and (D-F) PLA/CNT@MS hybrid nanofibers.

Fig.4-8 shows the effect of the presence of CNT@MS on the thermal stability of the PLA nanofiber matrix. The first step of weight loss in T= 220-400 ℃ was assigned to the complete decomposition of PLA polymer. The CNTs in the PLA/CNT@MS scaffold decomposed in the temperature range of 500-600 ℃, with a weight loss of ~3%, which was converted to 4.8 wt% of CNT@MS in the PLA/CNT@MS scaffold.

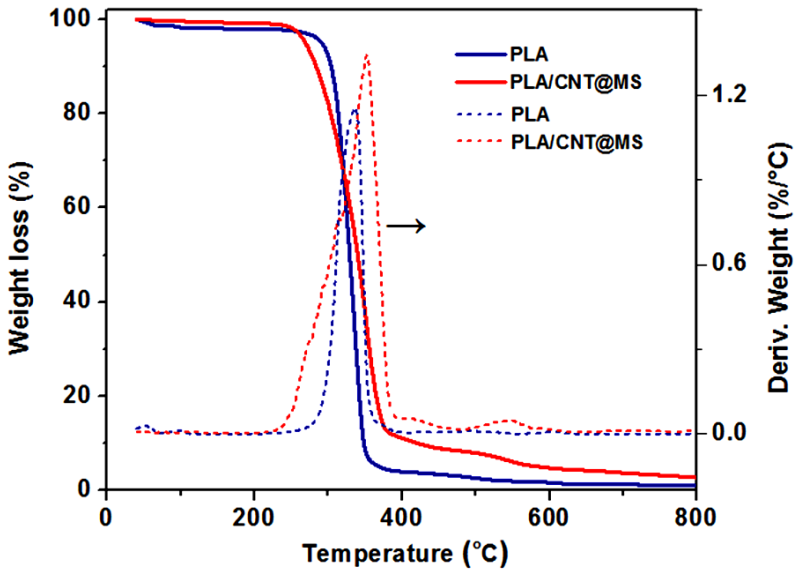

Fig.4-8 TGA and DTG curves of PLA-based electrospun scaffolds with and without CNT@MS

(2) Preparation of PLA/CNTs@MS scaffolds by electrospinning-electrospray

Electrospinning-electrospray was also carried out alternately by electrospinning of PLA blend and electrospraying of APTS-modified CNT@MS in ethanol to fabricate CNT@MS-incorporated PLA scaffold. The conducted SEM analysis of the produced PLA/CNT@MS (spray) scaffold is presented in **Fig.4-9**. It can be observed from **Fig.4-9 A** and **B** that CNT@MS is uniformly distributed on the PLA nanofibers in the form of clusters. This is due to the fact that the charged CNT@MS liquid jet is continuously sprayed onto the collector in the form of droplets/beads, thus forming clusters and dispersing on the surface of the PLA nanofibers. Larger magnification images (**Fig.4-9 C** and **D**) clearly reveal that the highly dispersed individual CNT@MS tubes are incorporated onto the polymer nanofibers. In order to confirm whether the CNT@MS clusters are strongly connected to the PLA nanofibers, the PLA/CNT@MS (spray) scaffold was rinsed in water with stirring for up to 65 h. The SEM images of the rinsed PLA/CNT@MS (spray) scaffold suggest that CNT@MS is still attached to the surface of PLA nanofibers after rinsing in water (**Fig.4-9 E-F**). The photographs in **S.4-5** show that the black blocks corresponding to the CNT@MS clusters remained unchanged before and after rinsing of the PLA/CNT@MS (spray) scaffold, neither less nor lighter. TGA was performed and it was confirmed that the amount of CNT@MS in the PLA/CNT@MS (spray) scaffold maintained the same before and after rinsing (**S.4-6**).

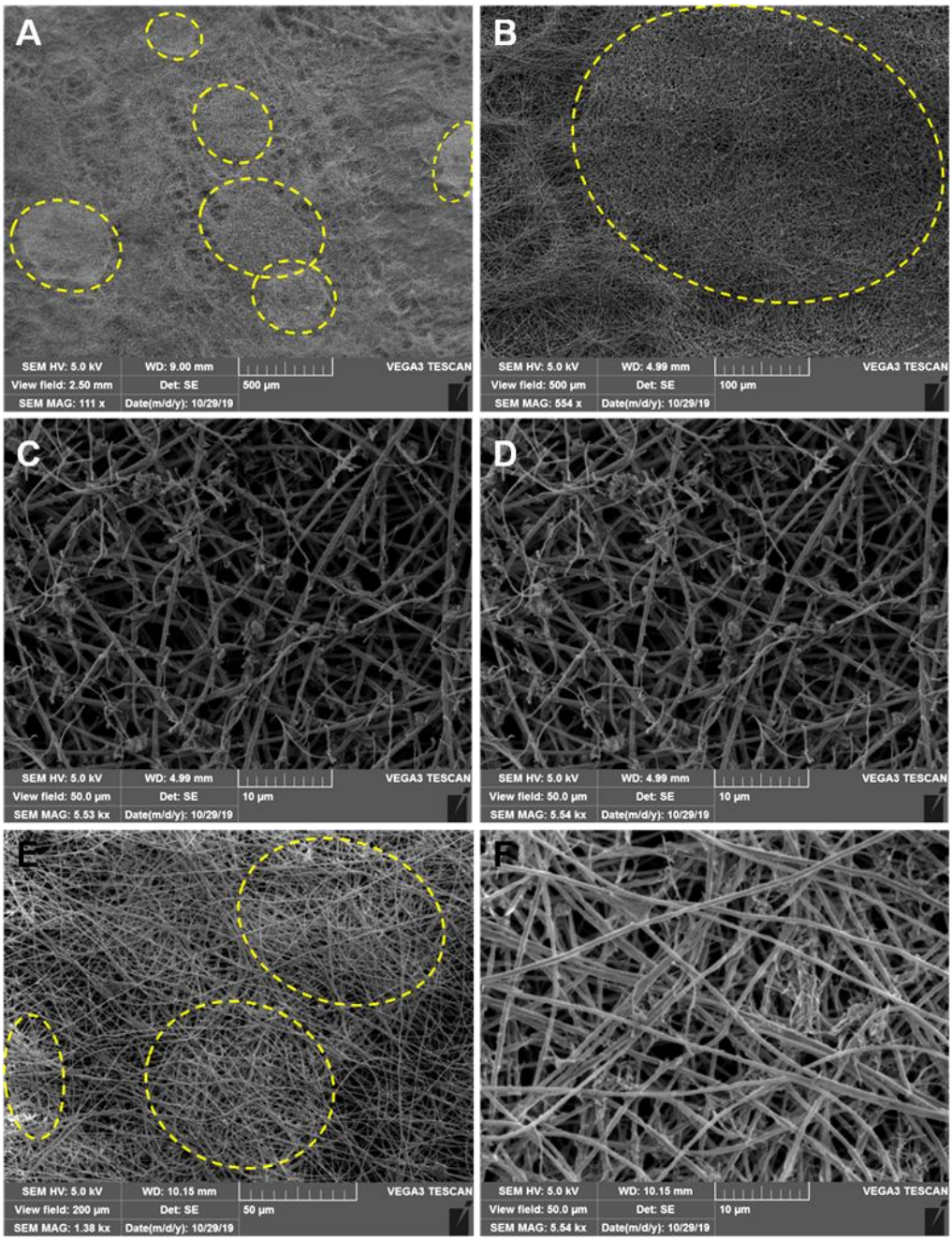

Fig.9 SEM images of the obtained PLA/CNT@MS (spray) nanofibers: (A-D) before rinsing and (E-F) after rinsing in water for 65 h.

Although the CNT@MS-incorporated PLA scaffold synthesized through combined electrospinning-electrospray method allowed to obtain highly dispersed CNT@MS on the surface of PLA nanofiber in a small range. The photographs in **S.4-5** show that the electrospinning-electrospray PLA/CNTs@MS scaffold is heterogeneous, some parts of the scaffold have CNT@MS (the black block), while others do not. It is difficult to achieve a homogeneous dispersion of CNT@MS in the entire scaffold by this method. Therefore, it may be a better choice to produce homogeneously dispersed CNT@MS by direct electrospinning

of the CNT@MS and PLA blend.

4.3.3 Properties of the CNT@MS-incorporated electrospun nanofiber scaffolds

(1) Mechanical properties of the CNT@MS-incorporated electrospun membranes

To get more insight into the influence of the introduction of CNT@MS into alginate and PLA electrospun scaffolds on their mechanical properties, tensile measurements were performed on the CNT@MS-doped nanofibers as well as on the simple (CNTS@MS free) Algin/PEO/PF127 and PLA scaffolds. The typical stress-strain curves of neat and CNT@MS-modified hybrid nanofibrous membranes, and the resulting maximum tensile strength and elongation at break for these samples are shown in **Fig.4-10**. As seen from the results, in the linear elastic deformation stage of initial stretching, the stress of all tested electrospun membranes increased rapidly with the increase of strain to approximately 4%, and then increased slowly in the tensile yield strengthening stage up to the breaking of the samples.

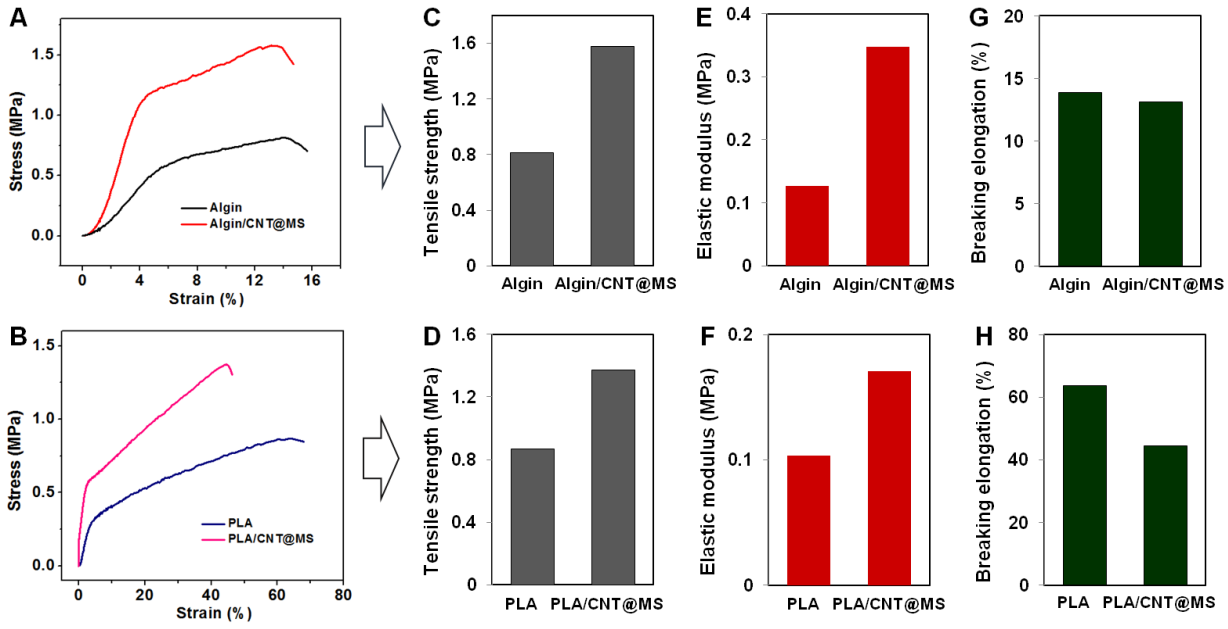

Fig.4-10 Mechanical properties: (A, B) tensile stress-strain curves, (C, D) maximum tensile strength, (E, F) elastic modulus, and (G, H) breaking elongation (blue bar) of alginate-based electrospun scaffolds and PLA-based electrospun scaffolds.

In the case of the tensile strength, the data present in **Fig.4-10 C** and **D** suggested that compared with Algin/PEO/PF127 and PLA electrospun nanofibers, when incorporated with 5 wt% of CNT@MS, the maximum tensile strength of Algin/PEO/PF127/CNT@MS and PLA/CNT@MS electrospun scaffolds was significantly improved by about 95% (from 0.81

MPa to 1.58 MPa) and 57% (from 0.87 MPa to 1.37 MPa), respectively. And the elastic modulus of the CNT@MS-incorporated electrospun scaffolds (**Fig.4-10 E** and **F**) was greatly improved as compared with the bare scaffolds. These results indicate that the resultant homogeneous dispersion of CNT@MS in electrospun nanofiber matrix leads to reinforcement. Indeed it is assumed that an effective load transfer from the matrix to CNT@MS due to their strong interfacial adhesion is achieved, resulting in a significant enhancement in the tensile properties. However, with the addition of 5 wt% of CNT@MS in alginate and PLA nanofiber matrix, the elongation at break emerged respectively a reduction by 6% and 29% (**Fig.4-10 G** and **H**), indicating a reduction in the ductility of the CNT@MS-incorporated nanofiber, which was probably caused by the stiffening of the fibers due to the adhesion of CNT@MS. Similar results have also been reported in other polymer systems with CNTs incorporated, such as polyamide 6 (PA 6),[67] and poly(3-caprolactone) (PCL).[61]

(2) Photothermal properties of the CNT@MS-incorporated electrospun membranes

In order to evaluate the photothermal properties of the CNT@MS-incorporated electrospun scaffolds, cross-linked Algin/PEO/PF127/CNT@MS membrane and PLA/CNT@MS membrane of similar weight (corresponding to ~90 μg of CNT@MS) were immersed in 1 mL of water and exposed to a 1064 nm NIR laser with a power density at 1 W/cm^2 for 16 min. As shown in **Fig. 4-11**, the temperature change of the solution versus time was recorded during the NIR irradiation. As expected, it was observed that the solution containing CNT@MS-incorporated scaffold exhibited a significant photothermal heating effect. For the solutions with Algin/PEO/PF127/CNT@MS, the temperature profile increased slowly from 24 to 50 ℃ and remained substantially constant with extending exposure time after 14 min of NIR irradiation. Similarly, for the solution containing PLA/CNT@MS scaffold, it was found that the temperature increased from 24 to 46 ℃ with the prolonged irradiation time. In contrast, by looking at the effect of the NIR laser in the solutions containing bare Algin/PEO/PF127 and PLA scaffolds without CNT@MS composites, the temperature showed only a slight change (from ca. 20 to 24 ℃) under the same conditions. The effect of NIR light irradiation on pure water (without CNTs composite material) showed a small increase in T similar to that of the bare scaffolds, confirming the photothermal effect of CNT@MS in the electrospun nanofiber scaffolds. The good photothermal performance of CNT@MS-incorporated alginate and PLA electrospun scaffold make them effective photothermal agents, which is expected to be used in the fields of drug delivery and tissue engineering.

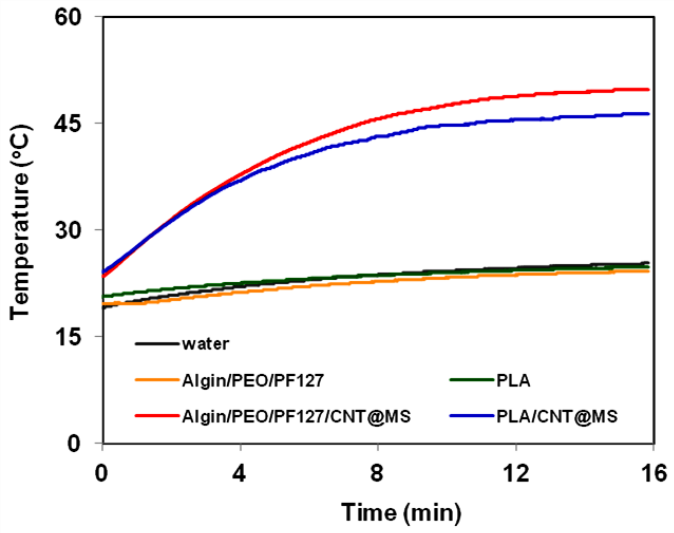

Fig.4-11 Photothermal properties of alginate-based and PLA-based electrospun scaffolds with and without CNT@MS composites

4.3.4 Biological evaluation of the CNT@MS-incorporated electrospun scaffolds

As part of the biological evaluation of membranes, we studied the biocompatibility of the following 4 membranes: PLA and PLA/CNT@MS, Algin/PEO/PF127 and Algin/PEO/PF127/CNT@MS. For this purpose, murine fibroblast cells BALB/3T3 were used. On the 7th day of incubation, environmental scanning electron microscopy analyses were performed to observe cell/material interaction and to monitor the cell morphology.

In terms of results, it appeared that the membranes of alginate (Algin/PEO/PF127 and Algin/PEO/PF127/CNT@MS) are dissolved when they came into contact with ethanol and the culture media. Therefore, the stability of the alginate electrospun scaffolds should be further improved that adapted for the biological tests. On the other hand, for PLA, PLA/CNT@MS membranes, viability tests could be performed (**Fig. 4-12**). The results showed that the PLA nanofibers were somewhat swellen after being immersed in the medium for 7 days but still maintained a good fibrous structure. The observed cell morphologies showed that the cells adhered to the PLA electrospun nanofibers with a spread phenotype corresponding to the classic morphology of normally proliferating fibroblast cells, indicating the good biocompatibility of these PLA electrospun scaffolds with and without CNT@MS incorporated.

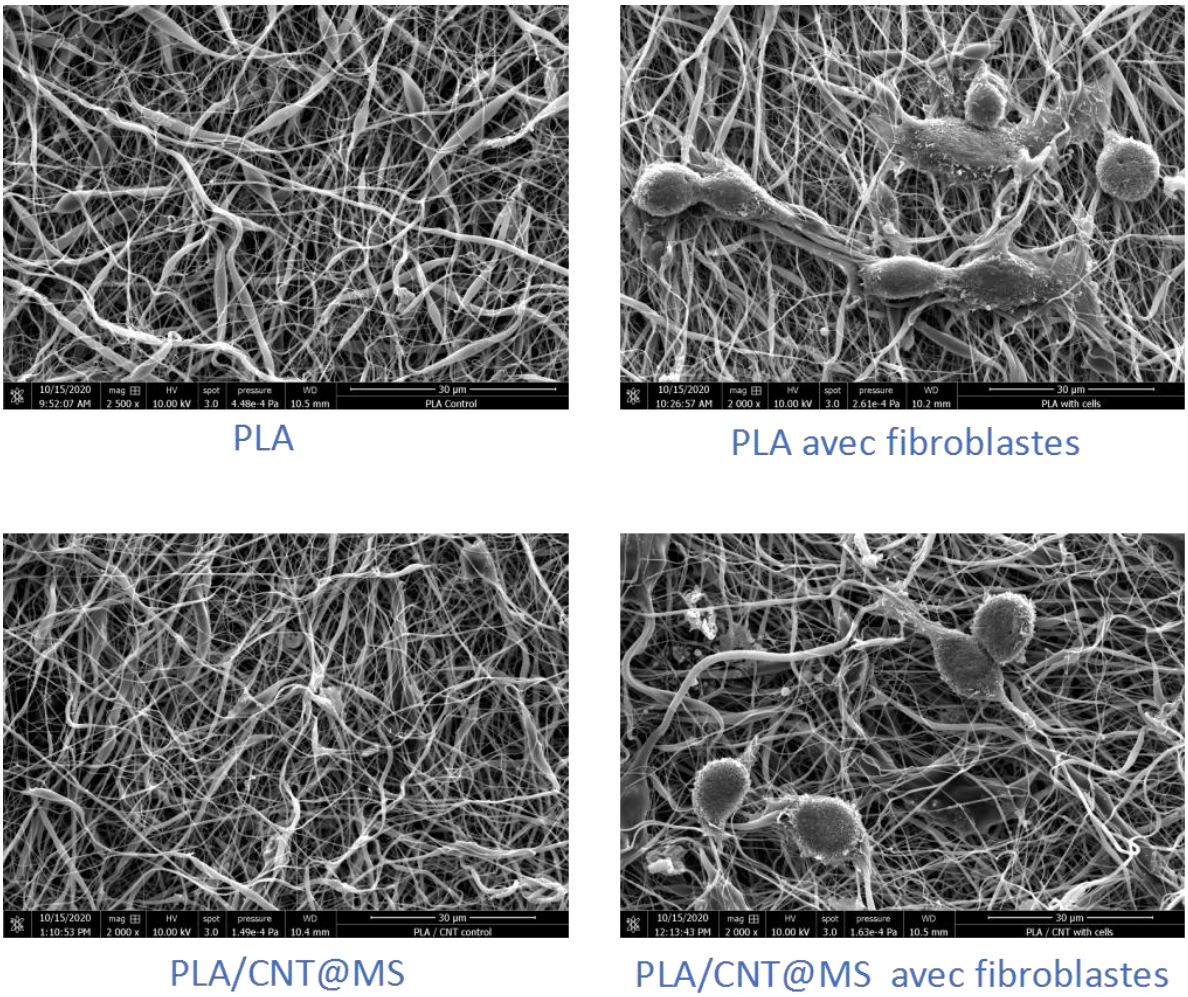

Fig.4-12 Observation by environmental scanning electron microscopy of PLA and PLA/ CNT@MS membranes incubated with and without fibroblast cells (inoculation for 7 days)

4.4 Conclusion

In this work, nanofibrous scaffolds with CNT@MS incorporation in alginate and PLA substrate were successfully prepared through the electrospinning process. The addition of CNT@MS led to a slight decrease in the average diameter of the resulting alginate-based and PLA-based nanofibers. It was observed by SEM that CNT@MS was mainly dispersed on the surface of the polymer nanofiber along the nanofiber axis. The CNT@MS-incorporated nanofiber membrance showed improved tensile mechanical properties, which significantly increased the tensile strength of Algin/PEO/PF/CNT@MS and PLA/CNT@MS membranes by 95% and 57%, respectively. Simultaneously, the embedding of CNT@MS on the polymer fiber also caused a slight decrease in the elongation at break of the resulting electrospun scaffolds. In addition, the CNT@MS-incorporated alginate and PLA nanofiber scaffolds

exhibited good photothermal performance under NIR laser irradiation, resulting in the T increased slowly from 24 to 50 ℃. These results suggested that the electrospinning of the alginate and PLA with addition of CNT@MS is an effective strategy to combine the good mechanical and optical properties of CNTs to fabricate new type of biocompatible and biodegradable nanofiber hybrid scaffolds. Such CNT@MS-incorporated alginate and PLA nanofiber membranes have good prospects as scaffold materials for tissue engineering.

4.5 References

1. J. A. Hubbell, *Nat. Biotechnol.*, 1995, **13**, 565-576.
2. K. Y. Lee and D. J. Mooney, *Chem. Rev.*, 2001, **101**, 1869–1880.
3. D. W. Hutmacher, *Biomaterials*, 2000, **21**, 2529}2543.
4. T. L. Jenkins and D. Little, *NPJ Regen. Med.*, 2019, **4**, 15.
5. F. J. O'Brien, *Materials Today*, 2011, **14**, 88-95.
6. S. Pina, V. P. Ribeiro, C. F. Marques, F. R. Maia, T. H. Silva, R. L. Reis and J. M. Oliveira, *Materials*, 2019, **12**, 1824.
7. M. P. Nikolova and M. S. Chavali, *Bioact. Mater.*, 2019, **4**, 271-292.
8. S. A. Sell, P. S. Wolfe, K. Garg, J. M. McCool, I. A. Rodriguez and G. L. Bowlin, *Polymers*, 2010, **2**, 522-553.
9. F. M. Chen and X. Liu, *Prog. Polym. Sci.*, 2016, **53**, 86-168.
10. T. G. Kim, H. Shin and D. W. Lim, *Advanced Functional Materials*, 2012, **22**, 2446-2468.
11. F. Rossi, M. Santoro and G. Perale, *J. Tissue Eng. Regen. Med.*, 2015, **9**, 1093-1119.
12. M. Zhu, W. Li, X. Dong, X. Yuan, A. C. Midgley, H. Chang, Y. Wang, H. Wang, K. Wang, P. X. Ma, H. Wang and D. Kong, *Nat. Commun.*, 2019, **10**, 4620.
13. T. S. KARANDE, J. L. ONG and C. M. AGRAWAL, *Annals of Biomedical Engineering,*, 2004, **32**, 1728–1743.
14. E. Stodolak-Zych, A. Frączek-Szczypta, A. Wiecheć and M. Błażewicz, *Acta Physica Polonica A*, 2012, **121**, 518-521.
15. U. Hersel, C. Dahmen and H. Kessler, *Biomaterials*, 2003, **24**, 4385-4415.
16. K. Klimek and G. Ginalska, *Polymers*, 2020, **12**, 844.
17. L. Wang, S. Wu, G. Cao, Y. Fan, N. Dunne and X. Li, *J. Mater. Chem. B*, 2019, **7**, 7439-7459.
18. D. K. Patel and K. T. Lim, *Materials*, 2019, **12**, 2950.
19. B. S. Harrison and A. Atala, *Biomaterials*, 2007, **28**, 344-353.
20. A. R. Boccaccini, F. Chicatun, J. Cho, O. Bretcanu, J. A. Roether, S. Novak and Q. Z. Chen, *Advanced Functional Materials*, 2007, **17**, 2815-2822.
21. E. L. Hopley, S. Salmasi, D. M. Kalaskar and A. M. Seifalian, *Biotechnol Adv.*, 2014, **32**, 1000-1014.
22. D. Mata, M. Amaral, A. J. Fernandes, B. Colaco, A. Gama, M. C. Paiva, P. S. Gomes, R. F. Silva and M. H. Fernandes, *Nanoscale*, 2015, **7**, 9238-9251.

23. X. Liu, M. N. George, L. Li, D. Gamble, A. L. Miller Ii, B. Gaihre, B. E. Waletzki and L. Lu, *ACS Biomaterials Science & Engineering*, 2020, **6**, 4653-4665.
24. J. Liu, C. Wang, X. Wang, X. Wang, L. Cheng, Y. Li and Z. Liu, *Advanced Functional Materials*, 2015, **25**, 384-392.
25. L. Zhu, D. Luo and Y. Liu, *Int. J. Oral. Sci.*, 2020, **12**, 6.
26. P. Wick, P. Manser, L. K. Limbach, U. Dettlaff-Weglikowska, F. Krumeich, S. Roth, W. J. Stark and A. Bruinink, *Toxicol. Lett.*, 2007, **168**, 121-131.
27. U. Wirnitzer, B. Herbold, M. Voetz and J. Ragot, *Toxicol. Lett.*, 2009, **186**, 160-165.
28. S. Hirano, Y. Fujitani, A. Furuyama and S. Kanno, *Toxicol. Appl. Pharmacol.*, 2010, **249**, 8-15.
29. S. Vardharajula, S. Z. Ali, P. M. Tiwari, E. Eroglu, K. Vig, V. A. Dennis and S. R. Singh, *Int. J. Nanomedicine*, 2012, **7**, 5361-5374.
30. S. T. R. Naqvi, T. Rasheed, D. Hussain, M. Najam ul Haq, S. Majeed, S. shafi, N. Ahmed and R. Nawaz, *Journal of Molecular Liquids*, 2020, **297**, 111919.
31. C. Wells, O. Vollin-Bringel, V. Fiegel, S. Harlepp, B. Van der Schueren, S. Bégin-Colin, D. Bégin and D. Mertz, *Advanced Functional Materials*, 2018, **28**, 1706996.
32. B. Li, S. Harlepp, V. Gensbittel, C. J. R. Wells, O. Bringel, J. G. Goetz, S. Begin-Colin, M. Tasso, D. Begin and D. Mertz, *Materials Today Chemistry*, 2020, **17**, 100308.
33. S. Jafari, H. Derakhshankhah, L. Alaei, A. Fattahi, B. S. Varnamkhasti and A. A. Saboury, *Biomed. Pharmacother.*, 2019, **109**, 1100-1111.
34. R. K. Kankala, Y. H. Han, J. Na, C. H. Lee, Z. Sun, S. B. Wang, T. Kimura, Y. S. Ok, Y. Yamauchi, A. Z. Chen and K. C. Wu, *Adv. Mater.*, 2020, **32**, e1907035.
35. D. Mertz, S. Harlepp, J. Goetz, D. Bégin, G. Schlatter, S. Bégin-Colin and A. Hébraud, *Advanced Therapeutics*, 2019, **3**, 1900143.
36. G. Sui, D. Liu, Y. Liu, W. Ji, Q. Zhang and Q. Fu, *Polymer*, 2019, **182**, 121838.
37. S. Liang, K. Wang, D. Chen, Q. Zhang, R. Du and Q. Fu, *Polymer*, 2008, **49**, 4925-4929.
38. X. Bai, X. Hu, S. Zhou, J. Yan, C. Sun, P. Chen and L. Li, *Electrochimica Acta*, 2013, **87**, 394-400.
39. L. Li, Y. Yang, G. Yang, X. Chen, B. S. Hsiao, B. Chu, J. E. Spanier and C. Y. Li, *NanoLett.*, 2006, **6**, 1007-1012.
40. H. Deka, N. Karak, R. D. Kalita and A. K. Buragohain, *Carbon*, 2010, **48**, 2013-2022.
41. D. Maziukiewicz, B. M. Maciejewska, J. Litowczenko, M. Kościński, A. Warowicka, J. K. Wychowaniec and S. Jurga, *Surface & Coatings Technology*, 2020, **385**, 125199.

42. H. Liu, X. Ding, G. Zhou, P. Li, X. Wei and Y. Fan, *Journal of Nanomaterials*, 2013, **2013**, 1-11.
43. D. Ahirwal, A. Hébraud, R. Kádár, M. Wilhelm and G. Schlatter, *Soft Matter*, 2013, **9**, 3164.
44. Y. Xu, Y. Zhu, F. Han, C. Luo and C. Wang, *Advanced Energy Materials*, 2015, **5**, 1400753.
45. M. E. Darzi, S. I. Golestaneh, M. Kamali and G. Karimi, *Renewable Energy*, 2019, **135**, 719-728.
46. Z. Xu, R. Zhao, X. Huang, X. Wang and S. Tang, *Carbohydr Polym*, 2018, **197**, 237-245.
47. S.-H. Teng, P. Wang and H.-E. Kim, *Materials Letters*, 2009, **63**, 2510-2512.
48. T. Hu, Q. Li, H. Dong, W. Xiao, L. Li and X. Cao, *Small*, 2017, **13**, 1602610.
49. J. A. Matthews, D. G. Simpson, G. E. Wnek and G. L. Bowlin, *Biomacromolecules*, 2002, **3**, 232-238.
50. A. M. Abdel-Mohsen, D. Pavlinak, M. Cilekova, P. Lepcio, R. M. Abdel-Rahman and J. Jancar, *Int. J. Biol. Macromol.*, 2019, **139**, 730-739.
51. J. Gutierrez-Gonzalez, E. Garcia-Cela, N. Magan and S. S. Rahatekar, *Materials Letters*, 2020, **270**, 127662.
52. D. Tao, Y. Higaki, W. Ma, H. Wu, T. Shinohara, T. Yano and A. Takahara, *Polymer*, 2015, **60**, 284-291.
53. F. Flaig, H. Ragot, A. Simon, G. Revet, M. Kitsara, L. Kitasato, A. Hébraud, O. Agbulut and G. Schlatter, *ACS Biomaterials Science & Engineering*, 2020, **6**, 2388-2400.
54. Y. Luo, H. Shen, Y. Fang, Y. Cao, J. Huang, M. Zhang, J. Dai, X. Shi and Z. Zhang, *ACS Appl. Mater. Interfaces*, 2015, **7**, 6331-6339.
55. B. A. Aderibigbe and B. Buyana, *Pharmaceutics*, 2018, **10**, 42.
56. N. A. Nallamuthu, M. Braden and M. P. Patel, *Dent. Mater.*, 2012, **28**, 756-762.
57. J. Wroblewska-Krepsztul, T. Rydzkowski, I. Michalska-Pozoga and V. K. Thakur, *Nanomaterials*, 2019, **9**, 404.
58. D. da Silva, M. Kaduri, M. Poley, O. Adir, N. Krinsky, J. Shainsky-Roitman and A. Schroeder, *Chem. Eng. J.*, 2018, **340**, 9-14.
59. Y. Ramot, M. Haim-Zada, A. J. Domb and A. Nyska, *Adv. Drug Deliv. Rev.*, 2016, **107**, 153-162.
60. S. Shao, S. Zhou, L. Li, J. Li, C. Luo, J. Wang, X. Li and J. Weng, *Biomaterials*, 2011, **32**, 2821-2833.

61. X. Zhao, J. Luo, C. Fang and J. Xiong, *RSC Adv.*, 2015, **5**, 99179-99187.
62. J. Mirtic, H. Balazic, S. Zupancic and J. Kristl, *Polymers*, 2019, **11**.
63. C. A. Bonino, M. D. Krebs, C. D. Saquing, S. I. Jeong, K. L. Shearer, E. Alsberg and S. A. Khan, *Carbohydrate Polymers*, 2011, **85**, 111-119.
64. C. A. Bonino, K. Efimenko, S. I. Jeong, M. D. Krebs, E. Alsberg and S. A. Khan, *Small*, 2012, **8**, 1928-1936.
65. T. C. Mokhena, M. J. Mochane, A. Mtibe, M. J. John, E. R. Sadiku and J. S. Sefadi, *Materials*, 2020, **13**, 934.
66. T. Yang, D. Wu, L. Lu, W. Zhou and M. Zhang, *Polymer Composites*, 2011, **32**, 1280-1288.
67. F. Zomer Volpato, S. L. Fernandes Ramos, A. Motta and C. Migliaresi, *J. Bioactive and Compatible Polymers*, 2010, **26**, 35-47.

4.6 Supporting information

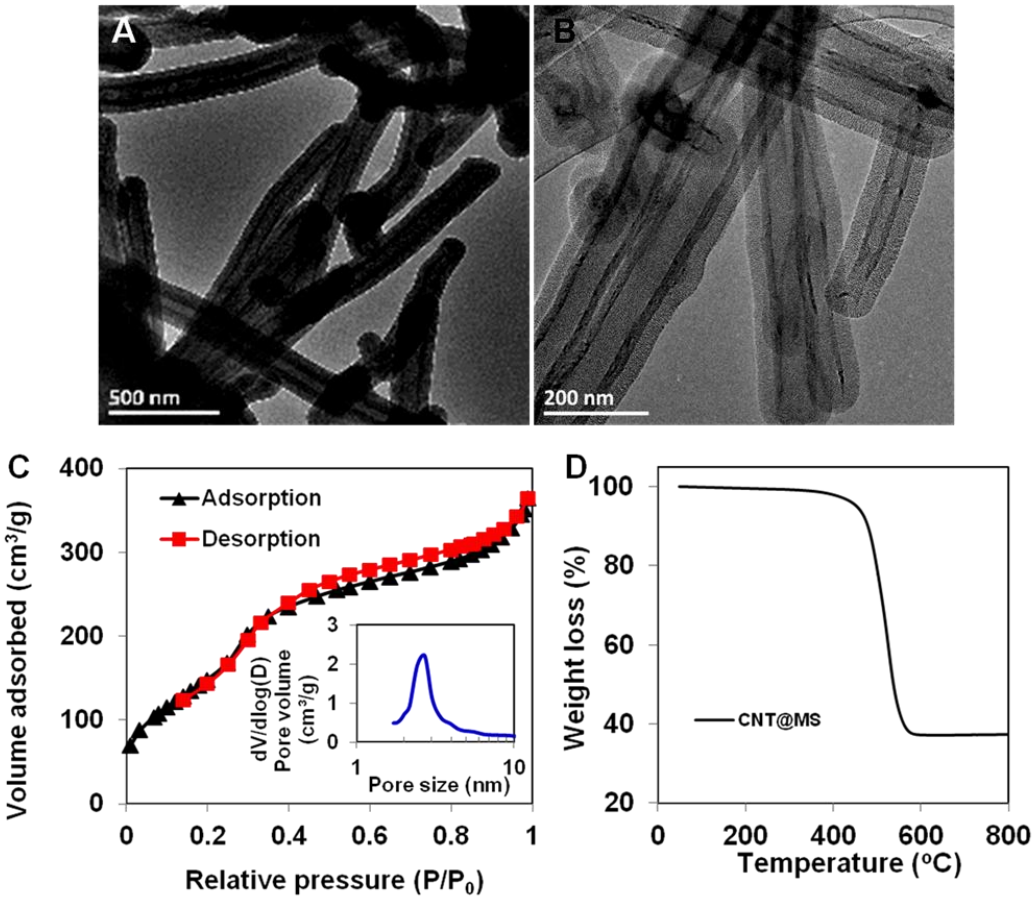

S.4-1 (A, B) TEM images of CNT@MS, (C) nitrogen adsorption-desorption isotherms of CNT@MS composite associated with the pore size distribution, and (D) TGA curve of CNT@MS

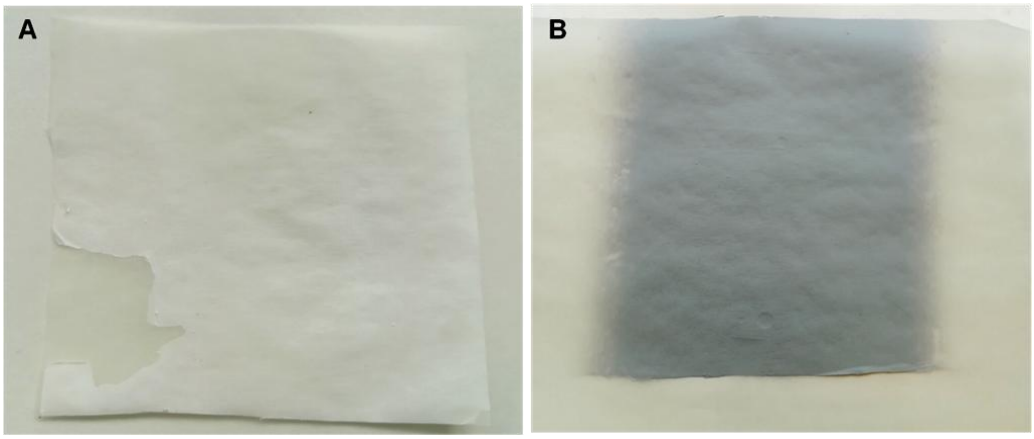

S.4-2 Photographs of (A) Algin/PEO/PF127 electrospun scaffold and (B) Algin/PEO/PF127/CNT@MS electrospun scaffold

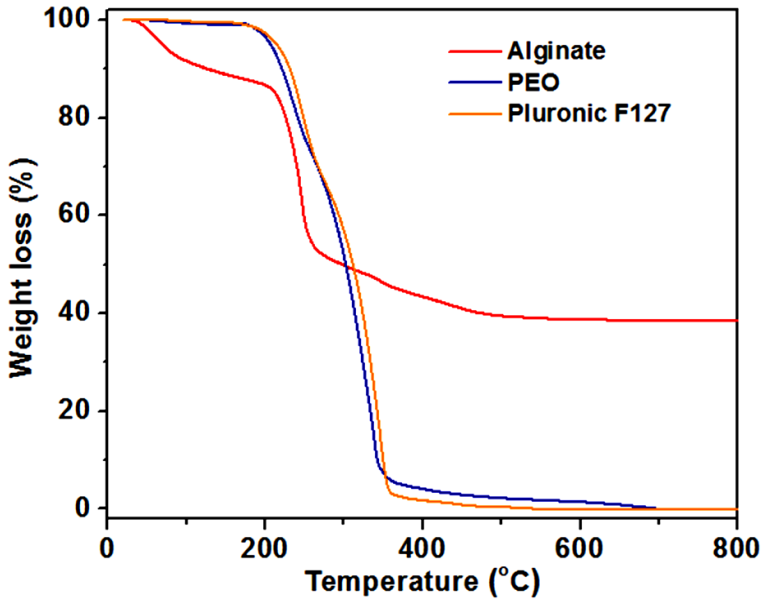

S.4-3 TGA curves of pure alginate, PEO and Pluronic F127 reagents

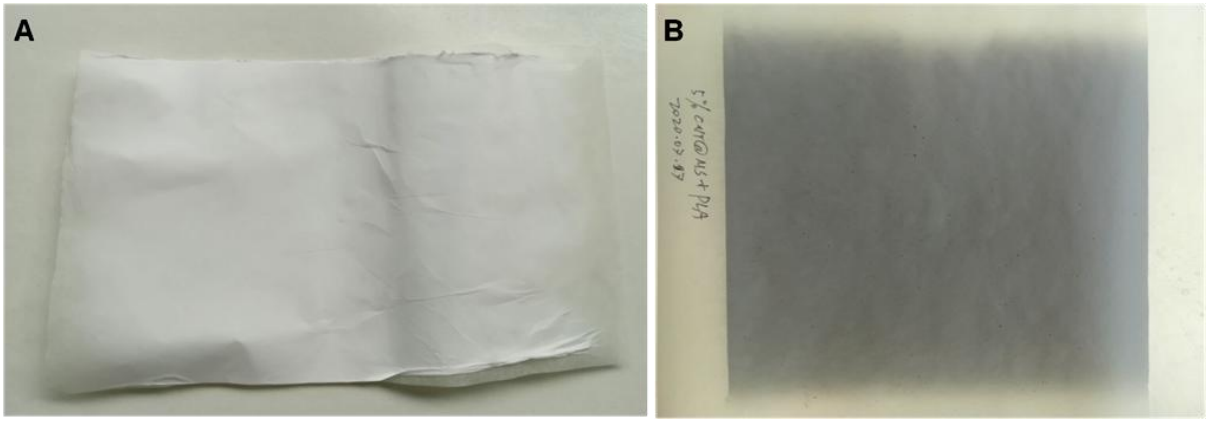

S.4-4 Photographs of (A) PLA electrospun scaffold and (B) PLA/CNT@MS electrospun scaffold

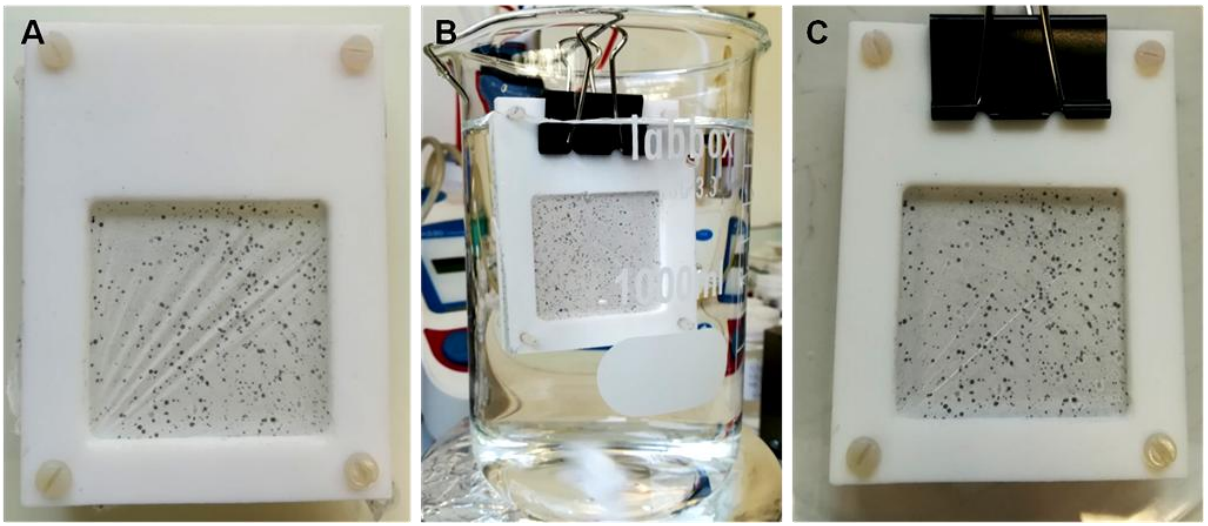

S.4-5 Photographs PLA/CNT@MS (spray) scaffold: (A) before rinsing, (B) during rinsing: immersed in water at room temperature stirring at 300 rpm for 65 h, and (C) after rinsing

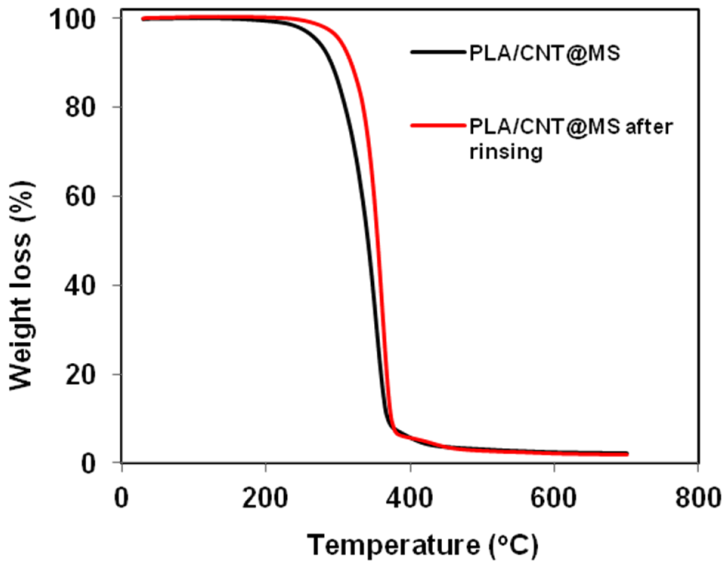

S.4-6 TGA curves of PLA/CNT@MS (spray) scaffold before and after rinsing.

Chapter 5 Conclusion and perspectives

5.1 Conclusion

The general introduction of CBMs/MS hybrid materials with non-porous, small mesoporous pore size and large mesoporous pore size MS matrix and their promising applications in the biomedical field including drug delivery, tissue engineering, imaging, and biosensing were summarized. In this thesis, CNTs as one of the most widely studied materials in carbon based materials were used to synthesize homogeneous mesoporous silica shell coated CNTs composites with tunable pore size. Such CNT@MS composites with small and large pore size were respectively used as nanoplatforms for loading of small MW molecule anticancer drug doxorubicin (DOX) and high MW molecules enzyme alkaline phosphatase (AP), and as components for the construction of hydrogel scaffolds for controllable drug delivery and cancer therapy. Such CNT@MS composites were also used as a reinforcing material to be embedded in the electrospinning nanofiber scaffolds to explore the possibility of being nanoplatforms for tissue engineering applications. The general conclusions obtained in the present work are summarized as follows:

5.1.1 Near infra-red light responsive carbon nanotubes@mesoporous silica for photothermia and drug delivery to cancer cells

In this work, we have designed new NIR light-responsive nanocomposites made of small pore MS shell coated CNTs, loaded with the antitumor drug doxorubicin (DOX), and capped with plasma protein human serum albumin (HSA) as a biocompatible interface and gate keeper. We have developed here a novel way to immobilize DOX with a DLC up to 80%, via the powerful strategy based on IBAM versatile non-covalent binders grafted on CNT@MS shells which additionally allow the tight anchoring of HSA. The photothermal properties of these composites were investigated as a function of their concentration and of the laser power. We found that adjusting the power at $1W/cm^2$ is well suited to control the temperature under the necrosis temperature (45 ℃). These drug-loaded CNT@MS@IBAM-DOX@HSA nanocomposites were shown to release DOX in response to NIR light applied. We demonstrated that this release occurs first by a burst that depends on the concentration of the composites but can also be controlled on a pulsatile fashion as a regular increase of DOX after each NIR light application. We demonstrated that a NIR power of 1 W/cm^2 is efficient to control the release of DOX dose on time. We further demonstrated the cytotoxic potential of DOX-loaded nanocomposites and highlighted a potentially

interesting feature of our nanocomposites: even if photothermic effect from the CNTs composites allows an important cancer cell cytotoxicity, the DOX –mediated release ensure an additional cytotoxicity allowing synergy of both effect to kill cancer cells. Finally, another originality of this work is the integration of such nanocomposites into a hydrogel mimicking the extracellular matrix which can have potential applications in the field of antitumoral scaffolds or polymer matrices for tissue engineering (if DOX is replaced by another molecule). We showed here that the application of NIR light on such nanocomposite hydrogel scaffold covered with D2A1 murine breast cancer cells allows triggering the release of DOX to the cellular media, which results in cell toxicity over time. Hence, such nanosystems may be of huge interest as components of implantable scaffolds for antitumor or tissue engineering applications. This approach would make it possible the development of new (nano) medical devices for the medicine of tomorrow.

5.1.2 Nanocomposite supramolecular hydrogels assembled through enzyme-loaded carbon nanotubes@large pore mesoporous silica for thermally induced drug release

In this work, a facile strategy to trigger the self-assembly of a peptide hydrogel from enzyme-coated CNT@LPMS composites was designed for thermal-induced drug delivery. First, CNTs were coated with a homogeneous large pore mesoporous silica layer, making them particularly suitable for loading high MW biomolecules. It is found that an ultra-high AP loading capacity (up to 400 wt%) was achieved within the porous with the IBAM binders grafted on the silica surface. The excellent AP loading capacity of CNT@LPMS@IBAM composites enabled them to act as initiators of the peptide self-assembly and cross-linking points of the resulting nanocomposite supramolecular hydrogel, allowing local growth of peptide self-assembled nanofibers architecture from the silica surface. In addition, the self-assembly of peptide hydrogel on AP-immobilized carbon-free silica NPs (STMS) with similar pore sizes was also performed, demonstrating the versatility of this surface engineering approach. Furthermore, significant DOX release from these hydrogels was obtained when the DOX-loaded hydrogels were submitted to external high temperature (42 ℃) stimulation. Rheological studies showed that the elastic modulus of these hydrogels increased with the introduction of DOX, while the storage modulus decreased significantly after T (42 ℃) treatment, indicating that the mechanical properties of hydrogels changed after T stimulation and led to the release of DOX. The above results indicate that this nanocomposite supramolecular hydrogels assembled from enzyme-coated large pore mesoporous materials can be used as T-induced thermally responsive controlled release nanoplatforms. The association of CNT@LPMS nanocomposites and self-assembled peptide supramolecular

hydrogels as scaffolds is an innovative strategy, which is expected to be used to develop a new generation of stimuli-responsive drug delivery systems suitable for the biomedical applications.

5.1.3 Electrospun nanofiber composite scaffolds incorporated with carbon nanotubes@mesoporous silica: fabrication, properties and biological evaluation

In this work, nanofibrous scaffolds with CNT@MS incorporation in alginate and PLA substrate were successfully prepared through the electrospinning process. It was observed by SEM that CNT@MS was mainly dispersed on the surface of the polymer nanofiber along the nanofiber axis. The CNT@MS-incorporated nanofiber membrance showed improved tensile mechanical properties, which significantly increased the tensile strength of Algin/PEO/PF/CNT@MS and PLA/CNT@MS membranes by 95% and 57%, respectively. Simultaneously, the embedding of CNT@MS onto the polymer fiber also caused a slight decrease in the elongation at break of the resulting electrospun scaffolds. In addition, such CNT@MS-incorporated alginate and PLA nanofiber scaffolds exhibited good photothermal performance under NIR laser irradiation, resulting in the T increased slowly from 24 to 50 ℃. These results suggested that the electrospinning of the alginate and PLA with addition of CNT@MS is an effective strategy to combine the good mechanical and optical properties of CNTs to fabricate new type of biocompatible and biodegradable nanofiber hybrid scaffolds. Such CNT@MS-incorporated alginate and PLA nanofiber membranes have good prospects as scaffold materials for tissue engineering.

5.2 Perspectives

We have described in this work the promising potential of CNT@MS composites with tunable pore size for biomedical applications. However, there is still much work that can be done to fully understand and truly realize the application of CNT@MS composite materials in the biomedical field. The following summarizes some of the prospects derived from the results obtained in this work.

In the chapter 2, we achieved a very high drug loading capacity on the functionalized CNT@MS composites, but the proportion of DOX release was very low in response to NIR light applied. Therefore, it is necessary to explore new strategies that can achieve high DOX release efficiency.

In chapter 3, the mechanism of thermally-induced DOX release and its influence on the internal structure of the peptide supramolecular hydrogels is not yet well understood and should be in-depth studied. Moreover, the ability of such CNT@LPMS-peptide

supramolecular hydrogels to release DOX in a long-term controlled manner under NIR laser irradiation can be further studied.

In chapter 4, we have confirmed the enhanced mechanical properties and excellent photothermal effect of the CNT@MS-incorporated electrospun nanofiber scaffolds, but the solvent used to synthesize the spinning solution conflicts with the active components to be loaded on CNT@MS composites. Therefore, it is necessary to find effective and reliable strategies to realize the loading of active components on CNT@MS composites for the subsequent applications in tissue engineering.

In addition, the potential toxicity of CNT@MS to organisms and ecosystems is still controversial. Before applying CNT@MS composite materials to the biomedical field, the problem of cytotoxicity must be solved. Therefore, innovative ideas and solutions are needed to develop efficient, safe and feasible bio-nanoplatforms based on CNT@MS hybrid materials.

Bing LI

Design of mesoporous silica-coated carbon nanotubes as components of scaffolds for biomedical applications

Résumé en français

Les nanomatériaux à base de carbone (CBMs), tels que les nanotubes de carbone (CNTs) ou le graphène possèdent des propriétés mécaniques, optiques, électriques et thermiques exceptionnelles, ce qui en fait d'excellentes nano-plateformes pour des applications biomédicales. Dans ce travail, les CNTs ont été utilisés pour synthétiser des composites (CNT@MS) de CNTs enrobés d'une coquille de silice mésoporeuse homogène (MS) avec une taille de pores modulable. Les composites CNT@MS avec des petits pores (3.4 nm) ont été utilisés comme nanoplateformes pour le chargement de molécules antitumorales (DOX) et comme composants pour la construction d'un échafaudage pour la libération contrôlée de médicaments et le traitement du cancer. Ces composites CNT@MS chargés de DOX ont montré leur efficacité pour la libération de DOX sous rayonnement NIR, permettant une synergie de cytotoxicité par photothermie et la DOX pour détruire les cellules cancéreuses. Les composites CNT@MS avec une coque de MS à larges pores (12 nm) (CNT@LPMS) ont été utilisés pour l'immobilisation de la phosphatase alcaline (AP) et une capacité d'immobilisation élevée de l'AP a été réalisée via les groupes isobutyramide (IBAM) greffés à la surface des LPMS. L'AP chargée dans ces composites a conservé son activité enzymatique et a permis de déclencher l'auto-assemblage d'échafaudages d'hydrogels supramoléculaires peptidiques contenant de la DOX. Sous l'effet de la chaleur, ces gels se dégradent et une libération efficace de médicament induite par la chaleur a été obtenue. En outre, ces composites CNT@MS ont été utilisés comme matériau de renforcement à incorporer dans les échafaudages de nanofibres électrofilées. Ces échafaudages électro-filés incorporés de CNT@MS, présentent des propriétés mécaniques améliorées et d'excellents effets photo-thermiques sous irradiation laser NIR.

Mots-clés: Nanotubes de carbone, Silice mésoporeuse, Nanoplateformes enzymatiques, Taille des pores ajustable, Électrofilage, Administration de médicaments, Ingénierie tissulaire

Résumé en anglais

Carbon based materials (CBMs), such as carbon nanotubes (CNTs) and graphenes, possess outstanding mechanical, optical, electrical and thermal properties, making them excellent nanoplatforms for biomedical applications. In this work, CNTs were used to synthesize homogeneous mesoporous silica (MS) shell coated CNTs composites (CNT@MS) with tunable pore size. Such CNT@MS composite with small pore size (3.4 nm) were used as nanoplatforms for loading of molecule anticancer drug (DOX) and as components for the construction of hydrogel scaffold for controllable drug delivery and photothermia-based cancer therapy. These DOX-loaded CNT@MS composites showed the release of DOX in response to NIR light applied, allowing synergy of photothermic and DOX -mediated cytotoxicity effect to kill cancer cells. The CNT@MS composites with large pore (12 nm) MS shell (CNT@LPMS) were used for immobilizing alkaline phosphatase (AP), and a high immobilization capacity of AP was realized via isobutyramide (IBAM) grafts at the surface of LPMS layer. These AP-immobilized CNT@LPMS composites were further applied to trigger the self-assembly of DOX-containing peptide supramolecular hydrogel scaffolds, and a effective heat-induced drug release was achieved through gel degradation. Furthermore, these CNT@MS composites were used as reinforcing material to be embedded in electrospun nanofiber scaffolds. These CNT@MS-incorporated electrospun scaffolds exhibited enhanced mechanical properties and excellent photothermal effect under NIR laser irradiation.

Keywords: Carbon nanotubes, Mesoporous silica, Enzymatic nanoplatforms, Tunable pore size, Electrospinning, Drug delivery, Tissue engineering